New approaches to radionuclide imaging of cancer with gallium-68

Imberti, Cinzia

Awarding institution:
King's College London

New approaches to radionuclide imaging of cancer with gallium-68

A thesis submitted by

Cinzia Imberti

In partial fulfilment of the requirements for the degree of

Doctor of Philosophy

University of London

2018

School of Biomedical Engineering and Imaging Sciences

King's College London

Abstract

The positron emitting isotope ^{68}Ga is gaining increasing interest in the radionuclide imaging community, due to its favourable decay properties and availability from a generator. Incorporation of ^{68}Ga into biomolecules requires conjugation to a bifunctional chelator. The *tris*(hydroxypyridinone) ligand THP^{Me} is a valuable chelator for ^{68}Ga, being able to coordinate Ga(III) effectively in extremely mild conditions. These outstanding radiolabelling properties prompted further investigation of THP^{Me}, as a prototype to develop improved *tris*(hydroxypyridinone) chelators, and as a tool to explore new strategies for cancer imaging with ^{68}Ga.

In the first part of this project, a new *tris*(hydroxypyridinone) chelator, THP^{H}, was developed, where the N^{1}-methyl group in the hydroxypyridinone ring was replaced by hydrogen. A new synthetic strategy was developed to achieve this. Quantitative ^{68}Ga labelling of THP^{H} was achieved in mild conditions and *in vivo* stability of the radiolabelled complex demonstrated. Spectrophotometric titration and competition experiments revealed preference for Ga(III) over Fe(III) for both THP^{Me} and THP^{H}, with the latter possessing higher Ga(III) selectivity. A library of THP derivatives is potentially available from an intermediate in THP^{H} synthesis as a result of the new strategy.

In a second part of this work, the ability of THP^{Me} to interfere with ^{68}Ga trafficking in biological systems was investigated. THP^{Me} (24 nmol) was found able to chelate ^{68}Ga *in vivo*, significantly accelerating its renal excretion in mice. We therefore explored use of THP^{Me} as a blood clearance agent, to increase the tumour-to-blood activity ratio in the context of cancer imaging with ^{68}Ga salts. Initial evaluation of THP^{Me} in a melanoma model lead to inconclusive results, due to inconsistency of ^{68}Ga-acetate biodistribution. However, successive evaluation in a colon cancer xenograft showed a three-fold increase in tumour-to-blood ratio for mice treated with THP^{Me} compared to a control group, demonstrating THP^{Me} potential as a blood clearance agent in this model.

Finally, a new pretargeting strategy for ^{68}Ga imaging with antibodies was investigated, based on the *in vivo* chelation of ^{68}Ga(III) by a pretargeted THP^{Me}-antibody conjugate. Two THP^{Me}-antibody conjugates were prepared by attachment of THP^{Me} derivatives to non-internalising antibodies and their favourable ^{68}Ga labelling properties and affinity for their target antigen verified. However, *in vitro/in vivo* evaluation, showed no pretargeting ability for either of these compounds, likely due to a low availability of THP^{Me}-antibody conjugates at the antigen site and to competitive binding of ^{68}Ga by transferrin or other proteins.

Declaration

I Cinzia Imberti confirm that no part of this thesis has been submitted in support of any other application for a degree or qualification of King's College London, or any other university or institute of learning. I confirm that this work is my own. Where information has been derived from other sources it has been indicated in this thesis.

The copyright of this thesis rests with the author and no quotation from it or information derived from it may be published without proper acknowledgement.

Acknowledgments

Thank you to all the people in KCL that helped me in these years, thanks to Dr Kavitha Sunassee, Dr Jayanta Bordoloy, Dr Julia Baguna Torres and Dr Nisha K. Ramakrishnan for the help with the preclinical facility. Thanks to Soba Akinwunmi, Davide Poccecai and the rest of the IT team for being so efficient and friendly! Thanks to Barry Crook, Steve Catchpole and David Thakor for their excellent lab management. Thank you, David, also for all the fun (and foolishness) in the lab all these years, I think that department without you would be a gloomy place to work in!

Thanks to all the PhD, master and undergraduate students that I had the pleasure to work with during these years. Thank you Maria, Calum, Catherine, Yifu, Tasnim, Joanna and Fahad for all your enthusiasm and passion, I feel honoured to have been able to help you during your projects. Thank you Jen for being an amazing lab buddy during these years, despite both of us being determined and competitive we have always managed to work nicely as a team (may be because you are ESTJ and I am ENTP?!). I could not have asked for a better companion for this journey!

A special thank you to all the postdocs who have held my hand in the lab in these years. Thank you for the enthusiasm, passion and tenacity that you were able to infect me with. In particular, thanks to Dr Brett Paterson for all the chemistry tips and the lifelong lesson that I can survive without a mass spectrometer (TLC for life!)! Thanks to Dr Samantha Terry, for teaching me to love biology (almost) as much as chemistry, for introducing me to the magic world of radiobiology and last, but not least, for supporting me in these last few months of writing! Thank you to Dr Julia Blower for your tireless help with all sorts of experiments, for all the early mornings and late evenings together, and for teaching me some of my favourite English terms (which would not be appropriate to write in these thesis)! Special thanks to Dr Levente Meszaros who, despite stubbornly refusing to be my postdoc, has been giving me so many useful advices (and thesis writing reminders!) to greatly make up for it.

The biggest of the thank you though goes to Dr Michelle Ma for all the incredible help, support and friendship during these four years. I started off as a scared little girl trotting behind you in the lab (understanding half of what you were saying with your Aussie accent!) and I am now submitting my thesis and having an exciting future ahead. Needless to say, I would not be here without you! Thanks for all the advices, the laughs, the revisions, the moment of despair and those of excitement! I am sure IB claims to be your first PhD student, but you must agree I was the first (unofficial) one.

I would also like to thank all the other friends in the Imaging Chemistry Group for making those years so incredible! Special thanks go to Brett for being the best desky

ever, to Andrea and Bruce, who started this journey with me, to my Aussie soulmate Jackie (I am coming soon!), and to my little Padawans Peter and Truc (good luck with being the new me!).

Finally, I would like to thank those people that more than any other have been there for me, you have witnessed the best and worst of me and (quite incredibly!) you are still here. Thank you Mattia, for your unbelievable persistence in being my friend over the past 10 years, despite the distance and the busyness of our lives. Thank You Filippo for our chats, the Disney sing-along, our inner jokes and all the laughs. Thank You Alessia for the never-ending conversations/phone calls/skype calls about the most trivial and serious things. Teresa and Salvo, I don't think I can possibly thank you enough for being my rocks in all these crazy years and for always standing on my side no matter what. Thanks to all of you for every single smile you were able to put on my face even when I thought I forgot how to do it.

Thank you to my partner, Michele for keep standing next to me, despite the distance and the small and big difficulties we went through in these years. New exciting adventures are beginning now for both of us, and if once again we will be far, once again we will go through this together, as we always do.

The final and warmest thank you goes to my family, to mamma Franca and papà Armando, for being my biggest supporters and for loving me unconditionally.

Table of contents

List of Abbreviations

ANOVA	Analysis of variances
AUC	Area under the curve
BFC	Bifunctional Chelator
BSA	Bovine serum albumin
bsmAb	Bispecific monoclonal antibody
CEA	Carcinoembryonic Antigen
CPM	Counts per minute
CPS	Counts per seconds
CT	Computed Tomography
DFO	Desferrioxamine, Deferoxamine, DFO-B
DEAD	Diethylazodicarboxylate
DIPEA	Diisopropylethylamine
DMA	Dimethylacetamide
DMEM	Dulbecco's Modified Eagle Medium
DMF	Dimethylformamide
DMSO	Dimethylsulfoxide
DOTA	1,4,7,10-tetraazacyclododecane-1,4,7,10-tetraacetic acid
DOTATOC	DOTA0-D -Phe1-Tyr3-octreotide
EC	Electron Capture
EMA	European Medicinal Agency
EDTA	Ethylenediaminetetraacetic acid
EGFR	Epidermal growth factor receptor
Fab	Antigen binding Fragment
FDA	Food and Drug Administration
FSC	Fusarinine-C
GLP-1R	Glucagon like peptide-1 receptor

GRPR	Gastrin-releasing peptide receptor
HATU	1-[Bis(dimethylamino)methylene]-1H-1,2,3-triazolo[4,5-b]pyridinium 3-oxide hexafluorophosphate
HBED	N,N'-bis(2-hydroxybenzyl)ethylenedinitrilo-N,N'-diacetic acid
HBSS	Hanks' Balanced Salt solution
HER2	Human Epidermal Growth Factor Receptor 2
HOBt	1-hydroxybenzotriazole
HP	Hydroxypyridinone
HPLC	High Performance Liquid Chromatography
HSA	Human serum albumin
ID	Injected dose
IEDDA	inverse electron demand Diels-Alder
iTLC-SG	Instant Thin Layer Chromatography-Silica Gel
kDa	Kilodalton
KEMP	cis-cis-1,3,5-trimethylcyclohexane-1,3,5-tricarboxylic acid
KeV	Kiloelectron volt
mAb	Monoclonal antibody
MALDI	Matrix-assisted laser desorption /ionization
MeV	Mega electron volt
MKSCC	Memorial Sloan Kettering Cancer Centre
MRI	Magnetic Resonance Imaging
MSA	Mannosylated albumin
MWCO	Molecular Weight Cut Off
NET	Neuroendocrine tumour
NFB	N-terminal 4-fluoro-benzoyl group
NOTA	1,4,7-triazacyclononane-1,4,7-triacetic acid
NSG	NOD scid gamma
NTP	Nitrilopropionic acid

PBS	Phosphate Buffered Saline
PCTA	3,6,9,15-tetraazabicyclo[9.3.1]pentadeca-1(15),11,13-triene-3,6,9,-triacetic acid
PET	Positron emission tomography
pKa	Acid dissociation coefficient
PRRT	Peptide receptor radionuclide therapy
PSMA	Prostate Specific Membrane Antigen
PVP	pulmonary vascular permeability
RCF	Relative Centrifugal Force
RCY	Radiochemical yield
Rf	Retention Factor
RGD	Arginine–glycine–aspartic acid
SDS	Sodium dodecyl sulfate
SDS-PAGE	sodium dodecyl sulfate polyacrylamide gel electrophoresis
SEP	Solid phase extraction
SLN	sentinel lymph node
SPECT	Single photon emission computed tomography
SSTR	Somatostatin receptor
TACN	1,4,7-Triazacyclononane
TAFC	Desferri-triacetylfusarinine C
TCEP	*tris*(2-carboxyethyl)phosphine
TEMED	Tetramethylethylenediamine
Tf	Transferrin
TFA	Trifluoroacetic acid
TfR	Transferrin receptor
TRIS	*tris*(hydroxymethyl)aminomethane
WBC	White blood cells

1 Chemistry of gallium and its interaction with biological systems: a radiochemistry perspective.

The chemistry of gallium, including the properties of its most important radioactive isotopes, is briefly reviewed in this chapter, and the interactions of this exogenous element with biological systems are described. It is beyond the scope of this review to comprehensively discuss gallium chemistry and biology. Owing to the nature of this research work, and to the paramount importance of gallium in nuclear medicine, a radiochemistry perspective is adopted throughout the chapter.

1.1 Radioactive isotopes of gallium

Natural gallium exists in two stable isotopes: ^{69}Ga and ^{71}Ga, which represent 60.1 % and 39.9 % of natural gallium, respectively. Several radioactive isotopes can be obtained synthetically. The most common radioisotopes are summarised in the table below.

Table 1.1. *Main radioisotopes of gallium.*

Isotope	Half-life	Decay mode	Emissions (keV)	Decay product	Reference
^{66}Ga	9.5 hours	43 % EC 57 % β$^+$	511 (γ) 4153 (β$^+$)	^{66}Zn	[1]
^{67}Ga	78 hours	EC	93, 184, 300 (γ) 84, 92 (IC e$^-$) 7.4, 8.4, 9.5 (Auger e$^-$)	^{67}Zn	[1,2]
^{68}Ga	68 min	10 % EC 90 % β$^+$	511 (γ) 1900 (β$^+$)	^{68}Zn	[1]
^{72}Ga	14.3 hours	100 % β	640, 960, 1480 (β) 630, 840, 2200, 2500 (γ)	^{72}Ge	[3]

1.1.1 Gallium-67

^{67}Ga is a cyclotron-produced isotope, obtained by proton irradiation (beam energy: 20 MeV) of enriched zinc, according to the nuclear reaction ^{68}Zn(p, 2n)^{67}Ga [4]. Alternatively, it can also be produced by irradiation with deuteron (8 MeV) or α-particles, according to the reactions ^{66}Zn(d, n)^{67}Ga and ^{64}Zn(α, p)^{67}Ga, respectively [4]. ^{67}Ga decays to stable ^{67}Zn by electron capture (EC) with a half-life of 78.26 hours. The decay is accompanied by an emission of de-excitation gamma-rays in the energy range

91-393 keV that can be useful for imaging studies with gamma camera imaging or single-photon emission computed tomography (SPECT) [1]. However, the resolution and contrast achievable for ^{67}Ga SPECT images is limited by the presence of different photopeak energies, combined with the down-scatter from high energy photons into lower energy windows [5]. Auger electrons of relatively high energy (7-9 keV) and long range (up to 2.4 μm in water) are also produced following electron capture, making gallium-67 worth investigating as a therapeutic radionuclide [2,6].

1.1.2 Gallium-68

^{68}Ga decays to stable ^{68}Zn by positron emission ($β^+$ yield: 89 %, E_{max} = 1.89 MeV, maximum positron range in water R_{max} = 9.2 mm [7]) with a half-life of 68 min. Annihilation of the emitted positron by an electron, results in the generation of two 511 keV photons with an angle of approximately 180° that are detected in Positron Emission Tomography (PET) scans. Owing to its short half-life, gallium-68 is commonly used to radiolabel receptor-targeting peptides through a bifunctional chelator (BFC). The most prominent clinical applications of this isotope are described in **Chapter 2**.

^{68}Ga generator

Gallium-68 is most commonly obtained from germanium-68/gallium-68 generators, which allow steady, and relatively inexpensive, availability of ^{68}Ga in centres without access to a cyclotron. In these long shelf-life, bench-top generators, the parent isotope ^{68}Ge^{4+} ($t_{1/2}$ = 271 days) is immobilised on a lead shielded glass column containing an organic/inorganic matrix, and decays over time to the daughter radionuclide ^{68}Ga by electron capture. Separation of the two radioisotopes exploits the different chemical properties of the two radiometals [1,8] and consists of selective elution of ^{68}Ga^{3+} using an appropriate mobile phase.

The first generators used Al_2O_3 as a solid phase and ^{68}Ga was selectively eluted with ethylenediaminetetraacetic acid (EDTA). The [^{68}Ga(EDTA)] complex produced by these generators could be used directly as a radiotracer (see **Chapter 2**), but transchelation to other ligands was challenging due to the thermodynamic stability of the EDTA complex [9]. Modern generators use several different combinations of solid/mobile phase, but they all produce gallium in an unchelated ionic form [8]. In the pharmaceutical grade Eckert & Ziegler generator that has been used in this thesis, germanium-68 is adsorbed on a TiO_2 bed contained in a borosilicate glass column. ^{68}Ga is eluted with ultrapure 0.1 M hydrochloric acid to yield Ga^{3+} as a chloride salt [10]. ^{68}Ga elution yield for a new generator, ranges between 70-80 % and decreases with the increase of the generator age. Daily elution of the generator minimises the level of co-

eluted ^{68}Zn. Because gallium-68 is continuously produced in the generator, multiple elutions can be performed in a day, with half of the maximum achievable activity already accumulated at one-hour post-elution.

Although extremely convenient, generator-production of gallium-68 still presents several drawbacks, which decrease the radiolabelling efficiency and specific activity achievable. Trace metal contamination from natural elements (aluminium, iron, titanium, lead *etc.*) as well as from ^{68}Zn and ^{68}Ge, is a major issue since those metals can compete with ^{68}Ga for chelator binding [10]. The use of large mobile phase volume for ^{68}Ga elution is another issue, resulting in low ^{68}Ga^{3+} concentration, which also can hamper radiolabelling. Several processing procedures have been developed to address these issues, mainly based on anion/cation exchange chromatography to concentrate and purify the eluate [10,11]. On the other hand, these techniques add complexity to the radiolabelling procedure and increase the time required for radiolabelling.

1.1.3 Other gallium isotopes

The positron emitting isotope gallium-66 has a convenient half-life of 9.5 hours. Nonetheless, the low positron yield and the very high energy associated with its decay, which impairs spatial resolution, are not ideal for radionuclide imaging. Therefore, ^{66}Ga has received little attention by the radiochemistry community [12].

Gallium-72 was used in many of the early nuclear medicine experiments. However, its production, by neutron irradiation of ^{71}Ga, resulted in the presence of large amount of stable gallium (carrier-added radioisotope) in the final product, thus limiting the specific activity achievable for this isotope [13]. With the advent of gallium-67 the use of gallium-72 in nuclear medicine was abandoned.

1.2 Coordination chemistry of gallium

Gallium (Ga) has an atomic number of 31 and electronic configuration of [Ar] *3d[10] 4s[2] 4p[1]*; it belongs to the 13th group and 4th period of the periodic table. Gallium is mainly found in its Ga(III) oxidation state, which dominates its aqueous chemistry. Ga(III) is an amphoteric ion and, similarly to Al(III), its aqua ion $[Ga(H_2O)_6]^{3+}$ is present in acidic conditions. Hydrolysis of this species occurs when raising the pH according to equations below.

$$[Ga(H_2O)_6]^{3+} + H_2O \rightleftarrows [Ga(OH)(H_2O)_5]^{2+} + H_3O^+$$

$$[Ga(OH)(H_2O)_5]^{2+} + H_2O \rightleftarrows [Ga(OH)_2(H_2O)_4]^+ + H_3O^+$$

$$[Ga(OH)_2(H_2O)_4]^+ + H_2O \rightleftarrows [Ga(OH)_3]_{(s)} + H_3O^+ + 3H_2O$$

$$[Ga(OH)_3]_{(s)} + OH^- \rightleftarrows [Ga(OH)_4]^-$$
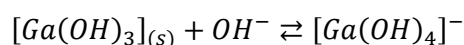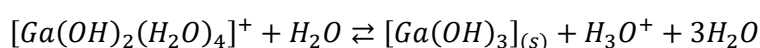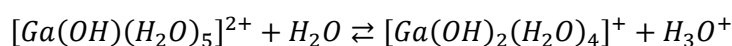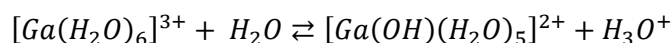
When the pH is raised above 3 poorly soluble hydroxide species dominate, while at higher pH these species re-dissolve as gallate $[Ga(OH)_4]^-$ [14], which represents 98 % of gallium in aqueous solution at pH > 7.4 [15]. At this pH, the maximum gallate concentration achievable without exceeding the solubility of $[Ga(OH)_3]$ was calculated to be 2.5 µM [16]. The predisposition of gallium towards extensive hydrolysis in aqueous solutions and in the mid pH range can hamper its ability to form complexes with multidentate ligands, whose complexation kinetics are often too slow to prevent formation of gallium hydroxide species. Therefore, for radiopharmaceutical applications, addition of stabilising ligands is usually required and complex formation occurs via ligand exchange reactions [17].

The ionic radius of Ga(III) as an hexacoordinated ion in solution is 62 pm (Shannon effective ionic radius) [18]. This value is larger than that found for Al in the same conditions (53.5 pm), but similar to that of Fe(III) in hexadentate high-spin complexes of this ion (64.5 pm). This resemblance to high-spin Fe(III) is not limited to oxidation state and ionic radius, but is also reflected in gallium coordination chemistry, which mainly consists of hexacoordinate complexes with ligands containing hard Lewis bases as donor atoms, such as oxygen and nitrogen.

Over the past three decades many different chelators have been explored for Ga(III) coordination and have been described in detail in several reviews [19-22]. Far from being exhaustive, this section aims to review the most important Ga(III) chelators for radiopharmaceutical applications. Ideally, the perfect chelator for radiotracer development (i) possesses fast complexation kinetics, (ii) forms a single species upon

radiolabelling and (iii) does not dissociate *in vivo*. Quick complex formation under mild reaction conditions is important to match the short half-life of ^{68}Ga and to allow radiolabelling of sensitive biomolecules. Stability and sufficient kinetic inertness of the resulting complex are required to avoid transchelation to serum proteins and to prevent dissociation *in vivo*. Finally, ligands leading to a single geometric isomer upon gallium complexation are preferred and more easily translatable into clinics.

The molecular structures of Ga(III) complexes presented in the following paragraphs were obtained from published crystal structures using the software Mercury 3.9 [23]. Gallium atoms are labelled and coloured in green, the other elements are coloured as follows: carbon = grey, nitrogen = light-blue, oxygen = red, phosphorous = orange. Hydrogen atoms are omitted for clarity. Gallium hexacoordinated complexes of bidentate, tridentate and hexadentate ligands can all exhibit two enantiomers, depending on the absolute configuration of the ligand about the metal centre. For clarity reasons only one of the enantiomers is represented for each complex structure. The different complexes will be described using a $[M(L)_n]$ notation. For ease of nomenclature, protonation states and charges will not be included in the ligands and complexes formulas.

When available, stability constant for the Ga(III) complexes are also reported. Generally, these are determined by spectrophotometric or potentiometric titration of the gallium complexes, assessing the competition between the investigated complex and $[Ga(H_2O)_6]^{3+}$ (titration with HCl), $[Ga(OH)_4]^-$ (titration with NaOH or KOH), or another complex for which stability constants are known (frequently $[Ga(EDTA)]$). However, these methods allow only a short equilibration period for the system which may not be sufficient to achieve thermodynamic equilibrium for the Ga(III) complex. Therefore, some authors prefer to use out-of-cell titration experiments (also referred to as "batch" titrations), where several separate samples, representing different points in the titration curve, are prepared and kept under an inert atmosphere until equilibrium is reached before measurement is performed [24]. Whenever, an out-of-cell equilibrium constant is reported it will be indicated in the text.

1.2.1 Polyaza macrocycles

Macrocycles containing multiple nitrogen atoms are among the most widely used ligands for metal-based radiotracers and lanthanide-based contrast agents for Magnetic Resonance Imaging (MRI) [21]. They represent the most prominent class of chelators for gallium and have been used in several ^{68}Ga-based radiotracers. Owing to the constrained geometries and pre-organised structures of macrocyclic ligands, their metal complexation increases the entropy of the system more than metal coordination by an acyclic chelator. This phenomenon, referred to as the "macrocycle effect" adds a thermodynamic drive to complex formation for these chelators. Macrocyclic ligands also present an increased kinetic inertness compared to acyclic chelators, which, on one hand, enhances the *in vivo* stability of their metal complexes, but on the other hand, it often results in slower complexation kinetics. The most common macrocyclic chelators for Ga(III) complexation are described below and their structure presented in **Figure 1.1**.

DOTA   **PCTA**   **NOTA**

$R_1 = R_2 =$ H **TRAP**

$R_1 = R_2 =$ COOH

TRAP-Pr

$R_1 =$ COOH

$R_2 =$ OH

NOPO

R = Me **DATA-m**

$(NH_2)_2$**sar**
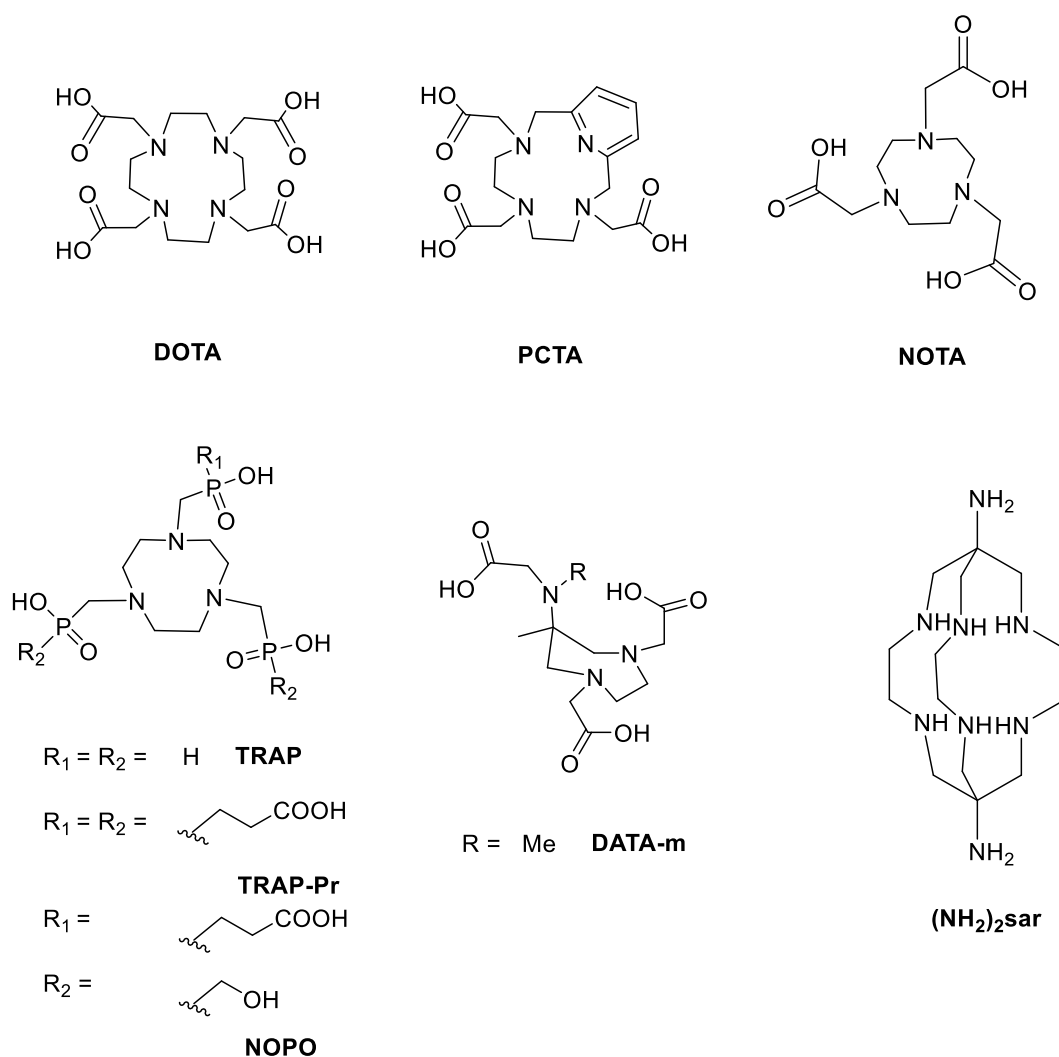
Figure 1.1. *Common macrocyclic chelators for Ga(III).*

DOTA is a cyclen type (1,4,7,10 tetra-azacyclododecane) chelator where each nitrogen atom has a pendant acetic acid group attached. It can coordinate Ga(III) in a distorted octahedral fashion through the four nitrogen atoms and two oxygen atoms from *trans* carboxylate groups, with Ga(III) being puckered from the N_4-plane by 0.84 Å, rather than sitting in the macrocycle cavity (**Figure 1.2**) [25]. Conveniently, one of the non-bonding carboxylate groups can be used to conjugate the chelator to a biomolecule either directly via amide bond formation or through functionalisation with an alternative reactive motif. Functionalisation can also be achieved by replacing one of the acetic acid arms with a glutaric acid (DOTAGA, **Figure 1.2**) or by modifying the cyclen scaffold of the chelator (*e.g.* p-SCN-Bn-DOTA, **Figure 1.2**) [22].
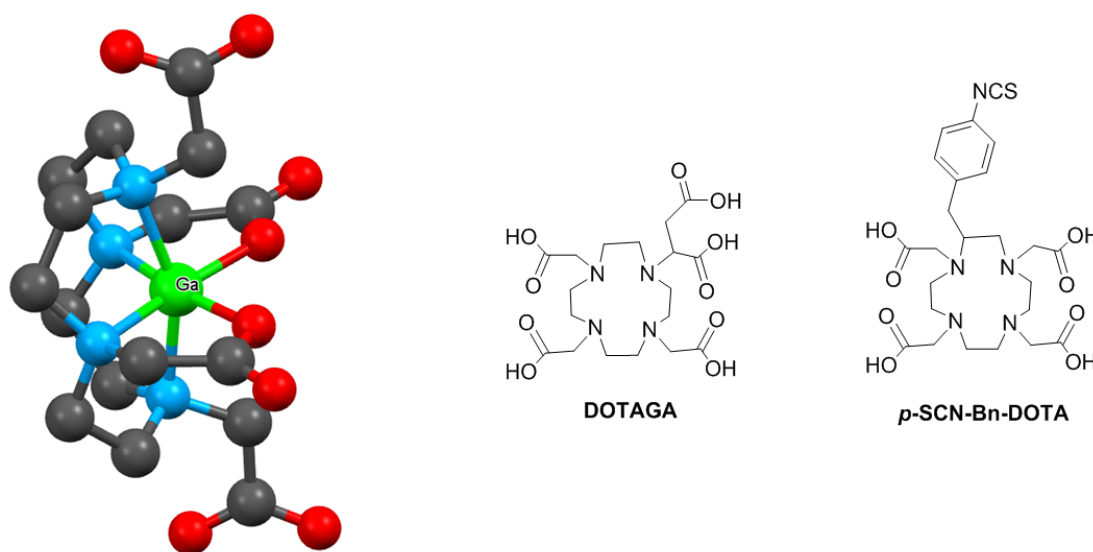
Figure 1.2. *Representation of the molecular structure of [Ga(DOTA)] as determined by X-ray crystallography (left) [25], and schematic structure of some DOTA-based bifunctional chelators.*

The thermodynamic affinity of this chelator for gallium (Log$K$ = 21.3) is lower than for other M^{3+} ions (and notably lower than for Cu^{2+}) [19,26], although a more recent out-of-cell measurement revealed a higher stability constant for this complex (Log$K$ = 26.05) [27]. Owing to a slow complexation kinetics for [Ga(DOTA)], quantitative [68/67]Ga radiolabelling of DOTA derivatives for clinical imaging use requires harsh conditions (heating 80-90 °C, pH < 5) and subsequent purification to remove unreacted ^{68}Ga and physiologically incompatible buffer component. This is not ideal for simple daily production of ^{68}Ga radiopharmaceuticals and precludes the possibility of ^{68}Ga labelling of sensitive biomolecules [19,28]. On the other hand, DOTA still represents one of the most popular chelators for ^{68}Ga, owing to the kinetic inertness of its Ga(III) complexes, but mainly to the widespread application of this chelator in radiochemistry and the subsequent availability of several bifunctional DOTA derivatives [19].

The macrocycle chelator PCTA (**Figure 1.1**) displays a similar structure, but incorporates a pyridine ring in the macrocycle [29,30]. Its bifunctional version *p*-NO$_2$-Bn-PCTA exploits a p-NO$_2$-benzyl attached to the scaffold to allow for functionalisation. Compared to DOTA this chelator possesses a lower stability constant for Ga(III) [29], but faster radiolabelling kinetics, with quantitative ^{68}Ga radiolabelling quickly achieved at room temperature and low concentration in the 3-5 pH range [31]. Preliminary preclinical studies showed sufficient stability *in vivo* and favourable biodistribution [32]; however, this chelator has only received limited attention due to the concomitant development of novel ligands, more specific for Ga(III).

1,4,7-Triazacyclononane (TACN) chelators display lower energies of activation to Ga(III) complexation than their cyclen analogues and possess an increased thermodynamic affinity for Ga(III) due to their smaller cavity size, which results in complexes with lower ring strain [33]. Accordingly, their use as ^{68}Ga chelators have rapidly increased over the past decade. The gold standard TACN chelator for gallium is NOTA (**Figure 1.1**, N,N',N''-(1,4,7-triazacyclononane-1,4,7-triyl)triacetic acid), which coordinates the Ga(III) ion through its N$_3$O$_3$ motif in a distorted octahedral fashion (**Figure 1.3**), as confirmed by crystal structure [34], and possesses high thermodynamic affinity (Log$K$ = 31.0) for the metal [33]. Gallium-68 radiolabelling of NOTA is fast at room temperature and acidic pH (< 5.5) [35]. Derivatisation at one of the acetic acid arms to include an additional carboxylic moiety results in the bifunctional chelators NODAGA and NODASA, where one of the acetic acid arms has been replaced by glutaric and succinic acid, respectively [36,37] (**Figure 1.3**). Derivatisation at the TACN scaffold to include a benzyl isothiocyanate arm led to *p*-SCN-Bn-NOTA, one of the most widely employed bifunctional chelators for [68]Ga [22] (**Figure 1.3**).

Figure 1.3. *Representation of the [Ga(NOTA)] complex as determined by X-ray crystallography (left) [34], and structures of bifunctional chelators based on NOTA.*

Modification of the NOTA structure to include pendant phosphinic in place of carboxylic acids resulted in a new family of TACN ligands, collectively known as TRAP (**Figure 1.1**). As a consequence of the lower pKa of phosphinic acids (<1) these ligands can coordinate gallium at lower pH compared to NOTA, thus expanding the range of useful pH for radiolabelling. The first TRAP chelator, TRAP-Pr (Log$K$ = 35.65, Log$K$ = 26.24 by out-of-cell titration), possesses additional distal carboxylate groups attached to the phosphinic moieties, which are supposed to help the coordination of the metal, in the low concentrations typical of radiochemistry, by acting as "pre-coordination" sites [38,39]. These three distal carboxylate groups also open the way to multimeric functionalisation of TRAP-Pr. A crystal structure of the gallium complex showed how the metal is coordinated in a trigonally distorted octahedral fashion (**Figure 1.4**) through the three nitrogen atoms of the ring and three oxygen atoms from the phosphinic acid moieties.
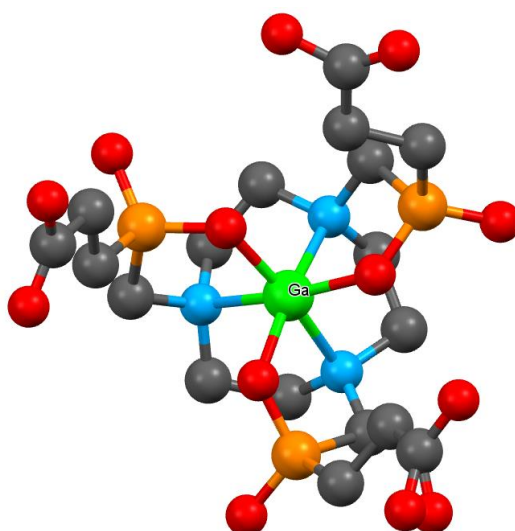
Figure 1.4. *Representation of the molecular structure of [Ga(TRAP-Pr)] as determined by X-ray crystallography [38].*

The second-generation derivative NOPO, designed for single functionalisation of the chelator, replaces two of the carboxylic acids with alcohol groups [40]. Interestingly, TRAP ligands possess increased selectivity for Ga^{3+} over competitor metal ions (*e.g.* Fe^{3+}, Zn^{2+}, Cu^{2+}) with respect to DOTA and NOTA type chelators. This has been proved by comparing the thermodynamic constants of these chelators for different metals [38] as well as by competition studies [41] and transchelation studies [42].

The macrobicyclic hexamine ligand, 1,8-diamino-3,6,10,13,16,19-hexaazabicyclo[6.6.6]icosane, better known as sarcophagine (**Figure 1.1**), famously forms particularly stable metal complexes, often referred to as cage complexes, because of the encapsulation of the metal into the byciclic structure. The two primary

amine groups at each cage extremity provide convenient access to bifunctional derivatives of this chelator. Although the main application of this ligand is radiolabelling with ^{64}Cu, sarcophagine complexes of ^{68}Ga, with the metal coordinated by the six secondary amine groups of the cage system (**Figure 1.5**), were found to be remarkably stable *in vivo* and resistant to transchelation in competition experiments with apotransferrin. On the other hand, the radiolabelling conditions for this ligand are far from ideal, requiring 35 min at high temperature and in non-aqueous solution for quantitative radiolabelling [43].
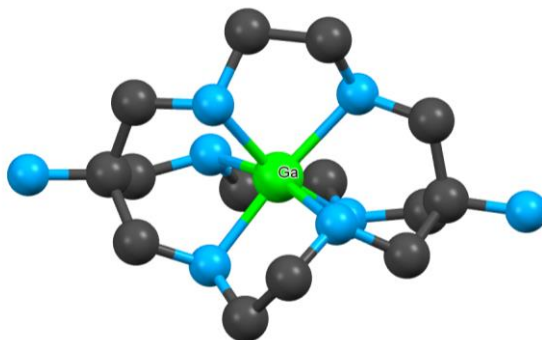
Figure 1.5. *Molecular representation of the [Ga(sarcophagine)] complex as determined by X-ray crystallography [43].*

Another promising gallium-68 chelator is the 6-amino-6-methylperhydro-1,4-diazepinetetraacetic acid AAZTA and its derivatives, collectively known as DATA chelators (**Figure 1.1**). AAZTA was initially developed as a Gd(III) chelator for application as a MRI contrast agent [44], but was also found to coordinate Ga(III) resulting in a stable $[Ga(AAZTA)OH]^{2-}$ complex at physiological pH [45]. Quantitative radiolabelling of AAZTA is performed under mild conditions (10 min, room temperature), but results in multiple species likely related to different conformers of the ligand [46], as illustrated in **Scheme 1.1**. Furthermore, preliminary *in vivo* studies of ^{68}Ga AAZTA peptide derivatives showed some instability in human plasma [47].
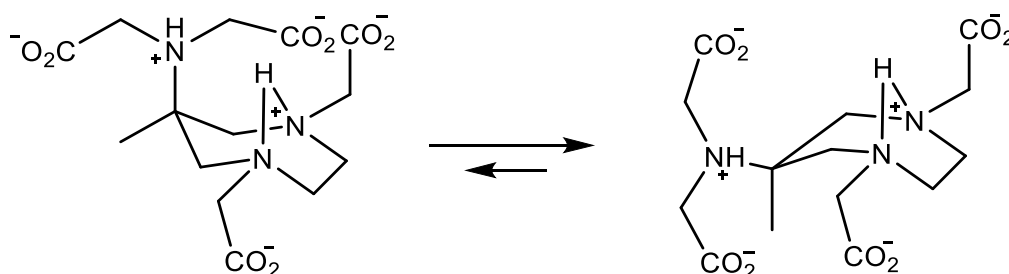
Scheme 1.1. *Proposed equilibrium between conformers for the AAZTA ligands [46]. Equilibrium is shifted to the right to minimise repulsion.*

Hexadentate derivatives of these chelators, possessing only three carboxylate moieties, were synthesised as part of the DATA family. These ligands coordinate the Ga(III) ion in a distorted octahedral fashion through the N_3O_3 donor atoms, forming neutral complexes (the [Ga(DATA^m)] complex is reported in **Figure 1.6**).
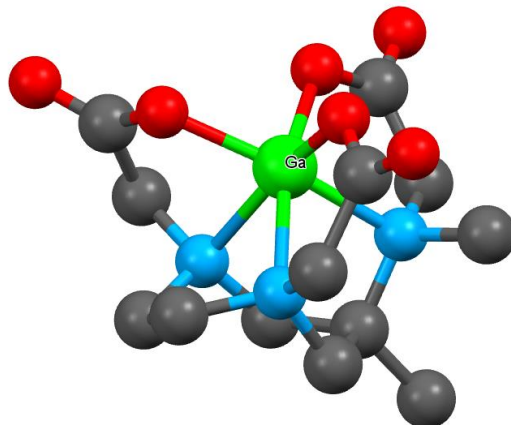
Figure 1.6. Molecular structure of [Ga(DATA^m)] as determined by X-ray crystallography [46].

Some of the DATA ligands were specifically designed to possess a pre-organised conformation for metal coordination, thus favouring the formation of a single and stable ^{68}Ga-labelled species [46]. This was achieved through the introduction of a bulky substituent in position C^6, shifting the equilibrium in **Scheme 1.1** towards the left, with the C^6-amino group taking up the axial position and resulting in a facing-capping array of nitrogen atoms [48]. The DATA chelators quantitatively bind gallium-68 at room temperature in the pH range 4-7 and competition studies showed how the radiolabelling tolerated the presence of Fe(III) (up to 4 equivalents compared to the ligand) while it was more susceptible to the presence of Cu(II) [49]. As expected the DATA chelators possessing a bulky substituent in C^6 formed a single radiolabelled species, while a minority species was also identified for the DATA^m chelator, which only possesses a methyl group in position 6 [46]. Surprisingly, DATA^m was the chelator chosen for further functionalisation and preclinical studies [50], likely due to the better radiolabelling properties compared to the rest of the DATA family [49].

1.2.2 Acyclic chelators based on ethylenediamine

Ethylenediamine tetracetic acid (EDTA) is a common chelator for metals and forms stable complexes with Ga(III) [14,34], and it was the first chelator to be used in ^{68}Ga preparations [22]. Different acyclic ligands based on the EDTA scaffold, or more broadly on ethylenediamine, were found to be more selective for Ga(III) and were developed as ^{68}Ga chelators (**Figure 1.7**).

EDTA   **HBED**   **H₂dedpa**
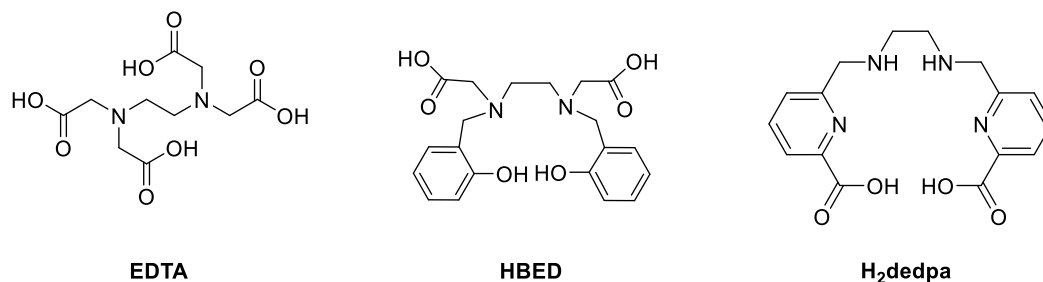
Figure 1.7. Chelators based on the ethylendiamine structure.

HBED (N,N'-bis(2-hydroxybenzyl)ethylenediamin-N,N'-diacetic acid) maintains an EDTA-based scaffold, but has two of the pendant acetic acids replaced by phenol groups. Since its first reported synthesis in 1967 [51], the outstanding thermodynamic stability of its iron(III) complex was noticed ($\text{Log}K$ = 39.01 [52]) and, hardly surprisingly, further studies revealed a similarly high affinity for Ga(III) ($\text{Log}K$ = 37.73 [53], 38.51 [52]). However, it was only recently, with the constantly increasing popularity of ^{68}Ga, that radiolabelling of HBED derivatives with this isotope was attempted. In particular, the bifunctional derivative HBED-CC (**Figure 1.8**), possessing two carboxyethyl groups *para* to the hydroxyl group of the phenols, was successfully used to radiolabel an antibody targeting the epidermal growth factor receptor (EGFR) under extremely mild conditions (5 min, pH 4.5, 40 °C) [54]. More recently, the use of HBED-CC as a chelator in the prostate membrane targeting radiotracer ^{68}Ga-PSMA has hugely increased the utility of this chelator [55]. Despite the many advantages of this chelator, a major disadvantage is represented by the multiple radiolabelled species obtained upon radiolabelling with ^{68}Ga due to the different coordination modes that this chelator can adopt [56] (**Figure 1.8**). Incomplete hexadentate coordination of Ga(III) by HBED has also been observed by our group [57] and suggests that similar species could possibly contribute to the mixed population obtained by ^{68}Ga radiolabelling.

HBED-CC

carboxylates *cis*
phenolates *trans*

carboxylates *cis*
phenolates *cis*

carboxylates *trans*
phenolates *cis*
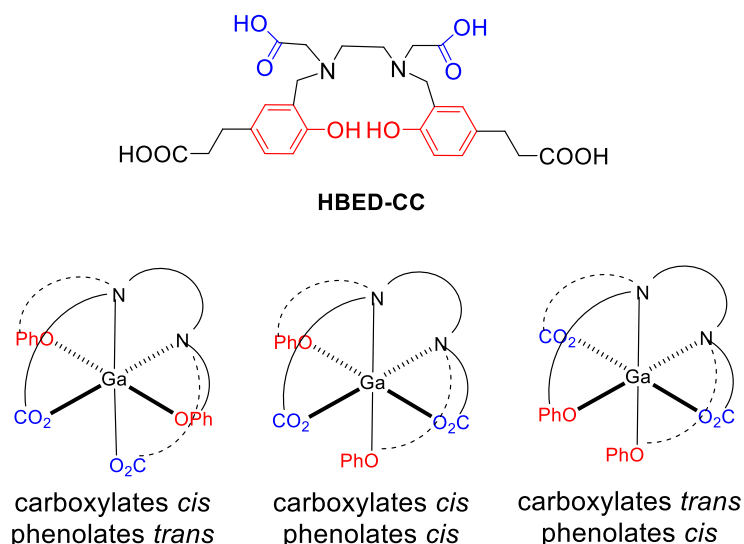
Figure 1.8. *Structure of the bifunctional chelator HBED-CC and representation of the different modes in which HBED can coordinate Ga(III), giving rise to 3 geometric isomers.*

A different type of chelators is the "pa" family, which uses two picolinic acid moieties attached to an ethylenediamine scaffold, to fulfil the coordination sphere of Ga(III). H_2dedpa, the progenitor of this family (**Figure 1.7**, [58]), coordinates Ga(III) through the N_4O_2 motif, forming a [Ga(dedpa)] complex of high thermodynamic stability (Log$K$ = 28.1) and distorted octahedral structure, as confirmed by X-ray crystallography (**Figure 1.9**, [59]). Notably H_2dedpa can be radiolabelled quantitatively with ^{68}Ga at ligand concentration as low as 0.1 µM without the need of pre-processing of the eluate or purification of the radiolabelling mixture [59], and the resulting complex [Ga(dedpa)] proved to be stable to transchelation to apotransferrin. Functionalisation of the H_2dedpa structure is feasible *via* modification of the ethylenediamine scaffold. This was exploited to yield isothiocyanate derivatives (**Figure 1.9**) that were conjugated to RGD peptides for a first preclinical imaging study [60].
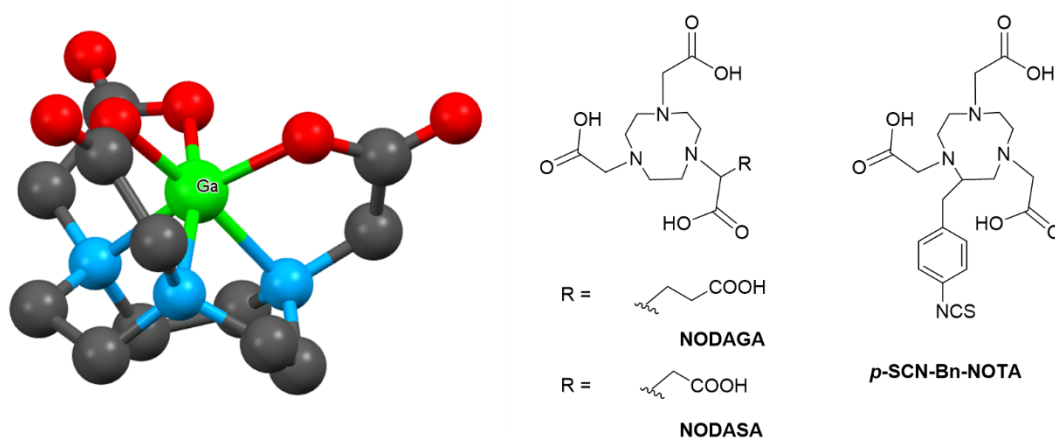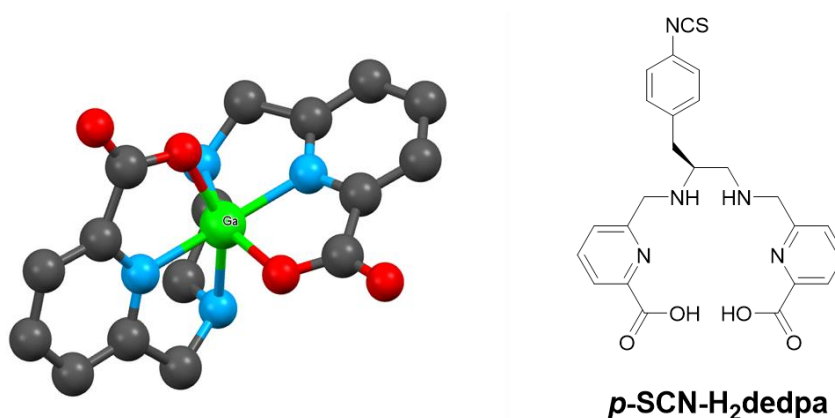

p-**SCN-H₂dedpa**

Figure 1.9. *Representation of the [Ga(dedpa)] complex as determined by X-ray crystallography (left) [34], and structure of the bifunctional derivative p-SCN-H₂dedpa (right). The bifunctional derivative is obtained as a single enantiomer.*

1.2.3 Siderophores

Siderophores (**Figure 1.10**) are iron chelating compounds secreted by microorganisms to acquire Fe(III) from the environment. Unsurprisingly, in light of the high similarity between Fe(III) and Ga(III) ions, siderophores are excellent gallium chelators and have been explored for ^{67}Ga and ^{68}Ga radiolabelling.

DFO-B (DFO)

R = Ac **TAFC**
R = H **FSC**
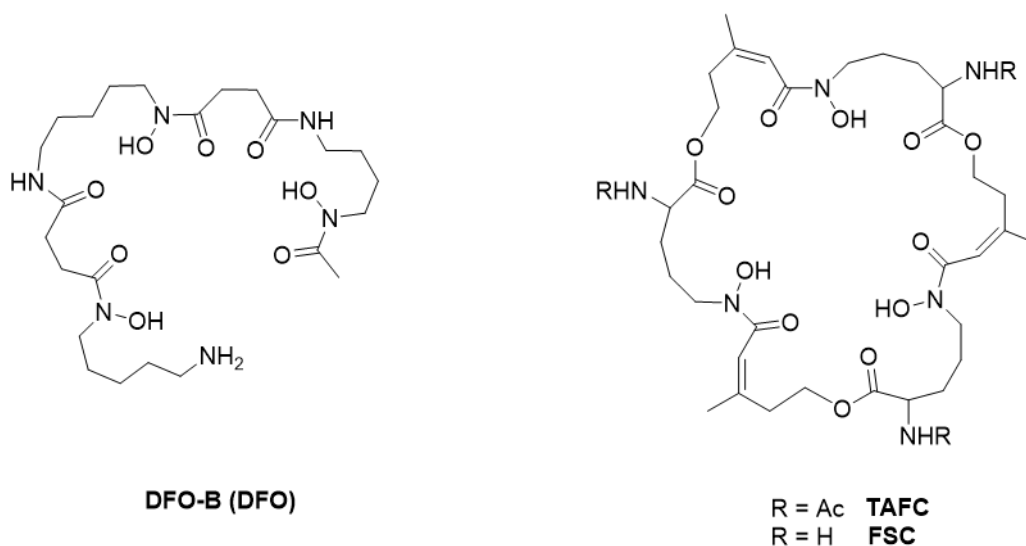
Figure 1.10. Structures of siderophores-based chelators.

Deferoxamine (also known as desferrioxamine, DFO-B and DFO **Figure 1.10**) is a hydroxamate-based bacterial siderophore used clinically for the treatment of iron overload [61]. This hexadentate chelator binds M(III) metals through the three hydroxamate groups, leaving a free amino group available for conjugation. Its Ga(III) complex proved to have high thermodynamic stability (Log$K$ = 28.17 [62], Log$K$ = 27.56 [63]) and NMR studies showed how only two of the eight possible geometric isomers of the [Ga(DFO)] complex are present in the pH range 2-9 (the likely structures of the two isomers are depicted in **Figure 1.11**) [63]. Conjugation of DFO-B to several proteins and peptides, subsequent radiolabelling with ^{67}Ga and *in serum* and *in vivo* stability was evaluated in several papers with promising results [64-66]. However, further evaluation of the chelator showed that dilution to low concentrations results in Ga(III) dissociation from the complex [67] and more recent studies with antibody conjugates of DFO-B revealed how the ^{67}Ga complex is unstable when left in physiological conditions (cell culture medium or phosphate buffered saline with human serum albumin) for more than 24 hours [68]. While these results clearly undermine the feasibility of gallium-67 in vivo studies with DFO-B, this may be not an issue for ^{68}Ga applications, given the shorter half-life of this isotope.

N-*cis,cis*   C-*trans,trans*

R= $(CH_2)_5NH_3^+$
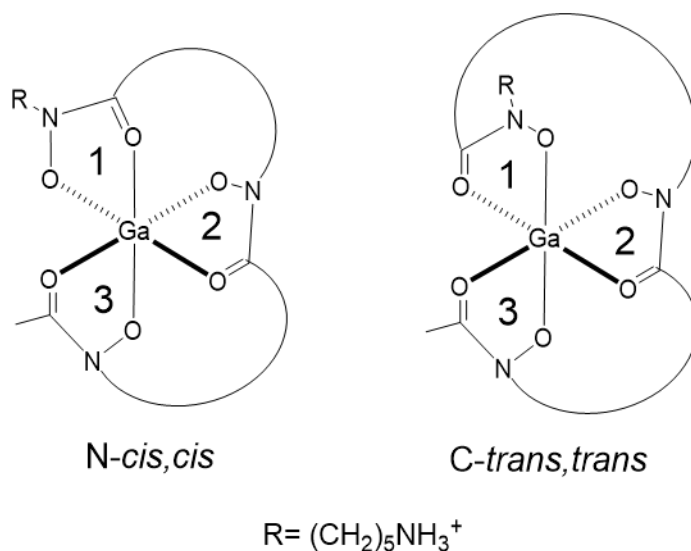
Figure 1.11. *structure of the two geometric isomers which are believed to be present in [Ga(DFO)] solution. Numbers define the different chelate rings starting from the N-terminus. N and C refers to the relative position of carbonyl and nitrogen in ring 1 (N = nitrogen in equatorial position, C= carbonyl in equatorial position), cis and trans refer to the relative orientation of ring 2 and 3 with respect to ring 1 (cis: same orientation, trans: opposite orientation).*

Desferri-triacetylfusarinine C (TAFC, **Figure 1.10**) is a different hydroxamate siderophore produced by the fungus *Aspergillus fumigatus*. TAFC radiolabelling with ^{68}Ga was first investigated as a way to detect fungal infections [69], but the facility of gallium-68 labelling prompted the further exploration of this siderophore as a bifunctional chelator for [68]Ga. As a proof of principle, its deacetylated version Fusarinine C (FSC) was conjugated to three RGD peptides via their lysine sidechains and radiolabelled with ^{68}Ga, achieving excellent radiolabelling over a wide (3-8) pH range [70,71]. Preclinical evaluation of the bioconjugate demonstrated specific tumour uptake of the radiotracer and favourable biodistribution [71].

1.2.4 3-Hydroxy-4-pyridinone based chelators

Hydroxypyridinone ligands (HP) are based on a six-membered aromatic N-heterocyclic ring, containing a carbonyl and a hydroxyl function on adjacent atoms. Three classes of hydroxypyridinone, namely 3,4-hydroxypyridinone, 1,2-hydroxypyridinone and 3,2-hydroxypyridinone, exist depending on the relative position of the carbonyl and hydroxyl function with respect to the pyridinone nitrogen (**Figure 1.12**).

Figure 1.12. General structures of hydroxypyridinone ligands.

Upon deprotonation of the hydroxyl function, hydroxypyridinones can bind metals in a bidentate O_2 fashion, yielding stable 5-membered chelate rings [72]. Owing to their high affinity for hard Lewis acid metal ions, hydroxypyridinones have been widely investigated as Fe(III) chelators. In particular, 3,4-hydroxypyridinones possess the highest stability constants for iron coordination compared to 1,2-hydroxypyridinones and 3,2-hydroxypyridinones due to an increased electron delocalisation over the pyridinone ring that results in more electron-rich oxygen donors [72]. The 1-methyl-3-hydroxy-4-pyridinone chelator deferiprone (also known as CP20 and marketed as ferriprox, **Figure 1.13**) is an *in vivo,* orally available iron chelator employed in clinics to treat iron overload diseases, alongside deferoxamine and the tridentate chelator Deferasirox [73].

Similar to other 3,4-hydroxypyridinones, deferiprone possesses two p*Ka* values of 3.56 and 9.64 for the carbonyl and hydroxyl function, respectively [73]. It complexes Fe(III) in a 3:1 ratio to yield the neutral complex [Fe(deferiprone)$_3$], which crystallises as a slightly distorted octahedron with the 3-hydroxy ligands in a facial (*fac)* arrangement [74] and displays high cumulative stability constant (Logβ_3 = 37.2, [73]). The same crystalline arrangement and very similar thermodynamic affinity constant was found for the Ga(III) complex reported in **Figure 1.13** (Logβ_3 = 38,42 [75], Logβ_3 = 38,42 [76]). Preliminary studies using ^{67}Ga demonstrated facile radiolabelling of deferiprone at pH 7.4 and a ligand concentration of 80 mM. The radiolabelled complex [^{67}Ga(deferiprone)$_3$] showed fast blood clearance *in vivo* [75].
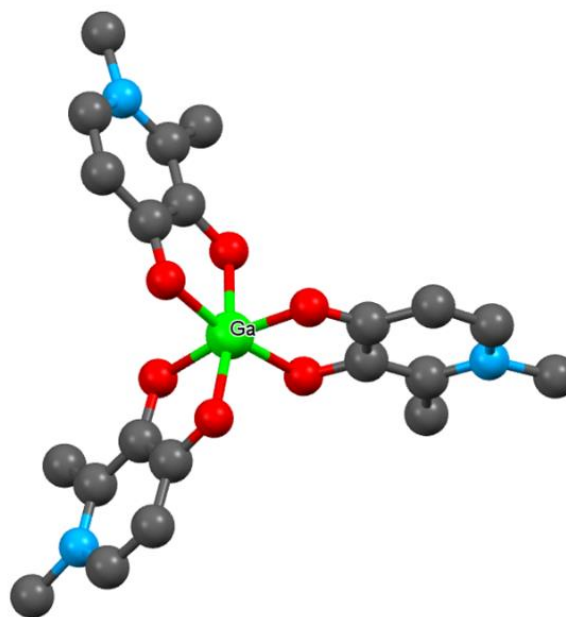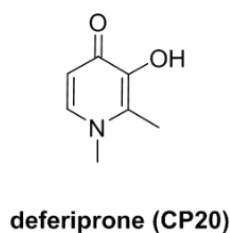
Figure 1.13. *Structure of the 3,4-hydroxypyridinone chelator deferiprone (left), and molecular representation of its gallium complex as determined by X-ray crystallography (right)* [77].

Incorporation of three 3,4-HP units onto a tripodal backbone provides an hexacoordinate environment ideal for M(III) coordination. The resulting complexes present higher kinetic stability compared to their bidentate counterparts and, importantly, first order dependence on the concentration of the ligand. Given the same stability constant, a first order dependence results in less unchelated metal present in solution (at a defined pH and total concentration of ligand and metal), in agreement with the equations below.

$$pM_{bidentate} = -\,\mathrm{Log}[M] = \mathrm{Log}\,\beta + \mathrm{Log}\frac{[L]^3}{[ML_3]}$$

$$pM_{hexadentate} = -\,\mathrm{Log[M]} = \mathrm{Log}\,K + \mathrm{Log}\frac{[L]}{[ML]}$$

pM values are conventionally calculated at pH 7.4, $[L]_{tot} = 10^{-5}$ M and $[M]_{tot} = 10^{-6}$ M. and are particularly useful to compare ligands intended for *in vivo* use [78].

Different examples of *tris*(hydroxypyridinone) chelators are reported in **Figure 1.14**. Notably, the geometry of the tripodal structure is of fundamental importance in determining the metal affinity of the chelator and its ability to form 1:1 metal:ligand complexes. In particular, attachment of the 3,4-HP unit to the tripodal framework at the *ortho* and *meta* positions with respect to the coordinating oxygen atoms is crucial

to minimise the loss of entropy associated with metal coordination, owing to a shorter linking chain [79,80], thus favouring the formation of 1:1 complexes.
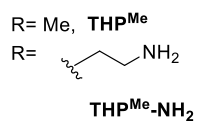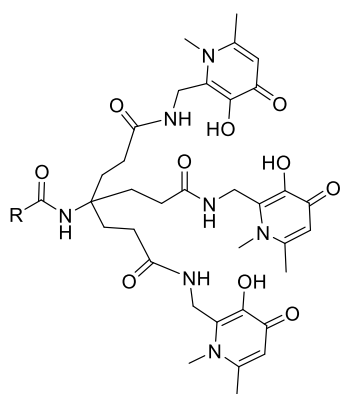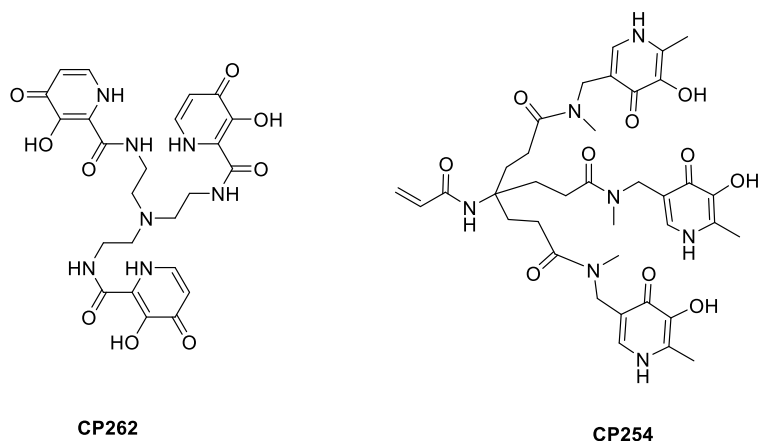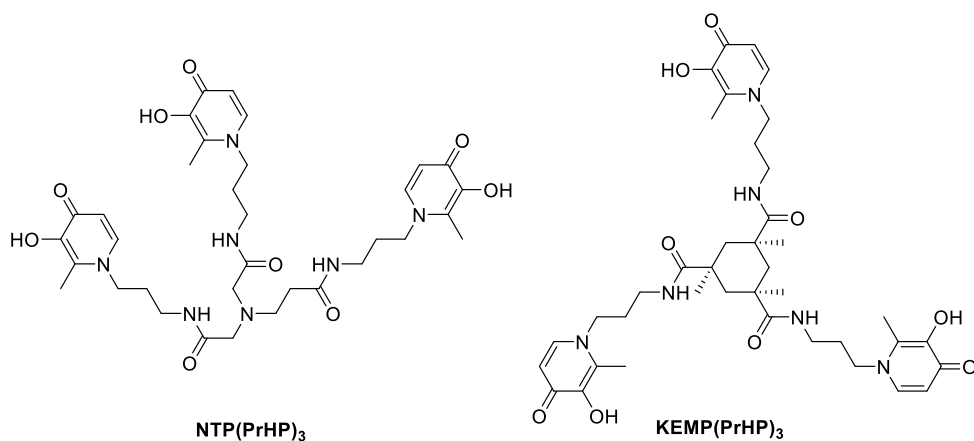
Figure 1.14. Examples of tris(hydroxypyridinone) chelators [81-86].

Santos and coworkers developed several hydroxypyridinone-based hexadentate ligands to be used as M(III) scavenging agents (**Figure 1.14**, top panel). These chelators comprise three 3,4-HP units connected *via* the pyridinone nitrogen to a tripodal framework, either acyclic like the nitrilopropionic acid NTP, or based on the cis-cis-1,3,5-trimethylcyclohexane-1,3,5-tricarboxylic acid KEMP. Fe(III), Al(III) and Ga(III) complexes of these chelators were found to be remarkably stable [81,82,87]. Radiolabelling with ^{67}Ga was achieved in mild conditions and the resulting compounds displayed favourable *in vivo* biodistribution and pharmacokinetics [81,82].

A similar chelator (CP262) was developed by Hider's group (**Figure 1.14**, [86]), possessing three 3,4-HP units attached to a *tris*(2-aminoethyl)amine framework in position C^2 and thus less likely to form labile dinuclear species upon metal complexation [79]. This chelator differs from other *tris*(hydroxypyridinone) ligands since it utilises 3,4-HP units where the N^1-methyl group has been substituted with hydrogen. This chelator possesses very high thermodynamic affinity for iron (Log$K$ = 30.7) and its pFe value is the highest reported for hexadentate HP ligand (pFe = 30.5) [86]. In subsequent studies, structurally related chelators with different N-R groups were also synthesised and tested as iron chelators [83], however, no studies with Ga(III) were performed. Despite their good M(III) binding capability, the structure of these *tris*(hydroxypyridinone) ligands does not allow straightforward modification to obtain bifunctional derivatives, thus preventing simple conjugation to biomolecules and accordingly, any sort of targeted imaging.

On the contrary, the *tris*(hydroxypyridinone) chelator THP[Me] (previously known as CP256 [84], **Figure 1.14**) and its free amine derivative THP[Me]-NH₂, also synthesised by Hider and co-workers [85], allows modification to obtain bifunctional derivatives and, consequently, its use as gallium chelator has been widely explored by our group. THP[Me] possesses three 1,6-methyl-3-hydroxy-4-pyridinone units connected in the C^2 position to a tripodal scaffold via amide linkages. THP[Me] coordinates Fe(III) in a 1:1 mode with high thermodynamic affinity (Log$K$ = 32.52) [85]. Investigation of this chelator for ^{68}Ga labelling by our group revealed fast radiolabelling in extremely mild conditions (< 5 min, room temperature, pH 6.5), achieving quantitative radiochemical yield at lower concentration compared to DOTA, NOTA and HBED [84]. [[67]Ga(THP[Me])] proved to be stable in serum and in the presence of an excess of apotransferrin, and preliminary *in vivo* experiment showed quick blood clearance of the [[68]Ga(THP[Me])] complex (blood half-life <3 min) [84]. Bifunctional derivatives of this chelator can be obtained *via* the free amine derivative THP[Me]-NH₂ [85] and include a maleimide derivative [84], two isothiocyanate derivatives [88] and a glutaric acid derivative [89] (**Figure 1.15**), which

have been conveniently conjugated to several peptides and tested *in vivo* with promising results.
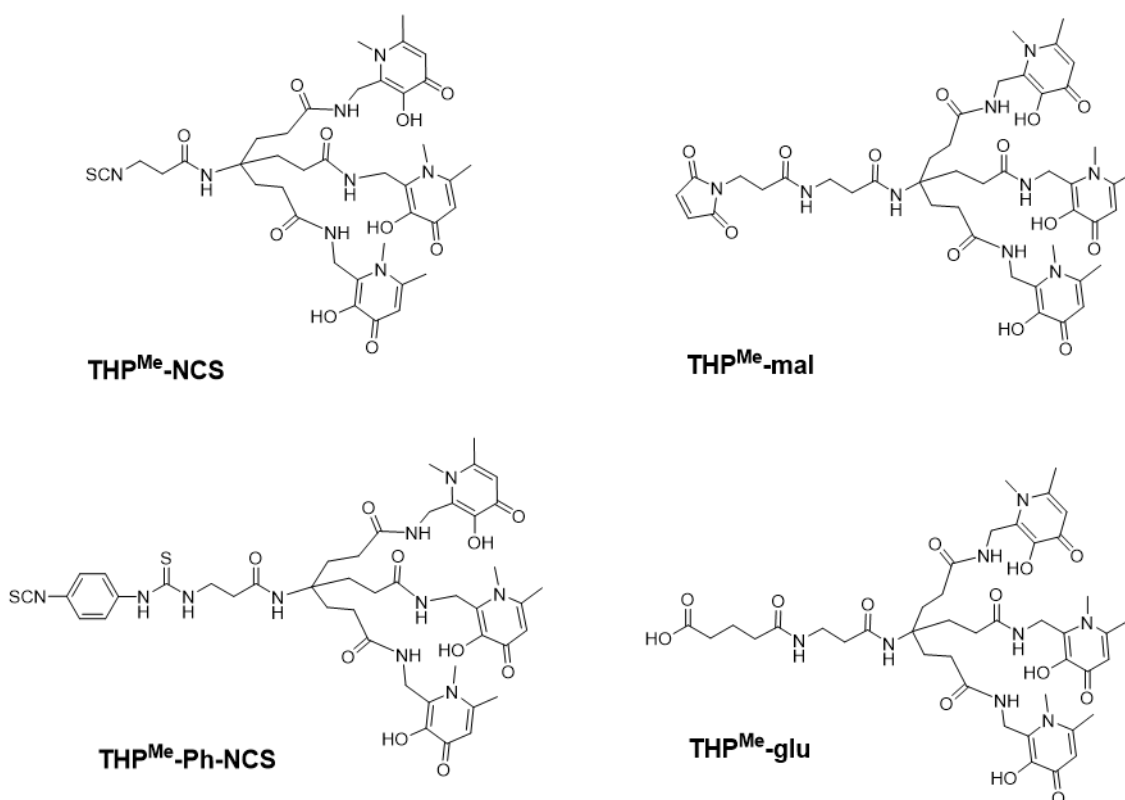
Figure 1.15. *Structures of bifunctional THP^{Me} derivatives*

A different *tris*(hydroxypyridinone) chelator amenable for further functionalisation, CP254 (**Figure 1.14**), was synthesised by Hider and co-workers [90]. Similar to CP262, this chelator also contains hydroxypyridinone units where the N^1-methyl moiety is replaced by N^1-H and attachment to the tripodal structure is provided in position C^5. However, unlike CP262 the tripodal scaffold provides an easy functionalisation route via the α,ß-unsaturated carbonyl in the apical position. Intriguingly, this compound was developed for incorporation into polymers and, despite its high affinity for Fe(III) (Log$K$ = 33.2) it was never tested for Ga(III) coordination [90].

1.2.5 Weak chelators for Ga(III)

Citrate and acetate (**Figure 1.16**) are weak chelators for Ga(III), not suitable in the context of ^{68}Ga radiopharmaceuticals design. They do, however, deserve a mention owing to their role as stabilising ligands in radiolabelling reactions, preventing the formation of insoluble hydroxide species [91]. Furthermore, ^{67}Ga-citrate has been extensively investigated clinically in the past, as will be discussed in the following section.

Acetic Acid   **Citric Acid**
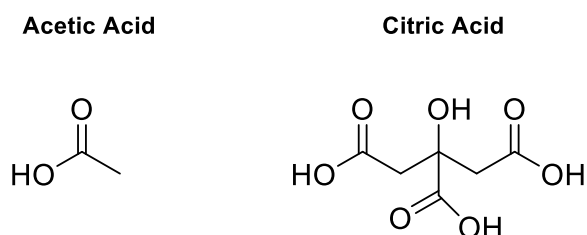
Figure 1.16. *Structure of acetic and citric acid.*

Citrate can coordinate Ga(III) yielding 2:1 or polymeric 1:1 = ligand: metal species, depending on citrate concentration and pH [92,93]. Martell measured a stability constant Log$K$ = 10.0 for the formation of the polymeric $(Ga_3(OH)_4 citrate_3)^{4-}{}_n$ species [92]. However, these complexes are easily hydrolysed to $[Ga(OH)_4]^-$ as the pH increases and gallate is the predominant species at pH > 6.3 in diluted aqueous solution of gallium citrate ([Ga] = 1 nM, [citrate] = 40 μM) [94]. Acetate can also coordinate Ga(III) in aqueous solution forming both 1:1 and 1:2 = ligand to metal species. However, the stability of these complexes is very low with Log$K$ = -2.1 for $[Ga(acetate)]^{2+}$ and Log$K$ = -5.7 for $[Ga_2(OH)_2Ac]^{3+}$ [95].

1.3 Gallium in biological systems

In the 1970s and 1980s, interaction of gallium with biological systems was of great interest due to the use of gallium-67 salts and complexes in nuclear medicine [96,97]. More recently the topic has gained renewed attention with the development of gallium-based anticancer drugs [98].

Gallium is not an endogenous metal; however, due to the striking similarity between the Ga(III) and Fe(III) ions, its interactions with proteins and biological systems resemble those of iron and its biological effects are at least partly due to disruption in iron-related biochemical pathways. Nevertheless, despite the similarity, some remarkable differences between gallium and iron exist and are responsible for the dissimilarities found in the biological pathways of these ions. The most remarkable difference is that Fe(III) can be reduced to Fe(II) and *vice versa,* while Ga(III) does not display any redox chemistry in solution under physiological conditions. Furthermore, the existence at physiological pH of a soluble gallate species, although in equilibrium with insoluble $Ga(OH)_3$, opens new possibilities for gallium behaviour in biological systems. In contrast, Fe(III) can only exist bound to proteins or chelators because of the comparative insolubility of iron hydroxide species.

1.3.1 Interaction with transferrin and other biomolecules

To understand *in vivo* biodistribution of gallium upon intravenous (IV) administration, and the mechanisms involved in gallium accumulation in specific tissues, it is crucial to analyse the interactions of this metal with proteins and other relevant biomolecules. The most prominent among these interactions involve the serum protein transferrin.

Transferrin (Tf) is a monomeric glycoprotein of 80 kDa responsible for iron transport in vertebrates. It displays two metal binding sites located in the N-terminus and C-terminus domains that can sequentially bind iron upon synergistic coordination of a carboxy anion, which is typically carbonate *in vivo* (serum bicarbonate concentration ≈ 27-35 mM [16,99]). Stability constants for Tf-Fe(III) binding at serum bicarbonate concentration were measured to be LogK_1 = 22.8 and LogK_2 = 21.5 [16]. In normal physiological conditions, only one third of transferrin binding sites are occupied by iron. At this level of iron saturation, diferric transferrin (holotransferrin) constitutes 30 % of the total plasma iron pool, while monoferric transferrins with iron bound at the N-terminus or at the C-terminus site represent the 41 % and 29 % of the plasma iron pool, respectively [100]. Transferrin delivers its iron load into cells through interaction with the transmembrane glycoproteins, transferrin receptors (TfR) 1 and 2. This interaction is regulated by TfR binding to the hereditary hemochromatosis

protein HFE, which competes with holotransferrin for TfR binding [101]. Transferrin receptor 1 is expressed on highly proliferating tissue, including neoplastic cells, and is therefore particularly interesting for our purposes. TfR1 exhibits greater affinity for holotransferrin compared to monoferric transferrin and apotransferrin [102], with a dissociation constant K_d = 2.3 nM [103]. Holotransferrin binds to transferrin receptors on cell surfaces inducing endocytosis and is internalised in membrane bound endosomes. Lowering of the pH in these vesicles results in release of Fe(III), which is reduced to Fe(II) by a ferrireductase and transported out of the endosome in the cytoplasm via a divalent metal transporter [104]. Membrane bound apotransferrin is recycled to the surface of the cells, where it is finally released due to its low affinity for the receptor at physiological pH. The greater importance of holotransferrin in iron delivery, compared to any of the monoferric forms, is such that most of the literature around this protein deliberately considers only the diferric version or uses the term FeTf to include any Fe-Transferrin species [100]. In this work, the term FeTf and GaTf will be used to indicate any transferrin species containing iron and gallium, irrespective of metal ion occupancy of Tf's binding sites. Intriguingly, the existence of mixed FeGaTf species is also possible, but will not be considered here.

Owing to the previously discussed similarity between Fe(III) and Ga(III), gallium represents an excellent candidate to bind unoccupied transferrin metal binding sites. The Ga(III) stability constants for binding to transferrin (LogK_1 = 20.3, LogK_2 = 19.3 at serum bicarbonate concentration, LogK_1 = 19.53, LogK_2 = 18.58 at 5 mM bicarbonate concentration) are remarkably high, although lower than the stability constants reported for Fe(III) [16]. Furthermore, modelling studies by Byrne [94] suggest that at a gallium concentration lower than 50 µM (the metal ion concentration needed to occupy all of the vacant metal binding sites in transferrin) and bicarbonate level above 2 mM, more than 99 % of gallium in plasma is bound to transferrin at equilibrium. At concentrations higher than this, the gallate form becomes progressively more important.

Early *in vitro* studies using ^{67}Ga support these calculations, highlighting that upon serum/blood incubation of gallium citrate, the majority of activity is associated with serum proteins [105], notably transferrin [106,107]. As for iron, transferrin binding to gallium is strongly dependent on bicarbonate levels. The lower threshold of bicarbonate concentration for quantitative binding of gallium to transferrin was experimentally determined to be 13 mM [108], higher than the 2 mM concentration threshold predicted in the above-mentioned modelling studies by Byrne [94]. The Ga-Tf binding is less stable than the original Fe-Tf binding and easily disrupted, either by

a slightly acidic environment (less than 50 % of gallium bound at pH 6.1) or increased citrate concentration (less than 80 % of gallium bound at a citrate concentration of 10 mM) [109]. Although these conditions are unlikely to be significant under normal physiological conditions, they could potentially be reached by injection of gallium salts, and weak chelates such as ^{67}Ga-citrate, especially in animal studies. Notably, neither low pH (down to pH 4.7), nor high citrate concentration (up to 0.1 M) had an effect on the Fe-Tf binding [109]. More recent studies have investigated the kinetics of GaTf formation and the mechanisms for GaTf interaction with transferrin receptors. While the overall affinity of GaTf towards TfR was substantially decreased (K_d = 1.1 μM) compared to that of FeTf (K_d = 2.3 nM), GaTf exhibited sufficient affinity for the helical domain of the receptor [103,110], allowing the same endocytosis-mediated pathway to internalise Ga(III) in TfR1 expressing cells.

In addition to transferrin, gallium was found to avidly bind the homologous iron binding protein lactoferrin, which is found in many epithelial secretions (milk, seminal fluid, tears) as apolactoferrin and possesses antimicrobial properties [111]. Gallium has higher thermodynamic affinity for lactoferrin than for transferrin. Stability constants for gallium binding to lactoferrin at 5 mM bicarbonate concentration were found to be LogK_1 = 21.43, LogK_2 = 20.57, approximately 90-fold higher than those for transferrin in the same conditions [112].

Finally, some evidence suggests that gallium may also bind to the iron storage protein ferritin upon dissociation from transferrin and lactoferrin, mediated by phosphate-containing compounds such as ATP [113-115]. However, rather than playing a role in uptake mechanisms of gallium, binding to ferritin appears only related to intracellular storage of this metal [116]. Furthermore, there is no evidence that gallium is actually incorporated into the ferritin core and not simply loosely bound to an external site [104]. If gallium incorporation in ferritin occurs, the mechanisms are likely to be different from that shown for iron, which is more easily incorporated as Fe(II) and then oxidised by ferroxidase centres in the protein [117].

Importantly, Ga(III) cannot be incorporated in Fe(II)-bearing proteins such as haemoglobin or cytochromes and is therefore not involved in oxygen transport mechanisms.

Ga(III) affinity for microbially-produced siderophores is well established, as discussed in the previous section, and could potentially play an important role in imaging/treatment of infections with radioactive isotopes. Importantly, Ga(III) is able

to displace Fe from siderophores in the presence of a reducing environment, with concomitant production of Fe(II) species [118].

1.3.2 Pharmacokinetics and biodistribution

The mechanisms by which gallium is distributed to tissues, and the pharmacokinetics of these processes, are important in order to evaluate the use of gallium/radioactive gallium salts for medical applications. Although the availability of gallium radioisotopes has enabled studies of Ga(III) biodistribution *in vivo,* some of the mechanisms underlying localisation in different tissues are not completely understood.

Although gallium and iron are both bound to transferrin in plasma, they present important differences in their pharmacokinetics and biodistribution. By measuring plasma concentration of the radioactive species after intravenous injections in humans, Logan found that ^{59}Fe-citrate was cleared from plasma 50 times more quickly than ^{67}Ga-citrate. ^{67}Ga-transferrin showed the same overall elimination rate constant as ^{67}Ga-citrate [119]. The biodistributions of ^{67}Ga- and ^{59}Fe-citrate were also found to be markedly different in preclinical studies. ^{59}Fe-citrate biodistribution changed over time, reflecting the progressive incorporation of radioactive iron into haemoglobin with ^{59}Fe accumulation in spleen, bone marrow and blood and no preferential tumour uptake in tumour bearing mice [120]. On the contrary, ^{67}Ga-citrate distribution in tissues was found to be largely established one hour after injection, although the amount of tissue-associated activity kept increasing over time as a result of its slow blood clearance. High concentration of ^{67}Ga was found in bone (but not in the marrow), as well as in the liver, spleen, kidneys, intestine and, where applicable, tumours.

Similar preclinical biodistribution data for ^{67}Ga-citrate were reported by several groups in the past decades [121,122]. Another study in mice showed that the concentration of citrate in the injected ^{67}Ga did not influence ^{67}Ga biodistribution, which did not differ from that of gallium chloride [123]. The same study claimed that distribution profile was the same also for ^{67}Ga-labelled serum/transferrin. However, this finding relies on the assumption that administered ^{67}Ga citrate binds to transferrin in serum: verification of transferrin radiolabelling was not undertaken and the radiolabelled serum was simply obtained by exsanguination of a mouse previously injected with ^{67}Ga-citrate. More recently, data on the biodistribution of ^{68}Ga-citrate, ^{68}Ga-acetate [124] and ^{68}Ga-chloride upon either neutralisation with NaOH [125,126] or buffered with PBS [127] also showed a similar biodistribution for Ga(III).

In a recent study, ^{68}Ga obtained from a generator used without pre-elution (> 24 hours from previous elution) was mixed with NaOH, with the aim of generating gallium

colloids. The ^{68}Ga-containing solution was then administered to mice via a retroorbital injection, followed by PET scanning and *ex vivo* biodistribution. In a side-by-side comparison, the biodistribution of ^{68}Ga-colloids, significantly differed from that of ^{68}Ga-citrate and ^{68}Ga-acetate, with ^{68}Ga-colloids predominantly found in the liver [124]. In light of the speciation of Ga(III), where an alkaline solution of Ga(III) should contain soluble $[Ga(OH)_4]^-$, any formation of colloids containing ^{68}Ga is likely due to the presence of other metal contaminants, whose concentration is higher in the eluate of generators used without pre-elution. Production of colloids containing ^{68}Ga by addition of an excess of $FeCl_3$ has previously been reported in the literature [128].

A first attempt to measure gallium biodistribution in humans was performed in the 1970s when a *post-mortem* study was performed on 26 cancer patients, who died at different times during the month following a ^{67}Ga-citrate scan. The biodistribution compared organ distribution of ^{67}Ga between patients, and attempted to correlate differences in ^{67}Ga biodistribution with patients' age, sex, nutrition and time of death after ^{67}Ga scan [129]. While the data were generally similar to preclinical findings, they also emphasised the high variability in tissue biodistribution of gallium-67. The most important factor found to influence biodistribution was the interval between ^{67}Ga-citrate injection and time of death, highlighting the slow pharmacokinetics of the tracer. Interestingly, higher accumulation in bones was measured for adolescent patients. Recently the whole-body biodistribution of ^{68}Ga-citrate has been evaluated by PET imaging within a clinical study for bone infections. Results were similar to those obtained for ^{67}Ga-citrate [130].

While providing useful information on the behaviour of ^{67}Ga/^{68}Ga in biological systems, all clinical and preclinical $^{68/67}$Ga biodistribution data were obtained using trace amounts of gallium, which is typical of modern radionuclide imaging where carrier-free formulations are used. Pharmacokinetics and biodistribution of gallium become different for chemotherapeutic doses of gallium, or carrier-added radiopharmaceuticals, as demonstrated by different clinical and preclinical observations comparing the biodistribution of carrier-added and carrier-free radioactive gallium. An early ^{67}Ga-citrate study in rats found significantly different biodistribution of this carrier-free tracer compared to ^{72}Ga-citrate that contained high amounts (in the mg/Kg range) of natural gallium [131]. Particularly, a carrier concentration above a 0.25 mg/Kg resulted in a modification of the excretion and distribution of radioactivity, with increased urinary excretion and accumulation in bones and decreased accumulation in soft tissues [131]. The same behaviour was exploited in a very early study using ^{68}Ga-citrate as a bone scanning agent, where

bone/soft tissue ratio was increased by co-administration of non-radioactive gallium salts. This study also demonstrated how the increased amount of citrate that accompanies the carrier-added administration could not, alone, produce the same effect [132].

Other studies have demonstrated that modified ^{67}Ga biodistribution, with increased bone uptake and renal clearance, was not exclusive to carrier-added ^{67}Ga, but could also be achieved by administration of with iron(III), scandium(III) or by treatments (irradiation or drugs) that resulted in increased concentration of iron in the blood (hyperferremia) [133-135], prior or concomitant to the ^{67}Ga injection.

These observations are at least partially explained by considering that transferrin can be saturated by high doses of Ga(III) or other competing metals such as Fe(III) or Sc(III). Formation of gallate will start to compete with Ga-transferrin even before reaching the saturation threshold (50 µM of gallium at physiological concentration of transferrin) and, as a small anion, gallate is expected to be rapidly cleared renally and accumulate less in tissues. The increased bone uptake observed in these conditions suggests that gallium accumulation in bones follows a different mechanism in comparison to soft tissues [111].

Effects of transferrin saturation on tumour uptake of ^{67}Ga were conflicting, thus casting doubts on whether tumour uptake of gallium actually follows a route similar to other tissues. Hayes found that ^{67}Ga uptake in 5123c hepatoma xenografts in rats was unaltered by saturation of transferrin with scandium or iron, while it was decreased by reduction in serum iron and consequent increase in available Tf binding sites [135,136]. In a later comprehensive study, Schomacker evaluated the effect of co-administration of natural (non-radioactive) gallium and iron citrate on the biodistribution of ^{67}Ga and ^{59}Fe in xenograft bearing mice. Notably, co-administration of natural gallium or iron was able to decrease the amount of activity associated with blood and tumours for both ^{67}Ga and ^{59}Fe and to increase the amount of activity excreted in urine [137]. This study elegantly pointed out some other dissimilarities between iron and gallium and how they affect each other's biological pathways. For ^{67}Ga the amount of activity associated with liver, spleen and muscle was decreased when natural gallium/iron was co-administered with the tracer, while deposition in bones (but not in bone marrow) increased. Conversely, gallium and iron addition increased the percentage of ^{59}Fe associated with liver and spleen while accumulation in muscle, bone and bone marrow was decreased by co-administration of iron and unaffected by gallium [137].

1.3.3 Mechanism for gallium uptake in tumours

Accumulation of gallium-67 in tumours was first described in 1969 by Hayes, who observed uptake of activity in a non-osseous tumour during the evaluation of ^{67}Ga-citrate as a bone-scanning agent in a Hodgkin lymphoma patient [138,139]. Since this serendipitous discovery, gallium-67 tumour scanning has been employed clinically for diagnosis of lymphomas, leukaemia, lung cancers, head and neck cancers and melanoma [140], although this technique has now largely been abandoned in favour of [^{18}F]-FDG PET. Several animal models, were also established to better study and characterise accumulation of ^{67}Ga in malignancies [141]. Nonetheless, the mechanisms underlying uptake of gallium in tumours are among the most controversial aspect of gallium biology, with the main point of contention being the role of transferrin in this process [142].

Larson was the first to introduce the concept of gallium as an iron analogue to explain its interaction with biological systems, and to hypothesise transferrin-mediated gallium accumulation in tumours and soft tissues. According to this hypothesis, as it was formulated at first, circulating gallium is quantitatively bound to transferrin and carried to the tumour proximity where GaTf binds to the transferrin receptor and is internalised by endocytosis. Once internalised, GaTf migrates to lysosomes and then associates with unknown acceptor macromolecules [143]. Although this hypothesis has been modified in the following 40 years to account for the increasing knowledge of iron uptake and trafficking in cells (for example, it is now established that metals are released from transferrin into the endosome following acidification of the environment), the fundamental core of this hypothesis has remained unchanged. Larson's hypothesis was supported by Harris and Sephton's observations that human serum or transferrin promoted tumour uptake of gallium *in vitro* in both human and mouse cancer cell lines [144,145]. Intriguingly, addition of serum from different animal species had different effects on gallium tumour uptake, suggesting different affinities of species-specific transferrin protein for species-specific transferrin receptors. While human, horse and rabbit serum proved to be very effective in enhancing the uptake in mouse-derived tumour cells, mouse serum had an intermediate efficacy, and the foetal calf serum used in normal cell culture did not have any effect [145]. Other studies further validating Larson's hypothesis have observed accumulation of gallium in lysosomes of viable tumour cells [146] and shown that *in vitro* [141,147] and *in vivo* [133] tumour uptake of gallium-67 is decreased, when ^{67}Ga binding to transferrin is inhibited. Importantly, Larson's hypothesis also provides a rationale for increased gallium accumulation in tumour cells relative to healthy cells: as highly proliferating

tissues require an increased amount of iron [148], cell-surface transferrin receptor expression is upregulated, increasing GaTf cell uptake.

On the other hand, Larson's hypothesis presented some critical issues. The experimental observation that, unlike ^{67}Ga, ^{59}Fe does not show any preferential accumulation in tumours *in vivo* [120], despite evidence of accumulation in cultured cells [143], clearly suggested that the analogy with iron was incorrect when considering tumour uptake, or at least incomplete. Furthermore, Larson's hypothesis failed to explain some other experimental observations by Hayes: iron saturation of transferrin generally decreased ^{67}Ga uptake in normal soft tissues but increased uptake in tumours [136]. Larson's hypothesis was also unable to explain clinical data showing how patients presenting transfusion-induced iron overload had inferior ^{67}Ga uptake in soft tissues but unaffected tumour uptake of the radiotracer [149]. To interpret these phenomena, Hayes hypothesised a different mechanism for gallium uptake in tumours, involving an unbound/loosely bound form of gallium (likely gallate), which could accumulate in the tumours owing to a hypothesised enhanced permeability of the tumour cell membrane [136]. This hypothesis was able to explain the lack of tumour uptake for ^{59}Fe, since soluble, unchelated iron species do not exist in physiological conditions. It also explained those experiments where tumour uptake of ^{67}Ga was increased by iron loading; in fact, this would result in a displacement of ^{67}Ga from transferrin to its unbound form, which could then accumulate in tumours. On the other hand, the rational of this theory, the hyperpermeability of tumour plasma membrane, was somewhat lacking, as no evidence of this phenomenon or of its potential causes was presented [150].

To explain these conflicting results, Sephton hypothesised that the actual species responsible for tumour uptake of gallium was extravascular transferrin (ETf) in contact with the tumor tissue [151]. In order to reach these transferrin molecules, gallium has to exit the circulation and penetrate the endothelium either in the form of GaTf or as unbound gallate. Extravasation of a large macromolecular complex, such as GaTf, is necessarily a slow process and can only be responsible for tumour uptake at late time points after gallium injection. On the contrary, the gallate ion can cross the endothelium, bind to extravascular transferrin molecules and consequently to transferrin receptors on tumour cell surfaces, thus accounting for the majority of tumour uptake at early time points. Although the percentage of unbound Ga(III) in plasma is extremely low compared to GaTf, this is only true once the thermodynamic equilibrium is reached. In their computational studies, Jackson and Byrne analysed the speciation of Ga-citrate in aqueous solution at pH 7.4, with a total Ga(III) concentration

of 90 nM and a concentration of citrate equal to 4 x 10^{-5} M, typical for a 185 MBq injection of ^{67}Ga-citrate [94]. Their studies showed how Ga-citrate initially exists mainly (>90%) as $[Ga(OH)_4]^-$ while, once thermodynamic equilibrium with Tf has been established >99% of Ga(III) is then associated with this protein, while the rest persists as $[Ga(OH)_4]$ [94]. Even when the equilibrium has been achieved, this involves a continuous re-equilibration between the two forms of gallium, so that removal of unbound Ga(III) from the circulation (*e.g.* by its diffusion into the extravascular space), would result in transferrin release of further Ga(III). The same reasoning applies to the extravascular space with opposite results: here the increase of unbound gallium would prompt binding to ETf to re-establish the equilibrium ratio and GaETf would then deliver gallium to the tumour tissue.

This elegant hypothesis can easily explain the differences observed *in vivo* between gallium and iron, since a soluble unbound form of iron does not exist under physiological conditions and thus extravasation of iron has to rely only on FeTf. Furthermore, this could explain why a faster and higher tumour uptake of ^{67}Ga could be achieved by iron loading of transferrin. In fact, decrease in the available transferrin binding sites would result in an increased release of gallium in its gallate form, which could rapidly penetrate the endothelium, bind ETf and be taken up by the tumour [151]. While this enhanced tumour uptake due to transferrin saturation would be very prominent at early time points, it would level off once extravasation as GaTf has also reached its equilibrium and can actively contribute to gallium delivery to tumour tissues. Interestingly, according to this hypothesis, the variability in the time points at which tumour uptake was measured in different studies could potentially explain the conflicting results obtained for tumour uptake in transferrin saturation experiments.

Notably, although Sephton's hypothesis can also be applied to ^{67}Ga uptake in normal tissues, its effects are amplified in malignant tumour lesions. This is likely due to their increased capillary permeability and expanded extracellular space, which facilitates ^{67}Ga delivery to the ETf and, ultimately, to the tumour [152].

While this revised theory could account for many experimental data, it still failed to explain some *in vitro* and *in vivo* observations, in which gallium uptake was measured in either mice congenitally lacking transferrin [153] or in a pair of matched cell-lines, one lacking Tf expression, and the other transfected to restore Tf expression [154]. These experiments demonstrated that although reduced, tumour uptake of gallium persisted when transferrin or transferrin receptor was absent, thus supporting the existence of transferrin-independent uptake mechanisms for gallium accumulation in tumours. In addition, in experiments where an anti-TfR monoclonal antibody was used

to block transferrin receptors prior to ^{67}Ga-citrate injection, a 75 % reduction in gallium uptake was observed, thus demonstrating the key role of GaTf interaction with TfR in gallium uptake, but also highlighting that the transferrin-mediated uptake mechanism cannot account for the totality of the uptake [155]. Similarly, ^{67}Ga uptake was inhibited but not eliminated in HeLa cells transfected to express the wild type Hemochromatosis protein HFE, which binds to TfR and inhibits TfR-mediated metal uptake pathways.

The existence of transferrin-independent mechanisms of uptake is also in agreement with Chitambar's findings that uptake of gallium in HL60 cells was still present, although to a lesser extent, in transferrin-free media and increased at higher gallium citrate concentration [116]. Whether these transferrin-independent mechanisms are related to those hypothesised for iron is still uncertain, but unlikely since Fe(III) reduction to Fe(II) and subsequent production of free radicals seems to be involved in its transferrin-independent cellular uptake [104].

1.3.4 Intracellular distribution of gallium

Little is known about the fate of gallium upon internalisation in both tumour and normal cells [104]. Similar to FeTf, GaTf is initially internalised in an endosome and gallium released from transferrin upon lowering of the pH. While in the case of iron, transfer to the cytoplasm is then mediated by divalent metal transporters, these biomolecules are not able to bind Ga(III), whose cellular trafficking remains elusive [156].

Intracellular distribution is also not completely understood. Both light and electron microscopy autoradiography showed accumulation of gallium granules in lysosome-like organelles [157]. However, the form in which gallium is stored in these organelles is debated, with some evidence suggesting binding to a macromolecule of 45 kDa [158,159]. Some other studies highlighted binding of gallium to ferritin, possibly mediated by phosphate molecules [115,116]. However, a more recent study showed that gallium binds to ferritin to a lesser extent compared to iron [160].

1.3.5 Mechanism for gallium uptake in bone

The ability of gallium to accumulate in bones, with particular affinity for growing and remodelling sites, has been documented [129,161]. Uptake of radioactive gallium in bones increases in the presence of carrier-added Ga(III) or Fe(III) above the threshold of transferrin saturation [132], and remains unaltered whenever transferrin dependent transport mechanisms are suppressed by different experimental procedures [153].

While these studies demonstrate that transferrin is not involved in bone accumulation of gallium [162], the mechanisms responsible for this accumulation remain largely unknown, although they are likely to involve the free gallate anion. Like many trivalent ions, gallium is known to adsorb to synthetic hydroxyapatite *in vitro* [163]. *In vivo* this adsorption could be directly mediated by the small concentration of gallate present in serum at physiological pH, or released by transferrin *in situ* in the presence of local acidic conditions or high concentrations of phosphates [115]. In fact, it has been shown *in vitro* that both ATP and pyrophosphate decrease binding of transferrin to ^{67}Ga, thus facilitating gallium transfer to other macromolecules. It is beyond the scope of this chapter to describe gallium interaction with bone cells function and the resulting pharmacological activity. Extensive description of these phaenomena can be found in a comprehensive review by Bernstein [111].

1.3.6 Mechanism for gallium uptake in infections and inflammation

Beside its accumulation in bones and cancer, gallium was also observed to localise in sites of inflammation and infection as demonstrated by several preclinical and clinical studies with ^{67}Ga [111]. Gallium localisation in inflammation and infections is linked to increased blood flow and vascular permeability in these lesions and has not been observed in the absence of an adequate blood supply [164]. Through this increased blood flow, gallium is delivered to the lesion in either its unbound or GaTf form. Here it can transchelate to lactoferrin, which is excreted by leukocytes (mainly neutrophils) as part of the inflammation process. Lactoferrin possesses higher affinity for gallium compared to transferrin (at 5 mM bicarbonate concentration LogK_1 = 21.43, LogK_2 = 20.57 vs LogK_1 = 19.53, LogK_2 = 18.58 for transferrin [112]). Once bound to lactoferrin, gallium can be incorporated in leukocytes as well as in macrophages [111] and these cells can then migrate to different sites of infection, transporting their intracellular gallium to new infection *foci* [165]. Direct ^{67}Ga labelling of leukocytes followed by their migration to sites of inflammation/infection has also been shown [166]. Where bacteria are present, they can bind gallium *via* siderophores, released at the infection site with the aim of acquiring iron from the environment [111]. Additional mechanisms for bacterial uptake of ^{67}Ga involve facilitated diffusion of the metal ion across the plasma membrane and non-specific uptake [167].

1.4 References

1. Weiner, R. E., and Thakur, M. L. (2005) Chemistry of Gallium and Indium Radiopharmaceuticals. in *Handbook of Radiopharmaceuticals*, John Wiley & Sons, Ltd. pp 363-399.
2. Howell, R. W. (1992) Radiation spectra for auger-electron emitting radionuclides - report no 2 of AAPM-nuclear-medicine-task-group no 6. *Med. Phys.* **19**, 1371-1383.
3. Brucer, M., and Bruner, H. D. (1953) A study of gallium .1. physics and radiation characteristics of gallium-72. *Radiology* **61**, 537-543.
4. Saha, G. B. (2010) *Fundamentals of nuclear pharmacy*, Springer Science & Business Media.
5. Ali, L., Khalil, M., and Hadi, N. (2010) Revisiting gallium-67 imaging: investigation of the energy photopeaks. *Nucl. Med. Commun.* **31**, 1068-1074.
6. Bin Othman, M. F., Mitry, N. R., Lewington, V. J., Blower, P. J., and Terry, S. Y. A. (2017) Re-assessing gallium-67 as a therapeutic radionuclide. *Nucl. Med. Biol.* **46**, 12-18.
7. Conti, M., and Eriksson, L. (2016) Physics of pure and non-pure positron emitters for PET: a review and a discussion. *Ejnmmi Physics* **3.**
8. Velikyan, I. (2014) Prospective of Ga-68-radiopharmaceutical development. *Theranostics* **4**, 47-80.
9. Yano, Y., and Anger, H. O. (1964) A gallium-68 positron cow for medical use. *J. Nucl. Med.* **5**, 485-487.
10. Velikyan, I. (2015) Ga-68-Based Radiopharmaceuticals: production and application relationship. *Molecules* **20**, 12913-12943.
11. He, P., Burke, B. P., Clemente, G. S., Brown, N., Pamme, N., and Archibald, S. J. (2016) Monolith-based Ga-68 processing: a new strategy for purification to facilitate direct radiolabelling methods. *React. Chem. Eng.* **1**, 361-365.
12. Graham, M. C., Pentlow, K. S., Mawlawi, O., Finn, R. D., Daghighian, F., and Larson, S. M. (1997) An investigation of the physical characteristics of Ga-66 as an isotope for PET imaging and quantification. *Med. Phys.* **24**, 317-326.
13. Andrews, G. A., Root, S. W., and Kerman, H. D. (1953) A study of gallium .6. clinical studies with gallium-72. *Radiology* **61**, 570-588.
14. Bartholoma, M. D., Louie, A. S., Valliant, J. F., and Zubieta, J. (2010) Technetium and gallium derived radiopharmaceuticals: comparing and contrasting the chemistry of two important radiometals for the molecular imaging era. *Chem. Rev.* **110**, 2903-2920.
15. Green, M. A., and Welch, M. J. (1989) Gallium radiopharmaceutical chemistry. *Nucl. Med. Biol.* **16**, 435-448.
16. Harris, W. R., and Pecoraro, V. L. (1983) Thermodynamic binding constants for gallium transferrin. *Biochemistry* **22**, 292-299.
17. Theobald, T. (2010) *Sampson's Textbook of Radiopharmacy*, Pharmaceutical Press, London.
18. Shannon, R. D. (1976) Revised effective ionic-radii and systematic studies of interatomic distances in halides and chalcogenides. *Acta Crystallogr. Sect.A* **32**, 751-767.
19. Price, E. W., and Orvig, C. (2014) Matching chelators to radiometals for radiopharmaceuticals. *Chem. Soc. Rev.* **43**, 260-290.
20. Bartholoma, M. D. (2012) Recent developments in the design of bifunctional chelators for metal-based radiopharmaceuticals used in Positron Emission Tomography. *Inorg. Chim. Acta* **389**, 36-51.
21. Burke, B. P., Clemente, G. S., and Archibald, S. J. (2014) Recent advances in chelator design and labelling methodology for Ga-68 radiopharmaceuticals. *J. Label. Compd. Radiopharm.* **57**, 239-243.

22. Spang, P., Herrmann, C., and Roesch, F. (2016) Bifunctional gallium-68 chelators: past, present, and future. *Semin. Nucl. Med.* **46**, 373-394.
23. Macrae, C. F., Bruno, I. J., Chisholm, J. A., Edgington, P. R., McCabe, P., Pidcock, E., Rodriguez-Monge, L., Taylor, R., van de Streek, J., and Wood, P. A. (2008) Mercury CSD 2.0 - new features for the visualization and investigation of crystal structures. *J. Appl. Crystallogr.* **41**, 466-470.
24. Pierre V. C., and Allen, M. J. (2017) *Contrast Agents for MRI: Experimental Methods*, Royal Society of Chemistry.
25. Viola-Villegas, N., and Doyle, R. P. (2009) The coordination chemistry of 1,4,7,10-tetraazacyclododecane-N,N',N'',N'''-tetraacetic acid (H_4DOTA): Structural overview and analyses on structure-stability relationships. *Coord. Chem. Rev.* **253**, 1906-1925.
26. Clarke, E. T., and Martell, A. E. (1991) Stabilities of trivalent metal-ion complexes of the tetraacetate derivatives of 12-membered, 13-membered and 14-membered tetraazamacrocycles. *Inorg. Chim. Acta* **190**, 37-46.
27. Kubicek, V., Havlickova, J., Kotek, J., Gyula, T., Hermann, P., Toth, E., and Lukes, I. (2010) Gallium(III) Complexes of DOTA and DOTA-Monoamide: Kinetic and Thermodynamic Studies. *Inorg. Chem.* **49**, 10960-10969.
28. Zeglis, B. M., Houghton, J. L., Evans, M. J., Viola-Villegas, N., and Lewis, J. S. (2013) Underscoring the Influence of Inorganic Chemistry on Nuclear Imaging with Radiometals. *Inorg. Chem.* **53**(4), 1880-1899.
29. Delgado, R., Quintino, S., Teixeira, M., and Zhang, A. (1997) Metal complexes of a 12-membered tetraaza macrocycle containing pyridine and N-carboxymethyl groups. *J. Chem. Soc., Dalton Trans.*, 55-63.
30. Kim, W. D., Kiefer, G. E., Maton, F., McMillan, K., Muller, R. N., and Sherry, A. D. (1995) Relaxometry, luminescence measurements, electrophoresis, and animal biodistribution of lanthanide(III) complexes of some polyaza macrocyclic acetates containing pyridine. *Inorg. Chem.* **34**, 2233-2243.
31. Ferreira, C. L., Lamsa, E., Woods, M., Duan, Y., Fernando, P., Bensimon, C., Kordos, M., Guenther, K., Jurek, P., and Kiefer, G. E. (2010) Evaluation of Bifunctional Chelates for the Development of Gallium-Based Radiopharmaceuticals. *Bioconjugate Chem.* **21**, 531-536.
32. Ferreira, C. L., Yapp, D. T. T., Mandel, D., Gill, R. K., Boros, E., Wong, M. Q., Jurek, P., and Kiefer, G. E. (2012) Ga-68 Small Peptide Imaging: Comparison of NOTA and PCTA. *Bioconjugate Chem.* **23**, 2239-2246.
33. Clarke, E. T., and Martell, A. E. (1991) Stabilities of the Fe(III), Ga(III) and In(III) Chelates Of N,N',N''-Triazacyclononanetriacetic Acid. *Inorg. Chim. Acta* **181**, 273-280.
34. Wadas, T. J., Wong, E. H., Weisman, G. R., and Anderson, C. J. (2010) Coordinating Radiometals of Copper, Gallium, Indium, Yttrium, and Zirconium for PET and SPECT Imaging of Disease. *Chem. Rev.* **110**, 2858-2902.
35. Velikyan, I., Maecke, H., and Langstrom, B. (2008) Convenient preparation of Ga-68-based PET-radiopharmaceuticals at room temperature. *Bioconjugate Chem.* **19**, 569-573.
36. P. Andre, J., R. Maecke, H., P. Andre, J., Zehnder, M., Macko, L., and G. Akyel, K. (1998) 1,4,7-Triazacyclononane-1-succinic acid-4,7-diacetic acid (NODASA): a new bifunctional chelator for radio gallium-labelling of biomolecules. *Chem. Commun.*, 1301-1302.
37. de Sa, A., Matias, A. A., Prata, M. I. M., Geraldes, C., Ferreira, P. M. T., and Andre, J. P. (2010) Gallium labeled NOTA-based conjugates for peptide receptor-mediated medical imaging. *Bioorg. Med. Chem. Lett.* **20**, 7345-7348.
38. Notni, J., Hermann, P., Havlickova, J., Kotek, J., Kubicek, V., Plutnar, J., Loktionova, N., Riss, P. J., Roesch, F., and Lukes, I. (2010) A triazacyclononane-based bifunctional phosphinate ligand for the preparation of multimeric Ga-68 tracers for positron emission tomography. *Chem. Eur. J.* **16**, 7174-7185.

39. Notni, J., Simecek, J., Hermann, P., and Wester, H.-J. (2011) TRAP, a powerful and versatile framework for gallium-68 radiopharmaceuticals. *Chem. Eur. J.* **17**, 14718-14722.

40. Simecek, J., Zemek, O., Hermann, P., Notni, J., and Wester, H.-J. (2014) Tailored gallium(III) chelator NOPO: synthesis, characterization, bioconjugation, and application in preclinical Ga-68-PET imaging. *Mol. Pharm.* **11**, 3893-3903.

41. Simecek, J., Hermann, P., Wester, H. J., and Notni, J. (2013) How is Ga-68 labeling of macrocyclic chelators influenced by metal Ion contaminants in Ge-68/Ga-68 generator eluates? *ChemMedChem* **8**, 95-103.

42. Notni, J., Hermann, P., Dregely, I., and Wester, H. J. (2013) convenient synthesis of Ga-68-labeled gadolinium(III) complexes: towards bimodal responsive probes for functional imaging with PET/MRI. *Chem. Eur. J.* **19**, 12602-12606.

43. Ma, M. T., Neels, O. C., Denoyer, D., Roselt, P., Karas, J. A., Scanlon, D. B., White, J. M., Hicks, R. J., and Donnelly, P. S. (2011) Gallium-68 complex of a macrobicyclic cage amine chelator tethered to two integrin-targeting peptides for diagnostic tumor imaging. *Bioconjugate Chem.* **22**, 2093-2103.

44. Aime, S., Calabi, L., Cavallotti, C., Gianolio, E., Giovenzana, G. B., Losi, P., Maiocchi, A., Palmisano, G., and Sisti, M. (2004) [Gd-AAZTA]⁻: A new structural entry for an improved generation of MRI contrast agents. *Inorg. Chem.* **43**, 7588-7590.

45. Baranyai, Z., Uggeri, F., Maiocchi, A., Giovenzana, G. B., Cavallotti, C., Takacs, A., Toth, I., Banyai, I., Benyei, A., Brucher, E., and Aime, S. (2013) Equilibrium, Kinetic and Structural Studies of AAZTA Complexes with Ga^{3+}, In^{3+} and Cu^{2+}. *Eur. J. Inorg. Chem.*, 147-162.

46. Waldron, B. P., Parker, D., Burchardt, C., Yufit, D. S., Zimny, M., and Roesch, F. (2013) Structure and stability of hexadentate complexes of ligands based on AAZTA for efficient PET labelling with gallium-68. *Chem. Commun.* **49**, 579-581.

47. Pfister, J., Summer, D., Rangger, C., Petrik, M., von Guggenberg, E., Minazzi, P., Giovenzana, G. B., Aloj, L., and Decristoforo, C. (2015) Influence of a novel, versatile bifunctional chelator on theranostic properties of a minigastrin analogue. *EJNMMI Res.* **5.**

48. Parker, D., Waldron, B. P., and Yufit, D. S. (2013) Crystallographic and solution NMR structural analyses of four hexacoordinated gallium(III) complexes based on ligands derived from 6-amino-perhydro-1,4-diazepine. *Dalton Trans.* **42**, 8001-8008.

49. Seemann, J., Waldron, B. P., Roesch, F., and Parker, D. (2015) Approaching "Kit-Type" Labelling with Ga-68: The DATA Chelators. *Chemmedchem* **10**, 1019-1026.

50. Nock, B. A., Kaloudi, A., Nagel, J., Sinnes, J.-P., Roesch, F., and Maina, T. (2017) Novel bifunctional DATA chelator for quick access to site-directed PET ⁶⁸Ga-radiotracers: preclinical proof-of-principle with [Tyr³]octreotide. *Dalton Trans.* **46**, 14584–14590.

51. Leplatte.F, Murase, I., and Martell, A. E. (1967) New multidentate ligands .6. chelating tendencies of N,N'-di(2-hydroxybenzyl) ethylenediamine-N,N'-diacetic acid. *J. Am. Chem. Soc.* **89(4)**, 837-843.

52. Ma, R., Motekaitis, R. J., and Martell, A. E. (1994) Stability of metal-ion complexes of N,N'-bis(2-hydroxybenzyl)ethylenediamine-N,N'-diacetic acid. *Inorg. Chim. Acta* **224**, 151-155.

53. Motekaitis, R. J., Sun, Y., Martell, A. E., and Welch, M. J. (1991) Stabilities of gallium(III), iron(III), and indium(III) chelates of hydroxyaromatic ligands with different overall charges. *Inorg. Chem.* **30**, 2737-2740.

54. Eder, M., Wangler, B., Knackmuss, S., LeGall, F., Little, M., Haberkorn, U., Mier, W., and Eisenhut, M. (2008) Tetrafluorophenolate of HBED-CC: a versatile conjugation agent for Ga-68-labeled small recombinant antibodies. *Eur. J. Nucl. Med. Mol. Imaging* **35**, 1878-1886.

55. Eder, M., Schafer, M., Bauder-Wust, U., Hull, W. E., Wangler, C., Mier, W., Haberkorn, U., and Eisenhut, M. (2012) Ga-68-Complex lipophilicity and the targeting property of a urea-based PSMA inhibitor for PET imaging. *Bioconjugate Chem.* **23**, 688-697.

56. Eder, M., Neels, O., Müller, M., Bauder-Wüst, U., Remde, Y., Schäfer, M., Hennrich, U., Eisenhut, M., Afshar-Oromieh, A., Haberkorn, U., and Kopka, K. (2014) Novel preclinical and radiopharmaceutical aspects of [^{68}Ga]Ga-PSMA-HBED-CC: A new PET tracer for imaging of prostate cancer. *Pharmaceuticals* **7**, 779-796.

57. Tsionou, M. I., Knapp, C. E., Foley, C. A., Munteanu, C. R., Cakebread, A., Imberti, C., Eykyn, T. R., Young, J. D., Paterson, B. M., Blower, P. J., and Ma, M. T. (2017) Comparison of macrocyclic and acyclic chelators for gallium-68 radiolabelling. *RSC Adv.* **7**, 49586-49599.

58. Ferreiros-Martinez, R., Esteban-Gomez, D., Platas-Iglesias, C., de Blas, A., and Rodriguez-Blas, T. (2008) Zn(II), Cd(II) and Pb(II) complexation with pyridinecarboxylate containing ligands. *Dalton Trans.*, 5754-5765.

59. Boros, E., Ferreira, C. L., Cawthray, J. F., Price, E. W., Patrick, B. O., Wester, D. W., Adam, M. J., and Orvig, C. (2010) Acyclic chelate with ideal properties for Ga-68 PET imaging agent elaboration. *J. Am. Chem. Soc.* **132**, 15726-15733.

60. Boros, E., Ferreira, C. L., Yapp, D. T. T., Gill, R. K., Price, E. W., Adam, M. J., and Orvig, C. (2012) RGD conjugates of the H(2)dedpa scaffold: synthesis, labeling and imaging with Ga-68. *Nucl. Med. Biol.* **39**, 785-794.

61. Moeschlin, S., and Schnider, U. (1963) Treatment of primary and secondary hemochromatosis and acute iron poisoning with a new, potent iron-eliminating agent (Desferrioxamine-B). *N. Engl. J. Med.* **269**, 57-66.

62. Evers, A., Hancock, R. D., Martell, A. E., and Motekaitis, R. J. (1989) Metal-ion recognition in ligands with negatively charged oxygen donor groups - complexation of Fe(III), Ga(III), In(III), Al(III), and other highly charged metal-ions. *Inorg. Chem.* **28**, 2189-2195.

63. Borgias, B., Hugi, A. D., and Raymond, K. N. (1989) Isomerization and solution structures of desferrioxamine-B complexes of Al^{3+} and Ga^{3+}. *Inorg. Chem.* **28**, 3538-3545

64. Yokoyama, A., Ohmomo, Y., Horiuchi, K., Saji, H., Tanaka, H., Yamamoto, K., Ishii, Y., and Torizuka, K. (1982) Deferoxamine, a promising bifunctional chelating agent for labeling proteins with gallium - Ga-67 Df-HSA - concise communication. *J. Nucl. Med.* **23**, 909-914.

65. Mathias, C. J., Wang, S., Lee, R. J., Waters, D. J., Low, P. S., and Green, M. A. (1996) Tumor-selective radiopharmaceutical targeting via receptor-mediated endocytosis of gallium-67-deferoxamine-folate. *J. Nucl. Med.* **37**, 1003-1008.

66. Smithjones, P. M., Stolz, B., Bruns, C., Albert, R., Reist, H. W., Fridrich, R., and Macke, H. R. (1994) Gallium-67/gallium-68- DFO -octreotide - a potential radiopharmaceutical for PET imaging of somatostatin receptor-positive tumors - synthesis and radiolabeling in-vitro and preliminary in-vivo studies. *J. Nucl. Med.* **35**, 317-325.

67. Caraco, C., Aloj, L., and Eckelman, W. C. (1998) The gallium-deferoxamine complex: Stability with different deferoxamine concentrations and incubation conditions. *Appl. Radiat. Isot.* **49**, 1477-1479.

68. Govindan, S. V., Michel, R. B., Griffiths, G. L., Goldenberg, D. M., and Mattes, M. J. (2005) Deferoxamine as a chelator for Ga-67 in the preparation of antibody conjugates. *Nucl. Med. Biol.* **32**, 513-519.

69. Petrik, M., Haas, H., Dobrozemsky, G., Lass-Florl, C., Helbok, A., Blatzer, M., Dietrich, H., and Decristoforo, C. (2010) Ga-68-Siderophores for PET Imaging of Invasive Pulmonary Aspergillosis: Proof of Principle. *J. Nucl. Med.* **51**, 639-645.

70. Zhai, C. Y., Summer, D., Rangger, C., Haas, H., Haubner, R., and Decristoforo, C. (2015) Fusarinine C, a novel siderophore-based bifunctional chelator for radiolabeling with Gallium-68. *J. Label. Compd. Radiopharm.* **58**, 209-214.

71. Knetsch, P. A., Zhai, C., Rangger, C., Blatzer, M., Haas, H., Kaeopookum, P., Haubner, R., and Decristoforo, C. (2015) Ga-68 FSC-(RGD)$_3$ a trimeric RGD peptide for imaging $\alpha_v\beta_3$ integrin expression based on a novel siderophore derived chelating scaffold-synthesis and evaluation. *Nucl. Med. Biol.* **42**, 115-122.

72. Scarrow, R. C., Riley, P. E., Abudari, K., White, D. L., and Raymond, K. N. (1985) Ferric ion sequestering agents. 13. synthesis, structures, and thermodynamics of complexation of cobalt(III) and iron(III) tris complexes of several chelating hydroxypyridinones. *Inorg. Chem.* **24**, 954-967.

73. Dobbin, P. S., Hider, R. C., Hall, A. D., Taylor, P. D., Sarpong, P., Porter, J. B., Xiao, G. Y., and Vanderhelm, D. (1993) Synthesis, physicochemical properties, and biological evaluation of N-substituted 2-alkyl-3-hydroxy-4(1*H*)-pyridinones - orally-active iron chelators with clinical potential. *J. Med. Chem.* **36**, 2448-2458.

74. Charalambous, J., Dodd, A., McPartlin, M., Matondo, S. O. C., Pathirana, N. D., and Powell, H. R. (1988) Synthesis and x-ray crystal-structure of tris(1,2-dimethyl-3-hydroxypyrid-4-onato)iron(III). *Polyhedron* **7**, 2235-2237.

75. Clevette, D. J., Lyster, D. M., Nelson, W. O., Rihela, T., Webb, G. A., and Orvig, C. (1990) Solution chemistry of gallium and indium 3-hydroxy-4-pyridinone complexes in vitro and in vivo. *Inorg. Chem.* **29**, 667-672.

76. Clarke, E. T., and Martell, A. E. (1992) Stabilities of 1,2-dimethyl-3-hydroxy-4-pyridinone chelates of divalent and trivalent metal-ions. *Inorg. Chim. Acta* **191**, 57-63.

77. Nelson, W. O., Karpishin, T. B., Rettig, S. J., and Orvig, C. (1988) Aluminum and gallium compounds of 3-hydroxy-4-pyridinones - Synthesis, characterization, and crystallography of biologically-active complexes with unusual hydrogen-bonding. *Inorg. Chem.* **27**, 1045-1051.

78. Burges J., and Rangel M. (2008) Advances in Inorganic Chemistry. (Van Eldik R.), Academic Press, Elsevier.

79. Zhou, T., Hider, R. C., and Kong, X. L. (2015) Mode of iron(III) chelation by hexadentate hydroxypyridinones. *Chem. Commun.* **51**, 5614-5617.

80. Xu, J., Kullgren, B., Durbin, P. W., and Raymond, K. N. (1995) Specific sequestering agents for the actinides .28. Synthesis and initial evaluation of multidentate 4-carbamoyl-3-hydroxy-1-methyl-2(1*H*)-pyridinone ligands for in-vivo plutonium(IV) chelation. *J. Med. Chem.* **38**, 2606-2614.

81. Chaves, S., Marques, S. M., Matos, A. M. F., Nunes, A., Gano, L., Tuccinardi, T., Martinelli, A., and Santos, M. A. (2010) New Tris(hydroxypyridinones) as iron and aluminium sequestering agents: synthesis, somplexation and in vivo studies. *Chem. Eur. J.* **16**, 10535-10545.

82. Grazina, R., Gano, L., Sebestik, J., and Santos, M. A. (2009) New tripodal hydroxypyridinone based chelating agents for Fe(III), Al(III) and Ga(III): Synthesis, physico-chemical properties and bioevaluation. *J. Inorg. Biochem.* **103**, 262-273.

83. Xie, Y. Y., Liu, M. S., Hu, P. P., Kong, X. L., Qiu, D. H., Xu, J. L., Hider, R. C., and Zhou, T. (2013) Synthesis, physico-chemical properties, and antimicrobial evaluation of a new series of iron(III) hexadentate chelators. *Med. Chem. Res.* **22**, 2351-2359.

84. Berry, D. J., Ma, Y., .Ballinger, J. R., Tavaré, R., Koers, A., Sunassee, K., Zhou, T., Nawaz, S., Mullen, G. E. D., Hider, R. C., and Blower, P. J. (2011) Efficient

bifunctional gallium-68 chelators for positron emission tomography: Tris(hydroxypyridinone) ligands. *Chem. Commun.* **47**, 7068-7070.

85. Zhou, T., Neubert, H., Liu, D. Y., Liu, Z. D., Ma, Y. M., Kong, X. L., Luo, W., Mark, S., and Hider, R. C. (2006) Iron binding dendrimers: A novel approach for the treatment of haemochromatosis. *J. Med. Chem.* **49**, 4171-4182.

86. Piyamongkol, S., Zhou, T., Liu, Z. D., Khodr, H. H., and Hider, R. C. (2005) Design and characterisation of novel hexadentate 3-hydroxypyridin-4-one ligands. *Tetrahedron Lett.* **46**, 1333-1336.

87. Chaves, S., Mendonca, A. C., Marques, S. M., Prata, M. I., Santos, A. C., Martins, A. F., Geraldes, C., and Santos, M. A. (2011) A gallium complex with a new tripodal tris-hydroxypyridinone for potential nuclear diagnostic imaging solution and in vivo studies of Ga-67-labeled species. *J. Inorg. Biochem.* **105**, 31-38.

88. Ma, M. T., Cullinane, C., Imberti, C., Baguna Torres, J., Terry, S. Y. A., Roselt, P., Hicks, R. J., and Blower, P. J. (2015) New tris(hydroxypyridinone) bifunctional chelators containing isothiocyanate groups provide a versatile platform for rapid one-step labeling and PET imaging with $^{68}Ga^{3+}$. *Bioconjugate Chem.* **27**, 309-318.

89. Young, J. D., Abbate, V., Imberti, C., Meszaros, L. K., Ma, M. T., Terry, S. Y. A., Hider, R. C., Mullen, G. E., and Blower, P. J. (2017) ^{68}Ga-THP-PSMA: a PET imaging agent for prostate cancer offering rapid, room-temperature, 1-step kit-based radiolabeling. *J. Nucl. Med.* **58**, 1270-1277.

90. Zhou, T., Le Kong, X., Liu, Z. D., Liu, D. Y., and Hider, R. C. (2008) Synthesis and iron(III)-chelating properties of novel 3-hydroxypyridin-4-one hexadentate ligand-containing copolymers. *Biomacromolecules* **9**, 1372-1380.

91. Morfin, J.-F., and Toth, E. (2011) Kinetics of Ga(NOTA) formation from weak Ga-Citrate complexes. *Inorg. Chem.* **50**, 10371-10378.

92. Harris, W. R., and Martell, A. E. (1976) Aqueous complexes of gallium(III). *Inorg. Chem.* **15**, 713-720.

93. Matzapetakis, M., Kourgiantakis, M., Dakanali, M., Raptopoulou, C. P., Terzis, A., Lakatos, A., Kiss, T., Banyai, I., Iordanidis, L., Mavromoustakos, T., and Salifoglou, A. (2001) Synthesis, pH-dependent structural characterization, and solution behavior of aqueous aluminum and gallium citrate complexes. *Inorg. Chem.* **40**, 1734-1744.

94. Jackson, G. E., and Byrne, M. J. (1996) Metal ion speciation in blood plasma: Gallium-67-citrate and MRI contrast agents. *J. Nucl. Med.* **37**, 379-386.

95. Clausen, M., Ohman, L. O., Kubicki, J. D., and Persson, P. (2002) Characterisation of gallium(III)-acetate complexes in aqueous solution: A potentiometric, EXAFS, IR and molecular orbital modelling study. *J. Chem. Soc., Dalton Trans.*, 2559-2564.

96. Larson, S. M., Grunbaum, Z., and Rasey, J. S. (1981) The role of transferrins in gallium uptake. *Int. J. Nucl. Med. Biol.* **8**, 257-266.

97. Hayes, R. L. (1977) Tissue distribution of gallium radionuclides. *J. Nucl. Med.* **18**, 740-742.

98. Chitambar, C. R. (2012) Gallium-containing anticancer compounds. *Future Med. Chem.* **4**, 1257-1272.

99. Sun, H. Z., Li, H. Y., and Sadler, P. J. (1999) Transferrin as a metal ion mediator. *Chem. Rev.* **99**, 2817-2842.

100. Huebers, H., Josephson, B., Huebers, E., Csiba, E., and Finch, C. (1981) Uptake and release of iron from human transferrin. *Proc. Natl. Acad. Sci. U.S.A-Biological Sciences* **78**, 2572-2576.

101. Goswami, T., and Andrews, N. C. (2006) Hereditary hemochromatosis protein, HFE, interaction with transferrin receptor 2 suggests a molecular mechanism for mammalian iron sensing. *J. Biol. Chem.* **281**, 28494-28498.

102.	Harris, W. R., and Messori, L. (2002) A comparative study of aluminum(III), gallium(III), indium(III), and thallium(III) binding to human serum transferrin. *Coord. Chem. Rev.* **228**, 237-262.
103.	Chahine, J. M. E., Hemadi, M., and Ha-Duong, N. T. (2012) Uptake and release of metal ions by transferrin and interaction with receptor 1. *Biochim. Biophys. Acta-Gen. Subj.* **1820**, 334-347.
104.	Chitambar, C. R. (2016) Gallium and its competing roles with iron in biological systems. *Biochim. Biophys. Acta-Mol. Cell Res.* **1863**, 2044-2053.
105.	Hartman, R. E., and Hayes, R. L. (1969) Binding of gallium by blood serum. *J. Pharmacol. Exp. Ther.* **168**, 193-198.
106.	Gunasekera, S. W., King, L. J., and Lavender, P. J. (1972) Behavior of tracer gallium-67 towards serum-proteins. *Clin. Chim. Acta* **39**, 401-406.
107.	Vallabhajosula, S. R., Harwig, J. F., Siemsen, J. K., and Wolf, W. (1980) Radiogallium localization in tumors - blood binding and transport and the role of transferrin. *J. Nucl. Med.* **21**, 650-656.
108.	Staker, B. L., Graham, M. M., and Evans, M. L. (1991) Effect of bicarbonate on stability of the gallium-transferrin complex. *J. Nucl. Med.* **32**, 1439-1441.
109.	McGregor, S. J., and Brock, J. H. (1992) Effect of pH and citrate on binding of iron and gallium by transferrin in serum. *Clin. Chem.* **38**, 1883-1885.
110.	Chikh, Z., Ha-Duong, N. T., Miquel, G., and Chahine, J. M. E. (2007) Gallium uptake by transferrin and interaction with receptor 1. *J. Biol. Inorg. Chem.* **12**, 90-100.
111.	Bernstein, L. R. (1998) Mechanisms of therapeutic activity for gallium. *Pharmacol. Rev.* **50**, 665-682.
112.	Harris, W. R. (1986) Thermodynamics of gallium complexation by human lactoferrin. *Biochemistry* **25**, 803-808.
113.	Weiner, R. E., Schreiber, G. J., and Hoffer, P. B. (1983) In vitro transfer of Ga-67 from transferrin to ferritin. *J. Nucl. Med.* **24**, 608-614.
114.	Weiner, R. E., Schreiber, G. J., Hoffer, P. B., and Bushberg, J. T. (1985) Compounds which mediate Ga-67 transfer from lactoferrin to ferritin. *J. Nucl. Med.* **26**, 908-916.
115.	Weiner, R. E. (1989) Role of phosphate-containing compounds in the transfer of In-111 and Ga-67 from transferrin to ferritin. *J. Nucl. Med.* **30**, 70-79.
116.	Chitambar, C. R., and Zivkovic, Z. (1987) Uptake of gallium-67 by Human Leukemic Cells: Demonstration of transferrin receptor-dependent and transferrin-independent mechanisms. *Cancer Res.* **47**, 3929-3934.
117.	Richardson, D. R., and Ponka, P. (1997) The molecular mechanisms of the metabolism and transport of iron in normal and neoplastic cells. *Biochim. Biophys. Acta-Reviews on Biomembranes* **1331**, 1-40.
118.	Emery, T. (1986) Exchange of iron by gallium in siderophores. *Biochemistry* **25**, 4629-4633.
119.	Logan, K. J., Ng, P. K., Turner, C. J., Schmidt, R. P., Terner, U. K., Scott, J. R., Lentle, B. C., and Noujaim, A. A. (1981) Comparative pharmacokinetics of Ga-67 and Fe-59 in humans. *Int. J. Nucl. Med. Biol.* **8**, 271-276.
120.	Sephton, R. G., Hodgson, G. S., Deabrew, S., and Harris, A. W. (1978) Ga-67 and Fe-59 distributions in mice. *J. Nucl. Med.* **19**, 930-935.
121.	Hayes, R. L., Byrd, B. L., Carlton, J. E., and Rafter, J. J. (1970) Factors affecting localization of Ga-67 in animal tumors. *J. Nucl. Med.* **11**, 324.
122.	Swartzendruber, D. C., Byrd, B. L., Hayes, R. L., and Nelson, B. (1970) Preferential localization of Ga-67 citrate in tissues of leukemic mice. *Jnci-J. Natl. Cancer Inst.* **44**, 695-700.
123.	Hammersley, P. A. G., and Zivanovic, M. A. (1980) The relationship of Ga-67 uptake to citrate dose, compared with Ga-67-chloride and Ga-67-transferrin in rodent tissues and tumors. *Nuklearmedizin* **19**, 25-28.

124. Petrik, M., Vlckova, A., Novy, Z., Urbanek, L., Haas, H., and Decristoforo, C. (2015) Selected Ga-68-siderophores versus Ga-68-colloid and Ga-68-citrate: biodistribution and small animal imaging in mice. *Biomedical Papers-Olomouc* **159**, 60-66.

125. Ujula, T., Salomaki, S., Autio, A., Luoto, P., Tolvanen, T., Lehikoinen, P., Viljanen, T., Sipila, H., Harkonen, P., and Roivainen, A. (2010) Ga-68-Chloride PET reveals human pancreatic adenocarcinoma xenografts in rats-comparison with FDG. *Mol. Imaging Biol.* **12**, 259-268.

126. Silvola, J. M. U., Laitinen, I., Sipila, H. J., Laine, V. J. O., Leppanen, P., Yla-Herttuala, S., Knuuti, J., and Roivainen, A. (2011) Uptake of [68]gallium in atherosclerotic plaques in LDLR^{-/-}ApoB[100/100] mice. *EJNMMI Res.* **1.**

127. Autio, A., Virtanen, H., Tolvanen, T., Liljenback, H., Oikonen, V., Saanijoki, T., Siitonen, R., Kakela, M., Schussele, A., Teras, M., and Roivainen, A. (2015) Absorption, distribution and excretion of intravenously injected [68]Ge/ [68]Ga generator eluate in healthy rats, and estimation of human radiation dosimetry. *EJNMMI Res.* **5.**

128. Ehrhardt, G. J., and Welch, M. J. (1978) New germanium-68-gallium-68 generator. *J. Nucl. Med.* **19**, 925-929.

129. Nelson, B., Andrews, G. A., Hayes, R. L., Kniseley, R. M., and Edwards, C. L. (1972) Distribution of gallium in human tissues after intravenous administration. *J. Nucl. Med.* **13**, 92-100.

130. Nanni, C., Errani, C., Boriani, L., Fantini, L., Ambrosini, V., Boschi, S., Rubello, D., Pettinato, C., Mercuri, M., Gasbarrini, A., and Fanti, S. (2010) Ga-68-citrate PET/CT for evaluating patients with infections of the bone: preliminary results. *J. Nucl. Med.* **51**, 1932-1936.

131. Bruner, H. D., Hayes, R. L., and Perkinson, J. D. (1953) A study of gallium .10. preliminary data on gallium-67. *Radiology* **61**, 602-613.

132. Hayes, R. L., Carlton, J. E., and Byrd, B. L. (1965) Bone scanning with gallium-68 - A carrier effect. *J. Nucl. Med.* **6**, 605-609.

133. Bradley, W. P., Alderson, P. O., Eckelman, W. C., Hamilton, R. G., and Weiss, J. F. (1978) Decreased tumor uptake of Ga-67 in animals after whole-body irradiation. *J. Nucl. Med.* **19**, 204-209.

134. Oster, Z. H., Larson, S. M., and Wagner, H. N. (1976) Possible enhancement of Ga-67-citrate imaging by iron dextran. *J. Nucl. Med.* **17**, 356-358.

135. Hayes, R. L., Byrd, B. L., Rafter, J. J., and Carlton, J. E. (1980) The effect of scandium on the tissue distribution of Ga-67 in normal and tumor-bearing rodents. *J. Nucl. Med.* **21**, 361-365.

136. Hayes, R. L., Rafter, J. J., Byrd, B. L., and Carlton, J. E. (1981) Studies of the in vivo entry of Ga-67 into normal and malignant-tissue. *J. Nucl. Med.* **22**, 325-332.

137. Schomacker, K., Franke, W. G., Henke, E., Fromm, W. D., Maka, G., and Beyer, G. J. (1986) The influence of isotopic and nonisotopic carriers on the biodistribution and biokinetics of M^{3+}-citrate complexes. *Eur. J. Nucl. Med.* **11**, 345-349.

138. Edwards, C. L., and Hayes, R. L. (1970) Scanning malignant neoplasms with gallium-67. *JAMA* **212**, 1181-1190.

139. Edwards, C. L., and Hayes, R. L. (1969) Tumor scanning with ^{67}Ga citrate. *J. Nucl. Med.* **10**, 103-105.

140. Larson, S. M., Milder, M. S., and Johnston, G. S. (1973) Interpretation of Ga-67 photoscan. *J. Nucl. Med.* **14**, 208-214.

141. Larson, S. M. (1978) Mechanisms of localization of Ga-67 in tumors. *Semin. Nucl. Med.* **8**, 193-203.

142. Weiner, R. E. (1996) The mechanism of Ga-67 localization in malignant disease. *Nucl. Med. Biol.* **23**, 745-751.

143. Larson, S. M., Rasey, J. S., Allen, D. R., Nelson, N. J., Grunbaum, Z., Harp, G. D., and Williams, D. L. (1980) Common pathway for tumor-cell uptake of Ga-67 and Fe-59 via a transferrin receptor. *J. Natl. Cancer Inst.* **64**, 41-53.

144. Harris, A. W., and Sephton, R. G. (1977) Transferrin promotion of Ga-67 and Fe-59 uptake by cultured mouse myeloma cells. *Cancer Res.* **37**, 3634-3638.

145. Sephton, R. G., and Harris, A. W. (1975) Gallium-67 citrate uptake by cultured tumor-cells, stimulated by serum transferrin. *J. Natl. Cancer Inst.* **54**, 1263-1266.

146. Swartzendruber, D. C., Nelson, B., and Hayes, R. L. (1971) Gallium-67 localization in lysosomal-like granules of leukemic and nonleukemic murine tissues. *Jnci-J. Natl. Cancer Inst.* **46**, 941-952.

147. Noujaim, A. A., Lentle, B. C., Hill, J. R., Terner, U. K., and Wong, H. (1979) Role of transferrin in the uptake of gallium by tumor-cells. *Int. J. Nucl. Med. Biol.* **6**, 193-199.

148. Taetle, R. (1990) The role of transferrin receptors in hematopoietic-cell growth. *Exp. Hematol.* **18**, 360-365.

149. Engelstad, B., Luk, S. S., and Hattner, R. S. (1982) Altered citrate-Ga-67 distribution in patients with multiple red-blood-cell transfusions. *AJR Am. J. Roentgenol.* **139**, 755-759.

150. Weiner, R. (1990) The role of transferrin and other receptors in the mechanism of Ga-67 localization. *Nucl. Med. Biol.* **17**, 141-149.

151. Sephton, R. (1981) Relationships between the metabolism of Ga-67 and iron. *Int. J. Nucl. Med. Biol.* **8**, 323-331.

152. Tsan, M. F., and Scheffel, U. (1986) Mechanism of Ga-67 accumulation in tumors. *J. Nucl. Med.* **27**, 1215-1219.

153. Sohn, M. H., Jones, B. J., Whiting, J. H., Datz, F. L., Lynch, R. E., and Morton, K. A. (1993) Distribution of Ga-67 in normal and hypotransferrinemic tumor-bearing mice. *J. Nucl. Med.* **34**, 2135-2143.

154. Luttropp, C. A., Jackson, J. A., Jones, B. J., Sohn, M. H., Lynch, R. E., and Morton, K. A. (1998) Uptake of gallium-67 in transfected cells and tumors absent or enriched in the transferrin receptor. *J. Nucl. Med.* **39**, 1405-1411.

155. Chan, S. M., Hoffer, P. B., Maric, N., and Duray, P. (1987) Inhibition of Ga-67 uptake in melanoma by an anti-human transferrin receptor monoclonal-antibody. *J. Nucl. Med.* **28**, 1303-1307.

156. Illing, A. C., Shawki, A., Cunningham, C. L., and Mackenzie, B. (2012) Substrate profile and metal-ion selectivity of human divalent metal-ion transporter-1. *J. Biol. Chem.* **287**, 30485-30496.

157. Brown, D. H., Byrd, B. L., Carlton, J. E., Swartzendruber, D. C., and Hayes, R. L. (1976) Quantitative study of subcellular-localization of Ga-67. *Cancer Res.* **36**, 956-963.

158. Hayes, R. L., and Carlton, J. E. (1973) A study of the macromolecular binding of ^{67}Ga in normal and malignant animal tissues. *Cancer Res.* **33**, 3265-3272.

159. Lawless, D., Brown, D. H., Hubner, K. F., Colyer, S. P., Carlton, J. E., and Hayes, R. L. (1978) Isolation and partial characterization of a ^{67}Ga-binding glycoprotein from Morris 5123C rat hepatoma. *Cancer Res.* **38**, 4440-4444.

160. Davies, N. P., Rahmanto, Y. S., Chitambar, C. R., and Richardson, D. R. (2006) Resistance to the antineoplastic agent gallium nitrate results in marked alterations in intracellular iron and gallium trafficking: Identification of novel intermediates. *J. Pharmacol. Exp. Ther.* **317**, 153-162.

161. Dudley, H. C., Maddox, G. E., and Larue, H. C. (1949) Studies of the metabolism of gallium. *J. Pharmacol. Exp. Ther.* **96**, 135-138.

162. Verron, E., Bouler, J. M., and Scimeca, J. C. (2012) Gallium as a potential candidate for treatment of osteoporosis. *Drug Discov. Today* **17**, 1127-1132.

163. Donnelly, R., and Boskey, A. (1989) The effect of gallium on seeded hydroxyapatite growth. *Calcified Tissue International* **44**, 138-142.

164. Tsan, M. F. (1985) Mechanism of Ga-67 accumulation in inflammatory lesions. *J. Nucl. Med.* **26**, 88-92.
165. Palestro, C. J. (1994) The current role of gallium imaging in infection. *Semin. Nucl. Med.* **24**, 128-141.
166. Hoffer, P. (1980) Gallium - mechanisms. *J. Nucl. Med.* **21**, 282-285.
167. Menon, S., Wagner, H. N., and Tsan, M. F. (1978) Studies on gallium accumulation in inflammatory lesions .2. Uptake by Staphylococcus-Aureus - concise communication. *J. Nucl. Med.* **19**, 44-47.

2 Clinical application of gallium compounds.

Radionuclide imaging with ^{68}Ga (and previously with ^{67}Ga), represents the main clinical application of gallium compounds and will be the focus of the chapter. In particular, targeted imaging of receptors, using ^{68}Ga-labelled peptides provides the principal driver for ^{68}Ga tracers development and will be described extensively in the first section. Different strategies for imaging with ^{68}Ga, including pretargeted and non-targeted imaging will also be described. Alongside the development of new radiotracers, research on gallium compounds as chemotherapeutics has also produced some compounds of clinical interest for the treatment of cancer and related pathologies that will also be briefly discussed.

2.1 ^{68}Ga as a game-changer in PET imaging

The interest of nuclear medicine researchers in gallium isotopes dates back in the 1950s, first with the use of ^{72}Ga [1] and then ^{67}Ga as a bone scanning agent [2] and, later, to detect several types of soft tumour exploiting its similarity with iron [3]. Gallium-68 itself had been considered for clinical use in the 1960s, when carrier added ^{68}Ga-citrate was exploited for bone scanning [4] and [^{68}Ga]Ga-EDTA used for the detection of brain tumours in association with the newly developed positron camera [5]. However, the following decades saw clinical application of these isotopes side-tracked in favour of targeted imaging using γ-emitting radiometals such as indium and technetium, performed using a planar γ-camera or, more recently, a SPECT scanner. While the sub-optimal imaging properties of ^{67}Ga account for the progressive abandonment of its clinical use, the delay in gallium-68 tracer development is attributable to the lack of a generator eluting ^{68}Ga in a convenient form (instead of as an EDTA complex [6]), and to the slow proliferation of positron cameras.

In the past three decades, the field of PET imaging has seen burgeoning development, mainly due to the success of [^{18}F]-fluorodeoxyglucose ([^{18}F]-FDG) scans, which has prompted the diffusion in hospitals of PET scanners and cyclotrons dedicated to the production of medical radioisotopes. While SPECT still represents the work-horse of nuclear medicine, due to higher availability and lower cost, PET presents several advantages compared to SPECT including higher sensitivity, better quantification and possibility of dynamic image reconstruction [7,8]. Furthermore, although PET resolution is intrinsically limited by the travelling distance of the positron before annihilation, current human PET systems provide higher resolution than SPECT [8,9].

In these new contexts, the advantageous emission properties of gallium-68, including an almost quantitative positron yield of 89 % and a half-life of 68 min, made it an ideal PET isotope for imaging with small biomolecules and prompted the development of novel generators systems as well as of ^{68}Ga-based tracers. Compared to fluorine-18, gallium-68 has the disadvantage of a higher positron energy (E_{max} = 1.9 MeV [10]), which results in a longer positron range (R_{mean} = 3.5 mm vs R_{mean} = 0.6 mm for [18]F [10]) and, consequently, in lower spatial resolution for ^{68}Ga images. On the other hand, gallium-68 presents distinct advantages over traditional PET isotopes such as ^{18}F and [11]C. For example, as a radiometal, gallium-68 can be used to radiolabel biological molecules exploiting suitable bifunctional chelators, such as those described in the previous chapter, without the need for complex radiosynthetic procedures. More importantly, the recent availability of gallium-68 *via* a pharmaceutical grade generator could play for PET the same role that the [99]Mo/^{99m}Tc generator has played for SPECT, thus enormously increasing the utility of PET beyond the centres possessing cyclotrons [11]. A description of [68]Ge/^{68}Ga generator development and of the techniques for pre-concentration and purification of the generator eluate, is beyond the scope of this chapter, readers are referred to other comprehensive reviews and books [12,13].

2.2 Targeted imaging of receptors with ^{68}Ga-labelled peptides

These attractive features, unique among the pool of PET radioisotopes, have contributed to the increasing clinical interest for gallium-68. The principal application of ^{68}Ga has been imaging the expression of receptors upregulated in cancer cells or in other pathological conditions, by radiolabelling molecules able to bind to these antigens with high selectivity. This is accomplished by means of a bifunctional chelator, which can be attached to the targeting molecule to allow its ^{68}Ga labelling. So far, targeted imaging with gallium-68 has mainly focused on ^{68}Ga-radiolabelled peptides, whose pharmacokinetic properties match the short half-life of the isotope [14]. In addition, the use of a short-lived isotope for imaging with radiolabelled peptides is advantageous owing to the improved dosimetry and to the possibility of performing repeat imaging of a patient on the same day. Finally, the possibility of using the same peptide-chelator conjugate for both gallium-68 imaging and targeted radiotherapy with lutetium-177 and yttrium-90 (especially when DOTA-based chelators are used) makes these systems a close to ideal theranostic pair for peptide receptor radionuclide therapy (PRRT). A review of the receptors investigated for imaging with[68]Ga and of the tracers developed to selectively target them is provided in the

paragraphs below, mainly focussing on their clinical translation. A brief description of interesting radiotracers in preclinical development is also presented.

2.2.1 Somatostatin Receptors

Imaging of somatostatin receptors with ^{68}Ga-based somatostatin analogues has led to the clinical success of ^{68}Ga PET and provided an enormous drive for the development of other gallium-68 radiotracers. Somatostatin receptors (SSTRs) are a family of G-protein-coupled membrane glycoproteins, which regulate exocrine and endocrine secretion. SSTRs are highly expressed in 70-90 % of neuroendocrine tumours (NETs), such as pituitary adenoma, pancreatic islet cell tumour, carcinoid, pheochromocytoma, paraganglioma, medullary thyroid cancer and small cell lung carcinoma and in other types of cancer such as renal cell carcinoma, small cell lung, breast and prostate cancer and malignant lymphoma [15,16]. Five different receptor types exist (SSTR1-SSTR5), with SSTR2 being the most widely expressed in malignancies. The traditional gold standard for radionuclide imaging of these receptor was [^{111}In]In-DTPA-octreotide (Octreoscan, **Figure 2.1**) which consisted of a SSTR agonist molecule (with sequence H_2N-D-Phe-Cys-Phe-D-Trp-Lys-Thr-Cys-Thr-ol) attached to a DTPA chelator at the amino terminus and radiolabelled with indium-111. Despite the success of Octreoscan and its widespread use in clinics, this radiotracer also showed some limitations, especially concerning the detection of small lesions, which proved to be difficult owing to the limited spatial resolution achievable with SPECT. On the other hand, since [^{18}F]FDG is not recommended for imaging of NETs, due to their low metabolic rate, which hinders [^{18}F]FDG uptake, another PET tracer able to specifically target SSTR receptor had been actively sought [16]. Three different DOTA derivatives of octreotide have been extensively evaluated in clinics for labelling with [68]Ga: namely [^{68}Ga]Ga-DOTA-TATE, [^{68}Ga]Ga-DOTA-NOC, [^{68}Ga]Ga-DOTA-TOC, which are all conjugated to DOTA at the N-terminus and differ only in the amino acid sequence (**Figure 2.1**); compared to octreotide, TOC and TATE have a tyrosine in position 3 and TATE also has the alcohol function at the C-terminus replaced by a carboxylic function; finally NOC displays a naphthalenyl-L-alanine in position 3 and maintains the alcohol group at the C-terminus. Despite a higher affinity of [^{68}Ga]Ga-DOTA-TATE for SSTR2 compared to [^{68}Ga]Ga-DOTA-TOC, their tumour uptake and *in vivo* biodistribution were found to be very similar [17]. On the contrary, [^{68}Ga]Ga-DOTA-NOC, which possesses even greater affinity for SSTR2 as well as SSTR3 and SSTR5 *in vitro* [18], displays an increased liver uptake, due to the presence of the lipophilic naphthalenyl group.
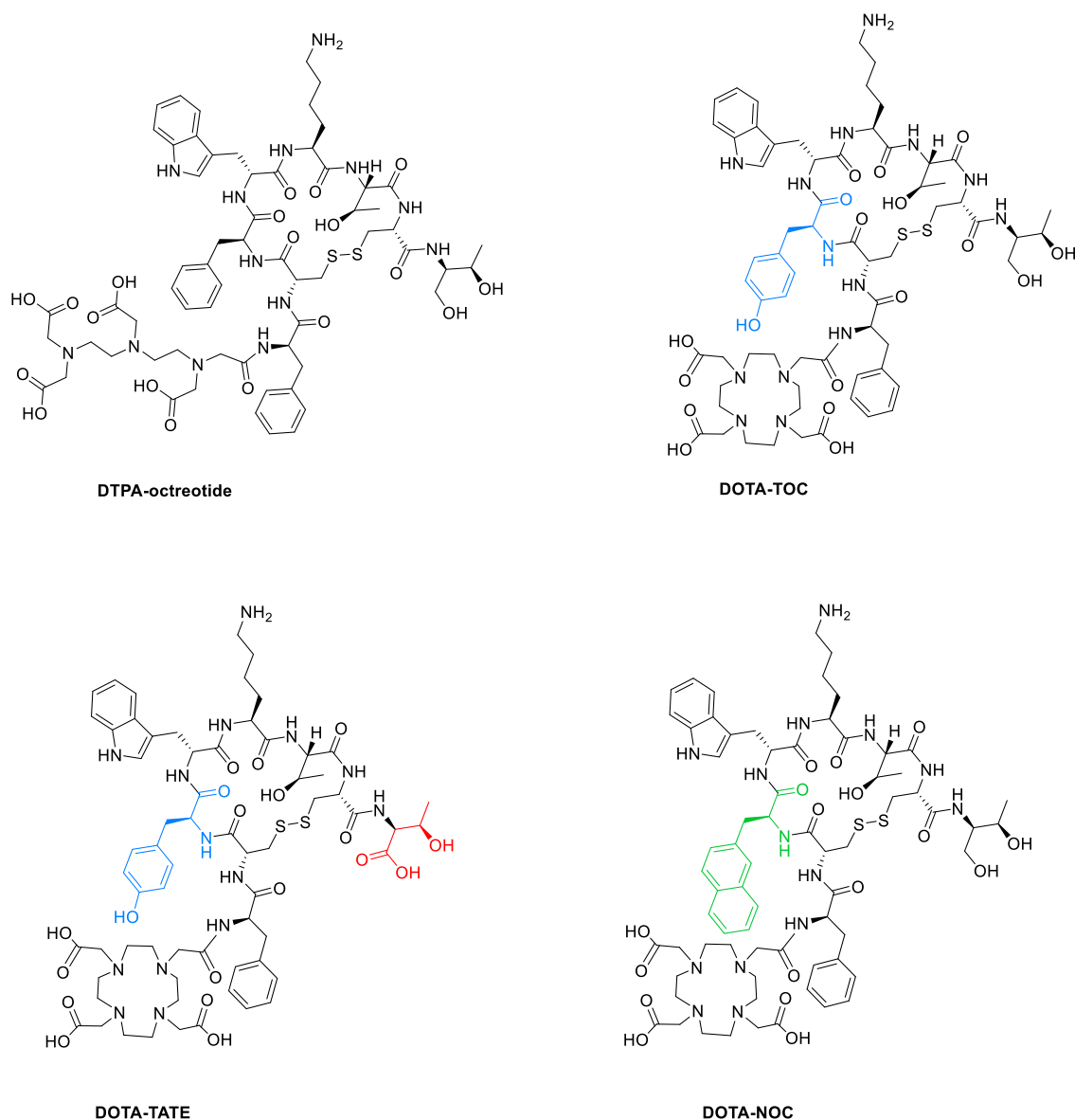
Figure 2.1. *Chemical structures of the more common somatostatin analogues ligands. For DOTA-TOC, DOTA-TATE and DOTA-NOC differences in the amino acid sequence compared to the prototype compound DTPA-octreotide are highlighted [14].*

While the three tracers have shared the interest of the nuclear medicine community so far, the FDA approval in June 2016 of [68Ga]Ga-DOTA-TATE (NETSPOT®) and the following approval of [68Ga]Ga-DOTA-TOC (SOMAKIT TOC®) by the EMA is likely to increase the prevalence of clinical studies using these radiotracers [19,20]. The analogous tracer [68Ga]Ga-DOTA-lanreotide ([68Ga]Ga-DOTA-2-Nal, Tyr[3], ThrNH2[8]-octreotide) has also been investigated in clinics, but was found inferior to [68Ga]Ga-DOTA-TOC in detecting NET lesions [21].

Overall, 68Ga tracers based on SSTR agonist proved to be extremely successful in the diagnosis of NETs and able to influence patient stratification and treatment [14].

Furthermore, they can be used in combination with PRRT exploiting DOTA's ability to coordinate some M^{3+} therapeutic isotopes such as lutetium-177 or yttrium-90 [22].

During the last two decades, a different class of SSTR imaging agents has been developed, mainly by Maecke and coworkers, based on antagonists of these receptors. Unexpectedly, in preliminary preclinical studies these compounds proved to be superior to SSTR agonists with comparable binding affinity [23], thus challenging the belief that internalisation of the radiotracer, which only occurs for agonist compounds, is important to obtain high tumour uptake [24]. Clinical evaluation of one of these compounds ([^{68}Ga]Ga-NODAGA-JR11 (**Figure 2.2**), also known as [^{68}Ga]Ga-OPS202) and its ^{177}Lu counterpart is still ongoing, but has already produced promising results [25,26].
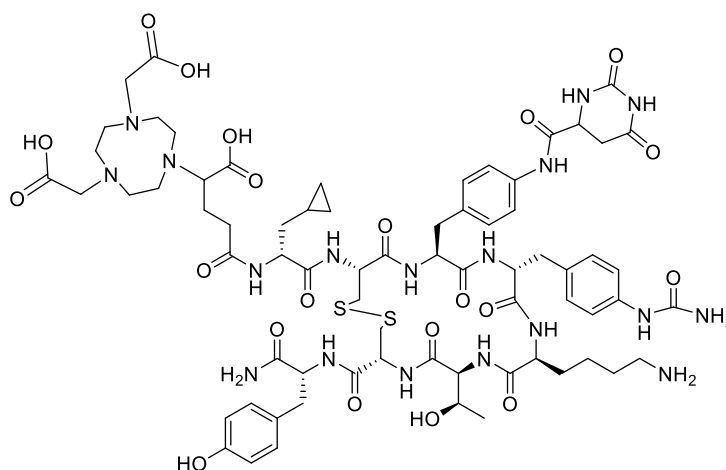
Figure 2.2. *Structure of the NODAGA-JR11 antagonist [23,24].*

2.2.2 Prostate Specific Membrane Antigen

More recently, the prostate specific membrane antigen (PSMA) has gained enormous attention within the nuclear medicine community as an imaging target. This receptor is overexpressed in the majority of prostate cancer (95 % of primary tumours, 80 % of metastasis [17]) as well as in some bladder cancers, schwannoma and in the neovasculature of many solid tumours [27]. PSMA is also expressed in kidneys, liver, salivary glands, lachrymal glands, colon, duodenal brush border, and the nervous system, where it is known as carboxypeptidase II because of its ability to cleave C-terminal glutamate residues from its substrates [27]. The recent development of several ^{68}Ga radiotracers based on the low molecular weight unit Glutamate-Urea-Lysine (Glu-NH-CO-NH-Lys), which is a known inhibitor of PSMA, yielded impressive results in clinical trials providing target specific imaging with favourable

biodistribution [28]. A brief description of the different ^{68}Ga radiotracers based on the Glu-NH-CO-NH-Lys pharmacophore is provided in the following paragraphs.

The first ^{68}Ga-based PSMA imaging agents were DOTA derivatives, with the chelators connected to the pharmacophore units *via* different linkers; their ability to detect PSMA expressing tumours *in vivo,* and their target specificity, was demonstrated in preclinical models [29]. More recently an HBED-CC derivative, connected to the peptidic unit *via* an aminohexanoic (Ahx) acid: Glu-NH-CO-NH-Lys-Ahx-[[^{68}Ga]Ga(HBED-CC)] (also known as [^{68}Ga]Ga-PSMA11 and [^{68}Ga]Ga-HBED-CC-Ahx-KuE, ligand shown in **Figure 2.3**) was found superior to its DOTA-based counterpart both in terms of its *in vitro* properties (reduced non-specific binding and increased internalisation) and in its ability to specifically delineate PSMA-expressing tumours in animal models [30]. These advantageous features have been ascribed to the increased lipophilic nature of the tracer, which would result in stronger interaction with a lipophilic pocket present in the active binding site of the receptor [30]. Furthermore, the facility of HBED radiolabelling compared to DOTA represents an additional advantage for this compound. Clinical evaluation of this radiotracer demonstrated its ability to visualise prostate cancer lesions with high detection rate [31] and superiority to traditional radioactive choline imaging of prostate cancer [32]. Optimisation of this ligand led to the development of a dimerised version with increased affinity for PSMA and prolonged tumour retention in preclinical models, which warrants further investigation [33]. As for the SSTR tracers, theranostic agents have been developed for PSMA, based on a DOTA scaffold, which is more suitable for radiolabelling with [177]Lu. PSMA-617 (**Figure 2.3**) is a DOTA-based peptidomimetic compound with optimised targeting properties [34], which has been used for theranostic application with ^{68}Ga and [177]Lu [35]. A modified version of one of the original DOTA tracers, PSMA I&T (**Figure 2.3**), was produced by switching to DOTAGA and performing a light modification of the hydrophobic substituents, to present higher *in vivo* stability and affinity for the target receptor and was investigated in first-in-man trials with promising results [36,37]. A different type of ^{68}Ga-PSMA tracer has been developed by our group, exploiting a THP[Me] chelator connected to the PSMA moiety *via* a glutaric acid linker ([^{68}Ga]Ga-THP[Me]-PSMA) [38]. Despite lower affinity for the target receptor, preclinical evaluation of this radiotracer produced results comparable to its HBED-CC counterpart. Furthermore, radiolabelling of this ligand is based on a single-step kit without need for further purification of the radiotracer, thus providing a great advantage over HBED and DOTA-based tracers. Phase I clinical evaluation of this imaging agent produced encouraging results [39] and the compound is now undergoing a phase II multicentre clinical trial in the UK.
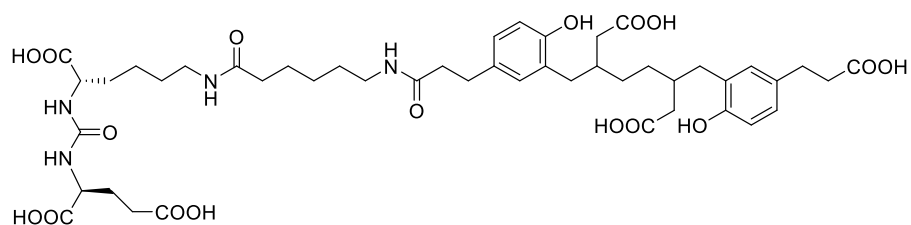
HBED-CC-Ahx-KuE
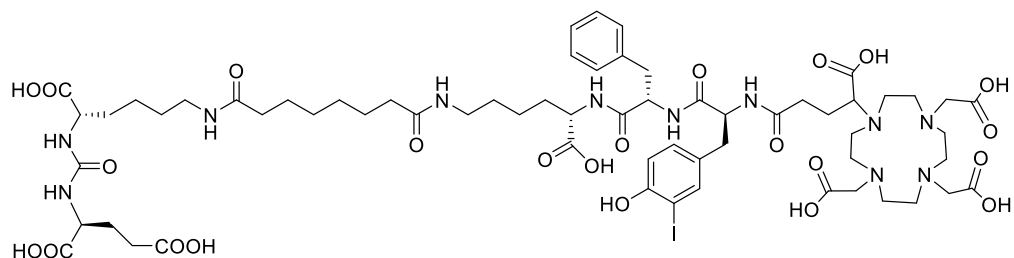
DOTAGA-(I-y)FK(Sub-KuE) (PSMA I &T)
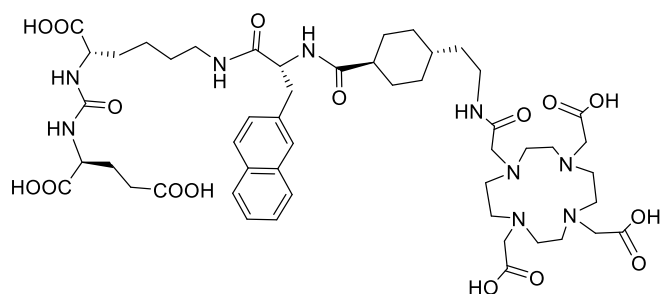
PSMA-617
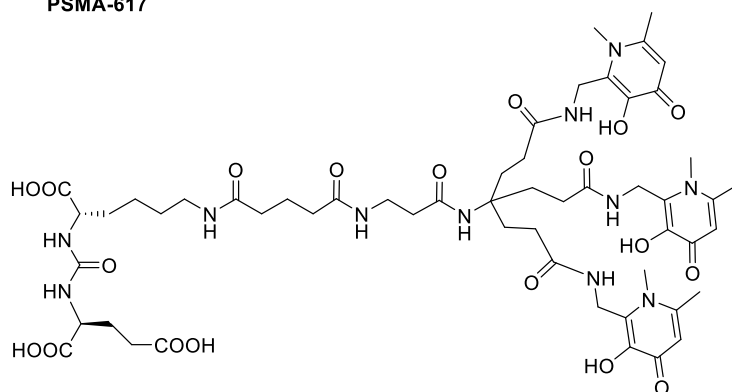
THP-PSMA

Figure 2.3. Chemical structure of different PSMA-chelator conjugates in clinical evaluation [30,34,36,38]. The chemical diversity of these agent, beyond the common PSMA targeting moiety, does not affect significantly their capability to delineate lesions in vivo.

2.2.3 α$_V$β$_3$ integrins

Owing to their major role in tumour angiogenesis and metastasis, integrins have been extensively investigated as a target for radionuclide imaging of cancer and other pathologies [40,41]. In particular, peptides based on the Arg-Gly-Asp (RGD) sequence have been used as the targeting moiety to visualise the α$_V$β$_3$ integrin, overexpressed on activated endothelial cells such as those involved in angiogenesis [40]. The first ^{68}Ga-labelled RGD peptide to enter clinical trials was [^{68}Ga]Ga-NOTA-RGD (**Figure 2.4**), consisting of a cyclic RGD peptide c(RGDyK) conjugated to the chelator *p*-SCN-Bn-NOTA *via* a thiourea linkage with the lysine side-chain [42]. Comparison of this tracer with [^{18}F]FDG was performed in patients with hepatic metastasis of colorectal cancer about to start an antiangiogenic therapy. Notably, although this tracer was able to delineate fewer metastatic lesions than [^{18}F]FDG, those patients with positive [^{68}Ga]Ga-NOTA-RGD uptake were found to respond to the subsequent antiangiogenic chemotherapy, thus highlighting the potential role of α$_V$β$_3$ imaging as a patient stratification tool [41]. On the other hand, since the α$_V$β$_3$ receptor is overexpressed also in several types of tumours it is always important to use histopathology techniques to verify whether the radiolabelled peptides are actually imaging angiogenesis or a simple upregulation of the receptor on tumour cell surfaces [43]. A similar radiotracer, where *p*-SCN-Bn-NOTA had been replaced by NODAGA in order to improve pharmacokinetic properties, was evaluated in patients with hepatocellular carcinoma showing outstanding *in vivo* stability, but insufficient uptake in metastatic lesion in order to image them [44].

Multimeric RGD peptides can enhance affinity for the integrin receptor through the covalency effect, thus resulting in increased tumour uptake and retention [45]. Among the several multimeric RGD peptides investigated preclinically, many see the incorporation of a PEG linker in their structure to improve their pharmacokinetic properties [46]. [^{68}Ga]Ga-NOTA-PRGD2 (also known as [^{68}Ga]Ga-NOTA-PEG4-E[c(RGDfK)]$_2$) ligand, shown in **Figure 2.4**, was compared to [^{18}F]FDG in patients suffering from lung cancer [47] and glioblastoma multiforme [48]; it showed higher specificity than [^{18}F]FDG in both cases. In the glioblastoma study, ^{68}Ga-NOTA-PRGD2 was able to differentiate between low and high-grade glioma with improved accuracy compared to [^{18}F]FDG and displayed higher sensitivity due to lack of integrin receptor in normal brain tissues. The same radiotracer has been evaluated with encouraging results in non-oncologic diseases involving angiogenic mechanisms, such as stroke, myocardial infarction and rheumatoid arthritis [49,50].

A different α$_V$β$_3$-targeting tracer is based on a peptidomimetic antagonist, which was found to possess increased binding affinity for the integrin receptor [51]. A NODAGA

derivative of this tracer (NODAGA-THERANOST, **Figure 2.4**) was radiolabelled with ^{68}Ga and first in human evaluation of this radiotracer showed increased sensitivity and specificity of this tracer compared to [^{18}F]FDG [52]. In particular, [^{68}Ga]Ga-NODAGA-THERANOST, but not [^{18}F]FDG, was able to identify areas of neovasculature in both primary tumours and metastases and a strong positive correlation was found between [^{68}Ga]Ga-NODAGA-THERANOST uptake and cancer proliferation [52].
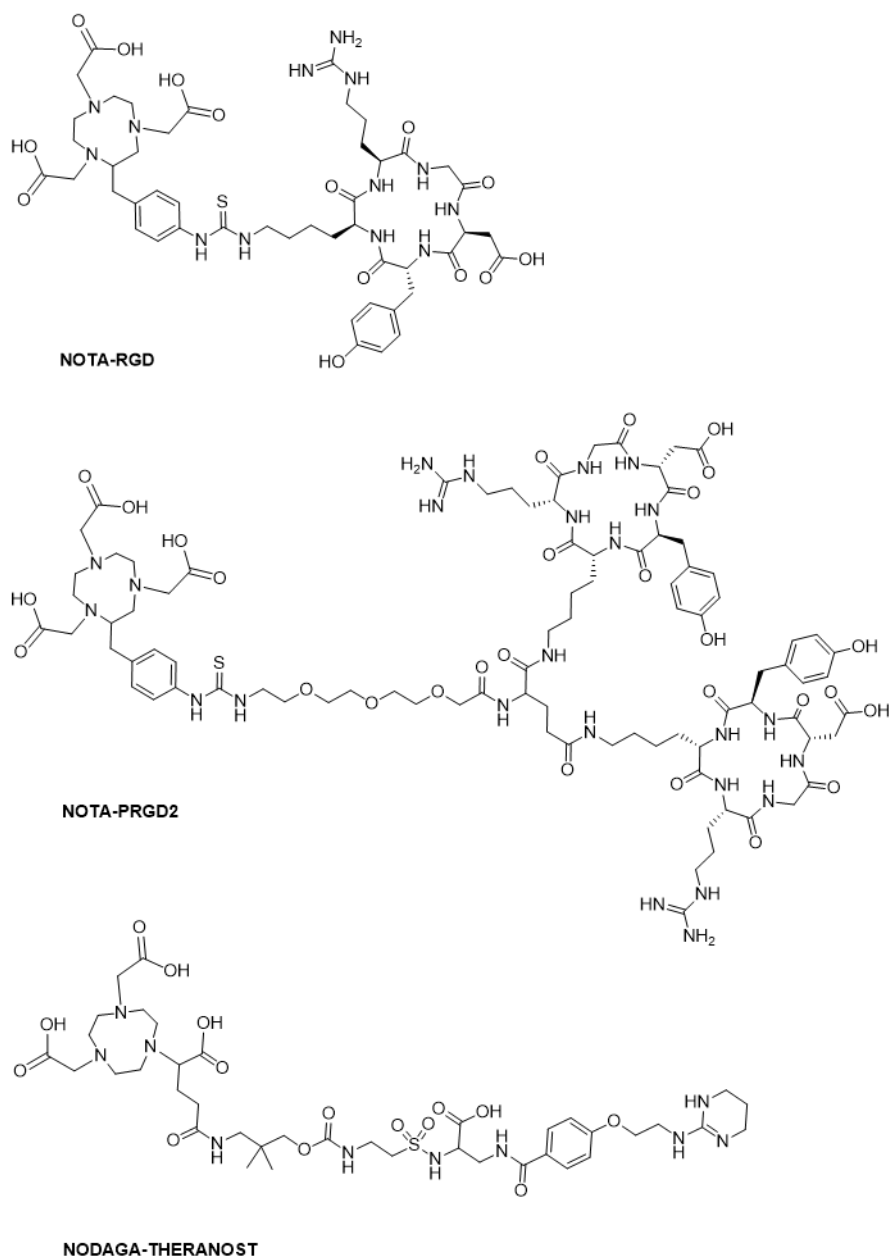
Figure 2.4. *Structures of α$_V$β$_3$-targeting ligands evaluated in clinical trials, including the monomeric and dimeric RGD-derivatives and the peptidomimetic antagonist NODAGA-THERANOST [42,47,51].*

2.2.4 Gastrin-releasing peptide receptors

Bombesin analogues, both agonists and antagonists, have also been proposed for the imaging of prostate cancer and other malignancies that express their target receptor: gastrin-releasing peptide receptor (GRPR), including breast, gastro-intestinal and small-cell lung cancers. In a first study, a GRPR agonist DOTA-PEG$_2$-[D-Tyr^6, β-Ala^{11},Thi^{13},Nle^{14}] Bombesin (BZH3) was radiolabelled with gallium-68 and, after encouraging preclinical results [53], evaluated in comparison with [^{18}F]FDG in patients with gastrointestinal stromal tumours. Despite the high affinity for the target receptor, [^{68}Ga]Ga-BZH3 was found inferior to [^{18}F]FDG in visualising tumour lesions in the same patient cohort [54]. Similar to somatostatin receptors antagonists, GRPR antagonists showed higher tumour accumulation and longer washout time compared to agonist compounds. The synthetic antagonist [^{68}Ga]Ga-BAY86-7548 (**Figure 2.5**, also known as [^{68}Ga]Ga-RM2)) was evaluated in prostate cancer patients and showed 83 % accuracy in the detection of organ-confined primary tumours [55]. A recent comparison between this tracer and [^{68}Ga]Ga-PSMA-11 in patients with biochemically recurrent prostate cancer showed similar ability to detect prostate cancer lesions for both radiotracers. However, the two radiotracers presented a different uptake in non-target organs (higher in the pancreas and blood for [^{68}Ga]Ga-RM2, and in small intestine, kidneys, lacrimal, parotid and submandibular glands, for [^{68}Ga]Ga-PSMA-11). This different biodistribution suggests that choice between the two radiotracers should depend on the type/position of the tumour in each individual patient.
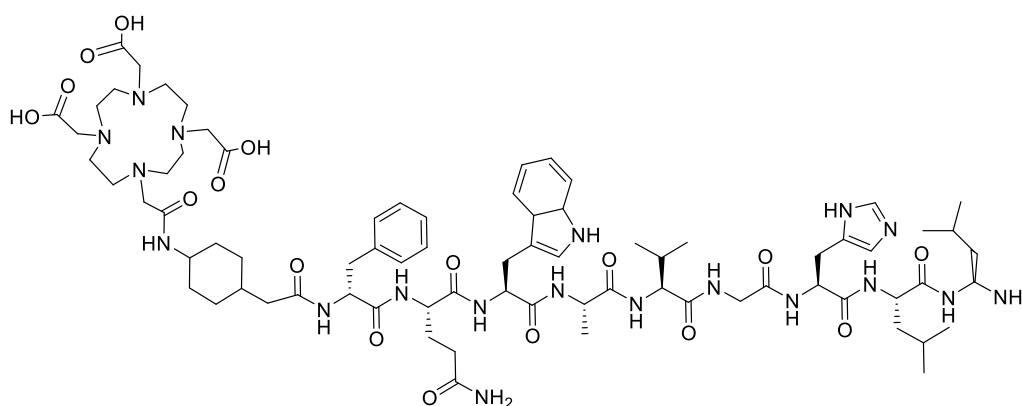
Figure 2.5. *Chemical structure of the GRPR antagonist [^{68}Ga]Ga-RM2 [55].*

In a different study a similar GRPR antagonist [^{68}Ga]GaSB3, an analogue of a ^{99m}Tc based antagonist which had showed promising imaging properties, was evaluated in patients with metastasised breast and prostate cancer and was able to visualise about 50 % of the lesions [56]. Although those values are inferior to those previously reported

for [^{68}Ga]Ga-RM2 [55], GRPR expression is known to decline in metastatic tissues and therefore a lower number of positive scans was expected [56].

2.2.5 Chemokine receptor CXCR4

The chemokine receptor CXCR4 plays a key role in the proliferation migration and survival of cancer cells. Overexpression of CXCR4 is common in numerous malignancies including breast, pancreatic, ovarian, lung, prostate, colorectal and skin cancers, leukaemia, and lymphoma [17] and generally correlates with poor prognosis and increased probability of recurrence [57]. Development of CXCR4-targeting imaging agents focussed on three classes of antagonists: cyclam-based tracers, tetradecapeptides and cyclopentapeptides. This last class of compounds was developed to improve pharmacokinetic and *in vivo* stability compared to the heavier counterparts tetradecapeptides [58]. Cyclam-based tracers were evaluated in mice for imaging with copper-64, but revealed extremely high uptake in liver and lymphoid organs, which prevented clinical evaluation of these tracers [59]. On the contrary, peptide-based imaging of CXCR4 produced the first two clinical studies in 2015 employing the pentacyclopeptide [^{68}Ga]Ga-pentixafor (**Figure 2.6**, also known as CPCR4-2) [60] and the tetradecapeptide [^{68}Ga]Ga-NOTA-NFB [61], respectively. [^{68}Ga]Ga-pentixafor has been by far the most widely investigated PET radiotracer for CXCR4 and has shown a favourable dosimetry [62], good specificity and uptake for CXCR4-expressing lesions, with results comparable or superior to [^{18}F]FDG for several haematological malignancies [60,63-65]. On the contrary, significantly lower ^{68}Ga-pentixafor uptake compared to [^{18}F]FDG was recently reported for solid tumours [66]. Unexpectedly, ^{68}Ga-pentixafor uptake in glioblastoma, small cell lung cancer and some neuroendocrine tumours [67] did not correlate with histological receptor expression probably due to receptor kinetics and internalisation mechanisms [68,69]. Based on the promising results in the diagnosis of haematological malignancies, radiotherapy with the ^{68}Ga-pentixafor analogue ^{177}Lu- and ^{90}Y-pentixather is now being investigated in clinics for advanced-stage multiple myeloma with encouraging preliminary results [70].
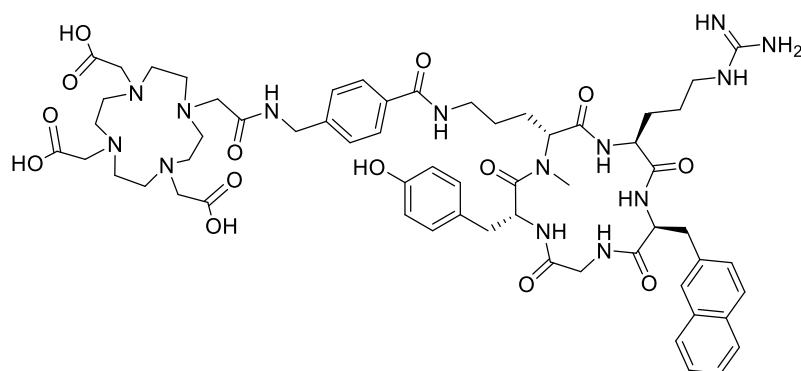
Figure 2.6. Chemical structure of the pentixafor ligand [60].

Interestingly, replacing the DOTA chelator in ^{68}Ga-pentixafor with NOTA was shown to markedly reduce tumour uptake in preclinical models, which was ascribed by the authors to decreased internalisation of this tracer [71]. This observation is at odds with the excellent tumour uptake observed for non-internalising SSTR radiotracers, and if confirmed it would be another indication on how imaging of different receptors may benefit from radiotracers with different properties.

The tetradecapeptide ^{68}Ga-NOTA-NFB is a derivative of the ^{18}F radiotracer 4-[^{18}F]F-T140, where the N-terminal 4-fluoro-benzoyl group (NFB) was substituted with the chelating agent NOTA [72]. In a preliminary clinical study a favourable dosimetry was measured for ^{68}Ga-NOTA-NFB in healthy volunteers and improved contrast compared to [^{18}F]FDG scan was demonstrated in glioma patients [61].

2.2.6 Glucagon-like peptide-1 receptor

Glucagon-like peptide-1 receptor (GLP-1R) represents an important target for quantifying the beta cells mass in diabetic patients and to image insulinomas, a NET tumour where SSTR expression is relatively low, but GLP-1R is upregulated [73]. Imaging of this receptor is based on the substrate analogue exendin, whose half-life *in vivo* exceeds that of the native ligand GLP-1 [17]. While ^{111}In-based tracers were initially evaluated, in the last few years the focus shifted towards ^{68}Ga-labelled tracers [74]. In 2014, a first case report described the use of ^{68}Ga-DO3A-VS-Cys40-Exendin-4 for the detection of a metastatic insulinoma in a hypoglycaemic patient [75]. Interestingly, this study used the unusual chelator DO3A-VS, in which one of the acetic arms of DOTA has been replaced by a vinylsulfonic group to provide attachment of the peptide through a cysteine residue. More recently, other exendin derivatives have been clinically investigated with encouraging results. [Nle[14],Lys[40](Ahx-DOTA-[^{68}Ga]Ga)NH$_2$]exendin-4 was evaluated in a small patient cohort for the detection of suspected benign insulinoma achieving higher tumour-to-background ratio compared

to its indium analogue [76]. A larger cohort study employing [^{68}Ga]Ga-NOTA-MAL-Cys^{40}-exendin-4 demonstrated a 97.7 % sensitivity in localising insulinoma, outperforming all conventional disease modality for this condition [77].

2.2.7   Other receptors

The urokinase-type plasminogen activator receptor (uPAR) and its peptide antagonist AE105 (Asp-Cha-Phe-D-Ser-D-Arg-Tyr-Leu-Trp-Ser-CONH$_2$) are among the most recent receptor/peptide couples investigated clinically for gallium-68 based imaging. uPAR is frequently overexpressed in several malignancies such as breast, prostate, colorectal and urinary bladder cancer and higher expression has been correlated to poorer prognosis [78]. Phase I clinical trials of ^{68}Ga-NOTA-AE105 proved the feasibility of cancer imaging with this tracer, which provided satisfactory image contrast and delineation of primary tumours and metastasis, with the most promising results obtained for breast cancer patients [79].

Imaging of the melanocortin system, whose receptor MC1R is overexpressed in melanomas, has also been attempted using ^{68}Ga-labelled DOTA analogues of the α-melanocyte stimulating hormone. Although results of preclinical examination in mouse melanoma models were encouraging [80], subsequent clinical evaluation had disappointing results, presumably due to lower expression of this receptor in human melanoma [81].

2.3 Targeted ^{68}Ga imaging beyond radiolabelled peptides

Alongside peptide-based ^{68}Ga imaging, in the last few years the radiochemistry community has started to explore new vectors for imaging with gallium-68.

2.3.1   Mannosylated albumin for sentinel lymph node imaging

Identification of the sentinel lymph node (SLN) and subsequent biopsy is crucial for decision making in the treatment of several cancers. The SLN can be identified by injection of radiolabelled mannosylated albumin (MSA) in the tumour area, owing to the expression of mannose-binding proteins in the reticuloendothelial system. Choi and coworkers developed a ^{68}Ga-labelled-(MSA) by conjugation of albumin with mannose and a NOTA chelator and subsequent radiolabelling [82]. After successful preclinical investigation, a recent clinical trial in lung cancer patients demonstrated the success of this technique with a detection rate of 100 % and 0 false negatives [83].

2.3.2 Bisphosphonates for the detection of skeletal metastasis

Bone metastases are a common complication of several cancers and therefore an important target for radionuclide imaging. Detection of skeletal metastasis in clinics was traditionally performed with [99mTc]-labelled bisphosphonates. In fact, geminal bis(phosphonate) groups can act as analogues of natural pyrophosphate (**Figure 2.7**) and efficiently deposit on skeletal hydroxyapatite [84]. More recently [18F]NaF has been progressively replacing [99mTc]-bisphosphonate in clinics, due to the higher sensitivity and resolution of PET compared to SPECT.

Pyrophosphate
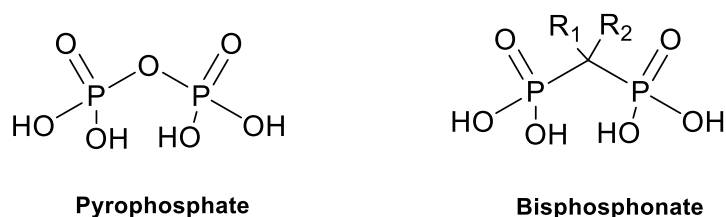
Bisphosphonate

Figure 2.7. *Chemical structure of pyrophosphate compared to that of a geminal bisphosphonate in their fully protonated form.*

[68Ga]-labelled bisphosphonates are therefore of great interest, because they can combine the superior imaging properties of PET contrast agents with the bone-seeking properties of bisphosphonate. Two different [68Ga]-labelled bisphosphonate derivatives (**Figure 2.8**) have been recently developed by Rösch and coworkers and tested clinically with promising results. [68Ga]Ga-BPAMD is a DOTA-based gallium bisphosphonate, which proved to be comparable to [18F]NaF in the detection of bone metastasis in a prostate cancer patient [85]. A more recently developed NOTA-bisphosphonate agent [68Ga]Ga-NO2A^{BP} [86] was also compared to [18F]NaF, and in some cases with a [99mTc]-bisphosphonate in a cohort of breast carcinoma patients showing results comparable to [18F]NaF and superior to [99mTc]-bisphosphonate, while resulting in a lower effective dose compared to the other tracers [87].

BPAMD

NO2AP^{BP}
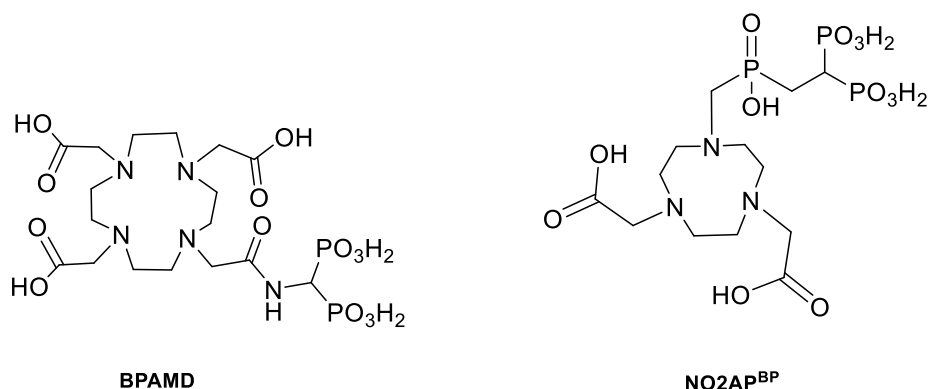
Figure 2.8. *Chemical structure of bisphosphonate ligands for ^{68}Ga imaging of skeletal metastasis.*

2.3.3 Antibody fragments and affibody molecules for HER2 imaging

Antibodies possess a striking targeting ability for their antigen, but their slow pharmacokinetics is not compatible with the short half-life of gallium-68. Different strategies have been investigated to overcome this limitation. Recent developments in antibody engineering have led to biomolecules that retain the antibody affinity for their target receptor while displaying faster pharmacokinetics, thus opening new possibility for ^{68}Ga-immunoPET.

Antibody binding fragments F(ab) and F(ab')$_2$ are obtained by enzymatic digestion of full antibodies and, given their lower molecular weight, they present faster clearance while retaining the binding affinity of their full antibody counterpart. Clinical evaluation of ^{68}Ga-DOTA-F(ab')$_2$-trastuzumab in breast cancer patients with and without HER2 expression was undertaken, demonstrating the safety and favourable pharmacokinetics of this imaging agent [88]. On the other hand, tumour targeting was suboptimal with malignant lesions identified in only 50 % of the HER2 positive group.

Nanobodies are antibody fragments consisting of a single variable domain, which retains full antigen-binding capability. Recently, a ^{68}Ga-NOTA-anti-HER2 nanobody was the first radiolabelled nanobody to be evaluated in clinical trials in breast cancer patients [89]. The tracer was found to be safe and able to visualise primary tumours and metastatic lesions. Contrary to the F(ab')$_2$ tracer, this nanobody targeted a different epitope of HER2 thus excluding any chance of competing with trastuzumab for binding to the target receptor in trastuzumab-treated patients.

Affibody molecules are obtained by a combinatorial engineering approach on a protein scaffold and then selected based on their affinity for the desired target *via* phage display. They combine the high affinity for their target receptor typical of antibodies with the pharmacokinetics of small molecules thus providing a useful platform for imaging with gallium-68. The HER2 targeting affibody molecules ABY-002 and ABY-025 were conjugated to DOTA either at the N-terminus (ABY-002 [90]) or at a cysteine site through a maleimide (ABY-025 [91]) and radiolabelled with indium-111 obtaining encouraging clinical/preclinical results. The same molecules were radiolabelled with gallium-68 and tested in breast cancer patients with encouraging results [92-94]. [^{68}Ga]Ga-ABY-002 and its indium counterpart were comparable in [^{18}F]FDG in detecting soft-tissue metastases although less sensitive for bone metastasis (suggesting lower HER2 expression in these tissues) [94]. High kidney and liver uptake was observed for both radiotracers. As part of the [^{68}Ga]Ga-ABY-025 clinical trial dosimetry was investigated for both the [68]Ga- and ^{111}In-radiolabelled affibodies, revealing more

favourable dosimetry and sensitivity for the ^{68}Ga-based tracer. Intriguingly, lower uptake in non-target organs (such as liver and kidney) and improved dosimetry for [^{68}Ga]Ga-ABY-025 were obtained when the affibody was labelled at lower specific activity, possibly due to a partial blocking of HER2 receptor in non-target organs by unlabelled affibody. However, since tumour uptake for the two groups was not investigated in the study, it is impossible to predict if this lower non-target organs uptake will result in an improved tumour-to-background contrast [92].

2.4 Different approaches for imaging with ^{68}Ga

2.4.1 Pretargeting strategies for antibody-based imaging

Another way to circumvent the short half-life limitation of gallium-68 in antibody-based imaging is pretargeting. Following this approach, the unlabelled antibody (or antibody fragment) is injected first and allowed to reach its receptor target; a radiolabelled probe is then administered, capable of binding the antibody *in vivo*, at its receptor site. Owing to its smaller size (compared to the antibody), the radiolabelled probe quickly clears from the blood pool, reaches its target antibody and radiolabels it *in vivo,* allowing imaging shortly after the injection of radioactivity. Furthermore, the faster blood clearance of the radiolabelled probe reduces the exposure of non-target organs to radiation and improves dosimetry.

Several pretargeting methods have been attempted so far for ^{68}Ga-immunoPET, all characterised by the presence of a high-affinity chemical pair, able to couple *in vivo* (*i.e.* in very mild conditions and low concentration) and they will be described in further details in **Chapter 5**. The bispecific monoclonal antibody (bsmAb)-hapten couple has been the more widely used high-affinity pair for ^{68}Ga-based pretargeting so far, and resulted in a few clinical trials. In 2001, a pioneering work by Schuhmacher and coworkers described the pretargeted imaging of breast cancer patients using bispecific Anti-Tag12/Anti-Ga-chelate antibodies [95]. A bispecific antibody was assembled, able to target both the mucin-like Tag12 receptor overexpressed in most adenocarcinoma and the ^{68}Ga-HBED-CC moiety. Eighteen hours after the administration of the bsmAb, blockage of the anti-Ga-HBED-CC sites in the circulating bsmAb was performed with ^{nat}Ga-HBED-CC-apotransferrin followed by administration of ^{68}Ga-HBED-CC and subsequent PET imaging. The results of the study highlight the limitation of the chosen model: relatively low bsmAb affinity for the target receptor resulted in low tumour uptake, while shedding of the receptors and slow clearance of the ^{68}Ga-HBED-CC lead to a disappointing tumour-to-blood ratio. On the other hand,

the trial confirmed the feasibility of this approach and its potential once a proper model is established.

The trivalent bsmAb TF2, composed of a humanised anti–histamine-succinyl-glycine Fab fragment and two humanised anti-CEA Fab fragments is a promising candidate for pretargeting strategies aimed at imaging the carcinoembryonic antigen, a slowly internalising receptor expressed in a variety of malignancies. Its hapten molecule IMP288 is a DOTA-conjugated D-Tyr-D-Lys-D-Glu-D-Lys peptide, where the ε-amino groups of both lysine residues are substituted with a histamine-succinyl-glycine moiety [96]. The high-affinity pair TF2/^{68}Ga IMP288 has been recently employed in clinical trials for imaging medullary thyroid carcinoma (clinical trial identifier: NCT01730638), HER2 negative breast carcinoma (NCT01730612), and metastatic colorectal cancer (NCT02587247). The first results of the study on medullary thyroid carcinoma patients were published recently [97] highlighting the feasibility of this approach with good image contrast and a radiation exposure comparable to an [^{18}F]FDG scan. Decreasing the TF2-to-IMP288 molar ratio and delaying between antibody and hapten administration resulted in increased ^{68}Ga-IMP288 blood clearance, but also decreased tumour uptake, with the best contrast achieved using a 20-fold excess of TF2 over IMP288 and a delay of 30 hours between the two injections.

2.4.2 Imaging exploiting gallium localisation properties

Historically radionuclide imaging with gallium isotopes has been focusing on exploiting gallium(III) ability to localise in malignancies, inflammation and infection sites (see **Chapter 1**). This imaging approach, which focused on the SPECT isotope gallium-67, has now been largely replaced by [^{18}F]FDG scans, which provide better sensitivity and spatial resolution and do not require long delays between radiotracer injection and imaging [98-101]. In the context of infection imaging, white blood cell (WBC) labelling has proved superior to gallium-67 [102] and is now used as a method of choice or as an alternative to [^{18}F]FDG [103].

Nonetheless, gallium-67 imaging still plays a marginal role in clinics, especially in developing countries that have no convenient access to cyclotrons and for some pathologies where no better alternatives are available. A review of the literature of the last decades reveals a small but established niche for gallium-67 citrate use as a second-choice method for imaging infections and certain type of tumours when [^{18}F]FDG/WBC scans are negative or not available. Recent research and retrospective studies have reassessed the use of gallium-67 citrate for the imaging of different conditions such as acute interstitial nephritis [104], tuberculosis related pathologies

[105,106] and occult sepsis [107]. However, the value of these studies is limited by a lack of direct comparison with [^{18}F]FDG scans. Evaluation of gallium-68 as PET alternative to gallium-67 has also been undertaken for those conditions whose imaging is compatible with the short half-life of gallium-68 and an overview of the clinically relevant work in this area is provided below. In particular, ^{68}Ga-citrate has been investigated for several purposes.

A recent study suggested that ^{68}Ga-citrate can be effectively used to detect a variety of inflammation and infection conditions and described an optimised method for the synthesis and quality control of tracer according to good laboratory practice [108]. Nanni and coworkers evaluated the use of ^{68}Ga-citrate for the detection of skeletal infection in a cohort of 31 patients, resulting in favourable dosimetry and performance comparable to traditional methods for the diagnosis bone infections such as MRI or WBC scintigraphy [109]. More recently, ^{68}Ga-citrate application in oncological settings has also been revaluated in clinics, with variable results. In a 2014 study on patients presenting indeterminate lung lesions, ^{68}Ga-citrate was able to detect all malignant lesions, but could not discriminate between these lesion and tuberculosis or other benign lesions [110]. In a different study, prostate cancer patients were imaged with ^{68}Ga-citrate, which could identify 75 % of the metastatic lesions detected *via* Computed Tomography (CT) or ^{99m}Tc-bisphosphonate bone scan [111]. The optimal delay time between radiotracer administration and PET scan was also variable, and while the authors of the first study claim deterioration of image quality at 120 min post gallium-68 injection, in the prostate cancer study a delay of >210 min was required to obtained images of an adequate quality. Ongoing clinical studies evaluating ^{68}Ga-citrate involve patients suffering from prostate cancer (NCT02391025), lymphoma (NCT02776891) and orthopaedic infections (NCT03123289).

2.4.3 Non-targeted imaging

^{68}Ga-citrate as pulmonary vascular permeability agent

Beside its potential role in imaging malignancies and infections, ^{68}Ga-citrate has also been evaluated in a non-targeted way, as a pulmonary vascular permeability (PVP) agent in healthy volunteers and in patients suffering from acute respiratory distress symptoms, assuming complete gallium transchelation to transferrin *in vivo* [112]. When administered ^{68}Ga-citrate, patients presented significantly increased vascular permeability compared to healthy volunteers, demonstrating the feasibility of the approach. Intriguingly, the calculated permeability values were higher than those obtained with [^{99m}Tc]Tc-albumin measurements. While the authors did not investigate

the origin of this phenomenon, it is possibly due to presence, in equilibrium with gallium-transferrin, of a small percentage of $[Ga(OH)_4]^-$ which can more easily diffuse through membranes. Similar results were obtained in a more recent study comparing ^{68}Ga-citrate/transferrin and [^{99m}Tc]Tc-albumin for evaluation of PVP in patients with pulmonary oedema [113]. However, neither of these methods proved able to distinguish between noncardiogenic and hydrostatic pulmonary oedema.

Ventilation and perfusion measurements

Ventilation/perfusion measurements are normally performed using ^{99m}Tc-based agents such as Technegas for ventilation and ^{99m}Tc-macroaggregated albumin for perfusion. However, the development of PET agents for these imaging procedures is warranted to further increase their accuracy and in the context of ^{99m}Tc shortage. Evaluation of gallium-68 for ventilation perfusion imaging has been undertaken by Hofman and coworkers in pulmonary embolism patients [114] with encouraging results, and confirmed by a further study by Ament, where favourable dosimetry was also demonstrated [115]. In both studies, gallium analogues of the ^{99m}Tc-based tracers were used, namely [^{68}Ga]Ga-macroaggregated albumin and Galligas: an ultrafine dispersion of ^{68}Ga-labelled carbon particles that can be inhaled by the patients to evaluate ventilation. The safety and dosimetry associated with Galligas use were assessed with encouraging results [116].

[^{68}Ga]Ga-EDTA

[^{68}Ga]Ga-EDTA has a long history in nuclear medicine, being the form in which gallium-68 was eluted from the first generator [13]. Over the decades this tracer has been used for a variety of non-targeted imaging applications. [^{68}Ga]Ga-EDTA has been used to measure cerebrospinal fluid flow, and changes in permeability of the blood brain barrier in patients suffering from brain tumours, Alzheimer's disease or multiple sclerosis [117,118]. Determination of the glomerular filtration rate also represents a classical application of [^{68}Ga]Ga-EDTA imaging with the first clinical evaluation performed in 1988 with encouraging results [119]. While, at that time different agents, such as [^{51}Cr]Cr-EDTA or [^{99m}Tc]Tc-DTPA, took over renal function evaluation, clinical use of [^{68}Ga]Ga-EDTA was recently reconsidered by Hofman and coworkers [120,121] and found superior to the other radionuclide-based techniques.

2.5 New directions for imaging with gallium-68

Although this chapter focussed on the clinical translation of gallium-68 imaging agents, the investigation of novel target receptors and the development of novel ^{68}Ga-based

radiotracers for their imaging is blossoming, driven by the diffusion of clinical grade ^{68}Ga generator and by the recent approval of [^{68}Ga]Ga-DOTA-TATE and [^{68}Ga]Ga-DOTA-TOC for clinical use. In this section, a brief overview of some of the most promising new directions for gallium-68 imaging is provided. A more exhaustive description of the pool of new ^{68}Ga-agents in preclinical development can be found in Baums's book "Theranostics, Gallium-68, and Other Radionuclides: A Pathway to Personalized Diagnosis and Treatment" [13] and in Velikyan's reviews [28,122].

2.5.1 Different biomarkers for cancer imaging

Alongside affibodies, nanobodies and F(ab')$_2$ fragments, other antibody-like molecules are potentially interesting for the development of ^{68}Ga-immunoPET tracers and are undergoing preclinical evaluation. Vascular endothelial growth factor (VEGF) receptor is an important marker for angiogenesis and single chain analogues of VEGF (scVEGF) have been conjugated with DOTA and NOTA based chelators and proved able to delineate VEGF expression *in vivo*, but suffered from high kidney uptake [123]. Development of novel derivatives with improved biodistribution is ongoing [124]. A nanobody targeting the epidermal growth factor HER1 has also been radiolabelled with gallium-68 upon conjugation with DFO and evaluated in tumour bearing mice showing good targeting capabilities, but also high kidney uptake [125].

Folate receptor is upregulated in variety of cancers and therefore represents an important target for both imaging and therapy. Several ^{68}Ga-folate radiotracers have been developed in the past few years and found able to detect tumours with high specificity in preclinical xenograft models [126]. However, clinical translation has been so far delayed due to high endogenous expression of the folate receptor in the kidneys, which results in low tumour/kidney ratio and in concerns about kidney radiation dose.

The G-protein coupled neurotensin receptor 1 is a potentially good target for imaging, being overexpressed in a variety of cancers. However, metabolic instability of neurotensin analogues have been delaying the research on radiotracers targeting this receptor. Recently, DOTA/NODAGA derivatives of peptoid-peptide hybrid neurotensin analogues, with improved stability, were radiolabelled with ^{68}Ga and evaluated preclinically in colon cancer xenograft with promising results [127].

Cholecystokinin-2/Gastrin receptors hold a great promise for those neuroendocrine tumours in which the sensitivity of SSTR is limited, such as medullary thyroid carcinoma. Although imaging of this receptor with ^{68}Ga is still a relatively unexplored field, preclinical results by Brom using DOTA-minigastrin peptides were encouraging and warrant further investigation [128].

Hypoxia is commonly observed in myocardial ischemia and cancer, where it correlates with poor response to therapy. Being able to image hypoxic areas would be therefore extremely important for treatment planning in these conditions. Several ^{68}Ga-based radiotracers have been developed and preclinically evaluated in the last decades, where the hypoxia-targeting nitroimidazole moiety has been conjugated to several chelators such as DOTA [129,130], NOTA [131] and TRAP, with the latter being a multimeric derivative [132]. Although these radiotracers showed tumour targeting *in vivo*, low tumour uptake and radiotracer accumulation in several non-target organs (kidney, liver and notably muscle for some of the derivative) is still a major issue, which need to be addressed.

2.5.2 Non-oncological targets

The decades-long quest for an agent able to selectively imaging inflammation and infection has been challenging due to the multitude of factors involved in these processes. It is beyond the scope of this chapter to review the several ^{68}Ga imaging agents that are currently under investigation for infection and inflammation imaging, a comprehensive review of these radiotracers was published by Velikyan earlier this year [133].

Recent development of new radiotracers for the imaging of infection and inflammatory processes has been driven by the identification of useful biomarkers for these conditions. Vascular adhesion protein 1 (VAP1) is translocated from intracellular storage granules onto the cell surface during inflammation and osteomyelitis and therefore represents a promising target receptor for imaging with radiolabelled peptides. Preclinical evaluation of several ^{68}Ga-based VAP1 tracers has been performed recently with encouraging results [134]. Distinction between inflammation and infection is also challenging. ^{68}Ga-labelling of the antimicrobial peptide ubiquicidin resulted in tracers potentially able to discriminate between infection and inflammation in preclinical models [118,135]. Siderophores such as TAFC and DFO can also be labelled with gallium-68 and localise at the infection site responding to bacterial iron requirements [136].

Fibrosis is involved in many chronic diseases and inflammatory injuries and a non-invasive method for the accurate and specific localisation of fibrotic lesion is key to their prompt treatment. Because this process involves the excessive production of extracellular matrix proteins such as collagen, radiotracers targeting these proteins represents a promising way to image fibrosis. [68]Ga radiotracers based on the collagen targeting peptide collagelin have been developed by Velikyan and co-workers and

showed targeting capability *in vitro* as well as favourable pharmacokinetics and dosimetry in healthy rats [137,138]. However, no data from a fibrosis animal model are available so far to confirm ability of the tracers to target the fibrotic process *in vivo*.

Gallium-68 imaging of cardiovascular diseases is also an expanding area with several preclinical studies ongoing. Imaging of atherosclerotic plaques is currently performed with [^{18}F]FDG, which is not ideal due to its high uptake in the heart. Development of new ^{68}Ga tracers for imaging atherosclerotic plaques focusses on targeting molecular processes important for active plaques. Fucoidan is a polysaccharide with high affinity for selectin-P, a protein overexpressed on the endothelium overlying active plaques. Although the chemical structure of fucoidan is still unknown, direct labelling with gallium-68 was feasible and the radiotracer demonstrated specific uptake in active plaques *in vivo* [139]. In a different study, a peptide mimetic of an apolipoprotein was radiolabelled with ^{68}Ga *via* a DOTA chelator and found able to delineate atherosclerotic plaques in preclinical models, based on their lipid burden [140]. Although both radiotracers could delineate atherosclerotic plaques a major limitation is their slow blood clearance and non-specific uptake in non-target organs.

2.6 Gallium compounds as therapeutic agents

The serendipitous discovery that gallium salts localise in tumour tissues and that gallium interactions with biological system can be treated, to a certain extent, as an iron mimetic (see **Chapter 1**), prompted the investigation on the possible use of gallium compounds in cancer chemotherapy.

2.6.1 Gallium salts

Initial investigation on the cytotoxic activity of gallium salts, with focus on gallium nitrate, started in the early seventies [141]. Irrespective of the anionic component, gallium salts showed remarkable cytotoxicity related to disruption of cellular iron homeostasis [142] and inhibition of ribonucleotide reductase activity, which requires Fe^{3+} as an essential cofactor [143]. To counteract iron deprivation following Ga^{3+} uptake, expression of transferrin receptors is increased, resulting in further gallium accumulation and finally apoptosis. *In vitro* experiments using ^{59}Fe suggested that gallium could induce iron deprivation also by inhibition of intracellular Fe(III) release from FeTf by insufficient acidification in the endosomes [142]. Gallium nitrate was investigated in several clinical trials, which demonstrated its potency in advanced bladder cancer and non-Hodgkin lymphoma, without showing any myelosuppresive activity [144]. However, injection of gallium nitrate as a bolus results in

nephrotoxicity, likely due to the inability of therapeutic doses of Ga(III) to bind to transferrin quantitatively upon rapid administration and consequent quick renal excretion of gallate [145]. On the other hand, the need for long intravenous infusion to administer the drug without incurring in nephrotoxicity is a major drawback for its widespread clinical use [146]. Beside its anti-tumour activity, gallium salts were found to affect bone metabolism and blood level of calcium [147]. Consequently, gallium nitrate (Ganite) was approved by the FDA for the treatment of malignancy-associated hypercalcemia [146].

2.6.2 Gallium complexes

Alternative gallium compounds have been developed in order to increase oral bioavailability of this metal. Among these, it is worth mentioning gallium maltolate (gallium tris(3-hydroxy-2-methyl-4H-pyran-4-onate), **Figure 2.9**), which exploits the ability of pyranone ligands to deliver M^{3+} metal ions to tissues [148]. With its Log$P$ of 0.42 and its stability towards hydrolysis, gallium maltolate greatly enhances the solubility and gastrointestinal absorption of gallium. This is followed by gallium transchelation to transferrin in circulation, which lead to increased tumour uptake and decreased renal toxicity compared to gallium nitrate [145]. *In vitro*, gallium maltolate displayed enhanced and faster cytotoxic activity compared to gallium nitrate and was effective in cell lines resistant to gallium salts treatment [149]. However, this different behaviour may simply be related to direct cellular uptake of the lipophilic complex before gallium dissociation, which is likely to happen at short time points *in vitro*. Phase I clinical trials in normal subject show no adverse event and favourable pharmacokinetics for gallium maltolate [145] and a preliminary investigation on a patient with advanced hepatocellular carcinoma provided promising results [150]. However, the outcomes of a phase II clinical trial (NCT00050687) were never published and no further clinical evaluation of this compound is ongoing.
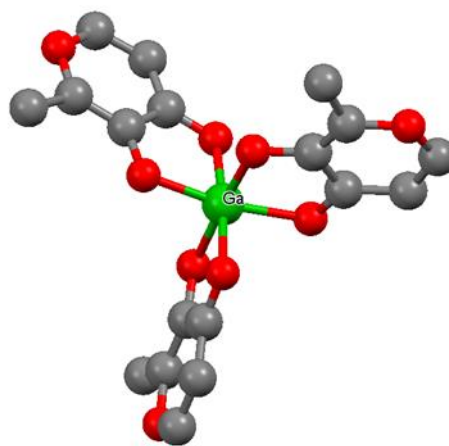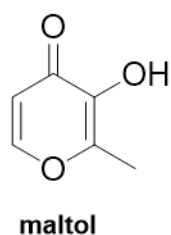
Figure 2.9. *Chemical structure of maltol and crystal structure of the (tris(3-hydroxy-2-methyl-4H-pyran-4-onate)gallium(III) complex [145].*

Tris(8-quinolonato)gallium(III) (**Figure 2.10**, also known as gallium-oxine, KP46 or FFC11) was originally investigated as a gallium-68 platelets-labelling agent [151]. More recently, this gallium complex has been reconsidered as an anticancer and antihypercalcemic agent, able to overcome the poor oral availability of gallium salts. In fact, owing to the lipophilic nature of 8-hydroxyquinoline ligands this complex is characterised by Log*P* = 0.88, which should ensure adequate membrane permeability, facilitating intestinal absorption of the drug and the achievement of adequate plasma levels [152]. Discordant literature exists on the interaction of this compound with transferrin and other serum proteins such as albumin [153-157], casting doubts on the mechanism of cellular uptake (*i.e.* whether it is transferrin dependent or rather diffusion of the lipophilic complex through the cell membrane) [146,158]. Similarly, the intracellular targets of gallium-oxine seem to be different from those of gallium nitrate [159]. Compared to gallium nitrate, KP46 displayed increased potency on a variety of cancer cell lines and in animal tumour models [146] and was found effective against renal cancer in phase I/II clinical trials [160,161]. Its mechanism of action is far from understood and investigations have been hampered by the low solubility of this drug [153].
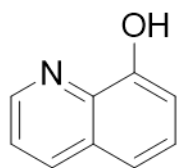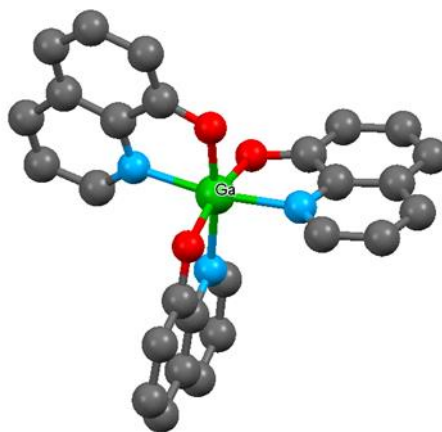
Figure 2.10. *Schematic structure of the 8-hydroxyquinoline ligand (left) and crystal structure of the resulting gallium complex* Tris*(8-quinolonato)gallium(III) (right) [162].*

2.7 References

1. Andrews, G. A., Root, S. W., and Kerman, H. D. (1953) A study of gallium .6. Clinical studies with gallium-72. *Radiology* **61**, 570-588.
2. Bruner, H. D., Hayes, R. L., and Perkinson, J. D. (1953) A study of gallium .10. Preliminary data on gallium-67. *Radiology* **61**, 602-613.
3. Edwards, C. L., and Hayes, R. L. (1970) Scanning malignant neoplasms with gallium-67. *JAMA* **212**, 1182-1190.
4. Hayes, R. L., Carlton, J. E., and Byrd, B. L. (1965) Bone scanning with gallium-68 - A carrier effect. *J. Nucl. Med.* **6**, 605-609.
5. Schaer, L. R., Anger, H. O., and Gottschalk, A. (1966) Gallium Edetate ^{68}Ga experiences in brain-lesion detection with positron camera. *JAMA* **198**, 811-813.
6. Rosch, F. (2013) Past, present and future of Ge-68/Ga-68 generators. *Appl. Radiat. Isot.* **76**, 24-30.
7. Torres Martin de Rosales, R., Arstad, E., and Blower, P. J. (2009) Nuclear imaging of molecular processes in cancer. *Targeted oncology* **4**, 183-197.
8. Hicks, R. J., and Hofman, M. S. (2012) Is there still a role for SPECT-CT in oncology in the PET-CT era? *Nature Reviews Clinical Oncology* **9**, 712-720.
9. Rahmim, A., and Zaidi, H. (2008) PET versus SPECT: strengths, limitations and challenges. *Nucl. Med. Commun.* **29**, 193-207.
10. Conti, M., and Eriksson, L. (2016) Physics of pure and non-pure positron emitters for PET: a review and a discussion. *Ejnmmi Physics* **3.**
11. Velikyan, I. (2011) Positron Emitting [Ga-68]Ga-Based Imaging Agents: Chemistry and Diversity. *Med. Chem.* **7**, 345-379.
12. Velikyan, I. (2015) Ga-68-Based Radiopharmaceuticals: Production and Application Relationship. *Molecules* **20**, 12913-12943.
13. Baum, R. P., and Rösch, F. (2012) *Theranostics, Gallium-68, and Other Radionuclides: A Pathway to Personalized Diagnosis and Treatment*, Springer Berlin Heidelberg.
14. Velikyan, I. (2013) Prospective of ^{68}Ga-radiopharmaceutical development. *Theranostics* **4**, 47-80.
15. Oberg, K. (2012) Gallium-68 somatostatin receptor PET/CT: Is it time to replace [111]Indium DTPA octreotide for patients with neuroendocrine tumors? *Endocrine* **42**, 3-4.
16. Banerjee, S. R., and Pomper, M. G. (2013) Clinical applications of Gallium-68. *Appl. Radiat. Isot.* **76**, 2-13.
17. Jackson, I. M., Scott, P. J. H., and Thompson, S. (2017) Clinical applications of radiolabeled peptides for PET. *Semin. Nucl. Med.* **47**, 493-523.
18. Wild, D., Schmitt, J. S., Ginj, M., Macke, H. R., Bernard, B. F., Krenning, E., de Jong, M., Wenger, S., and Reubi, J. C. (2003) DOTA-NOC, a high-affinity ligand of somatostatin receptor subtypes 2, 3 and 5 for labelling with various radiometals. *Eur. J. Nucl. Med. Mol. Imaging* **30**, 1338-1347.
19. Mullard, A. (2016) FDA approvals for the first 6 months of 2016. *Nat. Rev. Drug Discov.* **15**, 523-523.
20. Advanced Accelerator Applications (2016) Advanced Accelerator Applications Announces European Commission Approval of SomaKit TOC™. (Press Release).
21. Putzer, D., Kroiss, A., Waitz, D., Gabriel, M., Traub-Weidinger, T., Uprimny, C., von Guggenberg, E., Decristoforo, C., Warwitz, B., Widmann, G., and Virgolini, I. J. (2013) Somatostatin receptor PET in neuroendocrine tumours: Ga-68-DOTA[0],Tyr[3]-octreotide versus Ga-68-DOTA[0]-lanreotide. *Eur. J. Nucl. Med. Mol. Imaging* **40**, 364-372.
22. van Essen, M., Krenning, E. P., Kam, B. L. R., de Jong, M., Valkema, R., and Kwekkeboom, D. J. (2009) Peptide-receptor radionuclide therapy for endocrine tumors. *Nat. Rev. Endocrinol.* **5**, 382-393.

23. Cescato, R., Erchegyi, J., Waser, B., Piccand, V., Maecke, H. R., Rivier, J. E., and Reubi, J. C. (2008) Design and in vitro characterization of highly sst_2-selective somatostatin antagonists suitable for radiotargeting. *J. Med. Chem.* **51**, 4030-4037.

24. Ginj, M., Zhang, H. W., Waser, B., Cescato, R., Wild, D., Wang, X. J., Erchegyi, J., Rivier, J., Macke, H. R., and Reubi, J. C. (2006) Radiolabeled somatostatin receptor antagonists are preferable to agonists for in vivo peptide receptor targeting of tumors. *Proc. Natl. Acad. Sci. U.S.A* **103**, 16436-16441.

25. Fani, M., Peitl, P. K., and Velikyan, I. (2017) Current Status of Radiopharmaceuticals for the Theranostics of Neuroendocrine Neoplasms. *Pharmaceuticals* **10**.

26. Fani, M., Nicolas, G. P., and Wild, D. (2017) Somatostatin receptor antagonists for imaging and therapy. *J. Nucl. Med.* **58**, 61S-66S.

27. Mease, R. C., Foss, C. A., and Pomper, M. G. (2013) PET imaging in prostate cancer: focus on prostate-specific membrane antigen. *Curr. Top. Med. Chem.* **13**, 951-962.

28. Velikyan, I. (2015) Continued rapid growth in Ga-68 applications: update 2013 to June 2014. *J. Label. Compd. Radiopharm.* **58**, 99-121.

29. Banerjee, S. R., Pullambhatla, M., Byun, Y., Nimmagadda, S., Green, G., Fox, J. J., Horti, A., Mease, R. C., and Pomper, M. G. (2010) Ga-68-labeled inhibitors of Prostate-Specific Membrane Antigen (PSMA) for imaging prostate cancer. *J. Med. Chem.* **53**, 5333-5341.

30. Eder, M., Neels, O., Müller, M., Bauder-Wüst, U., Remde, Y., Schäfer, M., Hennrich, U., Eisenhut, M., Afshar-Oromieh, A., Haberkorn, U., and Kopka, K. (2014) Novel preclinical and radiopharmaceutical aspects of [^{68}Ga]Ga-PSMA-HBED-CC: a new PET tracer for imaging of prostate cancer. *Pharmaceuticals* **7**, 779-796.

31. Afshar-Oromieh, A., Haberkorn, U., Hadaschik, B., Habl, G., Eder, M., Eisenhut, M., Schlemmer, H.-P., and Roethke, M. C. (2013) PET/MRI with a Ga-68-PSMA ligand for the detection of prostate cancer. *Eur. J. Nucl. Med. Mol. Imaging* **40**, 1629-1630.

32. Afshar-Oromieh, A., Zechmann, C. M., Malcher, A., Eder, M., Eisenhut, M., Linhart, H. G., Holland-Letz, T., Hadaschik, B. A., Giesel, F. L., Debus, J., and Haberkorn, U. (2014) Comparison of PET imaging with a Ga-68-labelled PSMA ligand and F-18-choline-based PET/CT for the diagnosis of recurrent prostate cancer. *Eur. J. Nucl. Med. Mol. Imaging* **41**, 11-20.

33. Schafer, M., Bauder-Wust, U., Leotta, K., Zoller, F., Mier, W., Haberkorn, U., Eisenhut, M., and Eder, M. (2012) A dimerized urea-based inhibitor of the prostate-specific membrane antigen for Ga-68-PET imaging of prostate cancer. *EJNMMI Res.* **2**

34. Benesova, M., Schafer, M., Bauder-Wust, U., Afshar-Oromieh, A., Kratochwil, C., Mier, W., Haberkorn, U., Kopka, K., and Eder, M. (2015) Preclinical evaluation of a tailor-made DOTA-conjugated PSMA inhibitor with optimized linker moiety for imaging and endoradiotherapy of prostate cancer. *J. Nucl. Med.* **56**, 914-920.

35. Afshar-Oromieh, A., Hetzheim, H., Kratochwil, C., Benesova, M., Eder, M., Neels, O. C., Eisenhut, M., Kubler, W., Holland-Letz, T., Giesel, F. L., Mier, W., Kopka, K., and Haberkorn, U. (2015) The theranostic PSMA ligand PSMA-617 in the diagnosis of prostate cancer by PET/CT: biodistribution in humans, radiation dosimetry, and first evaluation of tumor lesions. *J. Nucl. Med.* **56**, 1697-1705.

36. Weineisen, M., Schottelius, M., Simecek, J., Baum, R. P., Yildiz, A., Beykan, S., Kulkarni, H. R., Lassmann, M., Klette, I., Eiber, M., Schwaiger, M., and Wester, H. J. (2015) Ga-68- and Lu-177-labeled PSMA I&T: Optimization of a

PSMA-targeted theranostic concept and first proof-of-concept human studies. *J. Nucl. Med.* **56**, 1169-1176.

37. Weineisen, M., Simecek, J., Schottelius, M., Schwaiger, M., and Wester, H. J. (2014) Synthesis and preclinical evaluation of DOTAGA-conjugated PSMA ligands for functional imaging and endoradiotherapy of prostate cancer. *EJNMMI Res.* **4.**

38. Young, J. D., Abbate, V., Imberti, C., Meszaros, L. K., Ma, M. T., Terry, S. Y., Hider, R. C., Mullen, G. E., and Blower, P. J. (2017) ^{68}Ga-THP-PSMA: a PET imaging agent for prostate cancer offering rapid, room-temperature, 1-step kit-based radiolabeling. *J. Nucl. Med.* **58,** 1270-1277.

39. Hofman, M. S., Eu, P., Jackson, P., Hong, E., Binns, D., Iravani, A., Murphy, D., Mitchell, C., Siva, S., Hicks, R. J., Young, J. D., Blower, P., and Mullen, G. E. (2017) Cold Kit PSMA PET Imaging: Phase I study of ^{68}Ga-THP-PSMA PET/CT in patients with prostate cancer. *J. Nucl. Med.* (ahead of print, doi:10.2967/jnumed.117.199554).

40. Chen, H. J., Niu, G., Wu, H., and Chen, X. Y. (2016) Clinical application of radiolabeled RGD Peptides for PET imaging of integrin $\alpha_V\beta_3$. *Theranostics* **6**, 78-92.

41. Haubner, R., Beer, A. J., Wang, H., and Chen, X. Y. (2010) Positron emission tomography tracers for imaging angiogenesis. *Eur. J. Nucl. Med. Mol. Imaging* **37**, S86-S103.

42. Jeong, J. M., Hong, M. K., Chang, Y. S., Lee, Y. S., Kim, Y. J., Cheon, G. J., Lee, D. S., Chung, J. K., and Lee, M. C. (2008) Preparation of a promising angiogenesis PET imaging agent: Ga-68-labeled c(RGDyK)-isothiocyanatobenzyl-1,4,7-triazacyclononane-1,4,7-triacetic acid and feasibility studies in mice. *J. Nucl. Med.* **49**, 830-836.

43. Withofs, N., Signolle, N., Somja, J., Lovinfosse, P., Nzaramba, E. M., Mievis, F., Giacomelli, F., Waltregny, D., Cataldo, D., Gambhir, S. S., and Hustinx, R. (2015) F-18-FPRGD2 PET/CT imaging of integrin $\alpha_V\beta_3$ in renal carcinomas: correlation with histopathology. *J. Nucl. Med.* **56**, 361-364.

44. Haubner, R., Finkenstedt, A., Stegmayr, A., Rangger, C., Decristoforo, C., Zoller, H., and Virgolini, I. J. (2016) Ga-68 NODAGA-RGD - Metabolic stability, biodistribution, and dosimetry data from patients with hepatocellular carcinoma and liver cirrhosis. *Eur. J. Nucl. Med. Mol. Imaging* **43**, 2005-2013.

45. Li, Z. B., Chen, K., and Chen, X. (2008) Ga-68-labeled multimeric RGD peptides for microPET imaging of integrin $\alpha_V\beta_3$ expression. *Eur. J. Nucl. Med. Mol. Imaging* **35**, 1100-1108.

46. Liu, S. (2009) Radiolabeled Cyclic RGD Peptides as Integrin $\alpha_V\beta_3$-Targeted Radiotracers: Maximizing Binding Affinity via Bivalency. *Bioconjugate Chem.* **20**, 2199-2213.

47. Zheng, K., Liang, N. X., Zhang, J. J., Lang, L. X., Zhang, W., Li, S. Q., Zhao, J., Niu, G., Li, F., Zhu, Z. H., and Chen, X. Y. (2015) Ga-68-NOTA-PRGD2 PET/CT for integrin imaging in patients with lung cancer. *J. Nucl. Med.* **56**, 1823-1827.

48. Li, D. L., Zhao, X. B., Zhang, L. W., Li, F., Ji, N., Gao, Z. X., Wang, J. S., Kang, P., Liu, Z. F., Shi, J. Y., Chen, X. Y., and Zhu, Z. H. (2014) Ga-68-PRGD2 PET/CT in the evaluation of glioma: a prospective study. *Mol. Pharm.* **11**, 3923-3929.

49. Sun, Y., Zeng, Y., Zhu, Y. C., Feng, F., Xu, W. H., Wu, C. X., Xing, B., Zhang, W. H., Wu, P. L., Cui, L. Y., Wang, R. Z., Li, F., Chen, X. Y., and Zhu, Z. H. (2014) Application of Ga-68-PRGD2 PET/CT for $\alpha_V\beta_3$-integrin imaging of myocardial infarction and stroke. *Theranostics* **4**, 778-786.

50. Zhu, Z., Yin, Y., Zheng, K., Li, F., Chen, X., Zhang, F., and Zhang, X. (2014) Evaluation of synovial angiogenesis in patients with rheumatoid arthritis using Ga-68-PRGD2 PET/CT: a prospective proof-of-concept cohort study. *Ann. Rheum. Dis.* **73**, 1269-1272.

51. Burnett, C. A., Xie, J. W., Quijano, J., Shen, Z. M., Hunter, F., Bur, M., Li, K. C. P., and Danthi, S. N. (2005) Synthesis, in vitro, and in vivo characterization of an integrin $\alpha_V\beta_3$-targeted molecular probe for optical imaging of tumor. *Bioorganic Med. Chem.* **13**, 3763-3771.

52. Baum, R. P., Kulkarni, H. R., Muller, D., Satz, S., Danthi, N., Kim, Y. S., and Brechbiel, M. W. (2015) First-In-Human study demonstrating tumor-angiogenesis by PET/CT imaging with Ga-68-NODAGA-THERANOST, a high-affinity peptidomimetic for $\alpha_V\beta_3$ integrin receptor targeting. *Cancer Biotherapy and Radiopharmaceuticals* **30**, 152-159.

53. Schuhmacher, J., Zhang, H. W., Doll, J., Macke, H. R., Matys, R., Hauser, H., Henze, M., Haberkorn, U., and Eisenhut, M. (2005) GRP receptor-targeted PET of a rat pancreas carcinoma xenograft in nude mice with a Ga-68-labeled bombesin(6-14) analog. *J. Nucl. Med.* **46**, 691-699.

54. Dimitrakopoulou-Strauss, A., Hohenberger, P., Haberkorn, U., Macke, H. R., Eisenhut, M., and Strauss, L. G. (2007) Ga-68-Labeled bombesin studies in patients with gastrointestinal stromal tumors: Comparison with F-18-FDG. *J. Nucl. Med.* **48**, 1245-1250.

55. Kahkonen, E., Jambor, I., Kemppainen, J., Lehtio, K., Gronroos, T. J., Kuisma, A., Luoto, P., Sipila, H. J., Tolvanen, T., Alanen, K., Silen, J., Kallajoki, M., Roivainen, A., Schafer, N., Schibli, R., Dragic, M., Johayem, A., Valencia, R., Borkowski, S., and Minn, H. (2013) In vivo imaging of prostate cancer using Ga-68 -labeled bombesin analog BAY86-7548. *Clin. Cancer Res.* **19**, 5434-5443.

56. Maina, T., Bergsma, H., Kulkarni, H. R., Mueller, D., Charalambidis, D., Krenning, E. P., Nock, B. A., de Jong, M., and Baum, R. P. (2016) Preclinical and first clinical experience with the gastrin-releasing peptide receptor-antagonist Ga-68 SB3 and PET/CT. *Eur. J. Nucl. Med. Mol. Imaging* **43**, 964-973.

57. George, G. P. C., Pisaneschi, F., Nguyen, Q. D., and Aboagye, E. O. (2015) Positron Emission Tomographic Imaging of CXCR4 in Cancer: Challenges and Promises. *Molecular Imaging* **14**.

58. Demmer, O., Gourni, E., Schumacher, U., Kessler, H., and Wester, H. J. (2011) PET imaging of CXCR4 receptors in cancer by a new optimized ligand. *Chemmedchem* **6**, 1789-1791.

59. Woodard, L. E., and Nimmagadda, S. (2011) CXCR4-based imaging agents. *J. Nucl. Med.* **52**, 1665-1669.

60. Wester, H. J., Keller, U., Schottelius, M., Beer, A., Philipp-Abbrederis, K., Hoffmann, F., Simecek, J., Gerngross, C., Lassmann, M., Herrmann, K., Pellegata, N., Rudelius, M., Kessler, H., and Schwaiger, M. (2015) Disclosing the CXCR4 expression in lymphoproliferative diseases by targeted molecular imaging. *Theranostics* **5**, 618-630.

61. Wang, Z., Zhang, M. R., Wang, L., Wang, S. J., Kang, F., Li, G. Q., Jacobson, O., Niu, G., Yang, W. D., Wang, J., and Chen, X. Y. (2015) Prospective study of Ga-68-NOTA-NFB: radiation dosimetry in healthy volunteers and first application in glioma patients. *Theranostics* **5**, 882-889.

62. Herrmann, K., Lapa, C., Wester, H. J., Schottelius, M., Schiepers, C., Eberlein, U., Bluemel, C., Keller, U., Knop, S., Kropf, S., Schirbel, A., Buck, A. K., and Lassmann, M. (2015) Biodistribution and radiation dosimetry for the chemokine receptor CXCR4-targeting probe Ga-68-Pentixafor. *J. Nucl. Med.* **56**, 410-416.

63. Philipp-Abbrederis, K., Herrmann, K., Knop, S., Schottelius, M., Eiber, M., Luckerath, K., Pietschmann, E., Habringer, S., Gerngross, C., Franke, K., Rudelius, M., Schirbel, A., Lapa, C., Schwamborn, K., Steidle, S., Hartmann, E., Rosenwald, A., Kropf, S., Beer, A. J., Peschel, C., Einsele, H., Buck, A. K., Schwaiger, M., Gotze, K., Wester, H. J., and Keller, U. (2015) In vivo molecular imaging of chemokine receptor CXCR4 expression in patients with advanced multiple myeloma. *Embo Mol. Med.* **7**, 477-487.

64. Herhaus, P., Habringer, S., Philipp-Abbrederis, K., Vag, T., Gerngross, C., Schottelius, M., Slotta-Huspenina, J., Steiger, K., Altmann, T., Weisser, T., Steidle, S., Schick, M., Jacobs, L., Slawska, J., Muller-Thomas, C., Verbeek, M., Subklewe, M., Peschel, C., Wester, H. J., Schwaiger, M., Gotze, K., and Keller, U. (2016) Targeted positron emission tomography imaging of CXCR4 expression in patients with acute myeloid leukemia. *Haematologica* **101**, 932-940.

65. Lapa, C., Schreder, M., Schirbel, A., Samnick, S., Kortum, K. M., Herrmann, K., Kropf, S., Einsele, H., Buck, A. K., Wester, H. J., Knop, S., and Luckerath, K. (2017) Ga-68 Pentixafor-PET/CT for imaging of chemokine receptor CXCR4 expression in multiple myeloma - Comparison to F-18 FDG and laboratory values. *Theranostics* **7**, 205-212.

66. Vag, T., Gerngross, C., Herhaus, P., Eiber, M., Philipp-Abbrederis, K., Graner, F. P., Ettl, J., Keller, U., Wester, H. J., and Schwaiger, M. (2016) First experience with chemokine receptor CXCR4-targeted PET imaging of patients with solid cancers. *J. Nucl. Med.* **57**, 741-746.

67. Werner, R. A., Weich, A., Higuchi, T., Schmid, J. S., Schirbel, A., Lassmann, M., Wild, V., Rudelius, M., Kudlich, T., Herrmann, K., Scheurlen, M., Buck, A. K., Kropf, S., Wester, H. J., and Lapa, C. (2017) Imaging of chemokine receptor 4 expression in neuroendocrine tumors - A triple tracer comparative approach. *Theranostics* **7**, 1489-1498.

68. Lapa, C., Luckerath, K., Rudelius, M., Schmid, J. S., Schoene, A., Schirbel, A., Samnick, S., Pelzer, T., Buck, A. K., Kropf, S., Wester, H. J., and Herrmann, K. (2016) Ga-68 Pentixafor-PET/CT for imaging of chemokine receptor 4 expression in small cell lung cancer - initial experience. *Oncotarget* **7**, 9288-9295.

69. Lapa, C., Luckerath, K., Kleinlein, I., Monoranu, C. M., Linsenmann, T., Kessler, A. F., Rudelius, M., Kropf, S., Buck, A. K., Ernestus, R. I., Wester, H. J., Lohr, M., and Herrmann, K. (2016) Ga-68-Pentixafor-PET/CT for Imaging of Chemokine Receptor 4 Expression in Glioblastoma. *Theranostics* **6**, 428-434.

70. Herrmann, K., Schottelius, M., Lapa, C., Osl, T., Poschenrieder, A., Hanscheid, H., Luckerath, K., Schreder, M., Bluemel, C., Knott, M., Keller, U., Schirbel, A., Samnick, S., Lassmann, M., Kropf, S., Buck, A. K., Einsele, H., Wester, H. J., and Knop, S. (2016) First-in-Human experience of CXCR4-directed endoradiotherapy with Lu-177- and Y-90-labeled Pentixather in advanced-stage multiple myeloma with extensive intra- and extramedullary disease. *J. Nucl. Med.* **57**, 248-251.

71. Poschenrieder, A., Schottelius, M., Schwaiger, M., and Wester, H. J. (2016) Preclinical evaluation of Ga-68 NOTA-pentixafor for PET imaging of CXCR4 expression in vivo - a comparison to Ga-68 pentixafor. *EJNMMI Res.* **6.**

72. Jacobson, O., Weiss, I. D., Szajek, L. P., Niu, G., Ma, Y., Kiesewetter, D. O., Peled, A., Eden, H. S., Farber, J. M., and Chen, X. (2012) Improvement of CXCR4 tracer specificity for PET imaging. *J. Control. Release* **157**, 216-223.

73. Christ, E., Wild, D., Ederer, S., Behe, M., Nicolas, G., Caplin, M. E., Braendle, M., Clerici, T., Fischli, S., Stettler, C., Ell, P. J., Seufert, J., Gloor, B., Perren, A., Reubi, J. C., and Forrer, F. (2013) Glucagon-like peptide-1 receptor imaging for the localisation of insulinomas: a prospective multicentre imaging study. *Lancet Diabetes & Endocrinol.* **1**, 115-122.

74. Hubalewska-Dydejczyk, A., Sowa-Staszczak, A., Tomaszuk, M., and Stefanska, A. (2015) GLP-1 and exendin-4 for imaging endocrine pancreas. A review Labelled glucagon-like peptide-1 analogues: past, present and future. *Q. J. Nucl. Med. Mol. Imaging* **59**, 152-160.

75. Eriksson, O., Velikyan, I., Selvaraju, R. K., Kandeel, F., Johansson, L., Antoni, G., Eriksson, B., Sorensen, J., and Korsgren, O. (2014) Detection of metastatic

insulinoma by positron emission tomography with Ga-68 Exendin-4-A Case Report. *Journal of Clinical Endocrinology & Metabolism* **99**, 1519-1524.

76. Antwi, K., Fani, M., Nicolas, G., Rottenburger, C., Heye, T., Reubi, J. C., Gloor, B., Christ, E., and Wild, D. (2015) Localization of Hidden Insulinomas with Ga-68-DOTA-Exendin-4 PET/CT: A Pilot Study. *J. Nucl. Med.* **56**, 1075-1078.

77. Luo, Y. P., Pan, Q. Q., Yao, S. B., Yu, M., Wu, W. M., Xue, H. D., Kiesewetter, D. O., Zhu, Z. H., Li, F., Zhao, Y. P., and Chen, X. Y. (2016) Glucagon-Like Peptide-1 Receptor PET/CT with Ga-68-NOTA-Exendin-4 for detecting localized insulinoma: a prospective cohort study. *J. Nucl. Med.* **57**, 715-720.

78. Jacobsen, B., and Ploug, M. (2008) The urokinase receptor and its structural homologue C4.4A in human cancer: expression, prognosis and pharmacological inhibition. *Curr. Med. Chem.* **15**, 2559-2573.

79. Skovgaard, D., Persson, M., and Kjaer, A. (2017) Imaging of prostate cancer using urokinase-type plasminogen activator receptor PET. *Pet Clinics* **12**, 243-255.

80. Froidevaux, S., Calame-Christe, M., Schuhmacher, J., Tanner, H., Saffrich, R., Henze, M., and Eberle, A. N. (2004) A gallium-labeled DOTA-alpha-melanocyte-stimulating hormone analog for PET Imaging of melanoma metastases. *J. Nucl. Med.* **45**, 116-123.

81. Maecke, H. R., Hofmann, M., and Haberkorn, U. (2005) Ga-68-labeled peptides in tumor imaging. *J. Nucl. Med.* **46**, 172S-178S.

82. Choi, J. Y., Jeong, J. M., Yoo, B. C., Kim, K., Kim, Y., Yang, B. Y., Lee, Y. S., Lee, D. S., Chung, J. K., and Lee, M. C. (2011) Development of Ga-68-labeled mannosylated human serum albumin (MSA) as a lymph node imaging agent for positron emission tomography. *Nucl. Med. Biol.* **38**, 371-379.

83. Eo, J. S., Kim, H. K., Kim, S., Lee, Y. S., Jeong, J. M., and Choi, Y. H. (2015) Gallium-68 Neomannosylated human serum albumin-based PET/CT lymphoscintigraphy for sentinel lymph node mapping in non-small cell lung cancer. *Ann. Surg. Oncol.* **22**, 636-641.

84. Kubicek, V., Rudovsky, J., Kotek, J., Hermann, P., Elst, L. V., Muller, R. N., Kolar, Z. I., Wolterbeek, H. T., Peters, J. A., and Lukes, I. (2005) A bisphosphonate monoamide analogue of DOTA: A potential agent for bone targeting. *J. Am. Chem. Soc.* **127**, 16477-16485.

85. Fellner, M., Baum, R. P., Kubicek, V., Hermann, P., Lukes, I., Prasad, V., and Roesch, F. (2010) PET/CT imaging of osteoblastic bone metastases with Ga-68-bisphosphonates: first human study. *Eur. J. Nucl. Med. Mol. Imaging* **37**, 834-834.

86. Holub, J., Meckel, M., Kubicek, V., Rosch, F., and Hermann, P. (2015) Gallium(III) complexes of NOTA-bis (phosphonate) conjugates as PET radiotracers for bone imaging. *Contrast Media Mol. Imaging* **10**, 122-134.

87. Passah, A., Tripathi, M., Ballal, S., Yadav, M. P., Kumar, R., Roesch, F., Meckel, M., Chakraborty, P. S., and Bal, C. (2017) Evaluation of bone-seeking novel radiotracer Ga-68-NO2AP-Bisphosphonate for the detection of skeletal metastases in carcinoma breast. *Eur. J. Nucl. Med. Mol. Imaging* **44**, 41-49.

88. Beylergil, V., Morris, P. G., Smith-Jones, P. M., Modi, S., Solit, D., Hudis, C. A., Lu, Y., O'Donoghue, J., Lyashchenko, S. K., Carrasquillo, J. A., Larson, S. M., and Akhurst, T. J. (2013) Pilot study of Ga-68-DOTA-F(ab')$_2$-trastuzumab in patients with breast cancer. *Nucl. Med. Commun.* **34**, 1157-1165.

89. Keyaerts, M., Xavier, C., Heemskerk, J., Devoogdt, N., Everaert, H., Ackaert, C., Vanhoeij, M., Duhoux, F. P., Gevaert, T., Simon, P., Schallier, D., Fontaine, C., Vaneycken, I., Vanhove, C., De Greve, J., Lamote, J., Caveliers, V., and Lahoutte, T. (2016) Phase I study of Ga-68-HER2-Nanobody for PET/CT assessment of HER2 expression in breast carcinoma. *J. Nucl. Med.* **57**, 27-33.

90. Orlova, A., Tolmachev, V., Pehrson, R., Lindborg, M., Tran, T., Sandstrom, M., Nilsson, F. Y., Wennborg, A., Abrahmsen, L., and Feldwisch, J. (2007) Synthetic

affibody molecules: A novel class of affinity ligands for molecular imaging of HER2-expressing malignant tumors. *Cancer Res.* **67**, 2178-2186.

91. Sorensen, J., Sandberg, D., Sandstrom, M., Wennborg, A., Feldwisch, J., Tolmachev, V., Astrom, G., Lubberink, M., Garske-Roman, U., Carlsson, J., and Lindman, H. (2014) First-in-Human molecular imaging of HER2 expression in breast cancer metastases using the In-111-ABY-025 affibody molecule. *J. Nucl. Med.* **55**, 730-735.

92. Sandstrom, M., Lindskog, K., Velikyan, I., Wennborg, A., Feldwisch, J., Sandberg, D., Tolmachev, V., Orlova, A., Sorensen, J., Carlsson, J., Lindman, H., and Lubberink, M. (2016) Biodistribution and radiation dosimetry of the Anti-HER2 affibody molecule Ga-68-ABY-025 in breast cancer patients. *J. Nucl. Med.* **57**, 867-871.

93. Sorensen, J., Velikyan, I., Sandberg, D., Wennborg, A., Feldwisch, J., Tolmachev, V., Orlova, A., Sandstrom, M., Lubberink, M., Olofsson, H., Carlsson, J., and Lindman, H. (2016) Measuring HER2-Receptor expression in metastatic breast cancer using Ga-68 ABY-025 affibody PET/CT. *Theranostics* **6**, 262-271.

94. Baum, R. P., Prasad, V., Mueller, D., Schuchardt, C., Orlova, A., Wennborg, A., Tolmachev, V., and Feldwisch, J. (2010) Molecular imaging of HER2-expressing malignant tumors in breast cancer patients using synthetic In-111- or Ga-68-Labeled Affibody Molecules. *J. Nucl. Med.* **51**, 892-897.

95. Schuhmacher, J., Kaul, S., Klivenyi, G., Junkermann, H., Magener, A., Henze, M., Doll, J., Haberkorn, U., Amelung, F., and Bastert, G. (2001) Immunoscintigraphy with positron emission tomography: Gallium-68 chelate imaging of breast cancer pretargeted with bispecific anti-MUC1/anti-Ga chelate antibodies. *Cancer Res.* **61**, 3712-3717.

96. Schoffelen, R., Sharkey, R. M., Goldenberg, D. M., Franssen, G., McBride, W. J., Rossi, E. A., Chang, C. H., Laverman, P., Disselhorst, J. A., Eek, A., van der Graaf, W. T. A., Oyen, W. J. G., and Boerman, O. C. (2010) Pretargeted Immuno-Positron Emission Tomography imaging of carcinoembryonic antigen-expressing tumors with a bispecific antibody and a Ga-68- and F-18-Labeled hapten peptide in mice with human tumor xenografts. *Mol. Cancer Ther.* **9**, 1019-1027.

97. Bodet-Milin, C., Faivre-Chauvet, A., Carlier, T., Rauscher, A., Bourgeois, M., Cerato, E., Rohmer, V., Couturier, O., Drui, D., Goldenberg, D. M., Sharkey, R. M., Barbet, J., and Kraeber-Bodere, F. (2016) Immuno-PET using anticarcinoembryonic antigen bispecific antibody and Ga-68-labeled peptide in metastatic medullary thyroid carcinoma: clinical optimization of the pretargeting parameters in a first-in-human trial. *J. Nucl. Med.* **57**, 1505-1511.

98. Baba, S., Abe, K., Isoda, T., Maruoka, Y., Sasaki, M., and Honda, H. (2011) Impact of FDG-PET/CT in the management of lymphoma. *Ann. Nucl. Med.* **25**, 701-716.

99. Hung, B. T., Wang, P. W., Su, Y. J., Huang, W. C., Chang, Y. H., Huang, S. H., and Chang, C. C. (2017) The efficacy of F-18-FDG PET/CT and Ga-67 SPECT/CT in diagnosing fever of unknown origin. *Int. J. Infect. Dis.* **62**, 10-17.

100. Kouranos, V., Wells, A. U., Sharma, R., Underwood, S. R., and Wechalekar, K. (2015) Advances in radionuclide imaging of cardiac sarcoidosis. *Br. Med. Bull.* **115**, 151-163.

101. Seam, P., Juweid, M. E., and Cheson, B. D. (2007) The role of FDG-PET scans in patients with lymphoma. *Blood* **110**, 3507-3516.

102. Vorster, M., Maes, A., van de Wiele, C., and Sathekge, M. (2016) Gallium-68 PET: a powerful generator-based alternative to infection and inflammation imaging. *Semin. Nucl. Med.* **46**, 436-447.

103. Signore, A., Soroa, V. E., and De Vries, E. E. J. (2009) Radiolabelled white blood cells or FDG for imaging of inflammation and infection? *Q. J. Nucl. Med. Mol. Imaging* **53**, 23-25.

104. Graham, F., Lord, M., Froment, D., Cardinal, H., and Bollee, G. (2016) The use of gallium-67 scintigraphy in the diagnosis of acute interstitial nephritis. *Clin. Kidney J.* **9**, 76-81.

105. Yeh, J. J., Huang, Y. C., Teng, W. B., Huang, Y. F., Chuang, Y. W., and Hsu, C. C. (2011) The role of gallium-67 scintigraphy in comparing inflammatory activity between tuberculous and nontuberculous mycobacterial pulmonary diseases. *Nucl. Med. Commun.* **32**, 392-401.

106. Hsu, C. C., Huang, Y. C., Chuang, Y. W., Lee, T. L., and Yeh, J. J. (2012) Association between gallium-67 uptake by lung foci and sputum smear status in patients with pulmonary tuberculosis. *Nucl. Med. Commun.* **33**, 941-946.

107. Chen, W. C., Tsai, K. D., Chen, C. H., Lin, M. S., Chen, C. M., Shih, C. M., and Chen, W. (2012) Role of Gallium-67 scintigraphy in the evaluation of occult sepsis in the medical ICU. *Intern. Emerg. Med.* **7**, 53-58.

108. Rizzello, A., Di Pierro, D., Lodi, F., Trespidi, S., Cicoria, G., Pancaldi, D., Nanni, C., Marengo, M., Marzola, M. C., Ai-Nahhas, A., Rubello, D., and Boschi, S. (2009) Synthesis and quality control of Ga-68 citrate for routine clinical PET. *Nucl. Med. Commun.* **30**, 542-545.

109. Nanni, C., Errani, C., Boriani, L., Fantini, L., Ambrosini, V., Boschi, S., Rubello, D., Pettinato, C., Mercuri, M., Gasbarrini, A., and Fanti, S. (2010) Ga-68-citrate PET/CT for evaluating patients with infections of the bone: preliminary results. *J. Nucl. Med.* **51**, 1932-1936.

110. Vorster, M., Maes, A., Jacobs, A., Malefahlo, S., Pottel, H., Van de Wiele, C., and Sathekge, M. M. (2014) Evaluating the possible role of Ga-68-citrate PET/CT in the characterization of indeterminate lung lesions. *Ann. Nucl. Med.* **28**, 523-530.

111. Behr, S. C., Aggarwal, R., Seo, Y., Aparici, C. M., Chang, E., Gao, K. T., Tao, D. H., Small, E. J., and Evans, M. J. (2016) A feasibility study showing Ga-68 citrate PET detects prostate cancer. *Mol. Imaging Biol.* **18**, 946-951.

112. Mintun, M. A., Dennis, D. R., Welch, M. J., Mathias, C. J., and Schuster, D. P. (1987) Measurements of pulmonary vascular-permeability with PET and Ga-68 transferrin. *J. Nucl. Med.* **28**, 1704-1716.

113. Schuster, D. P., Stark, T., Stephenson, J., and Royal, H. (2002) Detecting lung injury in patients with pulmonary edema. *Intensive Care Med.* **28**, 1246-1253.

114. Hofman, M. S., Beauregard, J.-M., Barber, T., Neels, O. C., Eu, P., and Hicks, R. J. (2011) Ga-68 PET/CT ventilation-perfusion imaging for pulmonary embolism: a pilot study with comparison to conventional scintigraphy. *J. Nucl. Med.* **52**, 1513-1519.

115. Ament, S. J., Maus, S., Reber, H., Buchholz, H. G., Bausbacher, N., Brochhausen, C., Graf, F., Miederer, M., and Schreckenberger, M. (2013) PET lung ventilation/perfusion imaging using ^{68}Ga aerosol (Galligas) and ^{68}Ga-labeled macroaggregated albumin. *Recent Results Cancer Res.* **194**, 395-423.

116. Kotzerke, J., Andreeff, M., and Wunderlich, G. (2010) PET aerosol lung scintigraphy using Galligas. *Eur. J. Nucl. Med. Mol. Imaging* **37**, 175-177.

117. Pozzilli, C., Bernardi, S., Mansi, L., Picozzi, P., Iannotti, F., Alfano, B., Bozzao, L., Lenzi, G. L., Salvatore, M., Conforti, P., and Fieschi, C. (1988) Quantitative assessment of blood-brain-barrier permeability in multiple-sclerosis using ^{68}Ga-EDTA and positron emission tomography. *J. Neurol. Neurosurg. Psychiatry* **51**, 1058-1062.

118. Vorster, M., Maes, A., Van deWiele, C., and Sathekge, M. (2013) Gallium-68: a systematic review of its nononcological applications. *Nucl. Med. Commun.* **34**, 834-854.

119. Yamashita, M., Inaba, T., Kawase, Y., Horii, H., Wakita, K., Fujii, R., and Nakahashi, H. (1988) Quantitative measurement of renal-function using GA-68-EDTA. *Tohoku J. Exp. Med.* **155**, 207-208.

120. Hofman, M., Binns, D., Johnston, V., Siva, S., Thompson, M., Eu, P., Collins, M., and Hicks, R. J. (2015) Ga-68-EDTA PET/CT imaging and plasma clearance for glomerular filtration rate quantification: comparison to conventional Cr-51-EDTA. *J. Nucl. Med.* **56**, 405-409.

121. Hofman, M. S., and Hicks, R. J. (2016) Gallium-68 EDTA PET/CT for renal imaging. *Semin. Nucl. Med.* **46**, 448-461.

122. Velikyan, I. (2014) Prospective of Ga-68-radiopharmaceutical development. *Theranostics* **4**, 47-80.

123. Blom, E., Velikyan, I., Monazzam, A., Razifar, P., Nair, M., Razifar, P., Vanderheyden, J. L., Krivoshein, A. V., Backer, M., Backer, J., and Langstrom, B. (2011) Synthesis and characterization of scVEGF-PEG- Ga-68 NOTA and scVEGF-PEG- Ga-68 DOTA PET tracers. *J. Label. Compd. Radiopharm.* **54**, 685-692.

124. Kang, C. M., Koo, H. J., Choe, Y. S., Choi, J. Y., Lee, K. H., and Kim, B. T. (2014) Ga-68-NODAGA-VEGF(121) for in vivo imaging of VEGF receptor expression. *Nucl. Med. Biol.* **41**, 51-57.

125. Vosjan, M. J. W. D., Perk, L. R., Roovers, R. C., Visser, G. W. M., Stigter-van Walsum, M., Henegouwen, P. M. P. v. B. E., and van Dongen, G. A. M. S. (2011) Facile labelling of an anti-epidermal growth factor receptor Nanobody with Ga-68 via a novel bifunctional desferal chelate for immuno-PET. *Eur. J. Nucl. Med. Mol. Imaging* **38**, 753-763.

126. Brand, C., Longo, V. A., Groaning, M., Weber, W. A., and Reiner, T. (2017) Development of a new folate-derived Ga-68-Based PET imaging agent. *Mol. Imaging Biol.* **19**, 754-761.

127. Maschauer, S., Einsiedel, J., Hubner, H., Gmeiner, P., and Prante, O. (2016) F-18- and Ga-68-labeled neurotensin peptides for PET imaging of neurotensin receptor 1. *J. Med. Chem.* **59**, 6480-6492.

128. Brom, M., Joosten, L., Laverman, P., Oyen, W. J. G., Behe, M., Gotthardt, M., and Boerman, O. C. (2011) Preclinical evaluation of Ga-68-DOTA-minigastrin for the detection of Cholecystokinin-2/Gastrin receptor-positive tumors. *Molecular Imaging* **10**, 144-152.

129. Hoigebazar, L., Jeong, J. M., Hong, M. K., Young, J. K., Lee, J. Y., Shetty, D., Lee, Y. S., Lee, D. S., Chung, J. K., and Lee, M. C. (2011) Synthesis of Ga-68-labeled DOTA-nitroimidazole derivatives and their feasibilities as hypoxia imaging PET tracers. *Bioorganic Med. Chem.* **19**, 2176-2181.

130. Fernandez, S., Dematteis, S., Giglio, J., Cerecetto, H., and Rey, A. (2013) Synthesis, in vitro and in vivo characterization of two novel Ga-68-labelled 5-nitroimidazole derivatives as potential agents for imaging hypoxia. *Nucl. Med. Biol.* **40**, 273-279.

131. Hoigebazar, L., Jeong, J. M., Choi, S. Y., Choi, J. Y., Shetty, D., Lee, Y. S., Lee, D. S., Chung, J. K., Lee, M. C., and Chung, Y. K. (2010) Synthesis and characterization of nitroimidazole derivatives for Ga-68-labeling and testing in tumor xenografted mice. *J. Med. Chem.* **53**, 6378-6385.

132. Seelam, S. R., Lee, J. Y., Lee, Y. S., Hong, M. K., Kim, Y. J., Banka, V. K., Lee, D. S., Chung, J. K., and Jeong, J. M. (2015) Development of Ga-68-labeled multivalent nitroimidazole derivatives for hypoxia imaging. *Bioorganic Med. Chem.* **23**, 7743-7750.

133. Velikyan, I. (2018) Prospective of Ga-68 radionuclide contribution to the development of imaging agents for infection and inflammation. *Contrast Media Mol. Imaging.* (ahead of print, https://doi.org/10.1155/2018/9713691).

134. Roivainen, A., Jalkanen, S., and Nanni, C. (2012) Gallium-labelled peptides for imaging of inflammation. *Eur. J. Nucl. Med. Mol. Imaging* **39**, 68-77.

135. Ebenhan, T., Govender, T., Kruger, G., Pulker, T., Zeevaart, J. R., Sathekge, M. (2012) Synthesis of Ga-68-NOTA-UBI-30-41 and *in vivo* bio-distribution in vervet monkeys towards potential PET/CT imaging of infection. *J. Nucl. Med.* **53** (Suppl),1520.

136. Petrik, M., Haas, H., Laverman, P., Schrettl, M., Franssen, G. M., Blatzer, M., and Decristoforo, C. (2014) Ga-68-Triacetylfusarinine C and Ga-68-Ferrioxamine E for Aspergillus infection imaging: uptake specificity in various microorganisms. *Mol. Imaging Biol.* **16**, 102-108.

137. Velikyan, I., Rosenstrom, U., Estrada, S., Ljungvall, I., Haggstrom, J., Eriksson, O., and Antoni, G. (2014) Synthesis and preclinical evaluation of Ga-68-labeled collagelin analogs for imaging and quantification of fibrosis. *Nucl. Med. Biol.* **41**, 728-736.

138. Velikyan, I., Rosenstrom, U., Bulenga, T. N., Eriksson, O., and Antoni, G. (2016) Feasibility of multiple examinations using Ga-68-labelled collagelin analogues: organ distribution in rat for extrapolation to human organ and whole-body radiation dosimetry. *Pharmaceuticals* **9**.

139. Li, X., Bauer, W. F., Israel, I., Kreissl, M. C., Weirather, J., Richter, D., Bauer, E., Herold, V., Jakob, P., Buck, A., Frantz, S., and Samnick, S. (2014) Targeting P-Selectin by gallium-68-labeled fucoidan positron emission tomography for noninvasive characterization of vulnerable plaques correlation with in vivo 17.6T MRI. *Arterioscler. Thromb. Vasc. Biol.* **34**, 1661-1667.

140. Kawachi, E., Uehara, Y., Hasegawa, K., Yahiro, E., Ando, S., Wada, Y., Yano, T., Nishikawa, H., Shiomi, M., Miura, S.-i., Watanabe, Y., and Saku, K. (2013) Novel molecular imaging of atherosclerosis with gallium-68-labeled apolipoprotein A-I mimetic peptide and positron emission tomography. *Circ. J.* **77**, 1482-1489.

141. Hart, M. M., and Adamson, R. H. (1971) Antitumor activity and toxicity of salts of inorganic group IIIa metals - aluminum, gallium, indium, and thallium. *Proc. Natl. Acad. Sci. U.S.A* **68**, 1623-1626.

142. Chitambar, C. R., and Seligman, P. A. (1986) Effects of different transferrin forms on transferrin receptor expression, iron uptake, and cellular proliferation of human-leukemic HL60 cells - mechanisms responsible for the specific cytotoxicity of transferrin-gallium. *J. Clin. Investig.* **78**, 1538-1546.

143. Chitambar, C. R., Matthaeus, W. G., Antholine, W. E., Graff, K., and Obrien, W. J. (1988) Inhibition of leukemic HL60 cell-growth by transferrin-gallium - effects on ribonucleotide reductase and demonstration of drug synergy with hydroxyurea. *Blood* **72**, 1930-1936.

144. Chitambar, C. R. (2010) Medical Applications and Toxicities of Gallium Compounds. *Int. J. Environ. Res. Public Health* **7**, 2337-2361.

145. Bernstein, L. R., Tanner, T., Godfrey, C., and Noll, B. (2000) Chemistry and pharmacokinetics of gallium maltolate, a compound with high oral gallium bioavailability. *Met. Based Drugs* **7**, 33-47.

146. Chitambar, C. R. (2012) Gallium-containing anticancer compounds. *Future Med. Chem.* **4**, 1257-1272.

147. Warrell, R. P., Bockman, R. S., Coonley, C. J., Isaacs, M., and Staszewski, H. (1984) Gallium nitrate inhibits calcium resorption from bone and is effective treatment for cancer-related hypercalcemia. *J. Clin. Investig.* **73**, 1487-1490.

148. Maxton, D. G., Thompson, R. P. H., and Hider, R. C. (1994) Absorption of iron from ferric hydroxypyranone complexes. *British Journal of Nutrition* **71**, 203-207.

149. Chitambar, C. R., Purpi, D. P., Woodliff, J., Yang, M. Y., and Wereley, J. P. (2007) Development of gallium compounds for treatment of lymphoma: Gallium maltolate, a novel hydroxypyrone gallium compound, induces apoptosis and circumvents lymphoma cell resistance to gallium nitrate. *J. Pharmacol. Exp. Ther.* **322**, 1228-1236.

150. Bernstein, L. R., van der Hoeven, J. J. M., and Boer, R. O. (2011) Hepatocellular Carcinoma Detection by Gallium Scan and Subsequent Treatment by Gallium Maltolate: Rationale and Case Study. *AntiCancer Agents Med. Chem.* **11**, 585-590.
151. Yano, Y., Budinger, T. F., Ebbe, S. N., Mathis, C. A., Singh, M., Brennan, K. M., and Moyer, B. R. (1985) Ga-68 lipophilic complexes for labeling platelets. *J. Nucl. Med.* **26**, 1429-1437.
152. Rudnev, A. V., Foteeva, L. S., Kowol, C., Berger, R., Jakupec, M. A., Arion, V. B., Timerbaev, A. R., and Keppler, B. K. (2006) Preclinical characterization of anticancer gallium(III) complexes: Solubility, stability, lipophilicity and binding to serum proteins. *J. Inorg. Biochem.* **100**, 1819-1826.
153. Enyedy, E. A., Doemoetoer, O., Bali, K., Hetenyi, A., Tuccinardi, T., and Keppler, B. K. (2015) Interaction of the anticancer gallium(III) complexes of 8-hydroxyquinoline and maltol with human serum proteins. *J. Biol. Inorg. Chem.* **20**, 77-88.
154. Ossipov, K., Foteeva, L. S., Seregina, I. F., Perevalov, S. A., Timerbaev, A. R., and Bolshov, M. A. (2013) Metallomics for drug development: Serum protein binding and analysis of an anticancer tris(8-quinolinolato)gallium(III) drug using inductively coupled plasma mass spectrometry. *Anal. Chim. Acta* **785**, 22-26.
155. Enyedy, E. A., Doemoetoer, O., Varga, E., Kiss, L., Trondl, R., Hartinger, C. G., and Keppler, B. K. (2012) Comparative solution equilibrium studies of anticancer gallium(III) complexes of 8-hydroxyquinoline and hydroxy(thio)pyrone ligands. *J. Inorg. Biochem.* **117**, 189-197.
156. Hummer, A. A., Bartel, C., Arion, V. B., Jakupec, M. A., Meyer-Klaucke, W., Geraki, T., Quinn, P. D., Mijovilovich, A., Keppler, B. K., and Rompel, A. (2012) X-ray absorption spectroscopy of an investigational anticancer gallium(III) drug: interaction with serum proteins, elemental distribution pattern, and coordination of the compound in tissue. *J. Med. Chem.* **55**, 5601-5613.
157. Groessl, M., Bytzek, A., and Hartinger, C. G. (2009) The serum protein binding of pharmacologically active gallium(III) compounds assessed by hyphenated CE-MS techniques. *Electrophoresis* **30**, 2720-2727.
158. Timerbaev, A. R. (2009) Advances in developing tris(8-quinolinolato)gallium(III) as an anticancer drug: critical appraisal and prospects. *Metallomics* **1**, 193-198.
159. Gogna, R., Madan, E., Keppler, B., and Pati, U. (2012) Gallium compound GaQ3-induced Ca^{2+} signalling triggers p53-dependent and -independent apoptosis in cancer cells. *Br. J. Pharmacol.* **166**, 617-636.
160. Collery, P., Jakupec, M. A., Kynast, B., and Keppler, B. K. (2006) Preclinical and early clinical development of the antitumor gallium complex KP46 (FFC11). in *Metal Ions in Biology and Medicine, Vol 9* (Editors: Alpoim, M. C., and Morais, P. V.). pp 521-524.
161. Hofheinz, R. D., Dittrich, C., Jakupec, M. A., Drescher, A., Jaehde, U., Gneist, M., Graf von Keyserlingk, N., Keppler, B. K., and Hochhaus, A. (2005) Early results from a phase I study on orally administered tris(8-quinolinolato)gallium(III) (FFC11, KP46) in patients with solid tumors--a CESAR study (Central European Society for Anticancer Drug Research--EWIV). *Int. J. Clin. Pharmacol. Ther.* **43**, 590-591.
162. Schmidbaur, H., Lettenbauer, J., Wilkinson, D. L., Muller, G., and Kumberger, O. (1991) Model systems for gallium extraction .1. structure and molecular-dynamics of aluminum and gallium tris(oxinates). *Z. Naturforsch. B Chem. Sci.* **46**, 901-911.

3 Design of novel *tris*(hydroxypyridinone) ligands and evaluation of their chemical properties.

3.1 Introduction

The *tris*(hydroxypyridinone) ligand THP^{Me}, developed by our group, has proven extremely successful for ^{68}Ga radiolabelling, achieving quantitative radiochemical yield in mild conditions and at low ligand concentration [1]. The ease of radiolabelling combined with a good (> 95 %) radiochemical purity obtained without eluate pre-processing or purification of the radiolabelled compound renders THP^{Me} a valuable candidate for the development of kit-based ^{68}Ga radiopharmaceuticals. Indeed, one such radiopharmaceutical (THP^{Me}-PSMA) is now commercially available and in clinical use for prostate cancer scanning [2].

Interestingly, the outstanding chelating ability of THP^{Me} for ^{68}Ga binding does not extend to other radiometals. Our group has previously demonstrated the instability of ^{89}Zr-THP^{Me} in animal models compared to ^{89}Zr-DFO [3] and *in vitro* investigations using different radiometals such as ^{213}Bi, ^{177}Lu and ^{111}In led to similar results (unpublished data). While the selectivity of THP^{Me} for gallium is certainly a limitation of our chelator in terms of the development of theranostic agents, it can also be advantageous when considering contamination from adventitious metals. In particular, owing to the very low concentration of ^{68}Ga^{3+} in the generator eluate, contamination from adventitious metal ions is an important caveat to ^{68}Ga radiolabelling. Therefore, preference for Ga^{3+} over other metal ions that may be present as contaminants in the ^{68}Ga eluate or in the radiolabelling equipment is a crucial feature of gallium chelators, and necessary to obtain radiotracers with high specific activity. Because *tris*(hydroxypyridinone) ligands were originally developed as iron chelators and the THP^{Me} structure has been optimised for Fe^{3+} binding [4], iron is the most critical contaminant for THP-based chelators. Selectivity for gallium(III) over iron(III) is all the more important since iron contamination is ubiquitous in syringe needles, vials and other equipment employed for radiolabelling.

In the last five years, bifunctional derivatives of THP^{Me} have been conjugated with several peptides to obtain radiotracers that specifically target receptors overexpressed in various diseases, enabling *in vivo* ^{68}Ga PET imaging. Conjugation of both THP^{Me}-NCS and THP^{Me}-Ph-NCS with cyclic-(RGDfK) provided an $\alpha_V\beta_3$ integrin targeting tracers

(Figure 3.1). These were evaluated in mice bearing U87MG glioblastoma xenografts, obtaining results comparable to other ^{68}Ga-based RGD tracers, although higher liver uptake was observed, especially for the THP[Me]-Ph-NCS derivative [5]. Extension of the tripodal scaffold to include three THP[Me] units and/or three RGD peptides was also performed [6] to obtain THP[Me]-Ph-NCS-RGD$_3$ and THP[Me]$_3$-Ph-NCS-RGD$_3$ (**Figure 3.1**). Unexpectedly these multimeric tracers did not show any significant improvement in the affinity for the $\alpha_v\beta_3$ receptor. On the other hand, they exhibited increased tumour accumulation (expresses as % ID/g) compared to THP-c(RGDfk), likely due to a slower blood clearance. For the dendritic tracer THP[Me]$_3$-Ph-NCS-RGD$_3$, increased specific activity was also obtained.

THP[Me]-Ph-NCS-RGD

THP[Me]-NCS-RGD

THP[Me]-Ph-NCS-RGD$_3$
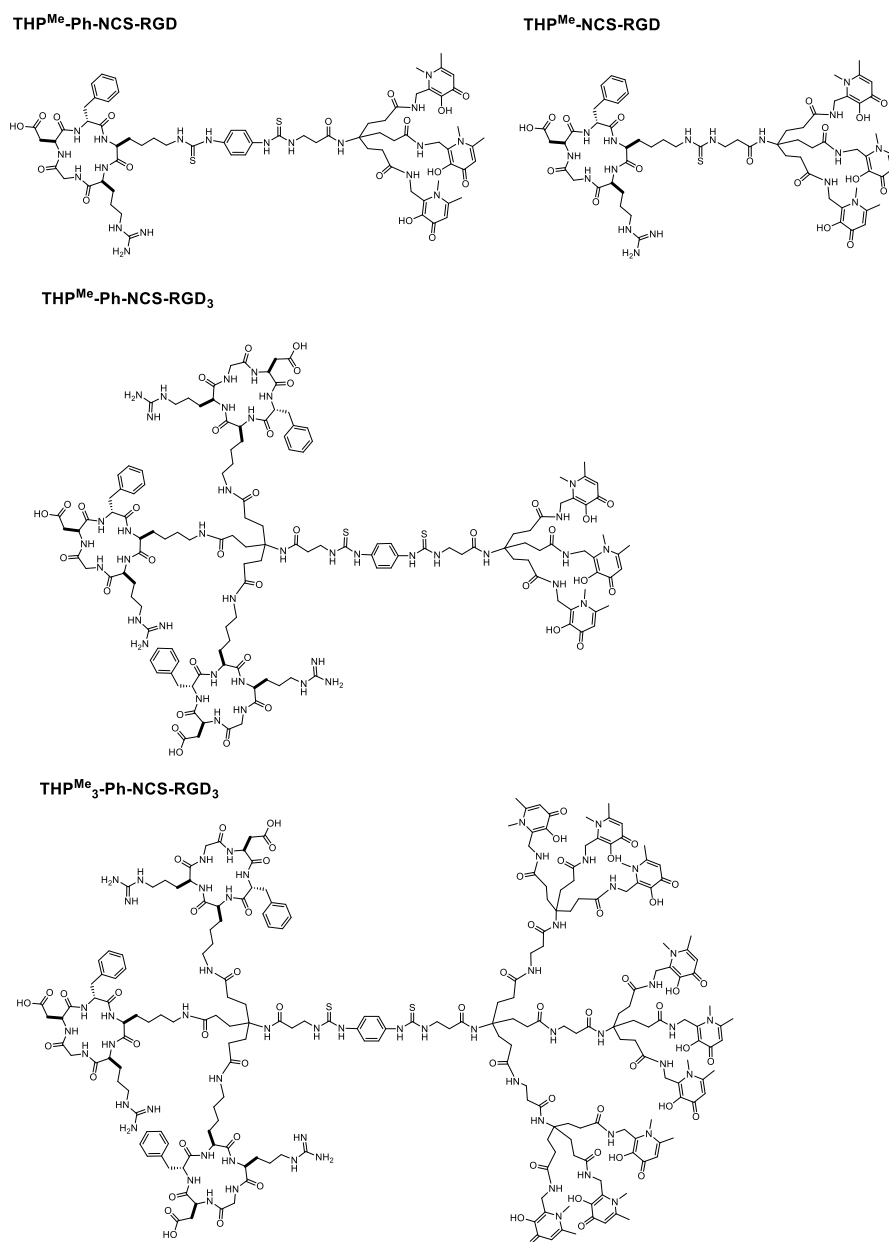
THP[Me]$_3$-Ph-NCS-RGD$_3$

Figure 3.1. *Structures of different THP[Me] derivatives conjugated to RGD peptides [5], including the dendrimeric derivative THP[Me]$_3$-Ph-NCS-RGD$_3$ [6].*

A THP^{Me}-TATE derivative was produced by conjugation of THP^{Me}-NCS with a PEGylated TATE peptide H-PEG$_2$-D-Phe-Cys-Tyr-D-Trp-Lys-Thr-Cys-Thr-OH [7] (**Figure 3.2**). Evaluation of THP^{Me}-TATE and DOTA-TATE in mice bearing AR42J xenografts showed comparable tumour uptake for both tracers, however a higher tumour-to-blood ratio was observed for the DOTA derivative. Finally, conjugation of a glutaric acid derivative with the PSMA moiety resulted in THP^{Me}-PSMA (**Figure 3.2**) which, despite lower affinity for the target receptor compared to the HBED derivative PSMA11, showed similar results in preclinical evaluation [8] and after a successful phase I trial [2] is now undergoing phase II multicentre clinical trials.

THP^{Me}-TATE
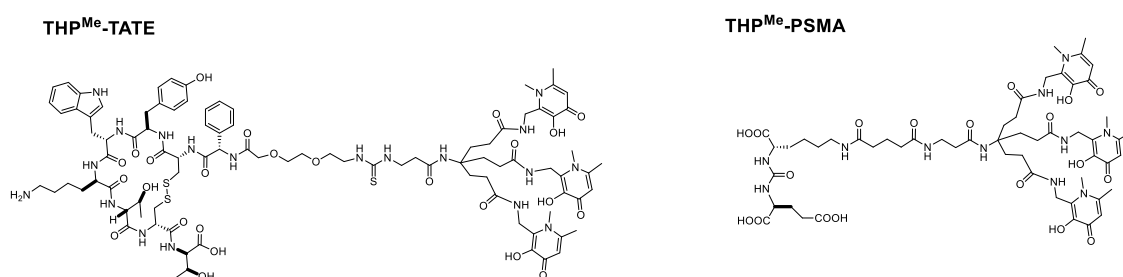
THP^{Me}-PSMA

Figure 3.2. *Structure of THP^{Me} derivatives of TATE and PSMA peptides [7,8] THP^{Me}-PSMA is currently undergoing phase II clinical trials.*

Notably, different THP^{Me}-based tracers have shown different affinity for their target receptors and variable capability to provide good tumour to non-target organ ratio. This can be partially attributed to the different linkers that have been used for the different radiotracers, but also suggests that imaging of different targets may benefit from chelators with different properties even when the targeting vector is well-established. The radiometallic complex itself is not simply a passive spectator of the peptide-receptor interaction, but plays an important role in determining the affinity of a radiotracer for its target receptors and the pharmacokinetics. This has been exquisitely illustrated by Maecke and co-workers, who compared SSTR2 agonists/antagonists attached to different chelators and radiometals (or no radiometal at all) in their affinity for SSTR2 receptors [9-11].

Based on this consideration, it is important to optimise a chelator system for different radiometals/imaging applications. In the case of THP derivatives, this includes modification of the linker, of the tripodal scaffold or of the hydroxypyridinone units, to optimise target affinity, pharmacokinetics and Ga^{3+} affinity and selectivity. While several linkers for THP have been developed, optimisation of the tripodal structures and of the hydroxypyridinone unit has so far been neglected. In this chapter, the synthesis of a new *tris*(hydroxypyridinone) chelator THP^H is described where the hydroxypyridinone unit has been modified to include a N^1-H group in place of the N^1-

CH$_3$ group. The benzylated *tris*(hydroxypyranone) BnTHPO is also described as a promising key intermediate in the synthesis of a library of THP and THPO chelators with different hydroxypyridinone units.

3.2 Materials and methods

3.2.1 Equipment and consumables

Chemicals were obtained from Sigma Aldrich, unless otherwise specified, and used without further purification.

^{1}H, ^{13}C and ^{71}Ga NMR spectra were acquired on Bruker Advance 400 MHz spectrometers (Bruker, Germany) equipped with either a 5 mm QNP probe or a 5 mm BBO probe at 298 K. Additional ^{1}H NMR spectra were acquired on a Bruker Advance 700 MHz spectrometer (Bruker, Germany) equipped with a 5 mm QNP probe. Chemical shifts are referenced to the appropriate solvent peak. Positive ion mode mass spectra were recorded using an Agilent 6510 QTOF spectrometer. Analytical reverse-phase LC-MS were acquired on a Thermo Scientific Exactive Orbitrap Mass Spectrometer coupled to a Thermo Scientific Accela Pump with CTC Autosampler, using a ThermoFisher HyperSil GOLD column (2.1 x 150 mm, 5 μm) with a 0.2 mL min^{-1} flow rate. Data were acquired and reference mass-corrected *via* a dual-spray electrospray ionisation source, using the factory-defined calibration procedure.

Semi-preparative High-performance liquid chromatography (HPLC) was carried out using an Agilent Eclipse XDB-C18 column (9.4 x 250 mm, 5 µm) with a 3 mL/min flow rate and UV detection at 214 nm on an Agilent 1200 LC system. Mobile phase A contained water with 0.1 % trifluoracetic acid (TFA), mobile phase B contained acetonitrile with 0.1 % TFA. For **method 1**, concentration of B increased from 0 to 100 % at a rate of 1 %/min. For **method 2**, concentration of B increased from 20 % to 100 % in 100 min. Analytical reverse-phase HPLC was performed on the same system using an Agilent Eclipse XDB-C18 column (4.6 x 150 mm, 5 µm) with a 1 mL/min flow rate and UV detection at 214 or 254 nM coupled to a LabLogic Flow-Count detector with a sodium iodide probe (B-FC-3200). For **methods 3** and **4**, UV detection was set at 254 nm and isocratic gradient were used with 10 % B and 15 % B, respectively. For **methods 5** and **6** UV detection was set at 214 nm and gradients included 5 min of equilibration at 0 % B at the start of the run. For **method 5** concentration of B increased from 0 % (at 5 min) to 45 % (at 15 min) and subsequently decreased to 0 (at 20 min). For **method 6** % B increased from 0 % (at 5 min) to 75 % (15 min) and back to 0 % (20 min). Size-exclusion chromatography was conducted using a BioSep SEC-s2000 column (145 Å, 300 x 7.8 mm, 5 µm) with a flow rate of 1 mL/min and the mobile phase was PBS or PBS + 50 mM EDTA.

^{68}Ga was obtained from an Eckert & Ziegler ^{68}Ge/^{68}Ga generator that was eluted with high-purity 0.1 M HCl (Fluka). ^{67}Ga-chloride (0.1 M HCl) was obtained by Nordion.

Instant thin layer chromatography strips (iTLC-SG, Varian Medical Systems) were run in two different mobile phases (**mobile phase 1**: 0.1 M citrate pH 5, **mobile phase 2**: 50:50 ammonium acetate (2 M):methanol) and visualised using a Cyclone Plus Phosphor Imager (Perkin Elmer) and a Raytest Rita-Star TLC scanner.

3.2.2 Synthesis

Compound **1** (2-hydroxymethyl-3-benzyloxy-6-methyl-pyran-4(1H)-one, **Figure 3.3**) and the tripodal acid **TA** (4-acetamido-4-(2-carboxyethyl)heptanedioic acid, **Figure 3.3**) were synthesised following established procedures [4,12]. In particular, compound **1** was synthesised from Kojic acid (Alfa Aesar) in four steps with an overall yield of 16 %. **TA** was synthesised in two steps from di-tert-butyl 4-Amino-4-[2-(tert-butoxycarbonyl)ethyl]-heptanedioate available in the laboratory with an overall yield of 35 %.

1   **TA**
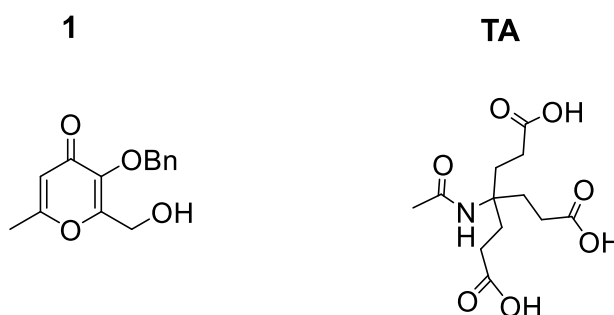
Figure 3.3. *Structures of the synthetic precursors 2-hydroxymethyl-3-benzyloxy-6-methyl-pyran-4(1H)-one (1) and 4-acetamido-4-(2-carboxyethyl)heptanedioic acid (2).*

A detailed synthetic procedure is reported below for the novel compounds, along with their chemical structures and characterisation data. High resolution ESI-MS, ^{1}H NMR and ^{13}C NMR were performed for all new compounds to demonstrate their identity and purity. For each compound, all signals above background are listed.

Synthesis of the *tris*(hydroxypyranone) derivative THPO was performed by the intern Calum Foley under my day-to-day supervision (supervisor: Dr Ma).

Compound 2 (3-benzyloxy-2-hydroxymethyl-6-methylpyridin-4(1*H*)-one)
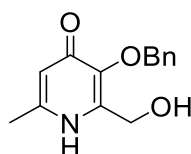
Two different procedures were used for the synthesis of this compound, the first involving protection of the C^2-CH$_2$-OH hydroxyl functionality, the second without it.

Route A: to a solution of **1** (0.245g, 1 mmol) in 1 mL dichloromethane, 3,4-dihydro-2H-pyran (185 μL , 2 mmol) and *p*-toluensulfonic acid monohydrate (6 mg, 0.1 mmol)

were added while stirring at room temperature. After 3 hours, the reaction mixture was washed with 5 % aqueous sodium carbonate (2 x 5 mL) and water (2 x 5 mL). The organic layer was then dried over anhydrous sodium sulfate, evaporated to give a yellow oil which was re-dissolved in 1 mL of ethanol/1 mL of 25 % aqueous ammonia solution (13 mmol). The reaction mixture was sealed in a thick-walled vial and stirred at 70 °C overnight. After removal of the solvent, the residue was re-dissolved in 5 mL ethanol. 1 mL of 2M hydrochloric acid was added and the mixture refluxed for 4 hours, prior to rotary evaporation and addition of 10 mL of water to the brown residue. Washes with diethyl ether (2 x 5 mL) were followed by adjustment of the aqueous phase pH to 11 with a concentrated NaOH solution and addition of NaCl. The aqueous phase was then extracted with ethyl acetate (4 x 15 mL), dried over anhydrous sodium sulfate, and evaporated to give a white solid (0.131 g, 53.5 % yield).

Route B: Compound **1** (1.010 g, 4 mmol) was dissolved in 5 mL of ethanol and sealed in a thick-walled glass vial containing 20 mL of 25 % aqueous ammonia solution. The mixture was stirred at 75 °C overnight. Addition of concentrated HCl to the mixture to reach neutral pH resulted in the precipitation of white crystals (0.609 g, 60.6 % yield), which were collected by filtration and washed with cold water and diethyl ether.

ESI-MS (m/z): 246.12 $[M+H]^+$, calculated: 246.11 for $C_{14}H_{15}NO_3 + H^+$.

^{1}**H NMR** (methanol-*d4,* 400 MHz) δ: 2.33 (s, 3H, C^6-**CH₃**), 4.34 (d, 2H, C^2-**CH₂**-OH), 5.08 (s, 2H, C^3-O-**CH₂**-Ph), 6.33 (s, 1H, **C^5-H** in pyridinone), 7.35 (m, 5H, C^3-O-CH₂-**Ph**).

^{13}**C NMR** (methanol-*d4,* 100 MHz) δ: 18.7 (C^6-**CH₃**), 57.0 (C^2-**CH₂**-OH), 74.6 (C^3-O-**CH₂**-Ph) 117.1 (**C^5-H** in pyridinone), 128.0 (*o*-**CH** in benzyl), 129.4 (*p*-**CH** in benzyl), 130.2 (*m*-**CH** in benzyl), 138.6 (*i*-**C**-CH₂ in benzyl), 143.0 (**C^2** in pyridinone), 144.7 (**C^3** in pyridinone), 147.8 (**C^6** in pyridinone), 176.0 (**C^4** in pyridinone).

Compound 3 (3-benzyloxy-6-methyl-2-phthalimidomethylpyran-4(1*H*)-one)
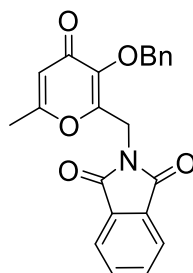
A solution of **1** (1.05 g, 4.0 mmol), triphenylphosphine (1.395 g, 8 mmol) and phthalimide (1.181 g, 8 mmol) in 20 mL dry tetrahydrofuran under nitrogen was cooled to 0 °C and diethyl azodicarboxylate (2 mL, 8 mmol) was added dropwise. The mixture was left stirring overnight, then methanol was added to quench excess diethyl

azodicarboxylate prior to solvent removal by rotary evaporation. The white residue was recrystallised from methanol affording 1.157 g of white crystals (72.3 % yield).

ESI-MS (m/z): 376.11 [M+H]$^+$, calculated: 376.12 for $C_{22}H_{17}NO_5 + H^+$.

^{1}H NMR (DMSO-d^6, 400 MHz) δ: 2.14 (s, 3H, C^6-**CH$_3$**), 4.73 (s, 2H, C^2-**CH$_2$-N**), 5.10 (s, 2H, C^3-O-**CH$_2$-Ph**), 6.26 (s, 1H, **C^5-H** in pyranone), 7.40 (m, 5H, C^3-O-CH$_2$-**Ph**), 7.89 (m, 4H, phthalimide).

^{13}C NMR (DMSO-$d6$, 100 MHz) δ: 19.0 (C^6-**CH$_3$**), 34.4 (C^2-**CH$_2$-N**), 72.9 (C^3-O-**CH$_2$-Ph**), 114.3 (**C^5-H** in pyranone), 123.4 (**C^7-H** and **C^4-H** in phthalimide), 128.2 (*o*-**CH** in benzyl), 128.4 (*p*-**CH** in benzyl), 128.5 (*m*-**CH** in benzyl), 131.4 (**C^5-H** and **C^6-H** in phthalimide), 134.7 (**C^{3a}** and **C^{7a}** in phthalimide), 136.8 (*i*-**C**-CH$_2$ in benzyl), 142.6 (**C^2** in pyranone), 153.9 (**C^3** in pyranone), 165.1 (**C^6** in pyranone) 167.2 (**C**=O in phthalimide), 174.6 (**C^4** pyranone).

Compound 4, BnHP^H (2-aminomethyl-3-benzyloxy-6-methylpyridin-4(1*H*)-one)
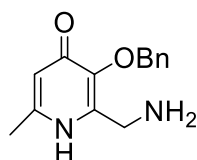
Route A: **3** (264 mg, 0.7 mmol) was dissolved in 6 mL of ethanol under moderate heating in a thick-walled glass vial and allowed to cool to room temperature, whereupon 24 mL of 25 % aqueous ammonia were added, the vial sealed and heated at 75 °C under stirring overnight. ESI-MS analysis of the mixture confirmed product identity ([M+H]$^+$ = 245 m/z). However after solvent removal under vacuum, ESI-MS of the mixture of the brown residue revealed a new principal species ([M+H]$^+$ = 393 m/z) identified as the by-product in **Scheme 3.4**.

Route B: 30 mL of a 7 M methanolic ammonia solution were added to a thick-walled glass vial containing **3** (500 mg, 1.3 mmol). The vial was sealed and heated overnight at 75 °C under stirring. ESI-MS analysis of the mixture confirmed presence of the phtalimido-protected pyridinone ([M+H]$^+$ = 375, **Scheme 3.4**) a as well as some product **4** ([M+H]$^+$= 245). 0.5 mL of aqueous hydrazine was added to the reaction mixture and the solution heated at reflux for 3 hours. ESI-MS of the reaction mixture revealed the presence of the desired product ([M+H]$^+$ = 245). Aqueous hydrazine (55 %, 0.2 mL) was then added to the reaction mixture and the solution heated at reflux for 3 hours. After removal of the solvent by rotary evaporation the brown residue was purified by silica-gel chromatography (dry loading, mobile phase: CH$_2$Cl$_2$:MeOH = 80:20) to afford 317 mg of pure product (45 % yield). Alternatively, reverse-phase solid phase extraction

(SPE) was performed using C18 cartridges (mobile phase: from 0 % to 20 % MeCN + 0.1 % TFA in H_2O + 0.1 % TFA) and the purified product re-dissolved in an 25 % aqueous solution of NH_3 and freeze-dried to obtain the free amine (47 % yield).

ESI-MS (m/z): 245.13 $[M+H]^+$, calculated: 245.13 for $C_{14}H_{16}N_2O_2 + H^+$.

^{1}H NMR (DMSO-*d6*, 400 MHz) δ: 2.20 (s, 3H, C^6-**CH₃**), 3.52 (s, 2H, C^2-**CH₂**-NH₂), 4.49 (broad, 2H, C^2-CH₂-**NH₂**), 5.04 (s, 2H, C^3-O-**CH₂**-Ph), 6.02 (s, 1H, **C^5-H** in pyridinone), 7.35 (m, 5H, C^3-O-CH₂-**Ph**), 8.33 (s, 1H, **N^1-H** in pyridinone).

^{1}H NMR (methanol-*d4*, 400 MHz) δ: 2.33 (s, 3H, C^6-**CH₃**), 3.60 (s, 2H, C^2-**CH₂**-NH₂), 5.14 (s, 2H, C^3-O-**CH₂**-Ph), 6.39 (s, 1H, **C^5-H** in pyridinone), 7.36 (m, 5H, C^3-O-CH₂-**Ph**).

^{13}C NMR (methanol-*d4*, 100 MHz) δ: 19.4 (C^6-**CH₃**), 38.8 (C^2-**CH₂**- NH₂), 74.6 (C^3-O-**CH₂**-Ph) 116.7 (**C^5-H** in pyridinone), 129.6 (*o*-**CH** in benzyl), 129.6 (*p*-**CH** in benzyl), 130.4 (*m*-**CH** in benzyl), 138.5 (*i*-**C**-CH₂ in benzyl) 143.6 (**C^2** in pyridinone), 143.8 (**C^3** in pyridinone), 149.0 (**C^6** in pyridinone), 174.2 (**C^4** in pyridinone).

Compound 5, BnTHP^H

4-acetamido-N^1,N^7-bis((3-(benzyloxy)-6-methyl-4-oxo-1,4-dihydropyridin-2-yl)methyl)-4-(3-(((3-(benzyloxy)-6-methyl-4-oxo-1,4-dihydropyridin-2-yl)methyl)amino)-3-oxopropyl)heptanediamide
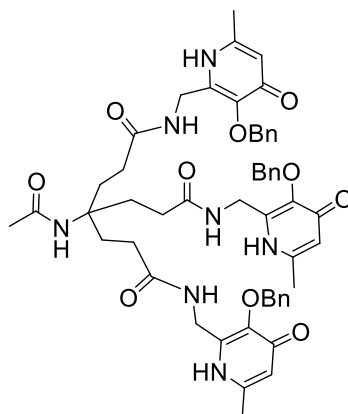
The tripodal acid **TA** (20 mg, 0.07 mmol), hydroxybenzotriazole (HOBT, 32.7 mg, 0.21 mmol) and dicyclohexylcarbodiimide (DCC, 44 mg, 0.21 mmol) were individually dissolved in 500 μL of DMF and then combined under stirring. **BnHP^H** (86 mg, 0.35 mmol) was also dissolved in 500 μL of DMF and added to the mixture which was then stirred at 50 °C for 48 h. Formation of the product over time was monitored *via* LC-MS ($[M+H]^+$= 968 m/z). DMF was removed under high-vacuum and the product purified by silica gel chromatography (eluent CH_3OH:$CHCl_3$ = 20:80 followed by CH_3OH:$CHCl_3$:40 % aqueous NH_3 = 20:80:2) to obtain 37 mg of product (48 % yield).

Observation: when the same reaction was performed in a microwave reactor (30 min, 120 °C) using HATU (80 mg, 0.21 mmol) and N,N-Diisopropylethylamine (DIPEA, 36 μL,

0.21 mmol) as coupling agents, a side product at [M+H]$^+$ = 724 m/z was found (**Scheme 3.7**).

ESI-MS (m/z): 968.45 [M+H]$^+$, 990.44 [M+Na]$^+$, calculated: 968.46 for $C_{54}H_{61}N_7O_{10}$ + H$^+$.

^{1}H NMR (methanol-*d4*, 400 MHz) δ: 1.86 (s, 3H, **CH$_3$**-CO-NH-tripod), 1.88 (m, 6H, CH$_2$-**CH$_2$**-CO-NH-CH$_2$-pyridinone), 2.09 (m, 6H, **CH$_2$**-CH$_2$-CO-NH-CH$_2$-pyridinone), 2.28 (s, 9H, C^6-**CH$_3$**), 4.10 (s, 6H, CO-NH-**CH$_2$**-pyridinone), 5.11 (s, 6H, C^3-O-**CH$_2$**-Ph), 6.31 (s, 3H, **C^5-H** in pyridinone), 7.35 (m, 15H, C^3-O-CH$_2$-**Ph**).

^{13}C NMR (methanol-*d4*, 100 MHz) δ: 18.8 (C^6-**CH$_3$**), 23.6 (**CH$_3$**-CO-NH-tripod), 30.8 (CH$_2$-**CH$_2$**-CO-NH-CH$_2$-pyridinone), 31.0 (**CH$_2$**-CH$_2$-CO-NH-CH$_2$-pyridinone), 37.7 (CH$_2$-CH$_2$-CO-NH-**CH$_2$**-pyridinone), 58.9 (NH**C**-tripod), 74.5 (C^3-O-**CH$_2$**-Ph) 117.3 (**C^5-H** in pyridinone), 129.5 (*p*-**CH** in benzyl), 130.2 (*m*-**CH** in benzyl), 138.5 (*i*-**C**-CH$_2$ in benzyl), 141.4 (**C^2** in pyridinone), 144.8 (**C^3** in pyridinone), 148.0 (**C^6** in pyridinone), 173.0 (**C^4** in pyridinone), 176.1 (CH$_2$-CH$_2$-**CO**-NH-CH$_2$-pyridinone).

Compound 6, THP^H

4-acetamido-N^1,N^7-bis((3-hydroxy-6-methyl-4-oxo-1,4-dihydropyridin-2-yl)methyl)-4-(3-(((3-hydroxy-6-methyl-4-oxo-1,4-dihydropyridin-2-yl)methyl)amino)-3-oxopropyl)heptanediamide
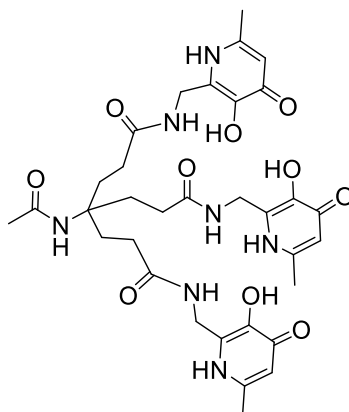
17 mg of **BnTHP^H** (0.018 mmol) were dissolved in the minimum amount of methanol and then diluted to 1 mL with dichloromethane. An excess of BCl$_3$ (3 mL of a 1 M solution in dichloromethane) was added under inert N$_2$ atmosphere. After 2 hours, the vial was placed on ice and an excess of methanol was added to quench excess BCl$_3$. Solvent was removed by rotary evaporation. The residue was then re-dissolved in methanol and precipitation of the product was achieved by addition of cold ether. **THP^H** (hydrochloride salt, 15.6 mg) were obtained (90 % yield).

Observation: BCl$_3$ is extremely toxic and corrosive. To safely add it to the reaction mixture, a PTFE cannula (Cole-Parmer) was used to connect the BCl$_3$ solution and the

reaction vessel, while both were closed and under nitrogen and the solution transferred exploiting a difference in pressure created by adding a vent needle to the reaction vessel.

ESI-MS (m/z): 698.32 [M+H]$^+$, 349.67 [M+2H]$^{2+}$, 233.44 [M+3H]$^{3+}$, calculated: 698.31 for $C_{33}H_{43}N_7O_{10}$+H$^+$.

^{1}H NMR (D$_2$O, 400 MHz) δ: 1.85 (s, 3H, **CH$_3$**-CO-NH-tripod), 1.87 (m, 6H, CH$_2$-**CH$_2$**-CO-NH-CH$_2$-pyridinone), 2.17 (m, 6H, **CH$_2$**-CH$_2$-CO-NH-CH$_2$-pyridinone), 2.47 (s, 9H, C^6-**CH$_3$**), 4.44 (d, 6H, CO-NH-**CH$_2$**-pyridinone), 6.93 (s, 3H, **C^5-H** in pyridinone).

^{13}C NMR (D$_2$O, 100 MHz) δ: 17.9 (C^6-**CH$_3$**), 22.6 (**CH$_3$**-CO-NH-tripod), 28.9 (CH$_2$-**CH$_2$**-CO-NH-CH$_2$-pyridinone), 29.2 (**CH$_2$**-CH$_2$-CO-NH-CH$_2$-pyridinone), 36.6 (CH$_2$-CH$_2$-CO-NH-**CH$_2$**-pyridinone), 58.0 (NH**C**-tripod), 111.7 (**C^5-H** in pyridinone), 136.4 (**C^2** in pyridinone), 140.6 (**C^3** in pyridinone), 146.7 (**C^6** in pyridinone), 160.9 (**C^4** in pyridinone), 173.3 (CH$_3$-**CO**-NH-tripod), 176.4 (CH$_2$-CH$_2$-**CO**-NH-CH$_2$-pyridinone).

HPLC: 10 min, 45 s (method 5, **Figure 3.4**), 3 min 26 s (method 3), only one peak was visible for both HPLC methods utilised thus confirming purity of the product.

Figure 3.4. *UV Chromatogram of THP^H (6) using RP-HPLC method 5.*

Compound 7, BnHPO (2-aminomethyl-3-benzyloxy-6-methylpyran-4(1H)-one)
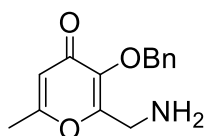
3 (499 mg, 1.33 mmol) was dissolved in 5 mL of ethanol and heated at reflux upon addition of aqueous hydrazine (1.5 mL, 5.5 % aqueous solution). After 3 hours, the pH was adjusted to 1 with concentrated HCl (37 %) and the flask cooled to 0 °C. Phthalhydrazide precipitate was then filtered and the solution evaporated to dryness. The resulting residue was redissolved in water (2 mL) and the pH adjusted to 10 using concentrated NaOH (10 M). The product was then extracted with dichloromethane (4 x 2mL) and the solvent removed by rotary evaporation. The crude product was purified by silica-gel chromatography (dry loading, CH_2Cl_2:MeOH = 90:10) to obtain 90.0 mg of product (28 % yield).

ESI-MS (m/z): 246.11 $[M+H]^+$, calculated: 246.11 for $C_{14}H_{15}NO_3 + H^+$.

^{1}H NMR (methanol-*d4*, 400 MHz) δ: 2.31 (s, 3H, C^6-**CH$_3$**), 3.51 (s, 2H, C^2-**CH$_2$**-NH$_2$), 5.09 (s, 2H, C^3-O-**CH$_2$**-Ph), 6.27 (s, 1H, **C^5-H** in pyranone), 7.37 (m, 5H, C^3-O-CH$_2$-**Ph**).

^{13}C NMR (methanol-*d4*, 400 MHz) δ: 19.5 (C^6-**CH$_3$**), 39.3(C^2-**CH$_2$**- NH$_2$), 74.9 (C^3-O-**CH$_2$**-Ph) 115.0 (**C^5-H** in pyridinone), 129.6 (*o*-**CH** in benzyl), 129.7 (*p*-**CH** in benzyl), 130.4 (*m*-**CH** in benzyl), 137.9 (*i*-**C**-CH$_2$ in benzyl) 142.3 (**C^2** in pyranone), 162.9 (**C^3** in pyranone), 167.9 (**C^6** in pyranone), 178.4 (**C^4** in pyranone).

Compound 8, BnTHPO

4-acetamido-N^1,N^7-bis((3-(benzyloxy)-6-methyl-4-oxo-4*H*-pyran-2-yl)methyl)-4-(3-(((3-(benzyloxy)-6-methyl-4-oxo-4*H*-pyran-2-yl)methyl)amino)-3-oxopropyl)heptanediamide
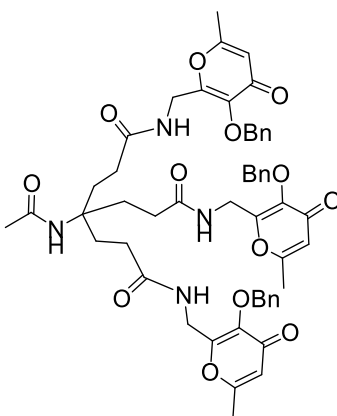
TA (14 mg, 0.049 mmol), DIPEA (25.6 µL, 0.15 mmol) and HATU (55.74 mg, 0.15 mmol) were dissolved in the minimum volume of dimethylacetamide (DMA), combined while stirring and left at room temperature for 1 hour. A DMA solution of **BnHPO** (52 mg, 0.16 mmol) was then added and the mixture left stirring for 72 hours. The DMA was removed under high vacuum and the product was purified using semi-preparative HPLC (method 1) to obtain 34.7 mg of isolated product (73.1 % yield).

ESI-MS (m/z): 486.21 $[M+2H]^{2+}$, 971.41 $[M+H]^+$, 993.38 $[M+Na]^+$, calculated: 971.41 for $C_{54}H_{58}N_4O_{13} + H^+$.

^{1}H NMR (methanol-*d4*, 400 MHz) δ: 1.91 (s, 3H, **CH$_3$**-CONH-tripod), 1.96 (m, 6H, **CH$_2$**-CH$_2$-CONH-CH$_2$-pyranone), 2.17 (m, 6H, **CH$_2$**-CH$_2$-CONH-CH$_2$-pyranone), 2.29 (s, 9H, C^6-**CH$_3$**), 4.23 (s, 6H, CONH-**CH$_2$**-pyranone), 5.12 (s, 6H, C^3-O-**CH$_2$**-Ph), 6.28 (s broad, 3H, **C^5-H** in pyranone), 7.35 (m, 15H, C^3-O-CH$_2$-**Ph**).

^{13}C NMR (methanol-*d4*, 100 MHz) δ: 19.5 (C^6-**CH$_3$**), 23.5 (**CH$_3$**-CO-NH-tripod), 30.9 (**CH$_2$**-CH$_2$-CO-NH-CH$_2$-pyranone), 31.2 (**CH$_2$**-CH$_2$-CO-NH-CH$_2$-pyranone), 37.3 (CH$_2$-CH$_2$-CO-NH-**CH$_2$**-pyranone), 58.9 (NH**C**-tripod), 75.0 (C^3-O-**CH$_2$**-Ph) 115.2 (**C^5-H** in pyridinone), 129.6 (*p*-**CH** in benzyl), 130.2 (*m*-**CH** in benzyl), 138.1 (*i*-**C**-CH$_2$ in benzyl), 143.7 (**C^2** in pyranone), 159.1 (**C^3** in pyranone), 167.9 (**C^6** in pyranone), 172.9 (**C^4** in pyranone), 175.7 (CH$_3$-**CO** 169.4), 178.2 (CH$_2$-CH$_2$-**CO**-NH-CH$_2$-pyridinone).

Compound 9, THPO

4-acetamido-N^1,N^7-bis((3-hydroxy-6-methyl-4-oxo-4H-pyran-2-yl)methyl)-4-(3-(((3-hydroxy-6-methyl-4-oxo-4*H*-pyran-2-yl)methyl)amino)-3-oxopropyl)heptanediamide
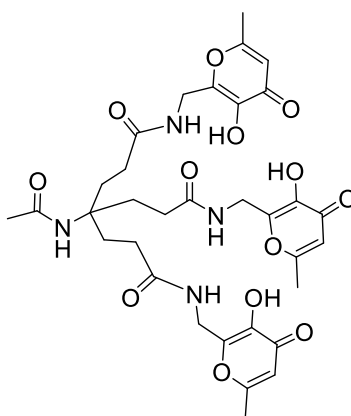
BnTHPO (6.65 mg, 0.0069 mmol) was dissolved in 7:1 = dichloromethane:MeOH (800 µL), BCl$_3$ was added *via* a cannula under N$_2$ atmosphere. After 2 hours, the vial was placed on ice, reaction was quenched with MeOH and solution evaporated under reduced pressure. The residue was dissolved in 60:40 = water:acetonitrile and purified

by preparative HPLC (method 1). 5.6 mg of TFA salt of THPO was recovered in 78 % yield.

ESI-MS (m/z): 702.26 $[M+H]^+$, 723.24 $[M+Na]^+$, 351.13 $[M+2H]^{2+}$. calculated: 701.27 for $C_{33}H_{41}N_4O_{13} + H^+$.

^{1}H NMR (methanol-*d4*, 400 MHz) δ: 1.91 (s, 3H, **CH$_3$**-CO-NH-tripod), 1.99 (t, 6H, CH$_2$-**CH$_2$**-CO-NH-CH$_2$-pyranone), 2.22 (t, 6H, **CH$_2$**-CH$_2$-CO-NH-CH$_2$-pyranone), 2.30 (s, 9H, C^6-**CH$_3$**), 4.40 (d, 6H, CO-NH-**CH$_2$**-pyranone), 6.24 (s, 3H, **C^5-H** in pyranone).

^{13}C NMR (methanol-*d4*, 100 MHz) δ: 19.7 (C^6-**CH$_3$**), 23.5 (**CH$_3$**-CO-NH-tripod), 31.0 (CH$_2$-**CH$_2$**-CO-NH-CH$_2$-pyranone), 31.3 (**CH$_2$**-CH$_2$-CO-NH-CH$_2$-pyranone), 37.3 (CH$_2$-CH$_2$-CO-NH-**CH$_2$**-pyranone), 59.0 (NH**C**-tripod), 112.3 (**C^5-H** in pyranone), 143.5 (**C^2** in pyranone), 148.9 (**C^3** in pyranone), 167.5 (**C^6** in pyranone), 173.0 (**C^4** in pyranone), 176.1 (CH$_3$-**CO**-NH-tripod), 176.4 (CH$_2$-CH$_2$-**CO**-NH-CH$_2$-pyranone).

HPLC: Retention time 11 min, 10 s (method 6, **Figure 3.5**), 4 min 43 s (method 4), only one peak above background was visible for both HPLC methods utilised thus confirming purity of the product.
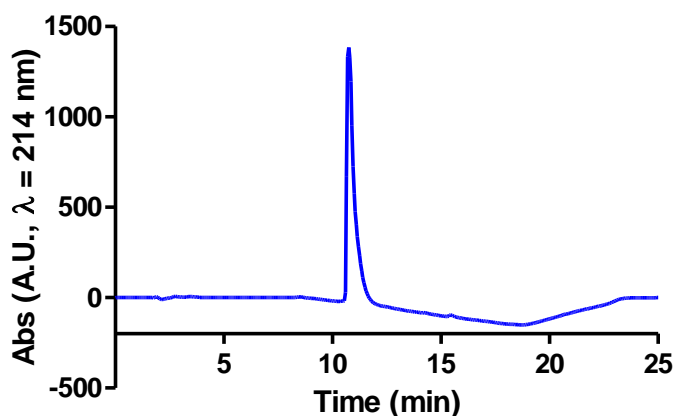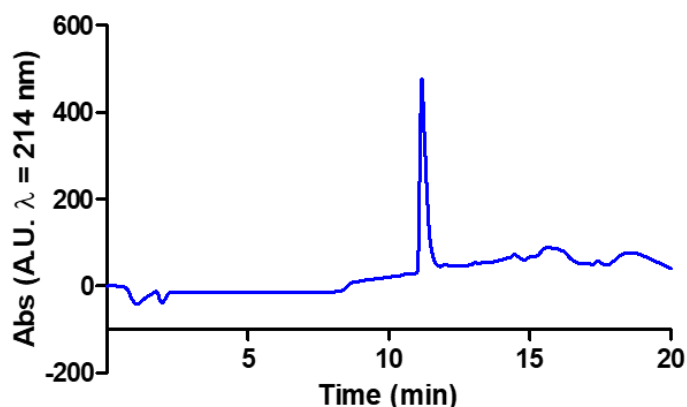

Figure 3.5. *UV Chromatogram of THPO (9) using RP-HPLC method 3.*

BnTHPO to BnTHP^H conversion

11 mL of 7 M ammonia in MeOH were added to 22.4 mg of **BnTHPO** (0.023 mmol) and the mixture stirred at 75 °C under pressure. Monitoring of the reaction *via* LC-MS allowed us to determine that the reaction was complete after 72 hours (mobile phase: A = H$_2$O + 0.1 % formic acid, B = acetonitrile + 0.1 % formic acid; gradient: 0-5 min 100 % A, 5-55 min from 100 % A to 100 % B, flow rate 0.2 mL/min, mass range 900-1100 m/z). The solvent was then removed under reduced pressure and the residue purified by preparative HPLC (method 2). 10.88 mg of product was obtained (49 % yield). Purity of the newly synthesised BnTHP^H was confirmed by ^{1}H NMR and ESI-MS.

3.2.3 Complexation

^{68}Ga Radiolabelling

For all the radiolabelling experiments, elution of an E&Z generator was performed with 5 mL of pure HCl 0.1 M (Fluka), the eluate was fractionated in five 1 mL fractions and their activity measured by a Capintec radionuclide dose calibrator. 100 µL of the highest activity fraction (15-20 MBq) were added to 100 µL of the ligand (concentration range 200-2 µM) in ammonium acetate 0.5 M. Radiolabelling of THP^H and THP^{Me} at 0.1M was performed using a different E&Z generator, eluted with clinical grade 0.1M HCl (E&Z). Verification of the radiolabelling was carried out after 5 min by reverse-phase HPLC (method 3 for THP^H, method 4 for THPO) and iTLC-SG (mobile phase 1 and 2).

Formation of the natural gallium complex

^{nat}Ga complexes of THP^H and THPO were prepared by addition of an aqueous solution of Ga(NO$_3$)$_3$ (5 µL, 2 mg/mL, excess) to a solution of the ligands (50 µL, 150 µM) in ammonium acetate 0.2 M. Reverse-phase HPLC was carried out after 5 min (using the same methods as above) to confirm complex formation.

[Ga(THP^H)] ESI-MS (m/z): 764.22 [M+H]$^+$, 698.32 [M-Ga+3H]$^+$, 382.61 [M+2H]$^{2+}$, 349.66 [M-Ga+4H]$^{2+}$. calcd: 764.22 for C$_{33}$H$_{40}$N$_7$O$_{10}$Ga + H$^+$. No peaks assignable to stoichiometry other than 1:1 were visible.

NMR characterisation of [Ga(THP^H)] complex

600 µL of a 2 mM solution of THP^H in H$_2$O + 10 % D$_2$O was mixed with 12 µL of a 50 mM solution of Ga(NO$_3$)$_3$ in the same solvent system, to obtain a Ga^{3+}/THP^H ratio of ratio of ≈ 1:2 (pH ≈ 2.5). ^{1}H NMR and ^{71}Ga NMR spectra were acquired on a 400 MHz Bruker spectrometer. Further addition of Ga(NO$_3$)$_3$ to obtain a Ga^{3+}/THP^H ratio of ratio of ≈ 1:1 was followed by ^{1}H NMR and ^{71}Ga NMR analysis of the new sample. Attempts to neutralise the pH resulted in sample precipitation.

300 µL of a 2 mM solution of NOTA (CheMatech) in H$_2$O + 10 % D$_2$O and 300 µL of Ga(NO$_3$)$_3$ 2 mM in the same solvent, were mixed (pH ≈ 2.5) and a ^{71}Ga NMR spectrum of the mixture acquired as a comparison.

^{1}H NMR spectrum of THP^H and ^{71}Ga spectrum of Ga(NO$_3$)$_3$ (2 mM in H$_2$O + 10 % D$_2$O, pH 2), were also acquired. The ^{71}Ga NMR spectrum of the Ga(NO$_3$)$_3$ solution showed a single peak attributable to the hexaaqua ion species [Ga(H$_2$O)$_6$]$^{3+}$, which was fixed at 0 ppm as a reference.

3.2.4 Affinity constants measurements by spectrophotometric titration

Spectrometric measurements of affinity constants were performed as a collaboration with Dr Yu-Lin Chen and Prof. Robert C. Hider (KCL).

The automated titration system employed in this study, consisted of an Metrohm 765 Dosimat autoburette, a Mettler Toledo MP230 pH meter with SENTEK pH electrode (P11), and an HP 8453 UV-visible spectrophotometer with a Hellem quartz flow cuvette. Circulation of the test solution between the titration chamber and the cuvette was controlled using Gilson Mini-plus #3 pump (speed capability: 20 mL/min). For pKa determinations, a cuvette path length of 10 mm was used, and for metal complex stability constant determinations, a cuvette path length of 50 mm was used. Analytical grade reagent materials were used in the preparation of all solutions. A potassium chloride electrolyte solution (0.1 M) was used to maintain the ionic strength. Temperature of the test solutions was maintained constant in a thermostatic jacketed titration vessel at 25 °C (± 0.1 °C) using a Fisherbrand Isotemp water bath. Vigorous stirring of the test solution was maintained during all the experiments.

Calibration of the pH electrodes was performed by titration of a volumetric standard HCl (0.1 M) in KCl (0.1 M) with KOH (0.1 M) under an argon gas atmosphere (calibration data were analysed using the software GLEE [33]). The automated titration adopted the following strategy: the pH of a solution was increased by 0.1 pH unit by the addition of potassium hydroxide solution (0.1 M) from the autoburette. The pH readings were judged to be stable if their values varied by less than 0.01 pH unit after a set incubation period. For pKa determinations, an incubation period of 1.5 min was adopted; for metal stability constant determinations, an incubation period of 3 min was adopted. The cycle was repeated until the defined end point pH value was achieved. All the titration data were analysed with the HypSpec2014 program [13,14] (http://www.hyperquad.co.uk/). If recorded pH values were higher than 11.3 (outside the pH range in which electrode measurements are considered accurate), the values were neglected and re-calculated from the added KOH quantity (using "no pH" and "relative weighting scheme" functions of the HypSpec2014 program). The associated hydrolysis constants used in the analysis were collected from Martell's *Critical Stability Constants* [15]. The metal affinity of compounds in this study was determined in competition with the metal hydrolysis species in a solution at a high pH (titrated up to pH 12.5). The speciation plot was calculated with the HYSS program [16].

3.2.5 Lipophilicity determination

Radiolabelling of the chelators THP^{Me}, THP^{H} and THPO (200 µM in ammonium acetate 0.5 M) was performed as described above and verified by means of iTLC-SG. 10 µL of each radiolabelling mixture were then added to vials containing a pre-equilibrated mixture of octanol/water = 500 µL/490 µL (for Log$P$ measurement) or octanol/PBS = 500 µL/490 µL (for Log$D_{7.4}$ measurement), vortexed and then shaken for 30 min before separation of the two phases by centrifugation (2000 RCF, 3 min). The activity present in aliquots of each phase (20 µL aqueous phase, 100 µL octanol phase) was measured in the gamma-counter and corrected for the different volumes considered. Each experiment was repeated 4 times.

3.2.6 Metal competition for THP binding

Standard ICP-MS solutions of gallium (Sigma Aldrich) and iron (Alfa Aesar) in nitric acid were diluted to a final concentration of 2250 µM and 225 µM in 0.1 M nitric acid (Fluka analytical). 20 µL of the 225 µM gallium solution were mixed with 20 µL of the iron solution (225 or 2250 µM Fe, 0.1 M nitric acid as a control) and 20 µL of ^{68}Ga eluate were added (Ga^{3+} concentration in the eluate is ≈ 2nM and was considered negligible). 440 µL of the relevant THP ligand (11.3 µM in 0.5 M ammonium acetate buffer) were added to the radiolabelling mixture (final concentration: [THP] = 10 µM, [Ga^{3+}] ≈ 9 µM, [Fe^{3+}] ≈ 0, 9 or 90 µM). The radiochemical yield at different time points was measured by iTLC-SG (mobile phase 2). Statistical analysis of the data at different time points (unpaired t-test between no Fe and 1 eq. Fe group) was performed.

3.2.7 Ligand competition for ^{68}Ga^{3+} binding

This competition experiment was performed by the Master's degree student Yifu Wang under my supervision. Data analysis was performed entirely by me.

A solution of THP^{Me} and THP^{H}, each 2 mM in D$_2$O was diluted in aqueous ammonium acetate (0.5 M) to a 100 µM solution in each of the ligands. After NMR analysis had confirmed equal concentration of the two compounds, 50 µL of the mixture were mixed with an equal volume of ^{68}Ga eluate. Verification of completed radiolabelling was carried out by iTLC-SG (mobile phase 2). Percentage of activity associated with each compound was measured by iTLC-SG (mobile phase 1) at different time points.

3.2.8 Serum stability of [^{67}Ga(THP^{H})]

50 µL (15 MBq) of ^{67}Ga-chloride, obtained from Nordion (Canada), were mixed with 50 µL of THP^{H} (100 µM) in 0.5 M ammonium acetate. Stability of the compound in serum

was measured using size-exclusion HPLC (mobile phase: PBS + 50 mM EDTA trisodium salt, 1 ml/min, 25 min). EDTA was added to the mobile phase to ensure complete elution of unchelated/non-protein-bound gallium and therefore quantitative measurements of radiochemical yield. Retention times for [^{67}Ga(THP^H)] (15.5 min) and ^{67}Ga-chloride (12.0 min, corresponding to [^{67}Ga(EDTA)] complex) were measured before incubation with serum. 60 μL of each solution were then added to 600 μL of male, AB human serum (Sigma) and incubated at 37 °C. Size-exclusion radiochromatography of both mixtures was performed at 1 hour, 1 day and 8 days of incubation.

3.2.9 *In vivo* biodistribution

Male SCID/beige mice (7 months old, Charles River) were used for the animal studies based on the availability of these mice at the time of the experiment. The choice of this strain is particularly relevant for future studies in a xenograft model, which are likely to be performed using the same strain of mice.

Dynamic PET scanning was performed using a nanoScan® PET/CT (Mediso Medical Imaging Systems) [17] using the following parameters:

- PET: 1:5 coincidence, 5 ns time window, 400-600 keV energy window.
- CT : 180 projection, 45 kVp.

Respiration rate and bed temperature were monitored throughout all scans. PET/CT datasets were reconstructed using the Monte-Carlo based full 3D iterative algorithm Tera-Tomo (Mediso Medical Imaging Systems) [18]. All reconstructed datasets were analysed using VivoQuant 1.21 software (inviCRO).

Mice were anesthetized with isoflurane (O$_2$ flow rate of 1.0-1.5 L/min and isoflurane levels of 2-2.5 %), cannulated at the tail vein using a catheter (25 μL volume) and a CT scan was performed. Subsequently, a PET scan was started and the radiotracer injected *via* a tail vein.

A 37 g mouse was injected with 307 μL of a [^{68}Ga(THP^H)] solution (5 μM, 6.59 MBq) and imaged for 1 hour to verify *in vivo* stability of the radiolabelled complex. A second mouse (33 g) was injected with 100 μL of acetate buffered ^{68}Ga (0.1 M ammonium acetate, 4.68 MBq) while scanning, followed at 30 min by an injection of THP^H (50 μL of a 50 μM solution in PBS). Upon procedure completion, animals were sacrificed by neck dislocation while still anesthetised, the urine collected and analysed by reverse-phase HPLC (method 3).

3.3 Results

3.3.1 Synthesis

A new *tris*(hydroxypyridinone) chelator THP[H], was developed in this work, containing a modified hydroxypyridinone unit in which the N^1-methyl group has been replaced by N^1-H. The pyranone precursor, compound **1** was initially synthesised from Kojic acid in 4 steps as described in the reaction scheme below, following published procedures [12] with an overall yield of 16 %.
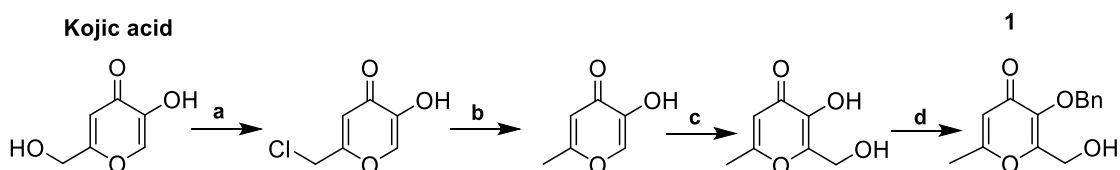
Scheme 3.1 *Precursor **1** synthesis from Kojic acid according to published procedures. (a) $SOCl_2$, 25 °C; (b) Zn/HCl, H_2O, 70 °C; (c) HCHO, NaOH, H_2O, 25 °C; (d) BnBr, NaOH, CH_3OH/H_2O, 70 °C.*

The tripodal acid **TA** was also synthesised following literature [4] procedures from the NH_2-tripodal ester precursor, as in the scheme below. An overall yield of 35 % was obtained.
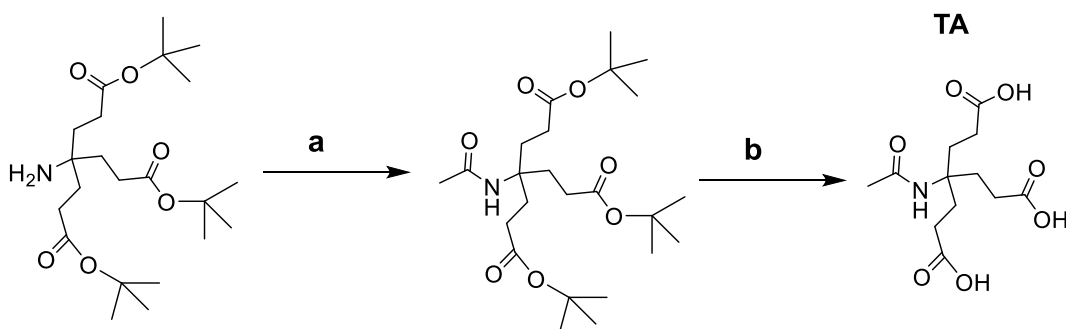
Scheme 3.2. *Synthesis of the tripodal acid **TA** from the NH_2-tripodal ester precursor. (a) CH_3COCl, triethylamine, dichloromethane, 0 °C, (d) formic acid.*

Different strategies were attempted for the synthesis of the new ligand, starting from these common precursors as represented in **Scheme 3.3.**
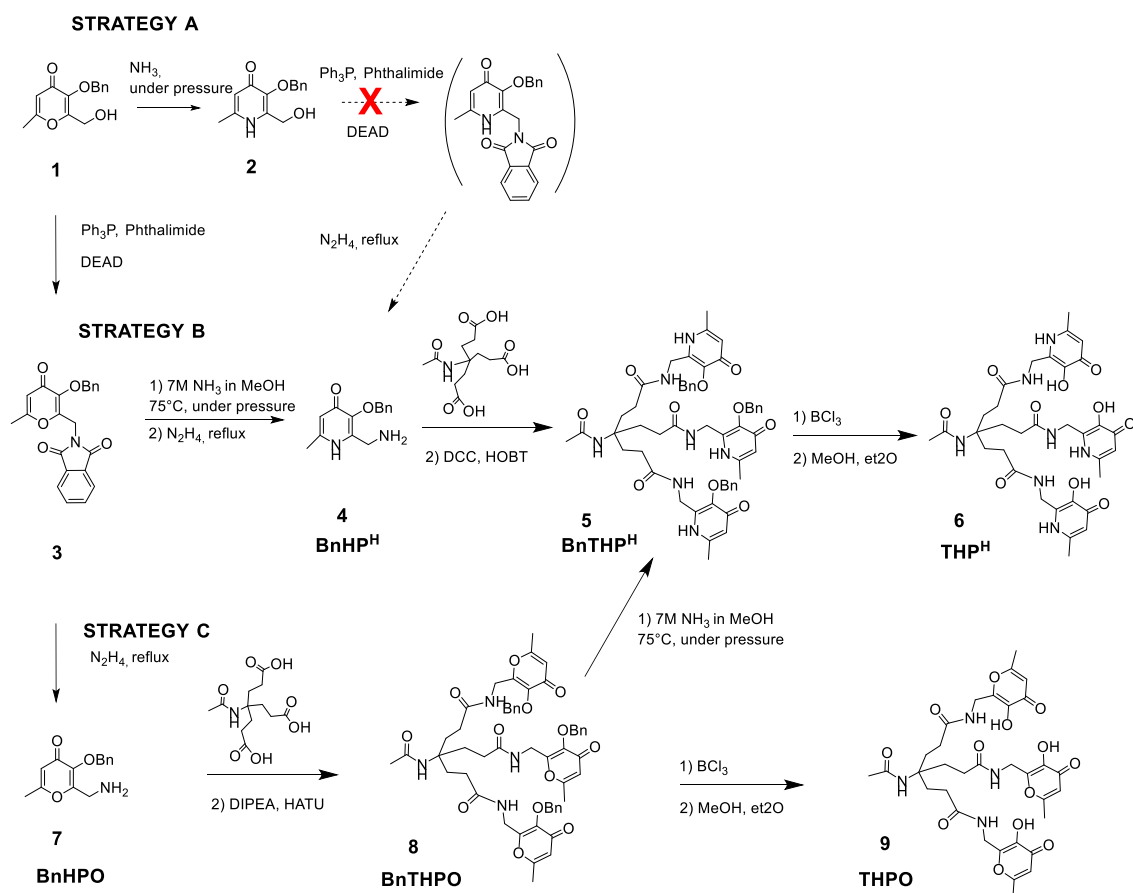
Scheme 3.3. *Synthetic pathways evaluated for the tris(hydroxypyridinone) compound THP[H] and its tris(hydroxypyranone) counterpart THPO (bottom). Dashed arrows represent unsuccessful synthetic steps.*

At first, the traditional approach to THP[Me] synthesis was employed (**strategy A,** [12]). Compound **1** was successfully converted into a pyridinone by reaction with ammonia. A subsequent Mitsunobu reaction using phthalimide as a nucleophile, followed by deprotection of the newly introduced nitrogen with hydrazine at reflux, was intended to yield the desired hydroxypyridinone precursor. However, the Mitsunobu reaction did not proceed to give the desired product, likely due to the presence of an N-H group in the hydroxypyridinone moiety (see **Discussion**). Therefore, new strategies for the synthesis of THP[H] were developed. In **strategy B**, the Mitsunobu reaction was performed directly on **1**, to avoid any side reaction with the heterocyclic N^1-H group. The pyranone-pyridinone conversion was then carried out on the product of the Mitsunobu reaction **3**, followed by deprotection of the NH_2 functionality without isolation of the phthalimido-protected pyridinone. The newly synthesised hydroxypyridinone unit BnHP[H] (**4**) was then coupled with the tripodal acid (**TA**), in the presence of HOBT and DCC to give compound BnTHP[H] (**5**). The overall yield for BnTHP[H] synthesis from compound **1** using **strategy B** was 16 %.

An alternative approach was also undertaken (**strategy C**), where the pyranone-pyridinone conversion step was not performed until after the assembly of the hexadentate tripodal unit. Here, the phthalimido-protected hydroxypyranone derivative **3** was deprotected to give the hydroxypyranone-NH_2 unit BnHPO **7** and then coupled to the tripodal acid, to obtain the benzyl-protected *tris*(hydroxypyranone) BnTHPO (**8**). Conversion of this derivative into BnTHP^H (**5**) was performed by reaction with ammonia under pressure and monitored using LC-MS (**Figure 3.6**). LC-MS indicated that under these reaction conditions, mixed hydroxy-pyranone/pyridinone species can be observed. The overall yield for **strategy C** synthesis of BnTHP^H (**5**) from compound **1** was 7.3 %.

Debenzylation of BnTHP^H (**5**) with BCl_3 furnished the chelator THP^H (**6**) in a quantitative yield. When the same deprotection procedure was applied to BnTHPO (**8**) the *tris*(hydroxypyranone) chelator THPO (**9**) was obtained in 78 % yield.

For both the successful synthetic strategies, the main difficulties were found in the optimisation of reaction conditions (solvent, work-up) and purification of compounds containing primary and secondary amines by silica-gel chromatography as further examined in the discussion section.
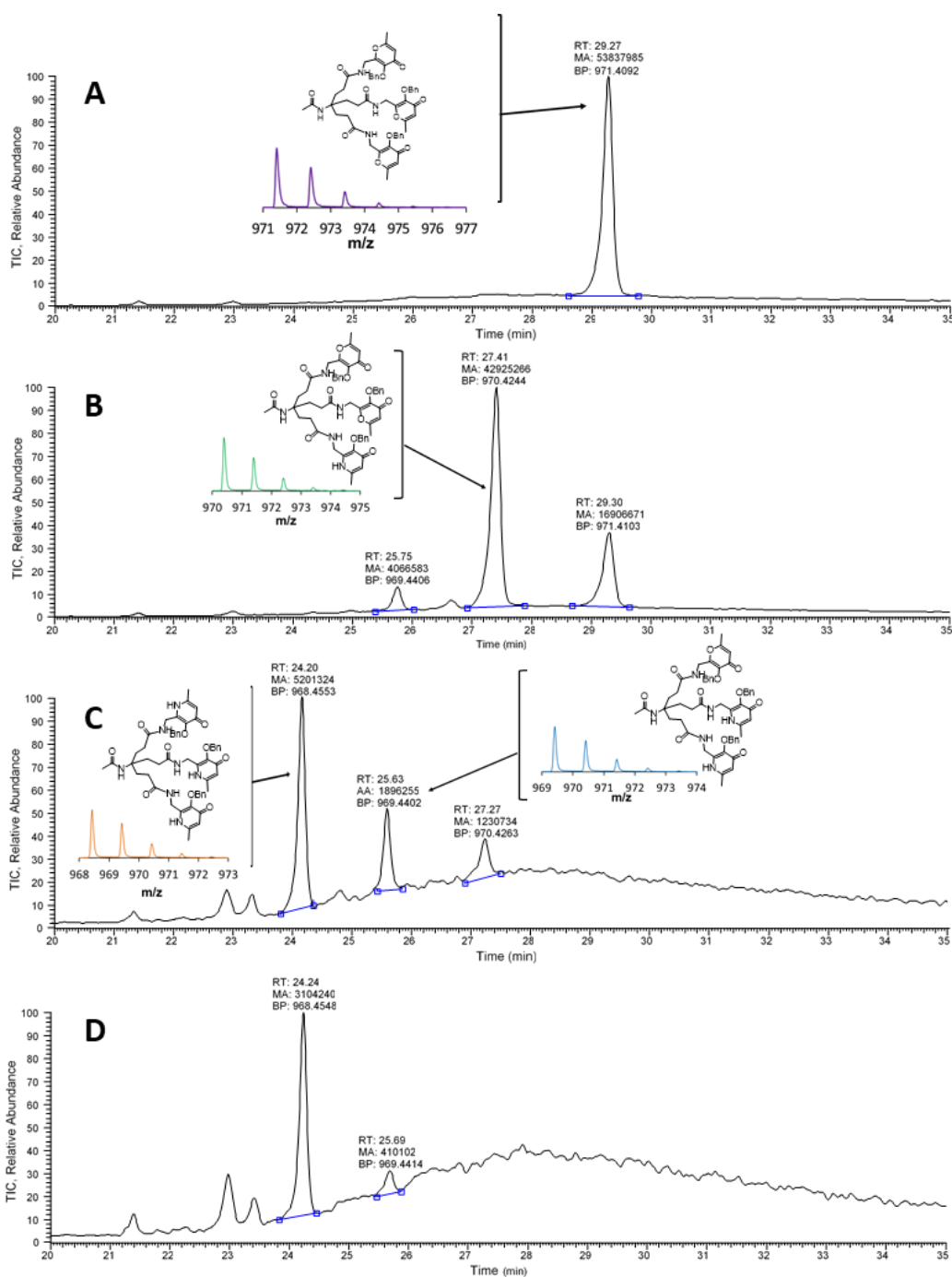
Figure 3.6. *LC-MS chromatograms showing the total ionic current (TIC) of the reaction mixture for the BnTHPO **8** to BnTHP^H **5** conversion (strategy C) at **A)** 0 h **B)** 8 h **C)** 48 h and **D)** 72 h. RT: Retention time, MA: area of the peak, BP: m/z signal for the peak. Insets: BnTHPO and MS signal of [BnTHPO +1H]^+ (purple), mono-substituted BnTHPO and MS signal (green), di-substituted BnTHPO and MS signal (blue), BnTHP^H structure and MS signal (orange).*

114

All the isolated compounds were analysed by accurate ESI-MS, ^{1}H NMR and ^{13}C-NMR to confirm identity and purity. ^{1}H NMR analysis of THP^H in H$_2$O (+10 % D$_2$O) was also performed on the 700 MHz spectrometer and the peaks assigned as below (**Figure 3.7**).
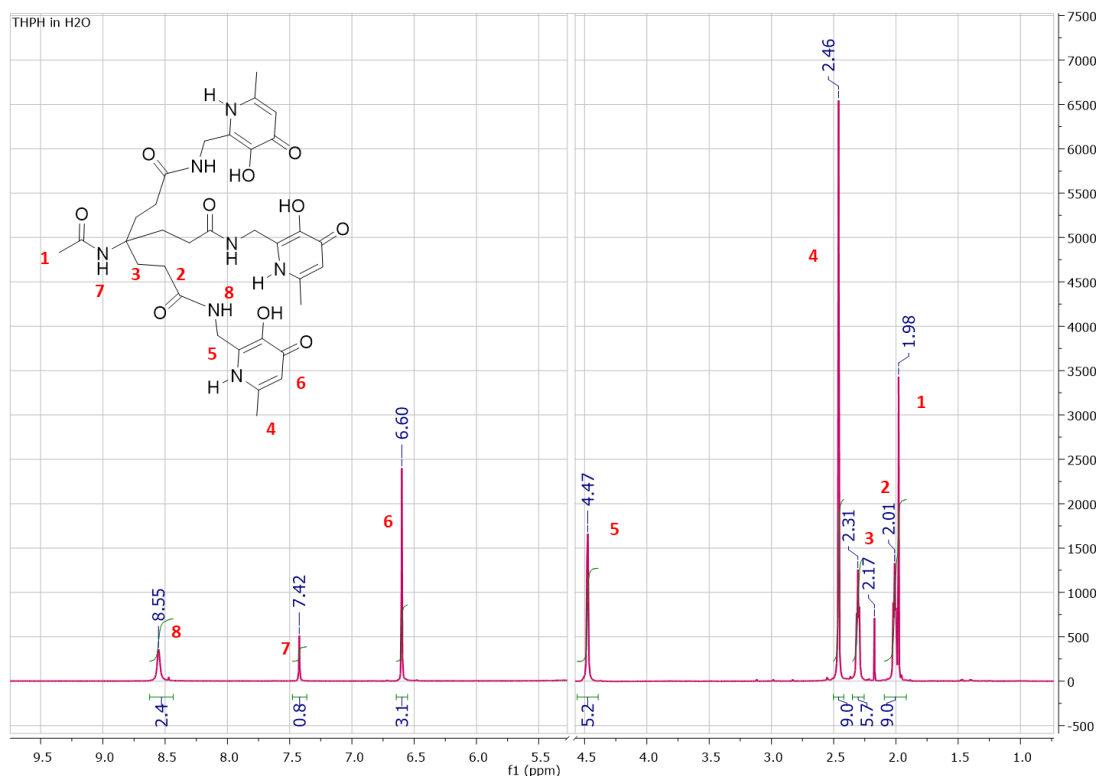
Figure 3.7. *^{1}H NMR spectrum of THP^H in H$_2$O +10 % D$_2$O. The small signal at 2.17 ppm was assigned to acetone.*

3.3.2 Preliminary NMR studies on [Ga(THP^H)]

The ^{1}H NMR of a mixture of THP^H (2 mM) and Ga(NO$_3$)$_3$ (1 or 2 mM) at pH ≈ 2.5 was acquired (**Figure 3.8**) and compared to the ^{1}H NMR of the THP^H ligand. An important change in the spectrum was visible after 0.5 equivalents of Ga(NO$_3$)$_3$ were added, but free ligand signals only completely disappeared at 1 equivalent of Ga(NO$_3$)$_3$, in agreement with the formation of a 1:1 complex only. The resulting spectrum is extremely complicated, with most signals splitting and broadening. This could result both from the presence of more than one species in these conditions, or in the presence of a single species with a reduced symmetry, compared to an idealised pseudo-octahedral complex with C$_3$ symmetry. Notably, an attempt to increase the pH of the solution by addition of d$_7$-ammonium acetate resulted in the precipitation of the complex and almost complete disappearance of ^{1}H NMR signals.
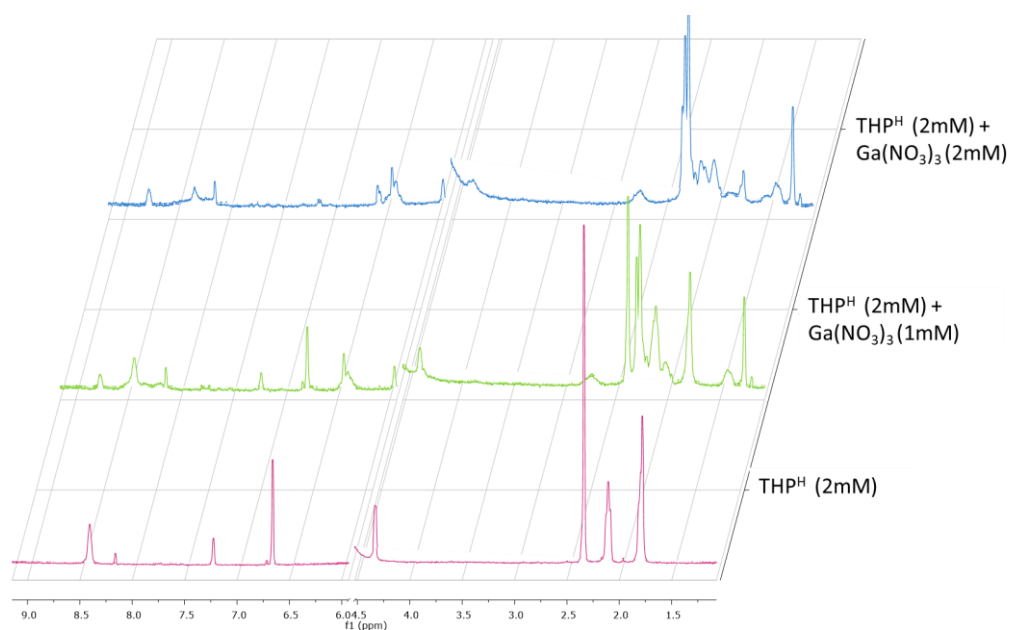
Figure 3.8. *^{1}H NMR spectra of the THP^H ligand in presence of different concentration of Ga(NO$_3$)$_3$.*

For each of the investigated ligand/metal ratios, the ^{71}Ga spectrum was also acquired and compared with that of [Ga(H$_2$O)$_6$]$^{3+}$ (solution of Ga(NO$_3$)$_3$ in H$_2$O + 10 % D$_2$O, set at 0 ppm as a reference) and of [Ga(NOTA)], whose chemical shift compared to the hexaaqua-ion is known [19]. ^{71}Ga NMR spectra are reported in **Figure 3.9**.
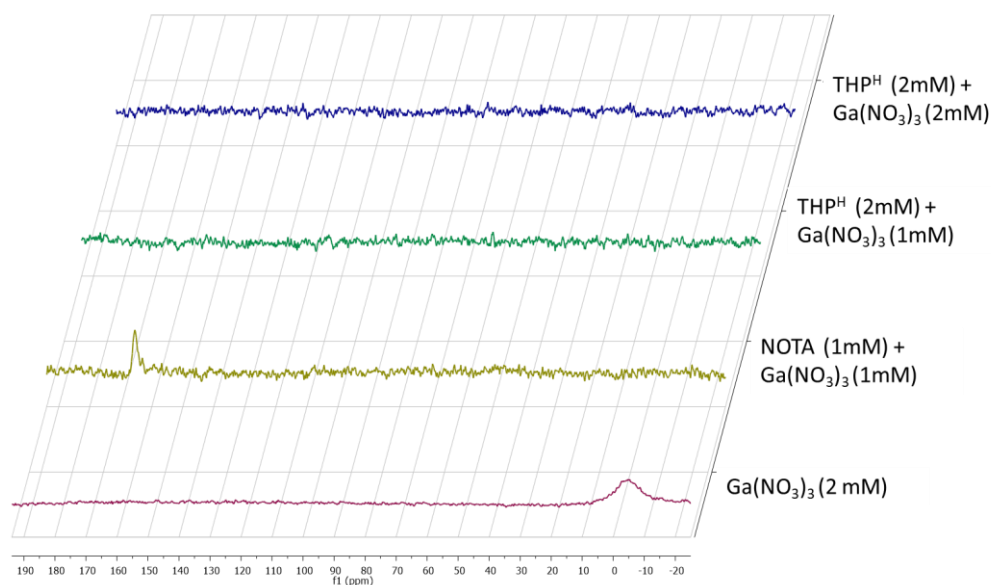
Figure 3.9. *^{71}Ga NMR spectra of different mixtures of Ga(NO$_3$)$_3$ and ligands in H$_2$O + 10 % D$_2$O. The spectrum of Ga(NO$_3$)$_3$ is also shown in the bottom panel, with one signal, representing [Ga(H$_2$O)$_6$]$^{3+}$, set a 0 ppm as a reference.*

Owing to the quadrupole moment of the ^{71}Ga nucleus [20], signals in a ^{71}Ga NMR tend to be broad and their width increases with decreasing of the symmetry around the

116

gallium ion. Complexes with a highly symmetric environment around the metal centre are most discernible in ^{71}Ga-NMR. Remarkably, the peak visible for the hexaaqua ion disappeared once gallium was mixed with the ligand suggesting low symmetry of the resulting complex, in agreement with the ^{1}H NMR data. On the contrary the [Ga(NOTA)] complex presented a sharp signal at 170.6 ppm, in agreement with literature reports [19].

3.3.3   Radiolabelling and comparison with THP^{Me} and THPO

The radiolabelling of THP^{H}, THPO and THP^{Me} (as a comparison) was investigated at room temperature, using ammonium acetate to control pH (final concentration 0.25 M, pH ≈ 6). A reaction time of 5 min was used for all experiments. Verification of the radiolabelling was performed by reverse-phase HPLC and iTLC-SG.

Analytical HPLC of a THP^{H} radiolabelling mixture (100 μM), showed only one peak in the in the UV chromatogram (3 min 26 s) attributed to unreacted ligand, and one peak in the radiochromatogram at 4 min 56 s attributed to the radioactive [^{68}Ga(THP^{H})] complex. HPLC analysis of non-radioactive [^{nat}Ga(THP^{H})] also showed a single peak in the UV-Vis chromatogram, whose retention time (4 min 20 s) matched that of [^{68}Ga(THP^{H})] when taking into account the different configuration of the two detectors in series (**Figure 3.10**). LC-MS of [^{nat}Ga(THP^{H})] confirmed the product as possessing a 1:1 ligand:metal stoichiometry, and no peaks suggestive of other gallium species were observed (**Figure 3.11**).

Chromatograms THP^{H}

— THP^{H} (Abs., λ = 254nm)
— [Ga(THP^{H})] (Abs., λ = 254nm)
— [^{68}Ga(THP^{H})] (CPS)

Time (min)
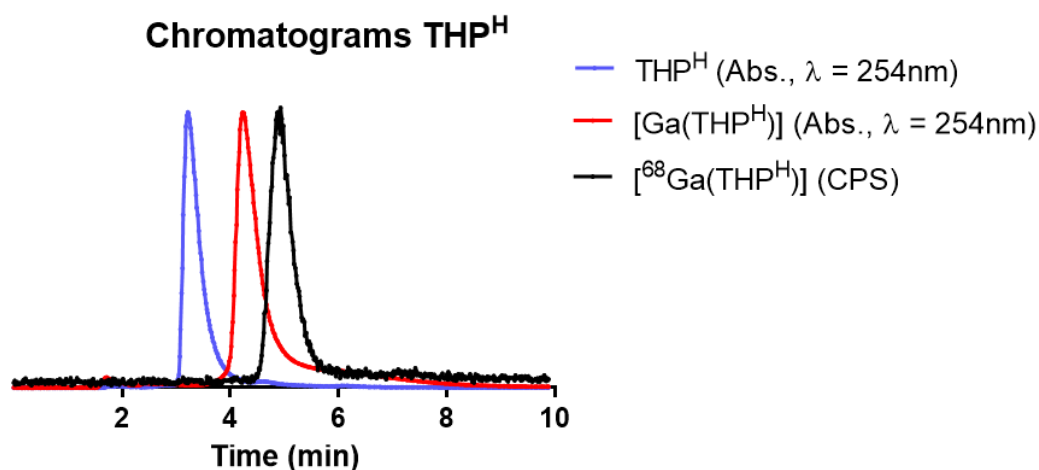
Figure 3.10. *Normalised chromatograms of THP^{H}, showing both UV Chromatogram at 254 nm for THP^{H} and [^{nat}Ga(THP^{H})] and the radiochromatogram for the [^{68}Ga(THP^{H})] (HPLC method 3; the different configuration of the two detectors in series accounts for the difference between the UV and radio-chromatograms of the [Ga(THP^{H})] complex).*
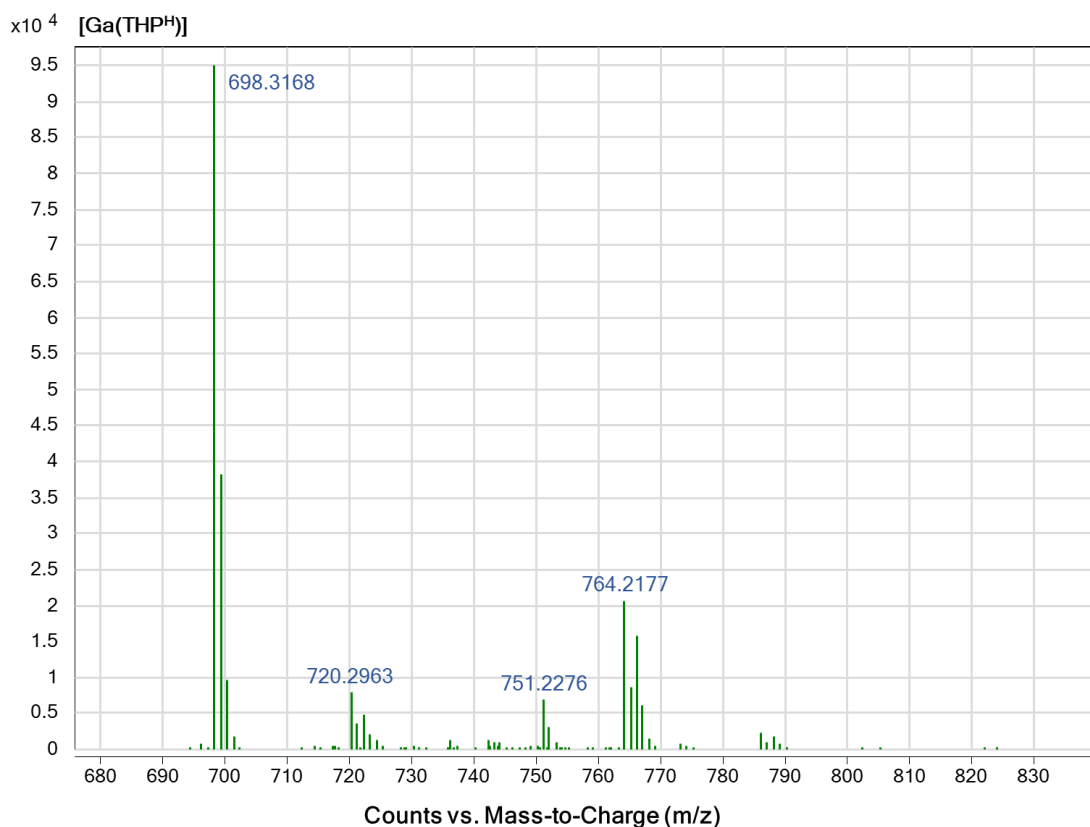
Figure 3.11. *Mass spectrum for the [Ga(THP^H)] complex. The peak at 764.22 m/z represent [Ga(THP^H)] and shows the typical isotopic pattern of a natural gallium complex. Peak at 698.32 represents the THP^H ligand, the other peaks are assigned to the sodium and iron complex of THP^H, respectively.*

For THPO, RP-HPLC analysis (100 µM) revealed one peak in the UV chromatogram (4 min 43 s) corresponding to the ligand and a single peak in the radiochromatogram at 8 min 18 s, matching the UV peak of [Ga(THPO)] at 7 min 42 s (**Figure 3.12**).
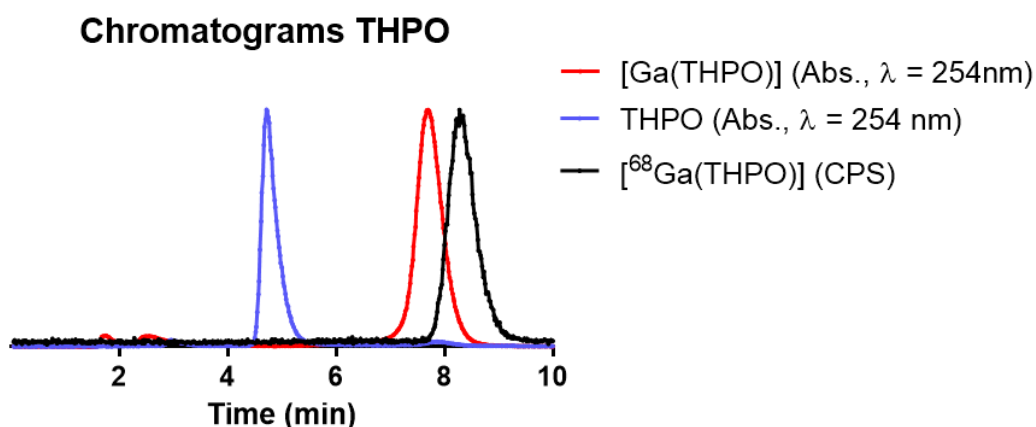
Figure 3.12. *Normalised chromatograms of THPO, showing both UV chromatogram at 254 nm for ligand and gallium complex and the radiochromatogram for the ^{68}Ga complex (HPLC method 2; the configuration in series of the detectors accounts for the difference between the UV and radio-chromatograms of the [Ga(THPO)] complex).*

The retention factors of the three radiolabelled complexes on iTLC-SG were determined for both mobile phase and compared with unchelated gallium in the same conditions (**Table 3.1**).

Table 3.1. *Retention factor (Rf) of the different gallium complexes in the two different mobile phases. *In the presence of gallium colloids, a species at Rf = 0 is also visible for unchelated gallium in mobile phase 1, in addition to the principal species at Rf = 1. Both colloidal and unchelated gallium are found at Rf = 0 for mobile phase 2.*

	Measured Rf	
	Mobile phase 1	Mobile phase 2
[Ga(THP^H)]	0.64	1
[Ga(THP^{Me})]	0	1
[Ga(THPO)]	0	1
Unchelated gallium	1	0
Colloidal gallium	0	0

iTLC analysis (mobile phase 2) of the radiochemical yield (RCY) at different ligand concentrations was performed using a phosphorimager. RCY higher than 95 % were considered quantitative. THP^H was found capable of quantitative radiolabelling in these conditions at a ligand concentration as low as 1 µM, similar to THP^{Me} (**Table 3.2**). When radiolabelling at a lower concentration (0.1 µM) was performed, THP^H achieved almost quantitative radiolabelling with RCY of 93.9 %. At the same concentration, THP^{Me} was only able to achieve a radiochemical yield of 83.0 %. The *tris*(hydroxypyranone) ligand THPO also radiolabelled quantitatively under the same conditions, but at higher ligand concentrations (100 µM) compared to THP derivatives (**Table 3.2**).

Determination of the partition and distribution coefficients (Log$P$ and Log$D_{7.4}$, **Table 3.2**) for the ^{68}Ga complexes of THP^{Me}, THP^H and THPO ligands was performed using the shake-flask method. Unexpectedly, [Ga(THP^H)] was found to be more lipophilic than [Ga(THP^{Me})]. The THPO complex proved to be the most lipophilic of the three, in agreement with the earlier LC-MS results for the BnTHPO to BnTHP^H conversion, where replacement of the 3 oxygens with N-H groups resulted in a decrease in elution time.

Table 3.2. Log$P$ and Log$D_{7.4}$ values for [Ga(THP^{Me})], [Ga(THP^{H})] and [Ga(THPO)] and radiolabelling yields for the same complexes at different ligand concentrations. Data are reported as mean ± standard deviation (N = 4 hydrophilicity measurements, N = 3 for radiolabelling yields). *Radiolabelling performed with ^{68}Ga eluate from a different E&Z generator, eluted with clinical grade HCl.

	[Ga(THP^{Me})]	[Ga(THP^{H})]	[Ga(THPO)]
Log$P$	-3.33 ± 0.02	-2.40 ± 0.02	-1.64 ± 0.01
Log$D_{7.4}$	-3.27 ± 0.02	-2.28 ± 0.05	-1.65 ± 0.03
	Radiochemical yields		
100 µM	96.9 ± 1.0	98.9 ± 0.7	95.6 ± 0.2
10 µM	97.8 ± 0.5	99.1 ± 0.2	83.0 ± 0.4
1 µM	96.7 ± 0.2	98.1 ± 0.4	27.5 ± 0.7
0.1 µM *	83.0 ± 0.5	93.9 ± 0.4	N/A

3.3.4 Spectrophotometric measurements

The proton affinity constants for the two *tris*(hydroxypyridinone) chelators THP^{H} and THP^{Me}, as well as their complex formation constants for Ga^{3+} and Fe^{3+} were studied using spectrophotometric measurements in the UV-Vis range. The bidentate hydroxypyridinone ligand deferiprone was also analysed using the same method to verify its reliability. Measurements of pKa were performed by titration in the pH range 2.5-11. Ligand spectra at selected pH values are provided in **Figure 3.13** and pKa values are reported in **Table 3.3**.
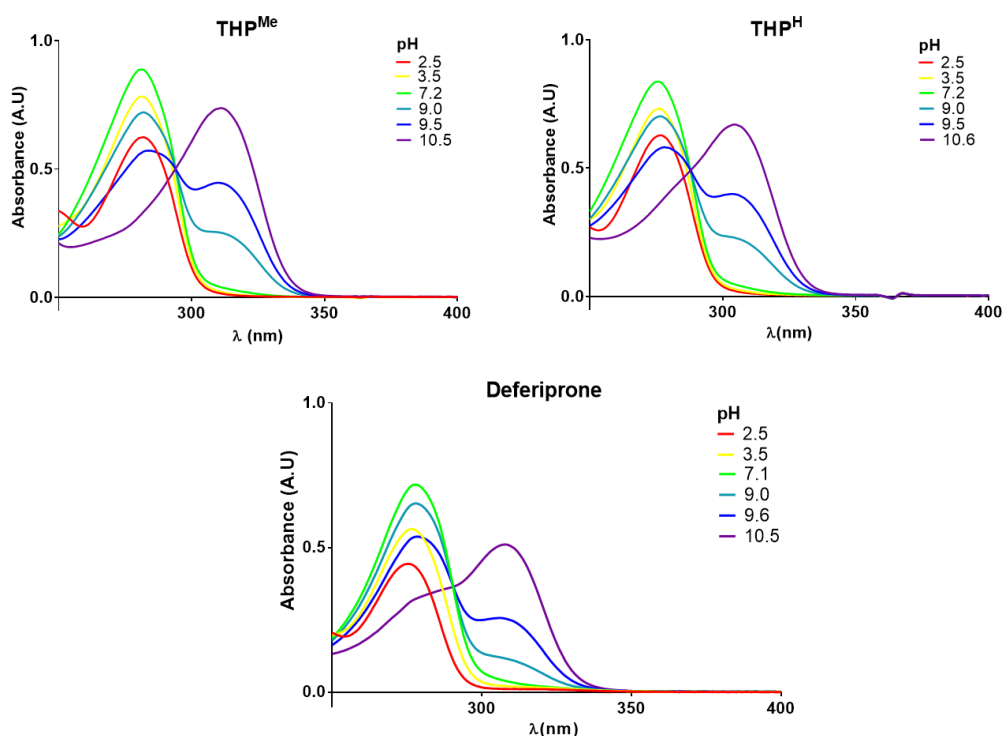
Figure 3.13. *Absorbance spectra of THP^{Me} and THP^{H} ligands (top panel) and deferiprone (bottom panel) at different pH values*

The pKa values for THP chelators are better described as intrinsic protonation constants [21] since they represent the average pKa of the three hydroxypyridinone units, which could not be distinguished in this measurement. The measured protonation constants for THP^H (**Scheme 3.4** for protonation equilibria) are slightly higher than those for THP^{Me} and lower than the pKa values measured for deferiprone with the same method. The first intrinsic protonation constant (pKa_1 values: 3.2 for THP^{Me}, 3.4 for THP^H) is attributed to the carbonyl group of the HP unit, while the second is assigned to the adjacent hydroxyl group (pKa_2 values: 9.4 for THP^{Me}, 9.5 for THP^H). For THP^H a third intrinsic protonation constant exists related to the N^1-H group in the pyridinone ring, but was not measurable in the pH range used for the titration and was estimated to be approximately 13 from the spectral change of the [Fe(THP^H)] complex in the pH 10-12.5 range.
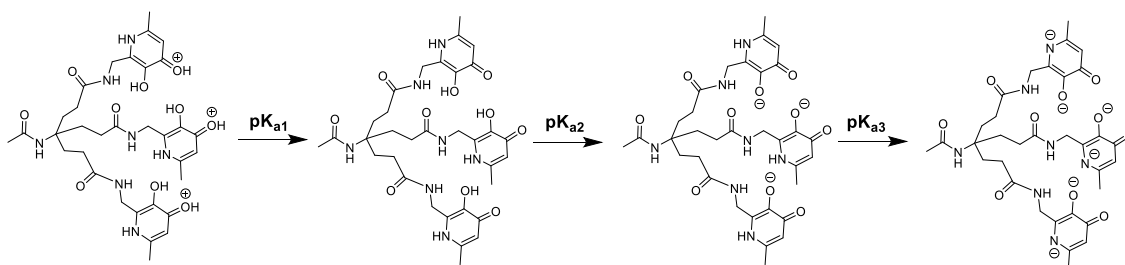
Scheme 3.4. *Protonation equilibria for THP^H.*

All the metal affinity constant measurements were performed by evaluating the competition between [M(THP)] species and [M(OH)$_4$]$^-$ species, whose formation constants from the hexaaqua ions are known (Logβ [Fe(OH)$_4$]$^-$ = -21.9, Logβ [Ga(OH)$_4$]$^-$ = -16.6 [15]). For every ML (metal-ligand) species observed in the system, relevant chemical equilibrium equations were defined and their equilibrium constants (Logβ, or Logβa for protonation equilibria) were calculated by fitting of the absorbance spectra in the UV regions (for gallium complexes) or in the visible region (for iron complexes). Values and speciation plots for every ligand are reported in the following pages (page 122-124). pM values are also summarised in **Table 3.3**.

Deferiprone

L=

Chemical equilibrium equations

$$M^{3+} + L^- \rightleftarrows [ML]^{2+} \qquad\qquad Log\ \beta_{[ML]^{2+}}$$

$$M^{3+} + 2\,L^- \rightleftarrows [ML_2]^+ \qquad\qquad Log\ \beta_{[ML_2]^+}$$

$$M^{3+} + 3\,L^- \rightleftarrows [ML_3] \qquad\qquad Log\ \beta_{[ML_3]}$$

$$M^{3+} + 4\,OH^- \rightleftarrows [M(OH)_4]^- \qquad\qquad Log\ \beta_{[M(OH_4)]^-}$$
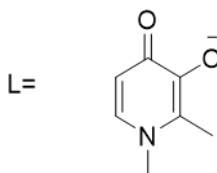
Equilibrium constants*

$[FeL]^{2+}$	15.0	$[GaL]^{2+}$	14.4
$[FeL_2]^+$	27.5	$[GaL_2]^+$	27.0
$[FeL_3]$	37.5	$[GaL_3]$	37.4
$[Fe(OH)_4]^-$	34.4 [15]	$[Ga(OH)_4]^-$	39.4 [15]
pFe	20.8	pGa	20.7

Speciation plots
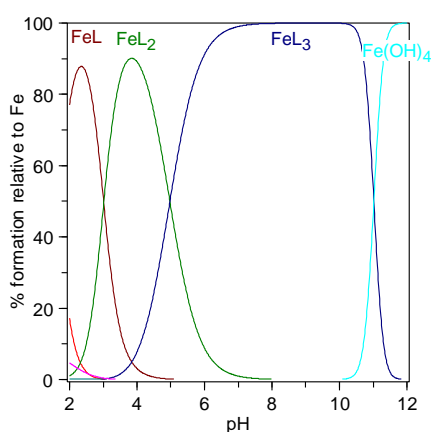
$[Fe]_{total}$: 10^{-6} M
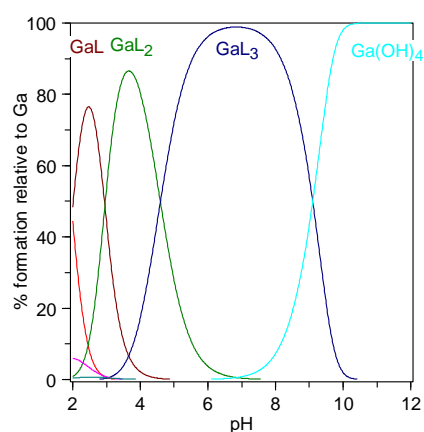
$[L]_{total}$: 10^{-5} M

$[Ga]_{total}$: 10^{-6} M

$[L]_{total}$: 10^{-5} M

* Overall experimental error <3% (fitting root mean square error <1%).

THP^{Me}

L^{3-} =

Chemical equilibrium equations

$$M^{3+} + L^{3-} \rightleftarrows [ML] \qquad\qquad Log\ \beta_{[ML]}$$

$$M^{3+} + 4\ OH^- \rightleftarrows [M(OH)_4]^- \qquad\qquad Log\ \beta_{[M(OH_4)]^-}$$
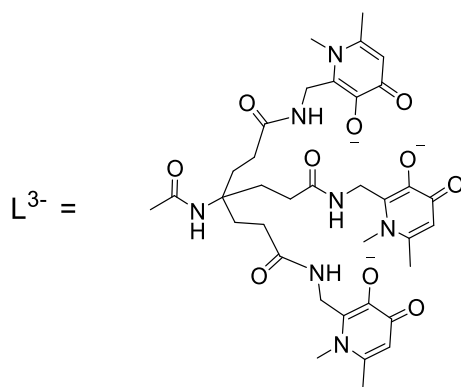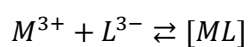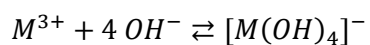
Equilibrium constants*

[FeL]	30.7	[GaL]	35.0
[Fe(OH)$_4$]$^-$	34.4 [15]	[Ga(OH)$_4$]$^-$	39.4 [15]
pFe	25.7	pGa	30.0

Speciation plots
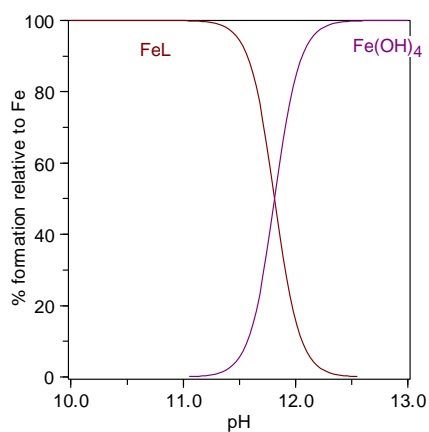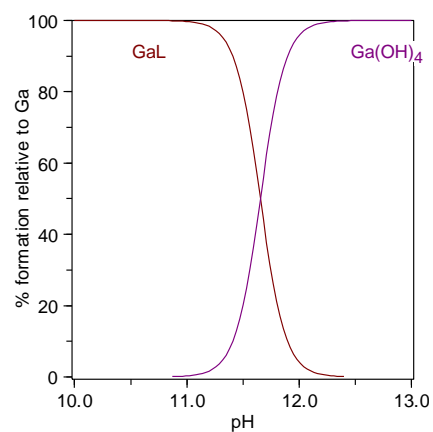
[Fe]$_{total}$: 10^{-6} M

[L]$_{total}$: 10^{-5} M

[Ga]$_{total}$: 10^{-6} M

[L]$_{total}$: 10^{-5} M

* Overall experimental error <3% (fitting root mean square error <1%).

$[LH_3]^{3-}$ =

L^{6-} =

Chemical equilibrium equations

$$M^{3+} + L^{6-} + 3\,H^+ \rightleftarrows [MLH_3] \qquad\qquad Log\ \beta_{[MLH_3]}$$

$$M^{3+} + L^{6-} \rightleftarrows [ML]^{3-} \qquad\qquad Log\ \beta_{[ML]^{3-}}$$

$$M^{3+} + 4\,OH^- \rightleftarrows [M(OH)_4]^- \qquad\qquad Log\ \beta_{[M(OH_4)]^-}$$
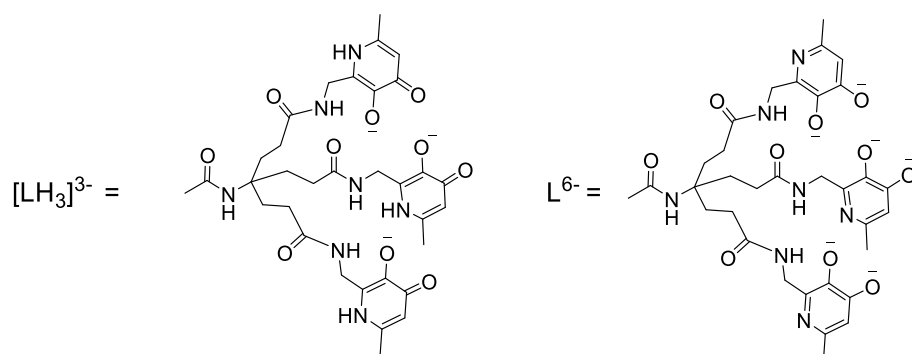
Equilibrium constants

$[FeLH_3]$	66.6	$[GaLH_3]$	76.2
$[FeL]^{3-}$	33.5	$[GaL]^{3-}$	42.5
$[Fe(OH)_4]^-$	34.4 [15]	$[Ga(OH)_4]^-$	39.4 [15]
pFe	22.3	pGa	31.8

Speciation plots
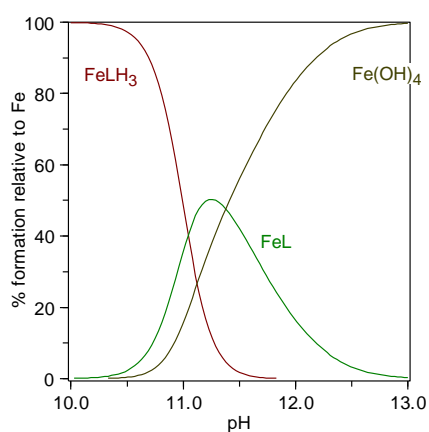
$[Fe]_{total}$: 10^{-6} M
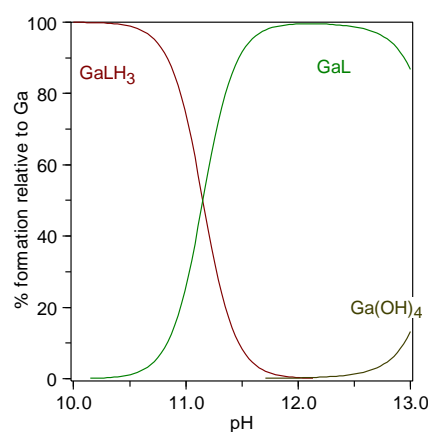
$[L]_{total}$: 10^{-5} M

$[Ga]_{total}$: 10^{-6} M

$[L]_{total}$: 10^{-5} M

* Overall experimental error <3% (fitting root mean square error <1%).

In the case of deferiprone, the $[M(OH)_4]^-$ species start to compete with the $[M(deferiprone)_3]$ complexes (annotated as $[ML_3]$ in the speciation plot) at pH < 12, thus a typical pH range (2-12) could be used in this titration study. Notably, deferiprone showed very high complex formation constants for both metals, in agreement with literature values [22]. For hexadentate ligands higher pH had to be reached for the competition with $[M(OH)_4]^-$ species to take place. Therefore, titrations for THP^H and THP^{Me} were performed in a very high pH range (9.7-12.6). When THP^H coordinate M^{3+} under these conditions, the resulting complex $[MLH_3]$ can undergo deprotonation at the pyridinone nitrogen atom, to give the triply negatively charged species $[ML]^{3-}$ (annotated as ML in the above THP^H speciation plot). Complex formation constant and protonation constant for this $[ML]^{3-}$ species were both calculated. Notably, the reported Logβ $[ML_3]^{3-}$ clearly show THP^H preference for Ga(III) over Fe(III). Interestingly, the neutral $[Ga(THP^H)]$ complex ($[GaLH_3]$) is also less prone to deprotonation than $[Fe(THP^H)]$, as indicated by the calculated protonation constants. In contrast, when THP^{Me} complexes M^{3+}, the resulting complex $[ML]$ (defined as ML in the above THP^{Me} speciation plot) does not undergo further deprotonation in these conditions. Hence, in this case complex formation constant was calculated for this neutral $[ML]$ species. Also for THP^{Me} a clear preference for Ga(III) over Fe(III) was visible.

Importantly, because of the different equilibria and species involved for THP^H and THP^{Me}, their complex formation constants are not directly comparable. Similarly, the complex formation constants for deferiprone are not accurately comparable with those of hexadentate ligands since they describe substantially different chemical equilibria.

A more correct way to compare the metal affinity for these three different ligands is to consider their pM values, which can be calculated for each of them from the measured equilibrium constants. pM values are defined for a system at pH 7.4, with total ligand concentration of 10 µM and total metal concentration of 1 µM, according to the equation below:

$$pM = -\log[M]_{free}$$

These values are particularly useful since, irrespective of the chemical species involved, they provide a measure of the concentration of free metal present in the solution at a specific pH and at a fixed total concentration of metal and ligand. pM values for the three ligands are summarised in **Table 3.3**.

Table 3.3 *Affinity constants for THP^{Me}, THP^H and deferiprone. *Intrinsic pKa values [21] were determined from a spectrophotometric titration; **Estimated pKa values were calculated from the intrinsic pKa values by plus/minus 0.6 log units (0.4-0.8 log units deviations from the intrinsic pKa values were also tried and no significant changes in pM values were found). ***This pKa value is estimated. No significant spectral change was observed from pH 11.5 up to 12.6. The change of the estimated pKa value can result in different Logβ values but no appreciable change in pM values.*

	THP^{Me}	THP^H	Deferiprone
pKa_1	3.8** 3.2* 2.6**	4.0** 3.4* 2.8**	3.5
pKa_2	10.0** 9.4* 8.8**	10.1** 9.5* 8.9**	9.8
pKa_3	n/a	13.6** 13.0*** 12.4**	n/a
pFe	25.7	22.3	20.8
pGa	30.0	31.8	20.7

The calculated pM values showed that THP^H has superior affinity for Ga(III) compared to THP^{Me}, while, unexpectedly, the situation is reversed for Fe(III), with THP^{Me} having much higher Fe(III) affinity than THP^H. Nevertheless, both hexadentate chelators have high selectivity for gallium over iron as shown by both pM values and the complex constants. On the contrary, deferiprone, displays lower pM values for both Ga(III) and Fe(III) and no marked preference for either metal.

Importantly, the affinity constant obtained for THP^{Me} (log $\beta_{[ML]}$ = 35.1) is lower than that measured for HBED (log $\beta_{[ML]}$ = 37.7 [23]), which represents the highest reported affinity constant for a gallium complex. However, the pGa value for THP^{Me} is notably higher (pGa = 30.0 for THP^{Me} and 27.7 for HBED) and it is even higher for THP^H (pGa = 31.8, log β of the neutral species MLH$_3$ is not available), indicating higher capability of these ligands to coordinate Ga(III) in physiological conditions.

Importantly, the metal affinity data obtained in this study has several limitations related to the method used. In general, the achievement of thermodynamic equilibrium for Ga(III) and Fe(III) complex formation and dissociation is a slow process [23]. Accordingly, Notni and co-workers recently emphasised how the traditional spectrophotometric and potentiometric techniques, which allow equilibration of the system for just a few minutes, only allow the determination of "short-term conditional constants" (defined in the paper as "non-equilibrium" stability constants [24]). The true equilibrium stability constants can only be obtained by lengthening the experiments over the course of weeks (out-of-cell titration).

In addition, the behaviours of gallium and iron interacting with oxygen-type ligands are substantially different when in the high pH range, as exemplified by the formation constant of $[M(OH)_4]^-$ species (Logβ [Fe(OH)$_4$]$^-$ = 34.4, Logβ [Ga(OH)$_4$]$^-$ = 39.4 [15]). On the other hand, titration in a high pH range was necessary to see competition with $[M(OH)_4]^-$ formation (due to the extremely high affinity of THP ligands for Fe^{3+} and Ga^{3+}). This could potentially result in different rates of metal complex formation. For these reasons, an accurate comparison of pM values for THP^{Me} and THP^{H} can only be performed for the same metal, whereas comparison of pFe and pGa values for both THP ligands only indicates their strong gallium preference over a short period of time.

3.3.5 Competition studies

Two different sets of competition experiments were performed to investigate how the obtained spectrophotometric data applied to a practical radiolabelling experiment. In the first competition experiment, ^{68}Ga radiolabelling of THP^{Me} and THP^{H} in the presence of different amounts of Fe^{3+} was investigated, to better quantify the preference of the two ligands for Ga^{3+} over Fe^{3+} in a radiolabelling setting. To avoid the presence of excess ligand that could complex ^{68}Ga, thus invalidating the competition, natural gallium was added to ^{68}Ga eluate to reach a gallium:ligand ratio of approximately 9:10, Additionally, a higher concentration of ammonium acetate buffer was used (final concentration 0.44 M), to ensure that the pH would not differ significantly for samples with different metal concentration. In the experiment, the relevant THP ligand (1 equivalent, in 0.5 M ammonium acetate) was added to mixtures of $^{nat/68}$Ga^{3+} ($\approx$ 0.9 equivalent) and Fe^{3+} (0, 0.9 or 9 equivalents) and radiochemical yield was measured at different time points by iTLC (mobile phase 2). Results are presented in **Figure 3.14**.
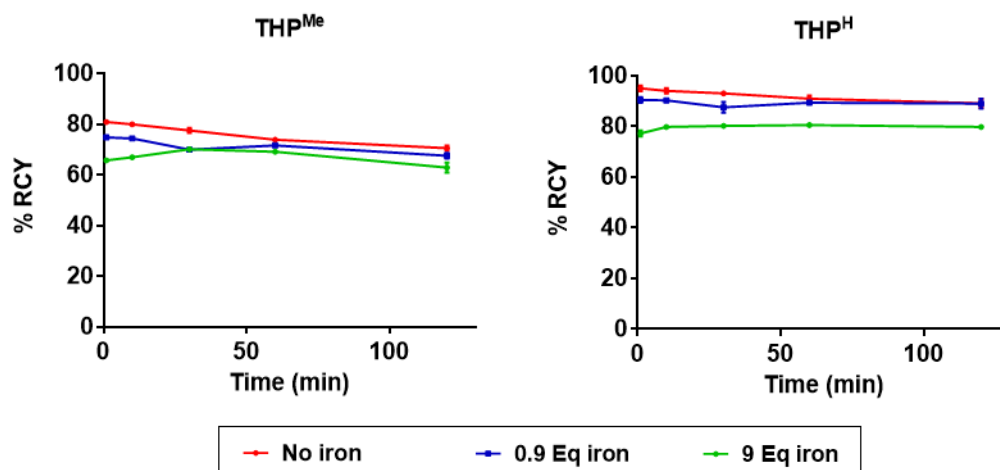
Figure 3.14. *Graphs showing the influence of different concentrations of Fe^{3+} on the radiochemical yield of $[^{68}Ga(THP^{Me})]$ and $[^{68}Ga(THP^{H})]$ in presence of 1 equivalent of ligand and 0.9 equivalent of $^{nat}Ga^{3+}$. Data are reported as mean ± standard deviation, N = 6 for control samples (without Fe), N = 3 for the rest of the samples (for most data points error bars are too small to be visible).*

Unexpectedly, in these conditions THP^{Me} could not reach quantitative radiochemical yield even in the absence of iron. This is likely related to the quasi-equimolar ratio between Ga(III) and ligand in the radiolabelling mixture, so that even the presence of a trace concentration of adventitious metals (*e.g.* from generator eluate, nitric acid or buffer), could significantly impact the radiochemical yield. Additionally, the presence of a higher concentration of buffers (ammonia, acetate, nitrate), compared to traditional radiolabelling conditions, could decrease the radiochemical yield since, at high concentration, those ligands can also compete for metal binding. Nonetheless, the experiment was able to demonstrate the effect of the presence of different Fe^{3+} amounts on the radiochemical yield. ^{68}Ga radiochemical yields were not dramatically reduced by even a ten-fold excess of Fe^{3+}, indicating strong preference for gallium over iron for both chelators. Notably, the presence of 0.9 equivalent of iron with 0.9 of gallium decreased the radiochemical yield for the two ligands only marginally (not significant for either ligand at later time points, P = 0.062 for THP^{Me}, P = 0.224 for THP^{H}), indicating that iron was not able to compete effectively with gallium for ligand binding when at the same concentration. When the amount of iron was increased to reach 9 equivalents (with 0.9 equivalent of gallium), still the majority of the ligand was binding gallium, indicating a ≈ 40-fold preference for gallium over iron in these conditions (calculated considering the 80:20 = gallium:iron complex ratio obtained in presence of a 10-fold excess of iron over gallium).

The relative capability of THP^{Me} and THP^{H} to bind gallium in radiolabelling conditions was also investigated by means of a competition study. A solution of THP^{Me} and THP^{H},

each at a concentration of 2 mM, was first prepared in D_2O and analysed by ^{1}H NMR (**Figure 3.15**) to verify the equal concentration of the two chelators.
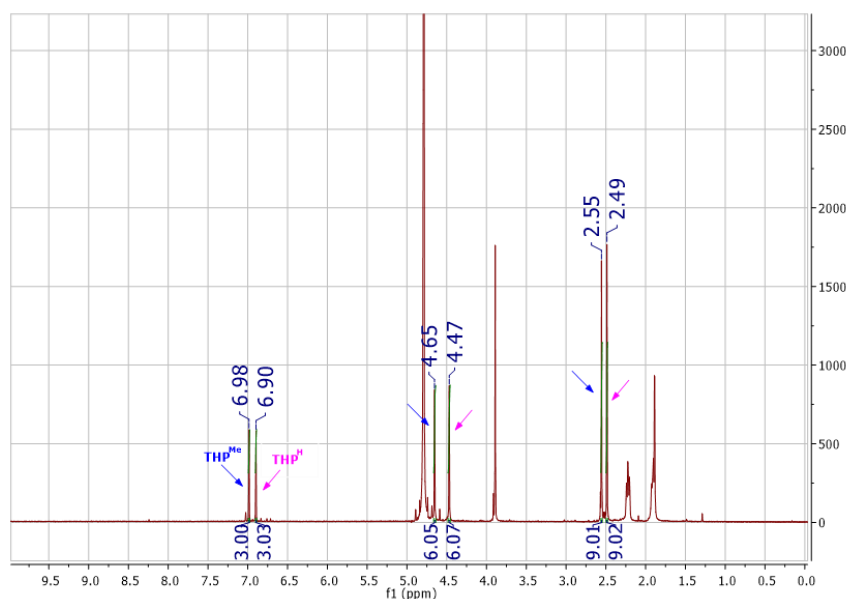
Figure 3.15. [1]*H NMR of a solution 2 mM in THP*[Me] *and 2 mM in THP*[H] *in D_2O. Peaks are referenced to residual solvent signal. Pink and blue arrows indicate signals from THP*[H] *and THP*[Me]*, respectively. Peak integration is reported (from left to right) for the pyridinone* **C^5-H** *hydrogen, the* C^2-**CH$_2$**-NH$_2$ *group and the* C^6-**CH$_3$**, *confirming equal concentration of the two ligands.*

Integration was performed on selected hydrogen groups, for which the peaks were well-separated and resolved (namely **C^5-H** hydrogen, the C^2-**CH$_2$**-NH$_2$ group and the C^6-**CH$_3$** for the hydroxypyridinone units) confirming equal concentration of the two ligands. The mixture was then diluted in ammonium acetate to obtain a solution in which the concentration of each ligand = 100 μM (in 0.5 M ammonium acetate). [68]Ga was then added and gallium speciation measured *via* iTLC by sampling at different time points after the addition. The difference in Rf between the two complexes in mobile phase 1 (citrate pH 5, iTLCs reported in **Figure 3.16 A**) was exploited to quantify the fraction of activity bound to each chelator. Mobile phase 2 was also used to verify quantitative radiolabelling at 1 min (no unchelated or colloidal gallium at Rf = 0). Results are reported in **Figure 3.16 B** and **C**.
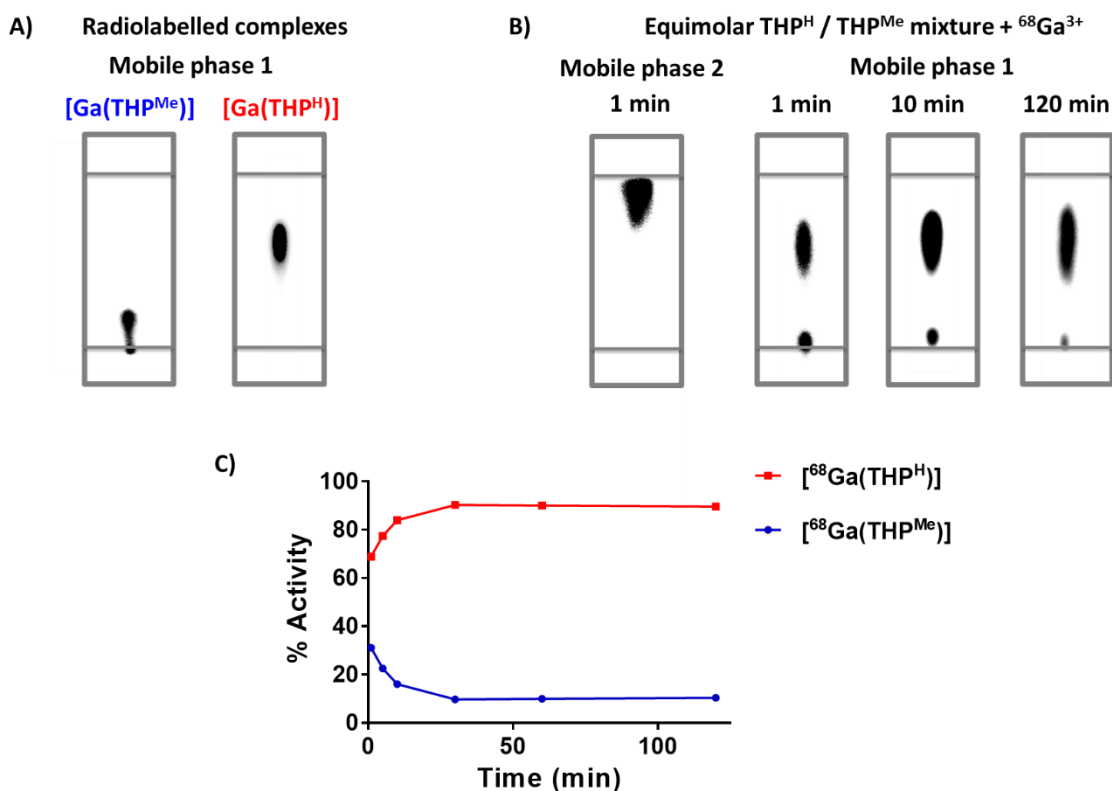
Figure 3.16. *iTLCs of the two radioactive complexes in mobile phase 1 (A) and of an equimolar mixture of THP^{Me} and THP^H treated with $^{68}Ga^{3+}$ in mobile phase 2 (1 min time point) or in mobile phase 1 (1, 10 and 120 min) (B), imaged with a phosphorimager. (C) shows how the percentage of activity associated with the two chelators, as calculated from the images, changes over time. For every data point mean ± standard deviation is reported (N = 3, error bars are too small to be visible).*

As visible in **Figure 3.16 B**, after one minute the radioactivity was already quantitatively bound to the chelators showing an extremely fast radiolabelling for both compounds, but with preference for *THP^H* (**Figure 3.16 C**, ratio: 70:30). Over time, the fraction of activity associated with THP^H increased (as plotted in **Figure 3.16 C**) to plateau at ≈ 90 % at 120 min, confirming a that THP^H binds gallium with higher thermodynamic affinity than THP^Me, as expected based on the spectrophotometric titration data.

3.3.6 Serum stability

Evaluation of the serum stability for [^{67}Ga(THP^Me)] was first performed by Berry et al., who observed no sign of transchelation to serum proteins after 4 hours incubation in serum at 37 °C [1]. [^{67}Ga(THP^H)] stability upon incubation with human serum was determined in this work using size-exclusion HPLC comparing the elution profile of the complex with that of unchelated ^{67}Ga in serum at different time points after incubation in serum at 37 °C (**Figure 3.17**). A high concentration EDTA (50 mM) was added to the PBS mobile phase in order complex any gallium not bound to either ligand and protein,

preventing precipitation onto the column and allowing its quantification by peak integration of the EDTA complex. [Ga(THP^H)] proved to be stable in serum for at least 8 days with no shift in its chromatographic peak (retention time 15 min 30 s) compared to the complex incubated in PBS. On the contrary, unchelated ^{68}Ga eluted at 12 min at early serum incubation time points (as [^{67}Ga(EDTA)]), but became more associated with serum proteins over time. After 8 days incubation, two different peaks were observed: one at 12 min ([^{67}Ga(EDTA)]) and one at 9 min 30 s, attributed to ^{68}Ga-protein adducts.
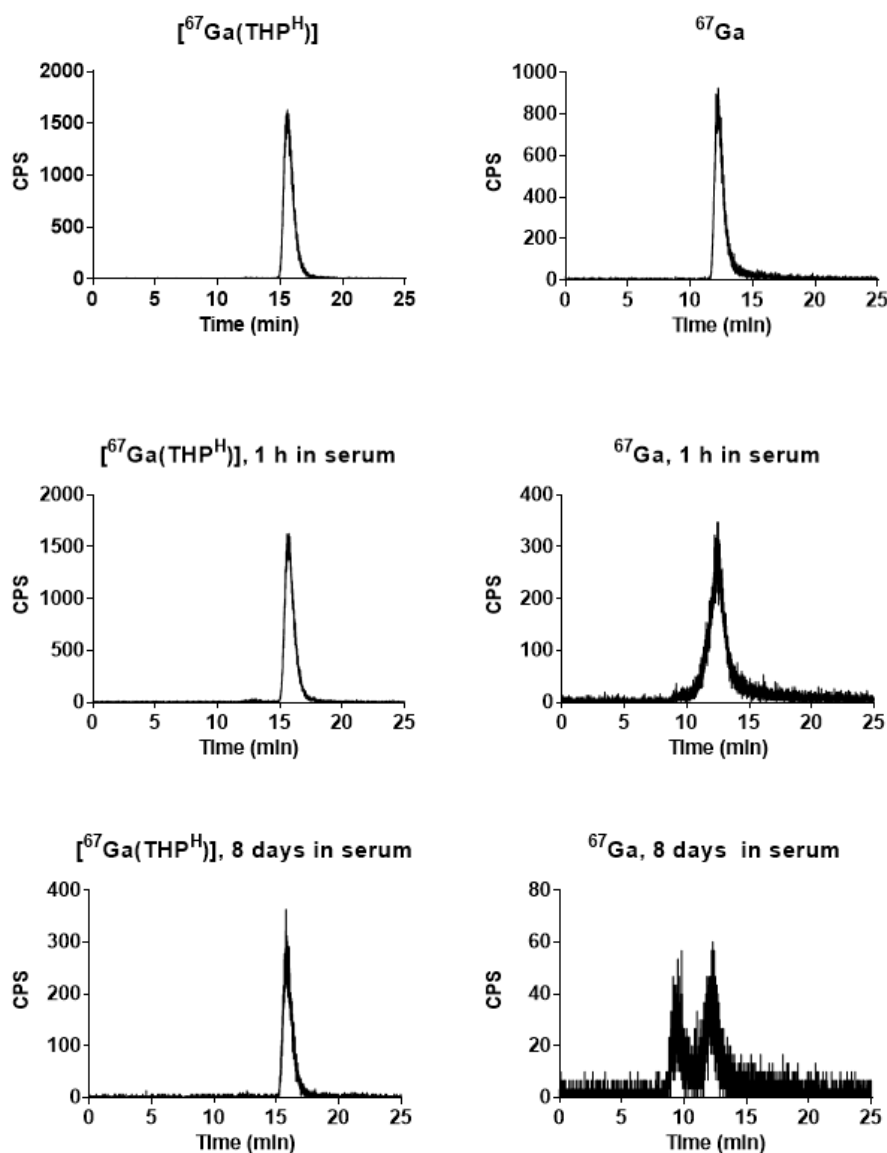
Figure 3.17. *Radiochromatograms of [^{67}Ga(THP^H)] (left column) and ^{67}Ga-chloride (right column) before and at different time points after incubation with human serum at 37 °C.*

3.3.7 *in vivo* biodistribution

The behaviour and stability of the [Ga(THP^H)] complex *in vivo* was investigated in a SCID beige mouse by dynamic PET-CT scanning. PET-CT scans (**Figure 3.18**) demonstrate that the radiolabelled complex is quickly cleared from the blood *via* the kidneys after intravenous (IV) injection. A similar biodistribution was reported for THP^{Me} [1]. HPLC analysis of the urine at 60 min post injection revealed the presence of a single radioactive species, corresponding to the intact radiolabelled [Ga(THP^H)] complex (4 min 54 s, **Figure 3.18).**
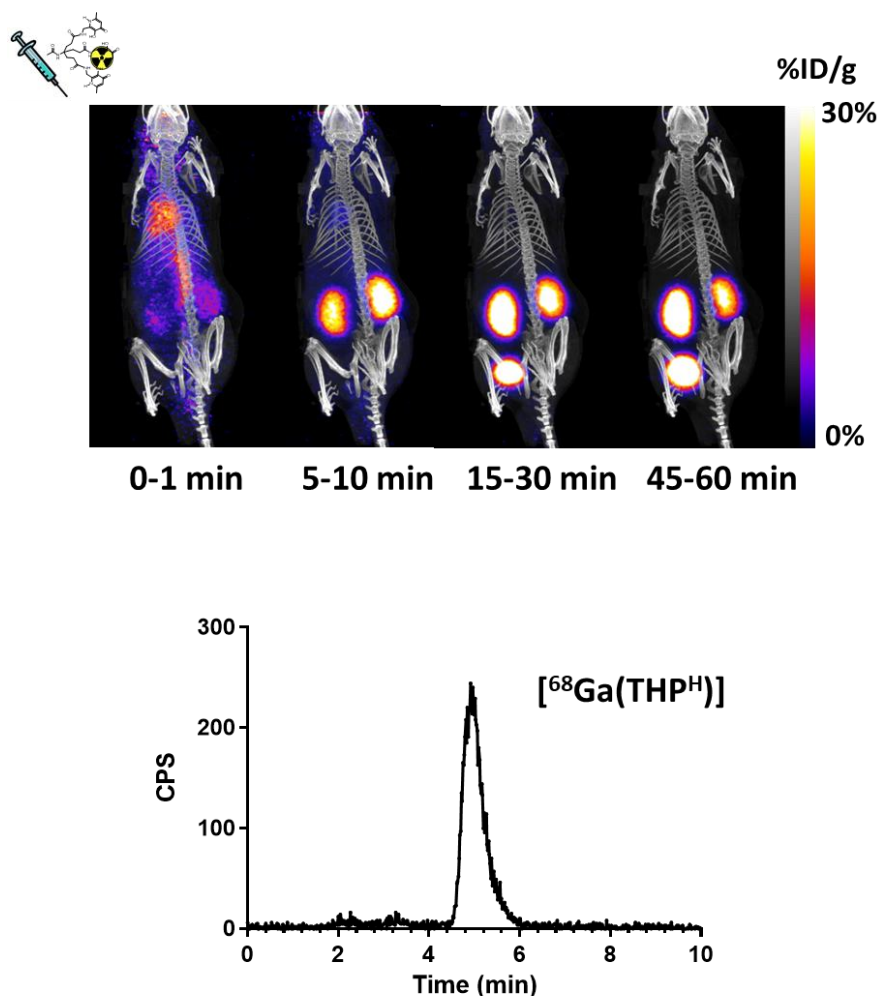
Figure 3.18. Top panel: Dynamic PET/CT maximum intensity projection (MIP) at different time points in a mouse injected with [^{68}Ga(THP^H)]. Quick blood clearance of the activity is visible with kidneys and bladder being the only visible organs already in the 15-30 min image. Bottom panel: radiochromatogram of the urine 60 min after injection (method 1), showing only one peak attributed to [^{68}Ga(THP^H)].

The ability of THP^H to bind gallium *in vivo,* acting as a ^{68}Ga scavenger, was also investigated. A mouse injected IV with acetate buffered ^{68}Ga (0.1 M ammonium acetate, 0.05 M HCl) was scanned for 30 min then injected with THP^H (20 µg) while PET scanning continued. As shown in **Figure 3.19**, the biodistribution of ^{68}Ga, initially

mainly in blood pool and clearing slowly to kidneys, liver and bone, dramatically changed upon injection of the chelator with most of the activity being cleared from the blood into the kidneys and the bladder. Analysis of the urine by HPLC confirmed the *in vivo* radiolabelling of the chelator (**Figure 3.19**) with the presence of one peak in the chromatogram with an elution time corresponding to [Ga(THP^H)]
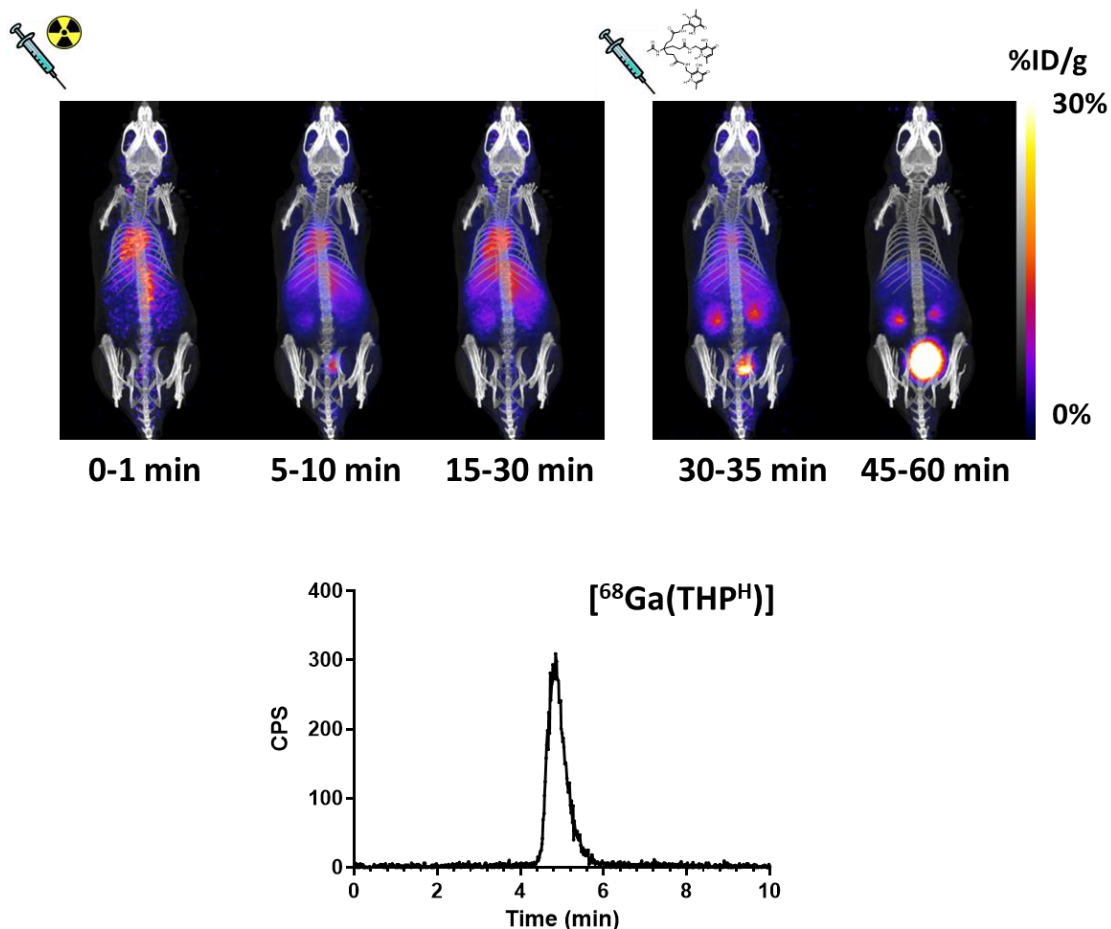
Figure 3.19. *Top panel: dynamic PET/CT MIP, at different time points, of a mouse injected with acetate buffered ^{68}Ga at time 0 followed by THP^H at 30 min (top panel). Blood clearance of ^{68}Ga proceeds very slowly in the first 30 min. With the injection of the chelator a sudden change of the biodistribution is visible with the blood pool activity quickly clearing through the kidneys into the bladder. Bottom panel: radiochromatogram of the urine at 60 min after ^{68}Ga injection (method 3), showing only one peak attributed to [^{68}Ga(THP^H)].*

3.4 Discussion

The *tris*(hydroxypyridinone) ligand THP^{Me}, and its bifunctional derivatives, are outstanding chelators for Ga^{3+}, achieving quantitative (> 95 % RCY) ^{68}Ga radiolabelling in mild conditions. This enables one-step, kit-based radiopharmaceutical manufacture of ^{68}Ga radiopharmaceuticals, in which ^{68}Ga generator eluate can be simply added to a kit vial containing chelator-bioconjugate and buffer components, to provide the formulated radiopharmaceutical ready for patient administration. This eliminates the need of laborious radiosynthetic procedures to obtain radiotracers with high radiochemical purity and puts the ease of manufacture of ^{68}Ga radiopharmaceuticals on a similar footing to that seen for ^{99m}Tc. Radiotracers based on peptide derivatives of THP^{Me} have been evaluated in preclinical models with promising results and ^{68}Ga-THP^{Me}-PSMA is undergoing a multicentre phase II clinical trial in the UK.

Development of second generation THP chelators is warranted to investigate how the physicochemical properties of this class of chelators, such as lipophilicity and the thermodynamics, kinetics and selectivity of Ga^{3+} binding, are influenced by modification of either the hydroxypyridinone unit or the tripodal scaffold.

Furthermore, it has been demonstrated that, far from being a passive spectator of the peptide/receptor interaction, the chelator plays a major role in determining the affinity of a peptide radiotracer for its receptor target [10], suggesting that, due to the variability of the chemical environment at the receptor binding sites, different targets will benefit from chelators with different structures and chemical properties. Therefore, the ultimate goal of this investigation would be the creation of a library of THP chelators able to meet the requirements of different imaging targets, rather than developing a single "ideal" THP chelator, optimised for any ^{68}Ga imaging application.

Previous preclinical investigations on THP^{Me} peptide derivatives suggested that a more water soluble/hydrophilic ligand would enhance the *in vivo* biodistribution of the radiotracers and prevent chelator precipitation during attachment to biomolecules. Therefore, in this work we replaced the N^1-CH$_3$ pyridinone unit with a N^1-H unit with the aim of increasing the water solubility and hydrophilicity of the resulting *tris*(hydroxypyridinone) ligand. This very simple chemical modification not only resulted in remarkably different chemical properties and metal preferences, but also required different synthetic routes to be developed, generating new intermediates that enable access to a library of THP compounds.

3.4.1 Synthesis

Strategy A

The traditional approach to the synthesis of hydroxypyridinone units involves pyranone to pyridinone conversion as an early step, prior to the substitution of the -CH$_2$OH moiety in position 2 with the desired -CH$_2$NH$_2$ functionality. Conversion was performed by reacting the pyranone **1** with an excess of the selected amine under pressure. To avoid side reactions, the -CH$_2$OH group is usually protected with 3,4-dihydropyrane prior to the conversion reaction and deprotected afterwards in acidic conditions. Compound **2** was successfully synthesised with this approach (53.5 % yield), but higher yields (60.6 %) were obtained when performing the pyrone to pyridinone conversion directly on **1** without the protection/deprotection step. The subsequent step in this traditional synthetic pathway is the S$_N$2 substitution at the C^2-CH$_2$-OH hydroxyl group, which is performed with a Mitsunobu reaction in the presence of phthalimide and is then followed by Ing-Manske deprotection of the newly introduced nitrogen to give the free -NH$_2$ functionality. Unfortunately, a Mitsunobu reaction (**scheme 3.5**) on compound **2** failed to give the desired phthalimido-hydroxypyridinone.
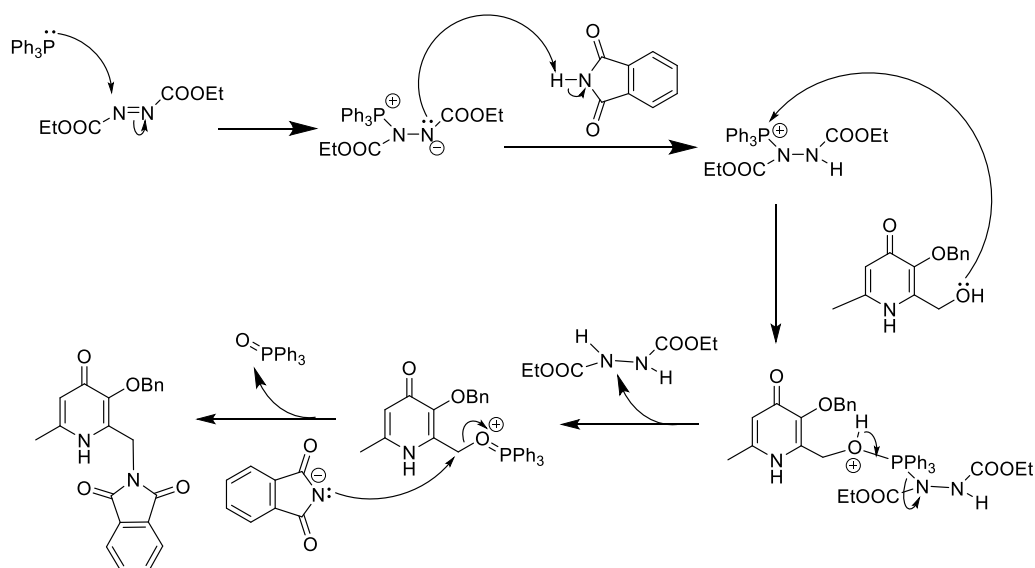
Scheme 3.5. *Mechanism of the Mitsunobu S$_N$2 substitution in the absence of side reactions.*

The purpose of the Mitsunobu reaction is to allow S$_N$2 substitution of an alcohol with a weaker nucleophile. The core step of this reaction is formation of the C^2-phosphine-oxide adduct which activates the methylene for the substitution by the deprotonated nucleophile. In case of compound **2**, two weak nucleophiles are present and able to attack the electrophile upon deprotonation: the phthalimide and the N^1-H group of another pyridinone molecule (intramolecular attack is excluded, since it would result

in the formation of a three-membered ring). In the case of attack by the pyridinone N^1-H group a variety of side products can form, resulting in an unsuccessful reaction. A number of different strategies could have been adopted to obviate this. BOC-protection of the N^1-H group would have been feasible, but would have increased the number of synthetic steps; use of *tert*-butyl amine instead of ammonia for the conversion step was hampered by the steric hindrance of this protected amine; finally, replacement of the Mitsunobu reaction and following Ing-Manske deprotection with a tosylation and subsequent S$_N$2 reaction was also possible, but was not explored due to success of strategies B and C.

Strategy B

In strategy B the Mitsunobu reaction was performed on the pyranone **1**, thus avoiding any side reaction due to the free amine group. Recrystallisation from hot methanol allowed recovery of the desired product **2** in good yield. Subsequent reaction with concentrated ammonia in methanol, at 75 °C and under pressure was expected to result in both conversion to pyridinone and deprotection in one step, given the harsh condition employed. However, mass spectrometry analysis of the reaction mixture revealed that deprotection from the phthalimide was not complete and any attempt to recover the product resulted in isolation of the phthalimido-protected intermediate. Changing the solvent from methanol to water enabled accomplishment of both reactions. However, another side-product with [M+H]$^+$ of 393 m/z was also formed in the reaction mixture. A literature survey revealed a similar issue encountered by Pfizer for a phthalimide deprotection in methylamine, with by-products attributed to instability of the phthalic diamide and different side reactions depending on the utilised solvent [25]. A similar mechanism can also be proposed for our ammonia deprotection, as represented below (**Scheme 3.6**).
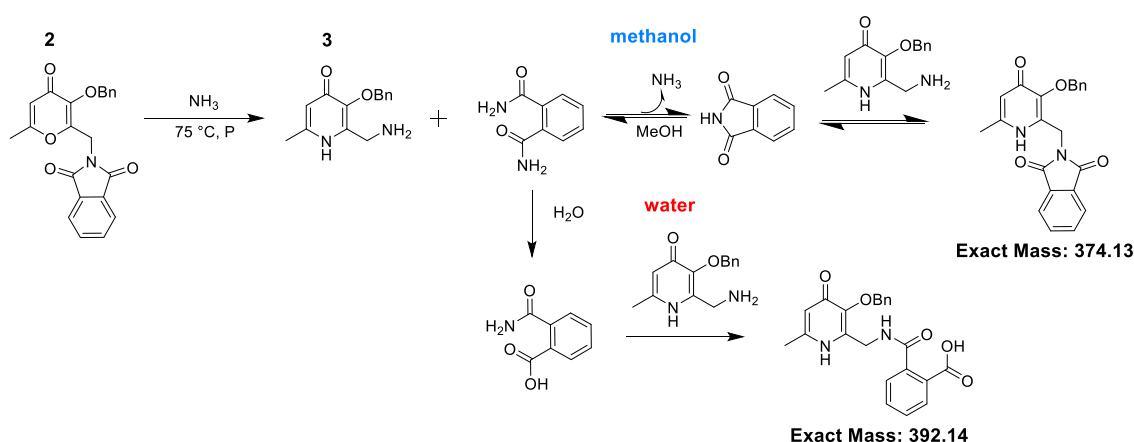
Scheme 3.6. *Mechanism proposed for pyrone/pyridinone conversion and subsequent side reactions in methanol and in water.*

136

According to this proposed mechanism, reaction of compound **2** with ammonia gave the desired product irrespective of the solvent utilised; however, the resulting phthalic diamide was not stable under the reaction conditions utilised. In methanol, this resulted in a reversible deprotection reaction whose equilibrium is shifted to the protected form when NH_3 is allowed to evaporate. On the contrary, the presence of water favours the irreversible hydrolysis of one amide group and reaction of the resulting acid group with **3** to obtain the observed side product with mass of 392 (**Scheme 3.6**).

Based on these observation, methanol was chosen as a preferred solvent for the reaction, and an additional step of reflux with hydrazine (without isolation of the phthalimide protected intermediate) was included in order to quantitatively deprotect the hydroxypyridinone unit, by precipitating the phthalhydrazide from the solution.

Purification of the product by silica gel chromatography with high methanol percentage yielded the pure product **4** as a yellow oil with a yield of 47 %. In an attempt to optimise the purification process and to avoid loss of the amine by binding to silica particles, reverse-phase SPE was used. In this case the isolated product had to be treated with ammonia in order to obtain the free base necessary for the coupling. With this new procedure the product was obtained as a solid powder instead of as an oil.

The new hydroxypyridinone precursor **4** was then reacted with **TA** to yield the benzylated *tris*(hydroxypyridinone) intermediate. A first attempt at coupling was performed using a microwave-assisted reaction with HATU and DIPEA as coupling reagents. However, mass spectrometric analysis of the reaction mixture revealed formation of a different compound with mass of 724.33 m/z $[M+H]^+$ as well as of the desired product at m/z 484.73 $[M+2H]^{2+}$. Although isolation and characterisation of the side product was not performed, it is possible that the harsh conditions employed in this first coupling favoured the intramolecular reaction between the secondary amine of one of the attached pyridinone and the free acid moiety of a different arm (proposed mechanism presented in **Scheme 3.7**).

Exact Mass: 741.34   Exact Mass: 723.33
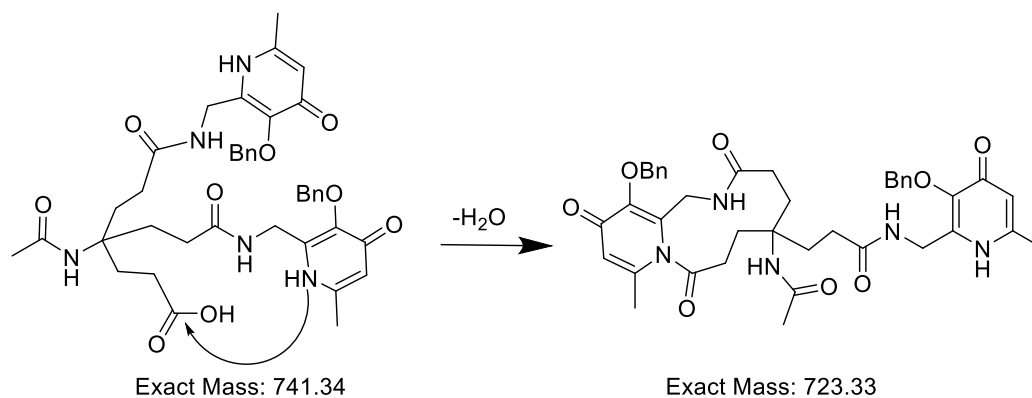
Scheme 3.7. *Proposed mechanism for the side reaction taking place when coupling was performed using HATU and DIPEA in a microwave reactor, yielding a by-product at [M+H]⁺ = 724.33 m/z.*

The coupling was then repeated in a conventionally heated vial (T = 50 °C), using HOBT and DCC as coupling agents. In these mild and neutral conditions, the reaction of a primary amine is favoured compared to that of a secondary amine, especially considering the reduced nucleophilicity of the pyridinone amine, which should display pyrrole-like reactivity. Switching to these milder conditions allowed the desired product to be obtained in 2 days. It was then purified using silica gel chromatography to yield the benzylated *tris*(hydroxypyridinone) **5**. Deprotection of this compound was performed using a dichloromethane solution of BCl$_3$. Owing to the insolubility of **5** in dichloromethane, pre-dissolution in methanol was necessary to carry out the reaction. Quenching of BCl$_3$ by methanol was minimised by using a minimum amount of methanol and a large excess of the reagent. To avoid metal contamination of the final product, the reaction was performed in new glass vials and BCl$_3$ was added using a PTFE cannula. Benzyl deprotection was achieved in an almost quantitative yield.

Strategy C

In this strategy, the hydroxypyranone unit **7** was attached to the tripodal framework and only then reacted with ammonia to obtain the benzylated *tris*(hydroxypyridinone) BnTHP^H (**5**). To achieve this, phthalimide deprotection with hydrazine at reflux was performed on product **3**, and the resulting hydroxypyranone unit was attached to the tripodal acid using mild conditions (to avoid any possible substitution at the pyranone ring).

Conversion of a *tris*(hydroxypyranone) into a *tris*(hydroxypyridinone) had already been performed for a different class of compounds [26]. In this case, we used the same conditions employed in strategy B (high pressure and temperature, excess of ammonia) and the reaction was monitored by LC-MS to verify formation of the desired product **5**.

Purification of this benzyl-protected *tris*(hydroxypyridinone), followed by debenzylation with BCl$_3$, yielded the final product THP^H.

Strategy C added an additional step and provided lower yields (overall yield for the synthesis of BnTHP^H from **1** was reduced from 16 % to 7.3 %). On the other hand, this strategy involves a benzylated *tris*(hydroxypyranone) precursor Bn(THPO), which is a flexible platform for the synthesis of a library of *tris*(hydroxypyridinone) compounds with different N-substituents, by reaction with a large excess of the relevant primary amine. Notably the conversion was found to take place in a step-wise manner, opening also the possibility of isolating mixed hydroxypyranone-hydroxypyridinone species. Debenzylation of BnTHPO using BCl$_3$ gave rise to a functional *tris*(hydroxypyridinone) ligand THPO which was also characterised and tested for radiolabelling.

3.4.2 Preliminary characterisation of [Ga(THP^H)]

The new chelator THP^H rapidly reacted with Ga(NO$_3$)$_3$ in ammonium acetate buffer to give a 1:1 complex [^{nat}Ga(THP^H)], which was characterised by ESI-MS and HPLC. Attempts to obtain the X-ray-quality crystals of the complex were unsuccessful. ^{1}H NMR also shows formation of a complex when mixing THP^H and Ga(NO$_3$)$_3$ in D$_2$O (pH ≈ 2.5). The resulting complicated spectrum, with splitting of most signals, suggests either formation of multiple species or a single species with low symmetry, either by protonation at low pH or by formation of intramolecular hydrogen bonds. ^{71}Ga NMR of the same mixture showed a huge broadening of signal (compared to the hexaaqua ion complex, or [Ga(NOTA)]) with no peaks visible in the ppm range considered. This supports the hypothesis that a low symmetry species is formed in these conditions or, potentially, a population of species in a dynamic equilibrium with each other.

Unfortunately, NMR experiments at neutral pH could not be performed because addition of deuterated ammonium acetate or bicarbonate to raise the pH caused precipitation and loss of any signal. No comparison with [^{nat}Ga(THP^{Me})] could be performed since the latter complex is even less soluble in water at any pH, precluding the possibility of a NMR. Although crystallographic and NMR data are unavailable, it is hypothesised that both THP^H and THP^{Me} coordinate Ga(III) in a hexadentate fashion, yielding complexes with a distorted octahedral structure, similar to that of the Ga(III) *tris*(deferiprone) complex [27]. In these crystallographic studies, both deferiprone and the N^1-H bidentate hydroxypyridinone were found exceptionally prone to hydrogen bonding (intramolecular and intermolecular with surrounding water molecules), both as ligands and complexes. A higher degree of intramolecular hydrogen bonding was found for the N^1-H ligand compared to the N^1-CH$_3$, owing to the additional hydrogen

bond donor. Based on these considerations, it is possible that hydrogen bonding is significant for the hexadentate chelators, where the presence of additional hydrogen bonding donors and recipients (namely, the NH and carbonyl oxygen of amide bonds) are available for participation in hydrogen bonding. Also in this case, the additional N^1-H moiety present for THP^H can only increase the amount of hydrogen bonding for both the ligand and the gallium complex.

3.4.3 Radiolabelling of THP^H and comparison with THP^{Me} and THPO

Radiolabelling of THP^H was easily accomplished under the conditions previously used for THP^{Me} and did not require either eluate pre-processing or post-labelling purification to achieve a radiochemically pure product. The nature of the radiolabelled species was confirmed using HPLC by coelution with [^{nat}Ga(THP^H)], the identity of which had been confirmed by mass spectrometry. The *tris*(hydroxypyranone) compound THPO, obtained by debenzylation of the BnTHPO intermediate, was also able to bind ^{68}Ga in the same mild conditions, but required significantly higher ligand concentration (100 μM) to reach quantitative radiolabelling. This decreased efficiency in gallium binding was not unexpected for pyranone derivatives, whose lower electron density of the heterocyclic ring compared to the pyridinone analogues is known to also compromise binding to iron [4,28].

An important characteristic of radiotracers is their lipophilicity, which influences their biodistribution and pharmacokinetics *in vivo*. Measurements of the lipophilicity of the radiolabelled complexes was performed using the shake-flask method followed by quantification of the activity in each solvent. Both Log$P$ and Log$D$ measurements were performed. As expected, [^{68}Ga(THPO)], in which the heterocyclic amine group has been replaced by an ether, was found to be more lipophilic than its pyridinone counterparts. Interestingly, lipophilicity measurements for the *tris*(hydroxypyridinone) complexes revealed not only that both are very hydrophilic (Log P/Log $D_{7.4}$ values < -2), but also that [^{68}Ga(THP^{Me})] is significantly more hydrophilic than [^{68}Ga(THP^H)]. This result was unexpected and could not be predicted by cLogP calculation following Hansch method [29], which resulted in a LogP = -1.9 for both complexes when performed using the software BIO-LOOM (BioByte Corp.). However, subsequent comparison with literature revealed a parallel with their bidentate analogues ligands [30,31], as well as some amido-3-hydroxypyridin-4-one ligands [32], where, in both cases, the N^1-H pyridinone derivative was more hydrophobic than the N^1-methyl analogue. In the case of the amido derivatives, the authors suggested that increases in lipophilicity for the N^1-H compound was due to the higher degree of intramolecular hydrogen bonding, as observed in crystallographic measurements, which reduced its ability to form

intermolecular hydrogen bonding with the solvent [32]. Likewise, the decreased hydrophilicity of the traditional bidentate N^1-H hydroxypyridinone compound compared with the N^1-methyl analogue, can be attributed to the increased intramolecular hydrogen bonding for this ligand, observed by Orvig [27]. Finally, a similar hypothesis can be formulated for [^{68}Ga(THP^{Me})] and [^{68}Ga(THP^H)], the latter more engaged in intramolecular interactions (*e.g.* hydrogen bonding between the pyridinone N^1-H and the amide carbonyl oxygen on a different arm or the tripod) and less able to form hydrogen bonding with the solvent. Although the absence of a crystal structure makes it difficult to prove the existence of such hydrogen bonding for [Ga(THP^H)], this hypothesis is in agreement with the complicated NMR spectra obtained for [Ga(THP^H)] as discussed above. However, the lower pH of the NMR solution compared to that of the radiolabelling solution used for lipophilicity studies, makes the two experiments not directly comparable. Notably, although more hydrophilic than its THP^H counterpart, the [Ga(THP^{Me})] complex was found to be less water soluble than [Ga(THP^H)], and no NMR spectrum could be acquired for this complex due to its low solubility at any pH. Energy minimisation studies for these complexes are warranted to verify the existence and extent of hydrogen bonding for these complexes.

As previously discussed, the stability of a radiolabelled chelator in biological environments is critical to its utility as BFC in radiotracers. Serum stability of [^{67}Ga(THP^{Me})] over 4 hours was previously demonstrated [1], and dynamic PET imaging of a mouse with [^{68}Ga(THP^{Me})] revealed a favourable biodistribution *in vivo*, with rapid renal clearance of the activity typical of small hydrophilic complexes. In this work, serum stability of [^{67}Ga(THP^H)] over 8 days was verified by size-exclusion radioHPLC and *in vivo* biodistribution of [^{68}Ga(THP^H)] evaluated by dynamic-PET imaging, revealed a biodistribution/clearance similar to that of [^{68}Ga(THP^{Me})]. The urine of the mouse was also analysed by radioHPLC confirming *in vivo* stability of the radiolabelled complex. Notably, THP^H was also able to bind ^{68}Ga(III) *in vivo*, when injected in a mouse 30 min after the radiometal, and to accelerate its renal excretion, acting as a scavenger for Ga(III). This ability highlights the extraordinary efficiency of THP^H radiolabelling, which can be performed even in extremely mild condition. The same behaviour was also observed for THP^{Me} and will be extensively discussed in **Chapter 4**.

3.4.4 Evaluation of metal affinity

Selectivity for the relevant radiometal is crucial when considering chelators for radiopharmaceutical applications. *Tris*(hydroxypyridinone) ligands were originally designed as iron chelators and, as such, combine features of both hydroxamate- and catechol-based siderophores. Therefore, selectivity for gallium over iron is a

particularly important concern for these chelators and was assessed in this work by determining stability constants using spectrophotometric titrations and competition studies.

Limitations of spectrophotometric titrations

The affinity of THP chelators (and deferiprone as a control) for Fe^{3+} and Ga^{3+} was determined by titration of the [M(THP)] complex with a 0.1 M NaOH solution, resulting in alkaline hydrolysis of the complexes and formation of $[M(OH)_4]^-$ species. Metal affinity constants were obtained using the software HYSS, by analysing changes in the [M(THP)] UV-Vis spectrum, following the titration [16]. Owing to the different species and equilibria present for the different chelators (see speciation plots in the **Results** section), these compounds are better compared using pM values which have been calculated from the determined Logβ values under the same predefined conditions for all chelators.

The affinity constants obtained in this study suffer from two limitations. In the first instance, these values may not be representative of the true thermodynamic affinity constants due to the slow achievement of the equilibrium for Ga^{3+} and Fe^{3+} complexation reactions, as highlighted in the results section. In order to obtain realistic values, the system should be left to equilibrate much longer than a few minutes for each titration point and the experiments extended over days/weeks as elegantly demonstrated by Notni [24]. On the other hand, the "short-term conditional constants" determined in our experiments are particularly suited to describing radiolabelling systems, whose reactions, especially for a short-lived radiometal such as ^{68}Ga, necessarily span minutes and include both kinetic and thermodynamic components.

A second limitation of the measurements is related to the high pH used for the spectrophotometric titrations. Owing to the THP chelators' outstanding affinity for Fe(III) and Ga(III), competitive formation of $[M(OH)_4]^-$ was observed for THP chelators only when titrating in the high pH range (pH > 11, see speciation plot), while it was already visible at pH 8 for deferiprone. The use of a higher pH range has several implications for the measurement. First, the different conditions used for deferiprone do not allow an accurate comparison with the hexadentate chelators; second, in the case of THP ligands an accurate comparison of pM values can only be performed for the same metal. In fact, the behaviour of gallium and iron interacting with oxygen-donor ligands is substantially different in the high pH range, as exemplified by the formation constant of $[M(OH)_4]^-$ species (Logβ $[Fe(OH)_4]^-$ = -21.9,

Logβ [Ga(OH)$_4$]$^-$ = - 16.6 [15]). This can potentially result in different rates of metal complex formation, thus influencing the determined "short-term conditional constants" values.

Finally, it is worth noting how the new pM values measured for THP^{Me} (pFe = 25.7, pGa = 30.0, **Table 3.3**) contradict some previous data from our group (pFe = 29.8 [33], 28.5 [4], pGa = 24.3 [34]) measured by competition against HBED. These differences reflect the different methods employed for their determination. Similar to the competition with [M(OH)$_4$]$^-$, competition against [M(HBED)] also suffers from kinetic components interfering with the thermodynamic measurement due, in this case, to slow transchelation between the two chelators. Furthermore, in the case of gallium, whose complexes are colourless, competition with another ligand increases the overlap in the UV region between the absorbance spectra of the two complexes, leading to a more difficult and error-prone data analysis. Therefore, we believe that our current data more accurately represent THP^{Me} affinity for Ga^{3+} and Fe^{3+}. In addition, while the previously reported data were not accompanied by determination of metal affinity constants for a known compound as a control, we also determined the affinity constants for deferiprone, obtaining values in agreement with those reported in the literature (Log β values in the range of 35.9-37.5 for Fe(III), in the range of 35.8-38.4 for Ga(III) [22]), confirming the reliability of our measurements.

Ga^{3+} vs Fe^{3+}

Our data revealed a clear preference of both *tris*(hydroxypyridinone) chelators for Ga^{3+} over Fe^{3+}, ranging from 5 orders of magnitude in the case of THP^{Me} to 9 in the case of THP^H. No preference for either metal was observed for deferiprone. Selectivity for Ga^{3+} over Fe^{3+} was confirmed, for both hexadentate chelators, by competition experiments in a radiolabelling setting. Remarkably, these experiments show that Fe^{3+} is not able to compete effectively with Ga^{3+} for THP ligands even when present in large excess. For both THP^{Me} and THP^H, when Fe^{3+} was added to give a Fe^{3+}-to-Ga^{3+} ratio of 1:1 at a ligand-to-Ga^{3+} ratio of 10:9, no significant impairment of radiochemical yield was measured. Even when the Fe^{3+}:Ga^{3+} ratio was increased to 10:1, the radiochemical yield only dropped to 80 % of the value in the absence of iron, indicating a $\approx$ 40-fold preference for Ga^{3+} over Fe^{3+} in these conditions. Although preference for Ga^{3+} was dramatically more marked in the spectrophotometric titration data, these results are not directly comparable, because of the different conditions in which the two studies were performed. Nevertheless, both spectrophotometric titration and competition experiments clearly indicate that THP^{Me} and THP^H have a strong preference for binding

Ga^{3+} over Fe^{3+} and that the presence of significant amounts of iron should not negatively impact the performance of the chelators during radiolabelling or *in vivo*.

By contrast, the bidentate hydroxypyridinone deferiprone displays a complete lack of selectivity for gallium. Although the different competition pH range used for deferiprone makes an accurate comparison of the pM values impossible, these data suggest that the tripodal scaffold plays an important role in determining the coordination preferences of these hexadentate chelators. Preference for Ga^{3+} is potentially linked to the geometric constraints imposed by the tripodal ligand, coupled with the different ionic radii (62 pm for Ga^{3+} vs 65 pm for Fe^{3+} [35]) and the different electron configurations of the two metals (d^{10} for Ga^{3+} vs. d^5 for Fe^{3+}), creating a better fit for Ga^{3+}. In the absence of a crystal structure for these complexes, these hypotheses remain to be verified with structural NMR data (for the Ga^{3+} complexes) and/or computational studies. Our preliminary ^1H and ^{71}Ga NMR studies for [Ga(THP^H)] (page 115) are in agreement with the hypothesis of a low symmetry complex. Further NMR studies in the same pH range used for the radiolabelling and/or spectrophotometric titration will need to address the solubility issues for these complexes.

THP^H vs THP^{Me}

The spectrophotometric titration data also provide a good basis to directly compare chemical properties and metal preferences of THP^H and THP^{Me}. The pKa values measured for the two chelators were very similar, with THP^{Me} displaying a slightly more acidic character, which was unexpected considering the presence of the electron donating N^1-methyl group and suggests that other chemical interactions (*e.g.* hydrogen bonding) may actively influence the pKa of these compounds. Significant differences were found in the affinity constants of the two ligands for Ga^{3+} and Fe^{3+}. Compared to THP^{Me}, THP^H shows slightly increased affinity for Ga^{3+} and markedly decreased affinity for Fe^{3+}. The multidentate tripodal structure of THP ligands was found to increase their affinity for Ga^{3+} and Fe^{3+} compared to deferiprone, as shown by the pM values and the speciation plots. This was already evident when considering the higher pH range required for competition with $[M(OH)_4]^-$ for the two hexadentate ligand.

The difference between THP^H and THP^{Me} in their binding affinity for Ga^{3+} was investigated by a second competition experiment, designed to determine which THP ligand is a more efficient chelator for ^{68}Ga under radiolabelling conditions. ^{68}Ga was incubated with an equimolar solution of THP^{Me} and THP^H and quantitative binding at the earliest time points (1 min) was verified by iTLC reflecting the fast complexation kinetics of both ligand.

The preference ^{68}Ga^{3+} for binding to THP^H over THP^{Me} was already noticeable at 1 min (≈ 70 % of ^{68}Ga associated to THP^H) and increased with time up to a plateau of ≈ 90 % from the 30 min time point onwards, in reasonable agreement with the spectrophotometric measurements. These data show how in a radiolabelling setting, THP^H outcompetes THP^{Me} for ^{68}Ga binding.

Notably, preference for THP^H at the 1 min time point does not necessarily reflect faster complexation kinetics for this ligand: it could be a result of a mixture of kinetic and thermodynamic factors. To accurately define a kinetic preference for gallium, measurements at even earlier time points (as soon as ^{68}Ga has been complexed) should ideally be performed.

Overall, these results show how modification at the hydroxypyridinone ring unexpectedly influences the preference of THP chelators for different metals. Because a similar effect was not observed for bidentate hydroxypyridinone compounds [36], this phenomenon could be related, once again, to geometric restrictions imposed by the tripodal structure of the ligand and their effect on metal complexation. By replacing the N^1-methyl group with hydrogen, the steric constraints that were present for THP^{Me} are altered, and the degree and type (*e.g.* intramolecular vs. intermolecular) of hydrogen bonding is modified compared to THP^{Me}. Both these factors could result in marked changes in the geometry and rigidity of the coordination sphere, leading to different metal affinities and selectivity for the two THP chelators.

3.5 Conclusion

A new *tris*(hydroxypyridinone) chelator THP^H has been synthesised in this work, exploiting two new synthetic strategies. Development of a new *tris*(hydroxypyranone) intermediate BnTHPO, as part of strategy C, holds promise as a flexible platform to generate a library of *tris*(hydroxypyridinone) ligands with different substituents at the pyridinone nitrogen. The development, using this strategy, of N^1-PEGylated derivatives could have particular importance, since PEGylation of the ligand may improve the solubility of the resulting gallium complexes allowing a more complete structural characterisation.

The newly developed ligand THP^H was radiolabelled quantitatively with ^{68}Ga, in the same mild conditions employed for THP^{Me} and with higher affinity and selectivity over Fe^{3+}. The radiolabelled complex was found stable in serum and *in vivo,* and displayed a favourable biodistribution with rapid blood clearance of the radioactive complex to the kidneys. Development of bifunctional derivatives is ongoing and will result in new radiotracers containing THP^H. Comparison of tracers only differing in the hydroxypyridinone unit of their THP ligand (*e.g.* THP^{Me}-TATE vs THP^H-TATE) will be particularly interesting to understand the role of the chelator in determining binding affinity, and pharmacokinetic properties of the radiotracer.

Evaluation of the Fe^{3+} and Ga^{3+} affinity for THP^{Me} and THP^H, revealed a marked preference of both chelators for Ga^{3+}, as confirmed by competition experiments in a radiolabelling setting. In particular, THP^H was found to be more even more selective towards Ga^{3+} than THP^{Me} and was able to bind the majority of ^{68}Ga in a head-to-head competition between the two chelators. Conversely, no preference was identified for the bidentate ligand deferiprone, suggesting that the tripodal framework plays an important role in defining metal affinity, likely by posing geometrical constraints which fit Ga^{3+} better than Fe^{3+}. A thorough structural analysis of *tris*(hydroxypyridinone)-metal complexes (by computational experiments, NMR or X-ray crystallography, where feasible) is warranted to accurately identify the factors determining the affinity of those chelators for a particular metal. This will lead to a new rational design of hydroxypyridinone-based chelators for ^{68}Ga and potentially other isotopes (*e.g.* ^{44}Sc, ^{177}Lu, ^{52}Mn).

As well as modification of the hydroxypyridinone unit, the tripodal framework could also be altered to better accommodate one specific metal ion or to change the overall chemical properties of the complex in terms of hydrophilicity or steric hindrance. Development of different tripodal framework is ongoing. Finally, different linkers have

already been developed for THP^Me [1,5,8], but the resulting bifunctional derivatives have not been compared in their ability to complex ^{68}Ga or to bind a specific receptor when conjugated to a targeting moiety.

3.6 References

1. Berry, D. J., Ma, Y., Ballinger, J. R., Tavaré, R., Koers, A., Sunassee, K., Zhou, T., Nawaz, S., Mullen, G. E. D., Hider, R. C., and Blower, P. J. (2011) Efficient bifunctional gallium-68 chelators for positron emission tomography: Tris(hydroxypyridinone) ligands. *Chem. Commun.* **47**, 7068-7070.
2. Hofman, M. S., Eu, P., Jackson, P., Hong, E., Binns, D., Iravani, A., Murphy, D., Mitchell, C., Siva, S., Hicks, R. J., Young, J. D., Blower, P., and Mullen, G. E. (2017) Cold Kit PSMA PET Imaging: Phase I study of ^{68}Ga-THP-PSMA PET/CT in patients with prostate cancer. *J. Nucl. Med.* (ahead of print, doi:10.2967/jnumed.117.199554).
3. Ma, M. T., Meszaros, L. K., Paterson, B. M., Berry, D. J., Cooper, M. S., Ma, Y., Hiderd, R. C., and Blower, P. J. (2015) Tripodal tris(hydroxypyridinone) ligands for immunoconjugate PET imaging with ^{89}Zr^{4+}: comparison with desferrioxamine-B. *Dalton Trans.* **44**, 4884-4900.
4. Zhou, T., Neubert, H., Liu, D. Y., Liu, Z. D., Ma, Y. M., Kong, X. L., Luo, W., Mark, S., and Hider, R. C. (2006) Iron binding dendrimers: A novel approach for the treatment of haemochromatosis. *J. Med. Chem.* **49**, 4171-4182.
5. Ma, M. T., Cullinane, C., Imberti, C., Baguna Torres, J., Terry, S. Y. A., Roselt, P., Hicks, R. J., and Blower, P. J. (2015) New tris(hydroxypyridinone) bifunctional chelators containing isothiocyanate groups provide a versatile platform for rapid one-step labeling and PET imaging with ^{68}Ga^{3+}. *Bioconjugate Chem.* **27**, 309-318.
6. Imberti, C., Terry, S. Y. A., Cullinane, C., Clarke, F., Cornish, G. H., Ramakrishnan, N. K., Roselt, P., Cope, A. P., Hicks, R. J., Blower, P. J., and Ma, M. T. (2017) Enhancing PET signal at target tissue in vivo: dendritic and multimeric Tris(hydroxypyridinone) conjugates for molecular imaging of $\alpha_v\beta_3$ integrin expression with gallium-68. *Bioconjugate Chem.* **28**, 481-495.
7. Ma, M. T., Cullinane, C., Waldeck, K., Roselt, P., Hicks, R. J., and Blower, P. J. (2015) Rapid kit-based Ga-68-labelling and PET imaging with THP-Tyr^3-octreotate: a preliminary comparison with DOTA-Tyr^3-octreotate. *EJNMMI Res.* **5**.
8. Young, J. D., Abbate, V., Imberti, C., Meszaros, L. K., Ma, M. T., Terry, S. Y., Hider, R. C., Mullen, G. E., and Blower, P. J. (2017) ^{68}Ga-THP-PSMA: a PET imaging agent for prostate cancer offering rapid, room-temperature, 1-step kit-based radiolabeling. *J. Nucl. Med.* **58**, 1270-1277.
9. Fani, M., Braun, F., Waser, B., Beetschen, K., Cescato, R., Erchegyi, J., Rivier, J. E., Weber, W. A., Maecke, H. R., and Reubi, J. C. (2012) Unexpected Sensitivity of sst$_2$ Antagonists to N-Terminal Radiometal Modifications. *J. Nucl. Med.* **53**, 1481-1489.
10. Fani, M., Del Pozzo, L., Abiraj, K., Mansi, R., Tamma, M. L., Cescato, R., Waser, B., Weber, W. A., Reubi, J. C., and Maecke, H. R. (2011) PET of somatostatin receptor-positive tumors using Cu-64- and Ga-68-somatostatin antagonists: the chelate makes the difference. *J. Nucl. Med.* **52**, 1110-1118.
11. Antunes, P., Ginj, M., Zhang, H., Waser, B., Baum, R. P., Reubi, J. C., and Maecke, H. (2007) Are radiogallium-labelled DOTA-conjugated somatostatin analogues superior to those labelled with other radiometals? *Eur. J. Nucl. Med. Mol. Imaging* **34**, 982-993.
12. Liu, Z. D., Kayyali, R., Hider, R. C., Porter, J. B., and Theobald, A. E. (2002) Design, synthesis, and evaluation of novel 2-substituted 3-hydroxypyridin-4-ones: Structure-activity investigation of metalloenzyme inhibition by iron chelators. *J. Med. Chem.* **45**, 631-639.
13. Gans, P., Sabatini, A., and Vacca, A. (1999) Determination of equilibrium constants from spectrophometric data obtained from solutions of known pH: The program pHab. *Ann. Chim.* **89**, 45-49.

14. Gans, P., Sabatini, A., and Vacca, A. (1996) Investigation of equilibria in solution. Determination of equilibrium constants with the HYPERQUAD suite of programs. *Talanta* **43**, 1739-1753.

15. Martell, E. A., Smith R. M. (1977-1989) *Critical Stability Constants*, Plenum Press, New York.

16. Alderighi, L., Gans, P., Ienco, A., Peters, D., Sabatini, A., and Vacca, A. (1999) Hyperquad simulation and speciation (HySS): a utility program for the investigation of equilibria involving soluble and partially soluble species. *Coord. Chem. Rev.* **184**, 311-318.

17. Szanda, I., Mackewn, J., Patay, G., Major, P., Sunassee, K., Mullen, G. E., Nemeth, G., Haemisch, Y., Blower, P. J., and Marsden, P. K. (2011) National electrical manufacturers association NU-4 performance evaluation of the PET component of the NanoPET/CT preclinical PET/CT scanner. *J. Nucl. Med.* **52**, 1741-1747.

18. Magdics, M., Szirmay-Kalos, L., Toth, B., Legrady, D., Cserkaszky, A., Balkay, L., Domonkos, B., Voelgyes, D., Patay, G., Major, P., Lantos, J., Buekki, T. (2011) Performance evaluation of scatter modeling of the GPU-based "Tera-Tomo" 3D PET reconstruction. *2011 IEEE (Nss/Mic)*, 4086-4088.

19. Parker, D., Waldron, B. P., and Yufit, D. S. (2013) Crystallographic and solution NMR structural analyses of four hexacoordinated gallium(III) complexes based on ligands derived from 6-amino-perhydro-1,4-diazepine. *Dalton Trans.* **42**, 8001-8008.

20. McGarvey, B. R., Taylor, M. J., and Tuck, D. G. (1981) Ga-71 nmr-studies of anionic gallium halide species in non-aqueous solution. *Inorg. Chem.* **20**, 2010-2013.

21. Taylor, P. D. (1995) Determination of the intrinsic site Pk_a value and cooperativity of the symmetrical hexadentate chelator N,N',N"-Tris 2-(3-Hydroxy-2-Oxo-1,2-Dihydropyridin-1-Yl)Acetamido Ethyl Amine. *Talanta* **42**, 845-850.

22. Cusnir, R., Imberti, C., Hider, R. C., Blower, P. J., and Ma, M. T. (2017) Hydroxypyridinone Chelators: From Iron Scavenging to Radiopharmaceuticals for PET Imaging with Gallium-68. *Int. J. Mol. Sci.* **18.**

23. Motekaitis, R. J., Sun, Y., Martell, A. E., and Welch, M. J. (1991) Stabilities of gallium(III), iron(III), and indium(III) chelates of hydroxyaromatic ligands with different overall charges. *Inorg. Chem.* **30**, 2737-2740.

24. Notni, J., Hermann, P., Havlickova, J., Kotek, J., Kubicek, V., Plutnar, J., Loktionova, N., Riss, P. J., Roesch, F., and Lukes, I. (2010) A triazacyclononane-based bifunctional phosphinate ligand for the preparation of multimeric Ga-68 tracers for positron emission tomography. *Chem. Eur. J.* **16**, 7174-7185.

25. Pettman, A. (2007) 'A blast from the past' - removal of azide protection in the identification and development of a manufacturing process to amlodipine. in *25th Process Development Symposium*, Churchill College, Cambridge.

26. Xie, Y. Y., Liu, M. S., Hu, P. P., Kong, X. L., Qiu, D. H., Xu, J. L., Hider, R. C., and Zhou, T. (2013) Synthesis, physico-chemical properties, and antimicrobial evaluation of a new series of iron(III) hexadentate chelators. *Med. Chem. Res.* **22**, 2351-2359.

27. Nelson, W. O., Karpishin, T. B., Rettig, S. J., and Orvig, C. (1988) Aluminum and gallium compounds of 3-hydroxy-4-pyridinones - Synthesis, characterization, and crystallography of biologically-active complexes with unusual hydrogen-bonding. *Inorg. Chem.* **27**, 1045-1051.

28. Hider, R. C., and Liu, Z. D. (2003) Emerging understanding of the advantage of small molecules such as hydroxypyridinones in the treatment of iron overload. *Curr. Med. Chem.* **10**, 1051-1064.

29. Hansch, C., Leo, A., and Taft, R. W. (1991) A survey of Hammett substituent constants and resonance and field parameters. Chem. Rev. **91**, 165-195.

30. Rai, B. L., Dekhordi, L. S., Khodr, H., Jin, Y., Liu, Z. D., and Hider, R. C. (1998) Synthesis, physicochemical properties, and evaluation of N-substituted-2-alkyl-3-hydroxy-4(1*H*)-pyridinones. *J. Med. Chem.* **41**, 3347-3359.

31. Xie, Y. Y., Lu, Z. D., Kong, X. L., Zhou, T., Bansal, S., and Hider, R. (2016) Systematic comparison of the mono-, dimethyl- and trimethyl 3-hydroxy-4(1*H*)-pyridones - Attempted optimization of the orally active iron chelator, deferiprone. *Eur. J. Med. Chem.* **115**, 132-140.

32. Piyamongkol, S., Ma, Y. M., Kong, X. L., Liu, Z. D., Aytemir, M. D., van der Helm, D., and Hider, R. C. (2010) Amido-3-hydroxypyridin-4-ones as Iron(III) Ligands. *Chemistry - A European Journal* **16**, 6374-6381.

33. Nunes, A., Podinovskaia, M., Leite, A., Gameiro, P., Zhou, T., Ma, Y. M., Kong, X. L., Schaible, U. E., Hider, R. C., and Rangel, M. (2010) Fluorescent 3-hydroxy-4-pyridinone hexadentate iron chelators: intracellular distribution and the relevance to antimycobacterial properties. *J. Biol. Inorg. Chem.* **15**, 861-877.

34. Berry, D. J.(2011) *Chelators for Gallium-68 Radiopharmaceuticals*, PhD thesis, King's College London

35. Shannon, R. D. (1976) Revised effective ionic-radii and systematic studies of interatomic distances in halides and chalcogenides. *Acta Crystallogr. Section A* **32**, 751-767

36. Dobbin, P. S., Hider, R. C., Hall, A. D., Taylor, P. D., Sarpong, P., Porter, J. B., Xiao, G. Y., and Vanderhelm, D. (1993) Synthesis, physicochemical properties, and biological evaluation of N-substituted 2-alkyl-3-hydroxy-4(1*H*)-pyridinones - orally-active iron chelators with clinical potential. *J. Med. Chem.* **36**, 2448-2458.

4 *Tris*(hydroxypyridinone) chelators as a tool to influence the *in vivo* trafficking of gallium

4.1 Introduction

As discussed in the introductory chapters, gallium tends to accumulate in some tumours as well as in sites of inflammation/infection. This property has been widely exploited by the nuclear medicine community in the past, when ^{67}Ga-citrate scintigraphy was the method of choice for the diagnosis of several malignancies including lymphoma [1]. Use of ^{67}Ga-citrate in clinics has progressively diminished in the last three decades, and currently this radiotracer retains a niche application as a second-choice method for imaging tumour and infections, especially in developing countries where access to PET isotopes is still limited. [67]Ga imaging presents several issues, such as significant ^{67}Ga uptake in non-target organs and high variability in tumour uptake among different patients [2]. However, the principal factor underlying the abandonment of this technique was the concomitant advent of [^{18}F]FDG, whose advantages over ^{67}Ga imaging in cancer are multiple [3]. As well as better understood targeting mechanisms, importantly, [^{18}F]FDG PET scans possess higher sensitivity and resolution than images obtained with ^{67}Ga SPECT and planar imaging. Furthermore, [^{18}F]FDG offered the possibility of scanning patients only 1 hour after injection [2], greatly simplifying the clinical practice compared to ^{67}Ga, whose slow pharmacokinetics requires 48-72 hours between injection and imaging to obtain acceptable tumour-to-background contrast.

Unlike its SPECT analogue ^{67}Ga, the PET radiometal ^{68}Ga can generate high quality images, comparable to those obtained with [18]F. Although the higher positron energy of ^{68}Ga results in lower intrinsic resolution of the reconstructed images compared to [18]F [4], this is only important for preclinical instruments, since in clinical settings the limiting factor is the resolution of the scanner. Use of ^{68}Ga-citrate to image gallium-avid cancers could therefore represent an interesting alternative to [^{18}F]FDG, especially in those centres that have no access to a cyclotron but could afford a ^{68}Ga generator. Recently, the use of ^{68}Ga-citrate in the imaging of lung and prostate cancer has been evaluated in clinical trials [5,6].

On the other hand, the poor match between the short half-life of this isotope and the long time required to get sufficient tumour-to-background ratio remains a major issue in the use of ^{68}Ga salts for the imaging of cancer. A higher tumour-to-blood ratio and, accordingly, improved image contrast, could be achieved by clearance of residual

151

blood pool activity by treatment with a suitable Ga^{3+} chelator. Ideally, this blood clearance agent should be able to bind ^{68}Ga quickly in mild conditions and low concentration, but unable to remove activity from tumour cells.

In the past decades, different chelators have been investigated in their capability to bind Ga^{3+} *in vivo* or in biological systems, as a tool to better understand the biology of gallium [7], to assess the binding efficiency of a chelator [8], or notably, to evaluate the use of a chelator as a contrast-enhancing agent [9-16], when imaging tumours or abscesses.

In particular, deferoxamine (DFO) was extensively evaluated for this purpose in preclinical studies, and found able to increase the tumour-to-blood ^{67}Ga uptake ratio when administered at suitable time points after ^{67}Ga injection [10,11,16]. Doses and modes of administration varied among the studies, with the lowest doses being 40 mg/kg for intravenous (IV) administration and 160 mg/kg for intramuscular (IM) administration. Notably, DFO is already approved by the FDA as a treatment for iron overload, therefore its clinical translation as a blood clearance agent for Ga^{3+} would be facilitated [17]. However, the dosage investigated for these preclinical studies clearly exceed those for clinical administration of this chelator in the context of iron overload (0.25 mg/kg per min for a maximum of 60 mg/kg per day in the case of IV administration, 1 g in case of IM administration [18]). The contrast-enhancing capability of DFO was also evaluated in a preliminary clinical study, where 5 patients with known malignancies were injected intramuscularly with 10 mg/kg DFO 24 hours after ^{67}Ga injection, and then imaged 24 hours later. Although blood clearance effect was visible in the scintigraphy images, only small contrast enhancement compared to control images of the same patients was obtained [12].

THP^{Me} has attributes that make it a good candidate as a blood clearance agent for ^{68}Ga, owing to its fast radiolabelling and high affinity for ^{68}Ga. In addition, THP^{Me} is likely to be incapable of removing ^{68}Ga previously internalised in cancer cells, owing to the high hydrophilicity of its gallium complex (**Chapter 3**), which is unlikely to cross cell membranes. Although clinical use of the THP^{Me} molecule is not approved, use of THP^{Me} derivatives in clinical trials [19] could potentially facilitate clinical translation of THP^{Me} itself.

As an alternative to gallium salts, complexes of gallium could also be investigated to deliver $^{68}Ga^{3+}$ to tumours. A compound of interest is the *tris*(8-quinolonato) gallium(III) complex (also known as gallium-oxine, see **Chapter 2**), which has been investigated as an orally available gallium chemotherapeutic, with increased potency compared to

gallium salts [20]. Mechanisms of accumulation of gallium-oxine in tumours are still unclear [21], and is therefore unknown whether ^{68}Ga-oxine would benefit from a blood clearance step using a chelator such as THP^{Me}.

In this chapter, the ability of the *tris*(hydroxypyridinone) chelator THP^{Me} to influence the trafficking of gallium in biological systems has been investigated in normal animals and in a cancer model (both *in vitro* and *in vivo)*, with the aim of evaluating this chelator as a ^{68}Ga blood clearance agent for imaging applications. Both ^{68}Ga-acetate and ^{68}Ga-oxine were examined as a way to deliver ^{68}Ga^{3+} to cancer cells.

4.2 Materials and methods

4.2.1 General equipment and consumables

THP^{Me} was previously synthesized in Blower's laboratory according to published procedures [22]. 8-hydroxyquinoline (oxine) and ammonium acetate (99.999 % trace metal basis) were obtained from Sigma Aldrich and used without further purification. ^{67}Ga-chloride (0.1 M HCl solution) was purchased from Nordion. ^{68}Ga was eluted from an E&Z generator using high purity 0.1 M HCl (Fluka) in five fractions of 1 mL each.

Reverse-phase HPLC analysis was performed on an Agilent 1200 LC system, using an Agilent Eclipse XDB-C18 column (4.6 x 150 mm, 5 μm) with a 1 mL/min flow rate and UV detection at 214 nM, coupled to a LabLogic Flow-Count gamma detector with a sodium iodide probe (B-FC-3200). Mobile phase A contained 0.1 % TFA in water, mobile phase B was acetonitrile + 0.1 % TFA. Gradient: 0-5 min 98 % A, 5-25 min from 98 % A to 100 % B, 25-30 min 98 % A. Instant thin layer chromatography strips (iTLC-SG, Varian Medical Systems) were quantified using a LabLogic iTLCS reader. Quantification of radioactivity in cells and organs was performed using a LKB Wallac 1282 Compugamma gamma-counter.

4.2.2 Preparation of $^{67/68}$Ga-acetate

Acetate-buffered ^{68}Ga was prepared immediately before use by mixing 200 μL of the highest activity fraction of the generator eluate (30-40 MBq) with 200 μL of an aqueous solution of 0.25 M ammonium acetate to reach pH 5-6. ^{67}Ga-acetate was prepared in the same way from the ^{67}Ga-chloride solution. For *in vivo* experiments, maximum final concentration of ammonium acetate was kept under 0.125 M.

4.2.3 Preparation of ^{68}Ga-oxine

Radiolabelling and *in vitro* tests for ^{68}Ga-oxine were performed by the then Master's degree student Joanna Bartnicka, under my day-to-day supervision. Data analysis was performed entirely by me.

Radiolabelling of oxine was performed according to a modified literature procedure [12]. Briefly, an oxine solution in ethanol (500 μL, 0.017 M) was mixed with ammonium acetate (250 μL of a 0.5 M aqueous solution) and ^{68}Ga eluate (250 μL of the highest activity fraction). The radiolabelling mixture was heated at 50 °C for 5 min then applied to a Sep-Pak C18 Plus Light Cartridge (Waters), previously preconditioned with ethanol (5 mL) followed by water (5 mL), and eluted in ethanol in five fractions of 100 μL. iTLC analysis of the highest activity fraction was performed using

chloroform:methanol = 95:5 as a mobile phase [23] (Rf ^{68}Ga-oxine = 1, Rf unchelated ^{68}Ga =0). ^{68}Ga-oxine was diluted in ammonium acetate 0.25 M (for cell uptake studies) or PBS (for *in vivo* studies) to have a maximum of 10 % ethanol in the radiotracer formulation.

4.2.4 Radiolabelling of THP^{Me}

Radiolabelling of THP^{Me} was performed by mixing 100 µL of the highest activity ^{68}Ga eluate fraction (15-20 MBq) with 100 µL of the ligand ($\approx$ 20 µM, in 0.5 M ammonium acetate). Verification of the radiolabelling was carried out after 5 min by reverse-phase HPLC.

4.2.5 Cell culture

The A375 melanoma cell line [24] was provided by Sophia Karagiannis's group (KCL). Cell cultures were maintained at 37 °C in a humidified atmosphere of 5 % CO$_2$. High-glucose DMEM (4500 mg/L, Gibco^{TM}, ThermoFisher) supplemented with 10 % foetal calf serum, L-glutamine (2 mM), penicillin (100 units/mL), and streptomycin (0.1 mg/mL) was used as medium. A trypsin EDTA solution (0.05 % trypsin, 0.02 % EDTA in PBS) was used to passage the cells.

For experimental procedures, cells were harvested using trypsin EDTA solution, subsequently deactivated with complete medium. Cell density and viability were determined by 1:2 dilution in trypan blue solution and counting with a haemocytometer. All the experiments were performed under serum-free conditions using Hank's Balanced Salt Solution (HBSS) as a medium.

4.2.6 Uptake of ^{68}Ga-acetate in A375 melanoma cells

A375 cells were harvested, counted, washed twice and resuspended in HBSS (or HBSS + 0.5 % Bovine Serum Albumin (BSA), when checking the effect of BSA on ^{68}Ga uptake). Then they were transferred into microcentrifuge tubes (500 µL, 2 million cells/mL) and incubated with 5 µL of acetate-buffered ^{68}Ga (50-70 kBq/tube) at 37 °C. After 30 min the cells were centrifuged (3 min, 250 RCF) and the supernatant removed. Cell pellets were washed twice with ice-cold HBSS buffer (500 µL/wash) and the uptake measured by γ-counting. Supernatant and washes were also collected and counted. The percentage of the added activity that was taken up by the cells (% uptake) was determined dividing the CPM obtained for the pellet-containing tube by the sum of CPM for pellet, supernatant and washes combined and multiplying by 100. As a control for non-specific binding to plastic, microcentrifuge tubes containing only buffer were treated in the same way. Each experiment was performed in triplicate.

4.2.7   Uptake of ^{68}Ga-oxine vs ^{68}Ga-acetate in A375 cells

A375 cells were trypsinised, washed twice and re-suspended in HBSS at 2 million cells/mL. 500 μL of cell suspension or HBSS only, as a control for non-specific binding to plastic, were transferred to microcentrifuge tubes and incubated with ^{68}Ga-oxine/acetate (5 μL, 50-70 kBq) for 60 min at 37 °C. Tubes were then centrifuged for 3 min at 250 RCF, supernatant removed, and cell pellet resuspended in HBSS (500 μL). This step was repeated twice. Activity in the cell pellet and in the supernatant and washings was determined by γ-counting.

4.2.8   Effect of THP^{Me} on the cellular uptake of ^{68}Ga-acetate

THP^{Me} solutions in saline (1 mM, 100 μM and 10 μM) were prepared by serial dilutions. A375 cells were harvested, counted, washed twice and resuspended in HBSS, then transferred into microcentrifuge tubes (500 μL, 2 million cells/mL).

In a first set of experiments, referred to as the "pre-^{68}Ga" study, cells were treated with 50 μL of the relevant THP^{Me} solution (or saline as a control) and incubated 37 °C for 30 min, before addition of 5 μL of acetate-buffered ^{68}Ga ($\approx$ 50 kBq/tube) and subsequent incubation at 37 °C for further 30 min. In a second "post-^{68}Ga" study, the order of the two incubations was reversed. The cells were centrifuged and washed as previously described, then cell pellets and the sum of supernatant/washings were γ-counted and the percentage uptake determined. Each experiment was performed in triplicate and repeated at least twice.

4.2.9   Cellular localisation of ^{67}Ga/^{68}Ga uptake in A375 cells

The uptake assay was performed as described above, assessing uptake of acetate-buffered ^{67}Ga ($\approx$ 50 kBq/tube), ^{68}Ga ($\approx$ 50 kBq/tube) or a mixture of the two (25 KBq of ^{67}Ga + 25 kBq ^{68}Ga per tube) and how this was affected by pre-Ga/post-Ga incubation with 100 mM of THP^{Me}. The cells were centrifuged and washed as previously described, then an acid wash was performed according to a published procedure [25]. Briefly, after the final wash with HBSS the cells were exposed to glycine 0.1 M (pH 2.5) for 6 min, then the cells were centrifuged and the pellets separated from the acid wash. Cell pellets, supernatant/washing and acid wash samples were then γ-counted. When γ-counting samples containing both isotopes, narrow energy windows were set on the γ-counter (175-235 bin for ^{68}Ga, and 101-115 bin for ^{67}Ga) to minimise spill over for each isotope. Each experiment was performed in triplicate.

4.2.10 Preparation of microautoradiography samples

Microautoradiography samples were prepared according to a modified literature procedure [26,27]. A375 cells were harvested, counted, washed twice and resuspended in HBSS, then transferred into microcentrifuge tubes (500 μL, 2 million cells/mL) and incubated with 50 kBq of ^{67}Ga-acetate for 45 min. After this time the cells were centrifuged (3 min, 250 RCF), the supernatant removed and the pellets washed twice with ice-cold HBSS buffer (500 μL/wash). Cells were then fixed by treatment with a 4 % formaldehyde solution for 20 min at room temperature, washed twice with PBS and resuspended in 200 μL of PBS. The suspension was embedded in 400 μL of warm gelatine (final concentration 12 % w/v in PBS) by gentle mixing and, after solidification at 4 °C, the resulting samples were snap-frozen in isopentane, cut into 10 μm slices using a cryostat (Bright Instrument Company Ltd) and the slices collected on positively charged polylysine-coated slides. Slices of samples containing untreated cells or ^{67}Ga in PBS only were also prepared as no-gallium and no-cells control, respectively.

4.2.11 Microautoradiography

Microautoradiography was performed according to a procedure previously established in Blower's laboratory [27]. In a dark room, the slides were coated with a nuclear emulsion (37.5 % v/v Ilford K2 emulsion in gel form, 0.01 % v/v glycerol in deionised water), left to dry on a level plate and then incubated overnight in the dark at 4 °C. The following day, slides were warmed to room temperature and then developed by incubating them in a developer buffer (Kodak D19) for 5 min. The developing process was then terminated by incubation in 1 % acetic acid solution (30 seconds) and the slides were finally dipped into a 0.5 % gelatine solution to prevent slice detachment from the slides. Once dried the slides were fixed by incubation with (sodium thiosulphate 30 % w/v in deionised water) for 5 min and washed in deionised water for 10 min. Coverslips were placed onto the slides using a DAPI-containing mounting solution and the slides were then imaged using an EVOS FL Cell imaging microscope (Life Technologies) using both fluorescence in the blue channel (λ_{exc} = 390 nm, λ_{em} ≈ 460 nm) and transmitted light to image cells nuclei and silver grains respectively.

4.2.12 Establishment of A375 xenografts in NSG mice

Female NOD scid gamma mice (NSG mice) between 42-49 days old were obtained from Charles River. Animals were allowed to acclimatise for at least a week after arrival prior to tumour inoculation. Establishment of the xenograft model was carried out by subcutaneous injection of A375 cells above the shoulder. Briefly,

A375 cells were trypsinised, washed twice with PBS and resuspended in PBS at 1 million cells/100 μL. Mice were anaesthetised using isoflurane (2.5 %, O_2 flow rate: 1 L/min) and 100 μL of PBS containing 1 million A375 cells was injected subcutaneously above the shoulder (right shoulder for the first study, left shoulder for the second study) after shaving of the area. Mice were monitored daily and, after tumours became palpable, tumour diameters were measured regularly until a mean orthogonal diameter of ≈ 8 mm was reached. An example of tumour growth curve (obtained for the second study) is reported below.
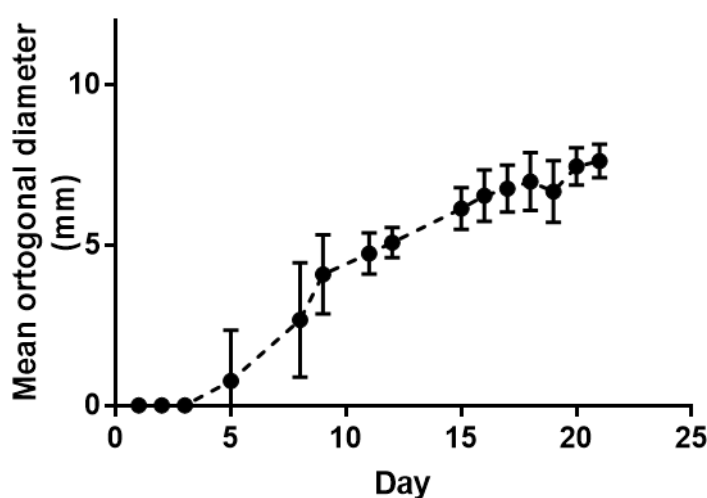
Figure 4.1. Growth curve determined for A375 xenografts in NSG mice. Mean orthogonal diameter was measured daily for all mice and is reported as mean ± SD (N = 15).

4.2.13 Biodistribution and clearance studies

Biodistribution and clearance experiments included both PET/CT imaging and *ex vivo* biodistribution. BALB/c mice (female, 7-9 weeks, Charles River) were used for clearance experiments in healthy animals. NSG mice (female, 7-9 weeks, Charles River) were used for experiments with A375 xenograft.

PET and CT scans were carried out on a nanoScan® PET/CT (Mediso Medical Imaging Systems) [28] with the following parameters:

- PET: 1:5 coincidence, 5 ns time window, 400-600 KeV energy window.

- CT: 180 projection, 45 KVp.

Respiration rate and bed temperature were monitored throughout all scans. PET/CT datasets were reconstructed using the Monte-Carlo based full 3D iterative algorithm Tera-Tomo (Mediso Medical Imaging Systems) [29] using 1:3 coincidence and a voxel

size of 0.21 x 0.21 x 0.21 mm^3. Images were analysed using VivoQuant software (inviCRO), which enables the co-registration of PET and CT images and the delineation of regions of interest for quantification of activity in specific organs (Otsu thresholding).

Mice were anesthetised with isoflurane (O$_2$ flow rate: 1.0-1.5 L/min and isoflurane levels: 2-2.5 %) and kept anaesthetised for all the procedure so that dynamic PET scan could be performed. Activity was injected into the tail vein using an in-house made catheter (25 µL volume) or an insulin syringe (0.3 mL, Terumo), followed, where applicable, with injection of the chelator after a defined time interval. Relevant PET/CT scans were performed. Upon procedure completion, animals were sacrificed by neck dislocation while still anesthetised, tissues harvested and *ex vivo* biodistribution assessed by γ-counting. Tubes containing different volumes of the radiotracer solution (corresponding to different % ID) were also counted as internal standards and the calibration curve obtained by linear regression of the data was used to convert measured CPM in % ID for every organ. An example of calibration curve is reported in **Figure 4.2**.
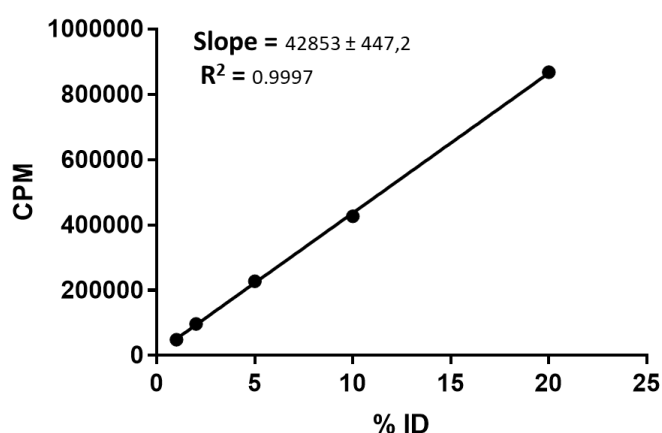
Figure 4.2. Example of a calibration curve obtained by linear regression of CPM/%ID data from internal standards.

Residual activity in the tail (due to an imperfect IV injection) was subtracted from the total activity injected, and tail-corrected % ID was calculated for each organ. % ID/g was obtained by dividing the tail-corrected % ID of each organ by its weight. Details for each experiment are reported in the following paragraphs.

Dose finding experiment (pilot study)

BALB/c mice were positioned on the PET/CT scanner bed and cannulated at the tail vein. A 90 min PET scan was started. Mice were injected with 100 µL of ^{68}Ga-acetate (5-10 MBq), followed, after 45 min, by 100 µL of THP[Me] solution in saline (amounts are

reported in **Table 4.1**, each dose was tested in at least one mouse, two mice were used for 0 and 20 µg doses). When pH of the THP^{Me} solution was lower than 5, pH was adjusted to 7 using 0.1 M NaOH. A CT scan was performed upon completion of the PET scan. Mice were culled at 100 min post ^{68}Ga-injection.

Table 4.1. *Doses of THP^{Me} (hydrochloride salt) utilised for in vivo experiments.*

Doses of THP^{Me}		
Amount/µg	Amount/nmol	neutralised
0	0	No
1	1.2	No
5	6	No
20	24	No
100	118	Yes
500	590	Yes

Ex vivo biodistribution was performed by collecting the whole organ in the case of tail, heart, lungs, liver, spleen, stomach and kidneys. The femur was used as representative of bone. Skin and fur were collected from the abdomen of the mouse and muscle was taken from the hindlimb. Only part of the small and large intestine was collected. Stomach, small and large intestine were emptied prior to counting. All organs were washed in water to eliminate residual blood. Urine of the mice treated with 0 or 20 µg of THP^{Me} (≈100 µL) was analysed by reverse-phase HPLC

Delay finding study

BALB/c mice were anaesthetised and injected with ^{68}Ga-acetate (100 µL, 5-10 MBq) *via* a tail vein cannula, as previously described. 100 µL of the relevant THP^{Me} solution (0, 1, 5 or 20 µg) was administered in the same way at 5 or 90 min after the first injection. For those animals that were scanned (1 mouse per time point), CT was first performed, followed by start of a PET scan and activity injection. All animals were kept under anaesthesia for the duration of the experiment. Mice were culled 15 min after the second injection (20 or 105 min post ^{68}Ga-injection). Biodistribution was determined as previously described.

^{68}Ga-acetate vs ^{68}Ga-oxine accumulation in A375 xenografts

Mice were anaesthetised and injected with ^{68}Ga-acetate or ^{68}Ga-oxine (200 µL, 13-18 MBq, 5 mice per group) *via* a tail vein injection. Mice were kept under anaesthesia for the duration of the experiment. After 4 hours mice were sacrificed and *ex vivo* biodistribution determined as described earlier. Three animals per group were also imaged for the whole experiment time.

THP^{Me} vs DFO Clearance in healthy mice and A375 xenografts

The same clearance experiment was performed in healthy mice (9 subjects, BALB/c) and immunocompromised mice bearing A375 melanoma xenografts (15 subjects, NSG mice). In both cases, mice were anaesthetised and injected with ^{68}Ga-acetate (100 µL, ≈10 MBq) *via* a tail vein injection, as previously described. After 1 hour, 50 µL of a clearance agent solution (24 nmol of THP^{Me} or DFO, or saline as a control) was administered in the same way. At least one mouse per group was imaged before and after the second injection (PET from 20 to 45 min and from 80 to 105 min after injection of ^{68}Ga-acetate). Mice were kept anaesthetised for the whole experiment, sacrificed at 130 min post ^{68}Ga injection and *ex vivo* biodistribution performed as described above. No emptying of stomach and intestines was carried out in these experiments and blood was collected by cardiac puncture.

4.2.14 Power calculations and statistical analysis of the data

Sample size for *in vivo* experiments was calculated in order to have a statistical power (1-ß) of 80% and a type I error probability (α) of 5%. A minimal sample size of n = 3 was calculated, to detect a difference between a signal-to-noise ratio of 10 ± 2 (experimental group) versus 5 ± 2 (control) when performing one-way analysis of variances (ANOVA) followed by up to 2 pairwise comparisons between groups (THP^{Me} vs DFO experiments). When 3 pairwise comparisons were considered (delay finding experiment) a minimal sample size of n = 4 was calculated.

Data obtained for *in vitro* and *in vivo* studies were analysed using GraphPad Prism, version 7.04 for Windows (GraphPad software). Unpaired, two-tailed Student's t-test was generally used when comparing two groups. One-way ANOVA was used to analyse results where more than two groups were compared. In this case, Tukey post-hoc test was employed to correct for multiple comparisons when those were performed between all the groups. Dunnett post-hoc test was used for comparison between each of the experimental groups and the control group. Whenever variances of groups were found to be significantly different (according to an F test when comparing two groups, and to both Brown-Forsythe and Bartlett's test when comparing more than two groups) the data were re-analysed using a Welch-adjusted t-test, which does not assume equal variances among groups.

4.3 Results

This work was aimed at evaluating the potential of THP^{Me} as a blood clearance agent to increase tumour-to-background contrast in ^{68}Ga salts imaging of cancer, using an A375 human melanoma model. To achieve this goal, two distinct streams of work were carried out. On one hand, the ^{68}Ga-acetate uptake in the selected model was investigated, both *in vitro* and *in vivo* and compared with the uptake of a different gallium species such as ^{68}Ga-oxine. On the other hand, the ability of THP^{Me} to bind gallium in biologically relevant contexts and to influence the distribution of this radiometal *in vitro* and *in vivo* was examined. These two parallel streams converged into a final *in vivo* experiment, where the use of THP^{Me} as a blood clearance agent was tested in mice bearing A375 melanoma xenografts.

4.3.1 *In vitro* assays

The A375 cell line was selected as a tumour model for this work based on preliminary evidence of ^{68}Ga-acetate uptake in A375 xenografts in NOD-SCID mice by our group (unpublished data). However, before replicating the same *in vivo* study and testing the clearance effect of THP^{Me} in tumour bearing animals, a set of *in vitro* experiments was performed to further characterise ^{68}Ga uptake in the selected cell line.

Cellular uptake of ^{68}Ga-acetate

The uptake of ^{68}Ga in A375 cells *in vitro* was evaluated using uptake assays in suspension, by measuring the percentage of activity retained by 10^6 cells compared to the total activity (calculated as the sum of the activity in the pellet, supernatant and washings). Ammonium acetate was used to buffer the ^{68}Ga eluate to pH of about 5.5 before addition to the cells. Different conditions were tested in different studies as described in the following paragraphs.

In a preliminary uptake study the effect of different amounts of ^{68}Ga (18-74 kBq) was investigated to establish a range of activity for which the percentage uptake did not vary considerably. As reported in **Figure 4.3**, no significant difference in the uptake was found for the range of activity tested (18-74 kBq/tube). In the following experiments the amount of activity added to each tube was kept in the range 50-70 kBq/tube.

The ratio between the concentration of activity in the cells pellet and in the supernatant/washings was also calculated (**Figure 4.3 B**), considering A375 cells in suspension as spheres with an average diameter of 16 μm [30]. This value provides a measure of the ^{68}Ga accumulation in cells, which is independent from the number of

cells used. Notably, the average % uptake of 5.5 ± 1.3 measured in this experiment over the three groups, corresponds to a 38 ± 9 higher concentration of activity in the cells pellet compared to the HBSS buffer.
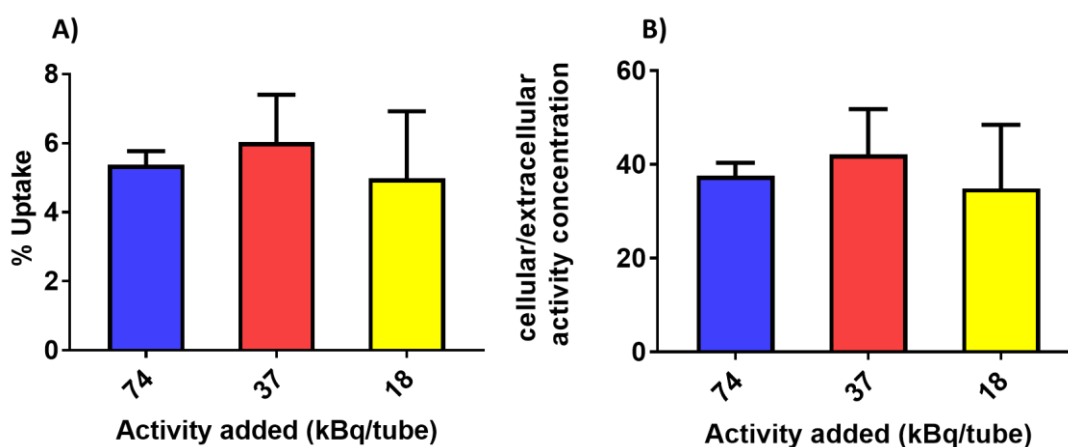
Figure 4.3. *Uptake of ^{68}Ga-acetate in A375 cells treated with different amount of activity (18-74 kBq), expressed both as a % Uptake (A) and as a ratio between cellular and extracellular concentration of activity (B). Data are represented as mean ± SD (N = 3) ANOVA analysis of the data was performed followed by Tukey post-hoc test for multiple comparisons between groups. No significant difference between the considered groups was found.*

Notably, this first experiment was performed in HBSS buffer containing 0.5 % of BSA, which is routinely added in uptake experiments by many investigators to avoid non-specific uptake of the activity (*e.g.* due to activity sticking to the plastic walls of a plate or a microcentrifuge tube). However, BSA can also interact with the unchelated radiometal, potentially altering its cellular uptake and the ability of a chelator to sequester the radiometal. Therefore, in a second experiment the effect of BSA on the uptake of ^{68}Ga was evaluated both in A375 cells and in a sham experiment, where the activity was added to microcentrifuge tubes containing the same buffer (with or without BSA) but no cells, to determine the fraction of uptake due to non-specific binding to plastic (**Figure 4.4**).
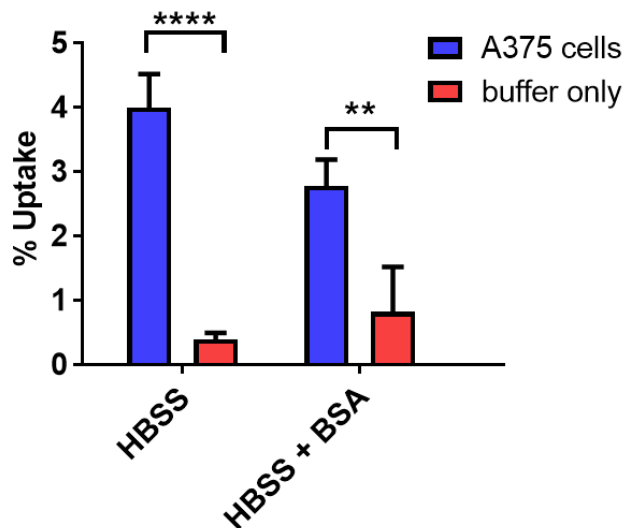
Figure 4.4. *Preliminary assay evaluating the effect of BSA presence in the buffer on ^{68}Ga uptake in A375 cells. Data are represented as mean ± SD (N = 3) Statistical analysis of the data was performed by ANOVA followed by Tukey post-hoc test for multiple comparisons between groups P values are defined as follows: **= 0.0048, and **** = P ≤ 0.0001.*

Notably, although no significant difference was found between cellular ^{68}Ga uptake in the presence of BSA and that in HBSS alone, a P value of 0.06 was calculated suggesting that % uptake in HBSS alone is higher, although the difference is not statistically significant owing to the low number of replicates. No difference was visible between ^{68}Ga uptake in HBSS only samples with or without BSA. Significant difference was found for both HBSS and HBSS + BSA groups when comparing the uptake in cells and in buffer only samples. Interestingly, this difference was even more pronounced in the absence of BSA (P value < 0.0001). Overall this experiment showed that BSA addition to the buffer was not necessary to minimise non-specific uptake of the microcentrifuge tube and subsequent experiments were all performed in HBSS only.

Notably, variability in the total uptake (2-10 %) was found between experiments performed on different days (different generator elution, different batch of cells). Therefore, another set of experiments was performed to verify that a change in cell culturing factors such as different flask confluency, different passage number could not significantly affect the results. Ruling out possible causes of variability was particularly important in our serum-free uptake studies, for which the measured ^{68}Ga uptake must be attributed to transferrin-independent pathways, whose mechanisms are still not understood. These additional experiments (**Figure 4.5**) showed that neither the confluency nor the passage number of the cells used in the assay had a significant effect on their ^{68}Ga uptake.
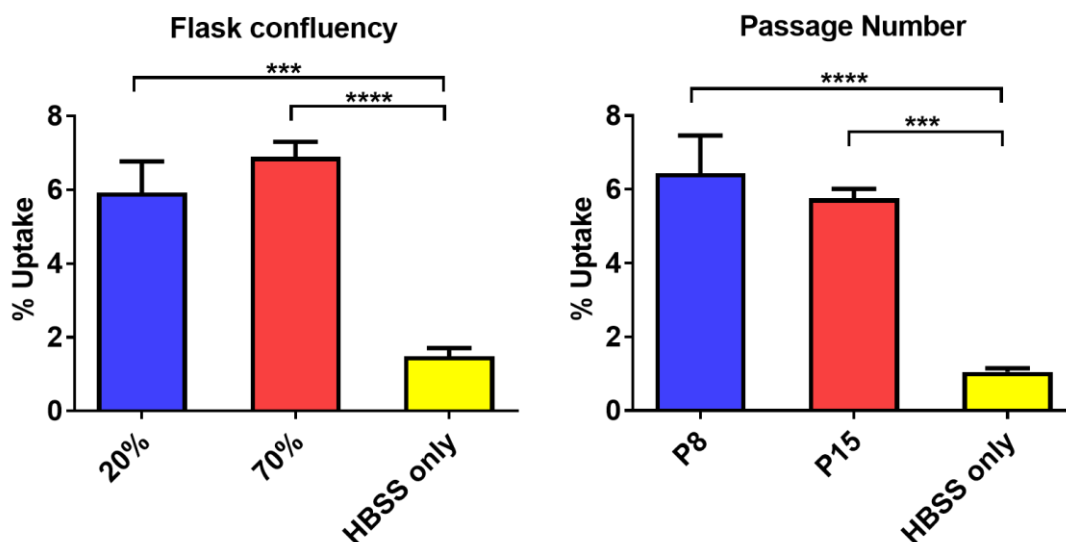
Figure 4.5. Uptake assays evaluating the effect of difference confluency and passage number on the ^{68}Ga cells uptake. Data are represented as mean ± SD (N = 3) ANOVA analysis of the data was performed followed by Tukey post-hoc test for multiple comparisons between groups. P values are defined as follows: *** = P ≤ 0.001, and **** = P ≤ 0.0001.

In the subsequent experiments, a normalised uptake was used, with the average ^{68}Ga-acetate uptake (control group) set to 1 and variation observed for the experimental condition expressed as a fraction of the original uptake. In this way, it was possible to average data obtained from experiments repeated in different days, irrespective of the absolute percentage uptake measured in each individual experiment.

^{68}Ga-acetate vs ^{68}Ga-oxine

^{68}Ga-oxine could in principle be used as an alternative way to deliver ^{68}Ga to tumour cells, exploiting the ionophore character of the oxine ligand, which is able to cross the cell membrane to deliver its metal ion load. ^{68}Ga-oxine was prepared according to literature procedures [31] and radiochemical purity > 95 % was verified by iTLC-SG.

Uptake of ^{68}Ga-oxine in A375 cells was assessed in comparison with that of ^{68}Ga-acetate in the same cell line. As expected, given the increased lipophilicity of the oxine complex [32], a significantly higher cellular uptake of ^{68}Ga-oxine compared to ^{68}Ga-acetate (≈ threefold higher uptake, **Figure 4.6 A**) was found. However, there was also a significantly higher plastic binding for ^{68}Ga-oxine. Data were therefore corrected for the respective non-specific uptake and reanalysed (**Figure 4.6 B**), showing a significant difference between the uptake of the two ^{68}Ga species, with a twofold increase in uptake measured for ^{68}Ga-oxine compared to ^{68}Ga-acetate.
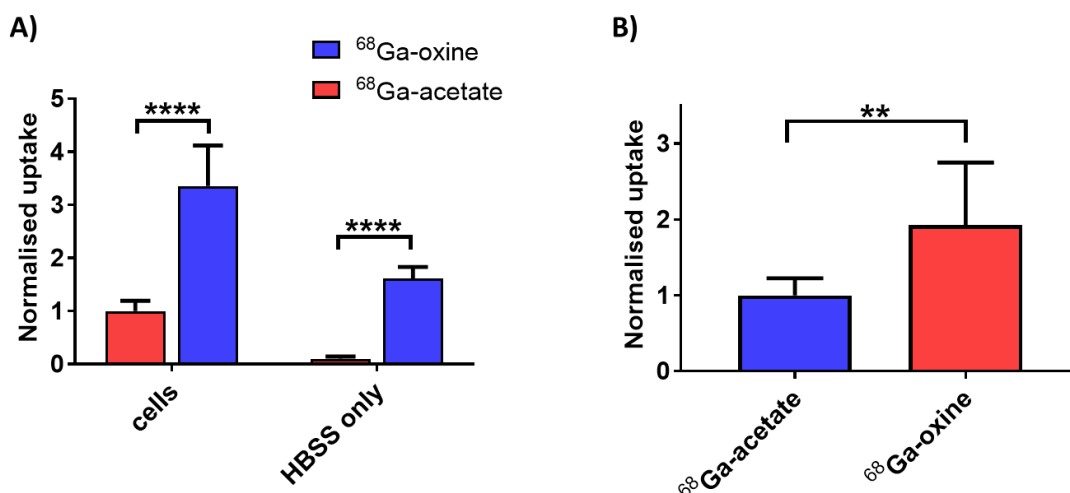
Figure 4.6. *Comparison between cellular uptake of ^{68}Ga-acetate and ^{68}Ga-oxine in A375 cells, expressed as a normalised uptake w/r to A375 uptake of ^{68}Ga-acetate (mean ± SD, n = 8). Data for experimental groups are represented together with their buffer-only control (A) or already corrected for plastic uptake (B). A t-test to evaluate the difference between ^{68}Ga-acetate and ^{68}Ga-oxine uptake was carried out for every group. P values are defined as follows: ** = P ≤ 0.01, and **** = P ≤ 0.0001.*

Effect of THP^{Me} on the cellular uptake of ^{68}Ga

Two different experiments were carried out to examine whether, and to what extent, THP^{Me} could influence the cellular uptake of ^{68}Ga. The first set of experiments was aimed at evaluating whether the presence of THP^{Me} in the system could prevent or reduce cellular uptake of activity. In these experiments, referred to as the "pre-^{68}Ga" studies, ^{68}Ga was added to cells already incubated for 30 min with different concentration of THP^{Me} in saline (or just saline as a negative control). Incubation was carried out for a further 30 min upon ^{68}Ga addition, followed by washings and determination of the cellular uptake. In a second set of experiments, the ability of THP^{Me} to remove ^{68}Ga already taken up by cells was evaluated. In these experiments, referred to as "post-^{68}Ga" studies, the order of the two additions was reversed: cells were first incubated for 30 min with ^{68}Ga and THP^{Me} was then added to the system. Results for both studies are reported in **Figure 4.7**. ^{68}Ga binding to plastic was also measured with buffer-only samples containing THP^{Me}, but values were very high and erratic and were therefore not considered.
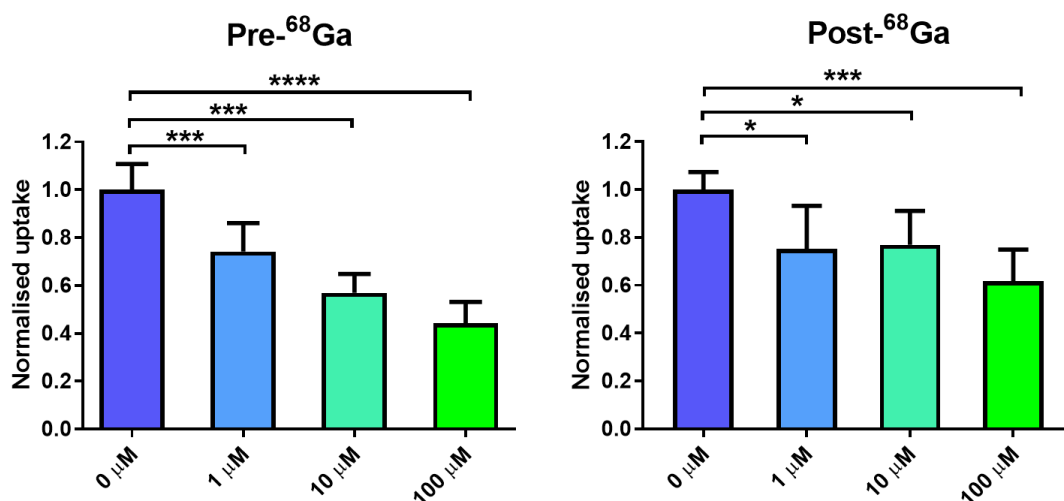
Figure 4.7. *^{68}Ga uptake in A375 cells at different THP^{Me} concentrations, expressed as a normalised uptake with respect to the 0 µM control, for cells treated with the chelator before (pre-^{68}Ga) or after (post-^{68}Ga) incubation with ^{68}Ga-acetate. Values are expressed as mean ± SD (N = 6). ANOVA analysis of the data was performed followed by Dunnett post-hoc test for multiple comparisons between groups. P values are defined as follows: * = P ≤ 0.05, *** = P ≤ 0.001 and **** = P ≤ 0.0001.*

The significant decrease in ^{68}Ga uptake observed in the presence of THP^{Me} for both experiments, demonstrates that, in both the conditions tested, chelator binding to ^{68}Ga is competing with cellular uptake of the radiometal. Notably, this also implies that the radiolabelled complex [^{68}Ga(THP^{Me})] does not accumulate in A375 cells (or accumulates less than unchelated ^{68}Ga). In the pre-^{68}Ga experiment, this decrease was more marked and showed a concentration dependent trend. This was expected as, in this study, the chelator starts to compete with cellular uptake of ^{68}Ga from time 0 after addition of the radiometal. Concentration dependence of the decrease reflects the increased ability of THP^{Me} to compete for ^{68}Ga binding when present at higher concentration. The less marked decrease in uptake observed for the post-^{68}Ga experiment suggests that addition of the chelator to cells already incubated with ^{68}Ga can only hamper further uptake of the radiometal, but cannot deplete the intracellular pool of ^{68}Ga. No obvious concentration dependent trend was visible for the post-^{68}Ga experiment although the maximum decrease in uptake was found at the highest concentration of the chelator.

The two experiments were repeated, for the highest concentration group and the control, with the addition of an acid wash step, to strip any activity bound to the surface of the cells, thus discriminating membrane bound activity from the intracellular pool. This allowed further investigation on the distribution of the activity in the cells and how this could be affected by THP^{Me}. Results are presented in **Figure 4.8**.
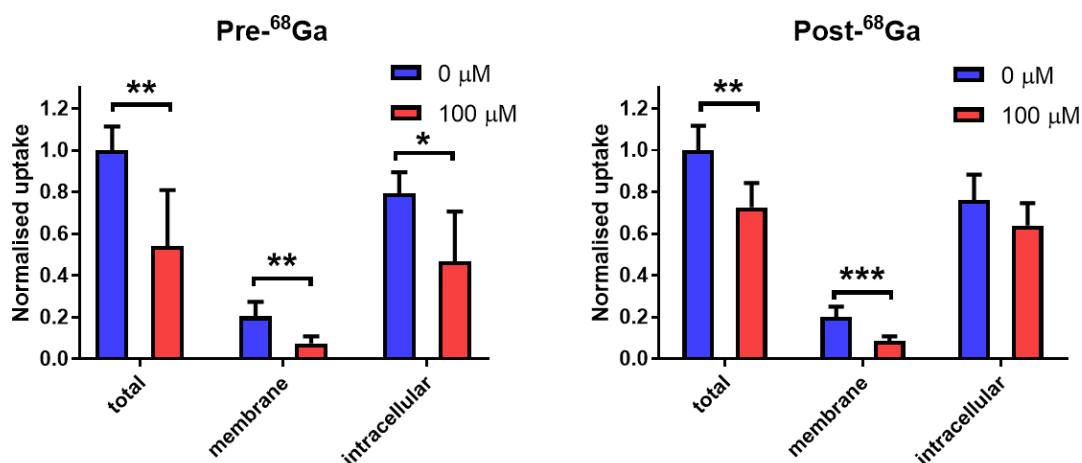
Figure 4.8. *^{68}Ga uptake in A375 cells with and without THP^{Me} treatment, expressed as normalised uptake (mean ± SD, N = 6) for both pre-^{68}Ga and post-^{68}Ga experiments. For all the samples an acid wash was performed to distinguish between intracellular and membrane uptake. A t-test to evaluate the difference between THP^{Me} treated samples and control was carried out for every group (* = P ≤ 0.05, ** = P ≤ 0.01, *** = P ≤ 0.001).*

As already observed in the previous study, addition of THP^{Me} before incubation with the radiometal resulted in a larger decrease in total ^{68}Ga uptake (to 54 % of that measured in the absence of THP^{Me}), compared to addition of THP^{Me} after 30 min of incubation (73 % of the uptake measured in the absence of THP^{Me}). Notably, the vast majority of the activity was located intracellularly for all the considered groups and this percentage increased for the THP^{Me} treated groups. In fact, while the membrane bound activity was drastically reduced for both experiments (to 36 and 43 % of that in the absence of THP^{Me} for the pre-^{68}Ga and post-^{68}Ga experiments, respectively), a less marked reduction was found for the intracellular pool of ^{68}Ga. In particular, for the post-^{68}Ga experiment, the percentage of intracellular activity only decreased by 16 % compared to the untreated sample, while a 51 % decrease was measured for the pre-^{68}Ga experiment. These results agree with the hypothesis that the intracellular pool of gallium is not readily accessible to THP^{Me}, which can only chelate the radiometal in the extracellular solution, thus preventing its cellular uptake. THP^{Me} affects the percentage of intracellular activity to a lesser extent in the post-^{68}Ga experiment, because in this case a large part of the activity has already been internalised before addition of the chelator. Notably, although no significant difference was found between the intracellular uptake groups for the post-^{68}Ga experiment, the low P value calculated (P = 0.09) suggests that a difference may be present and detectable when increasing the number of replicates.

Microautoradiography and ⁶⁷Ga uptake assays

Microautoradiography (MAR) was used to further investigate the uptake of gallium in the A375 cell line. This technique allows visualisation of the activity taken up by single cells as dark silver grains in bright field microscopy images. In MAR experiments, cells are treated with the radioisotope and sectioned in thin slices upon freezing and/or fixation/embedding in a suitable matrix. Sections are immobilised on a slide and then covered with a thin film of a nuclear emulsion containing silver bromide. Interaction of AgBr with the particulate emission of the radionuclide results in formation of silver grains that can be visualised using bright field microscopy. Generally, sensitivity of this technique increases with the half-life of the radionuclide and the abundance of low energy electron emissions. On the contrary high-energy emission and large thickness of section and films impair the spatial resolution of MAR images [26]. Accordingly, ^{68}Ga could not be used in this experiment and was replaced by ^{67}Ga, for which MAR has been previously reported [33]. The amount of radioactivity added per tube was kept the same as in the uptake studies (50-70 kBq/tube). Cells were fixed and embedded in gelatine prior to snap-freezing in isopentane, and sections were cut at a 10 μm thickness with a cryostat.

Some representative MAR images (blue channel and bright field images) are reported below (**Figure 4.9**) for ^{67}Ga treated cells.
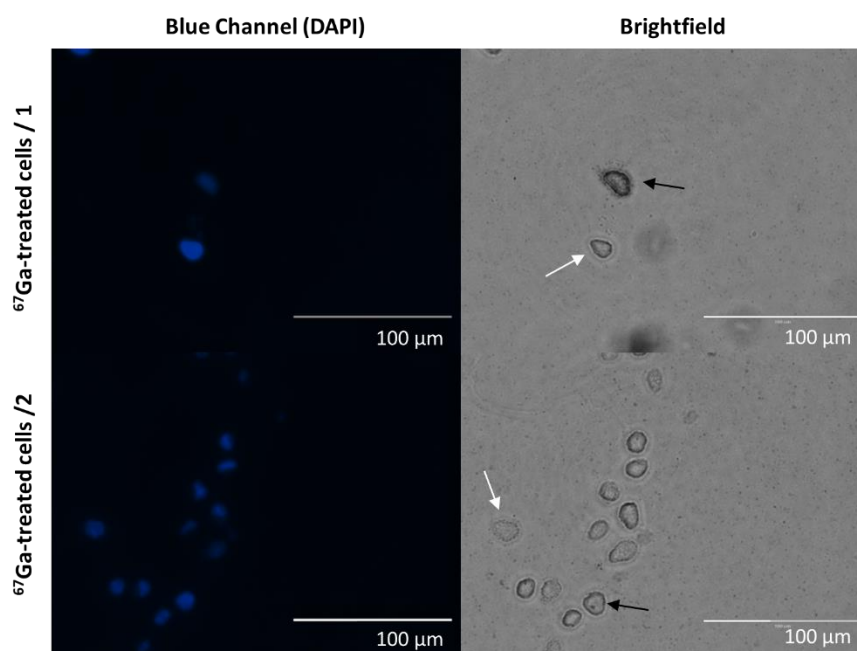
Figure 4.9. *Microautoradiography images of A375 cells treated with ^{67}Ga. Blue fluorescence (DAPI) images are displayed on the left, bright field transmitted light images are on the right. Arrows indicate cells where radiometal accumulation is evident (black arrows) or low/absent (white arrow).*

Representative images for control samples such as the cells only (no gallium) sample and the gallium only (no cells) sample are also reported in **Figure 4.10**.
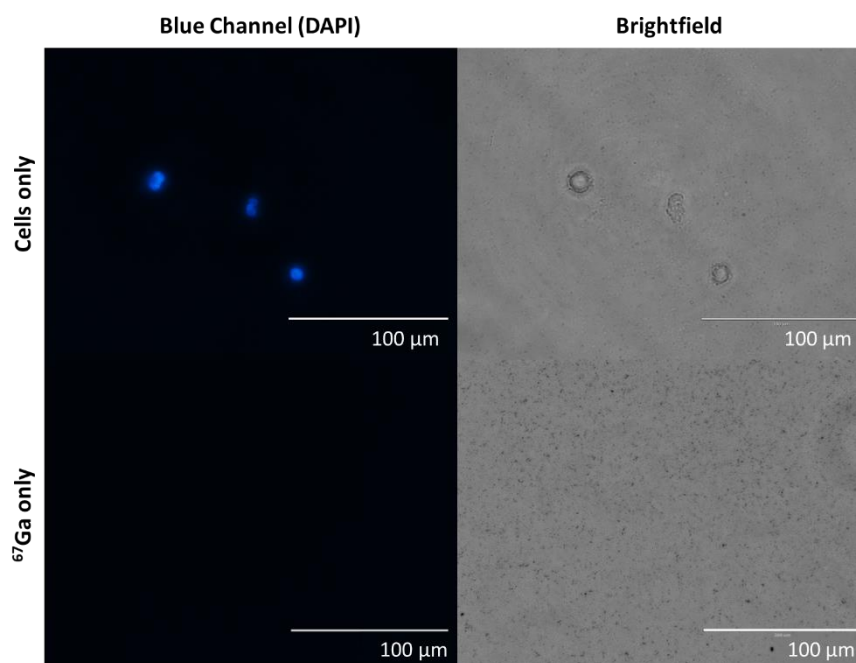
Figure 4.10. *Microautoradiography images of cells only sample (no ⁶⁷Ga treatment) and gallium only samples (no cells). Blue fluorescence (DAPI) images are displayed on the left, bright field transmitted light images are on the right.*

MAR images for ^{67}Ga treated cells clearly show cellular uptake of ^{67}Ga both at a surface and intracellular level. On the contrary, a uniform distribution of the activity was seen in the ^{67}Ga-only control, while almost no silver grains were found in the cells-only samples. This technique revealed a highly inhomogeneous distribution of the activity in the cells, with many cells showing little or no evidence of ^{67}Ga uptake and others taking up a high level of activity. Interestingly, these images also showed how the activity seemed prevalently located at the membrane level in contrast with the results obtained for ^{68}Ga uptake assays.

To verify whether this difference in distribution was due to the different gallium isotope used in this experiment, the uptake assay with acid wash was repeated using ^{67}Ga. Evaluation of the effects of pre-^{67}Ga and post-^{67}Ga incubation with THP^{Me} was also included. Results are reported in **Figure 4.11**.
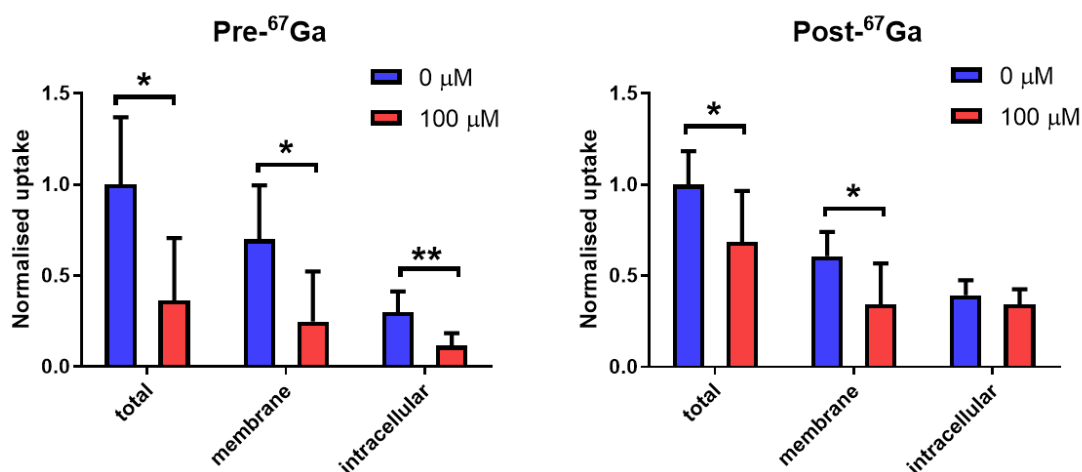
Figure 4.11. ^{67}Ga uptake in A375 cells with and without THP^{Me} treatment expressed as normalised uptake (mean ± SD, n = 6) for both pre-^{67}Ga and post-^{67}Ga experiments. For all the samples an acid wash was carried out to distinguish between intracellular and membrane uptake. A t-test to evaluate the difference between THP^{Me} treated samples and control was carried out for every group (* = P ≤ 0.05, ** = P ≤ 0.01).

Notably, similar to what was seen in the MAR images, membrane-bound activity was higher than the intracellular uptake for this ^{67}Ga uptake study in contrast to what was previously observed for the same experiment with ^{68}Ga. Interestingly, the effect of THP^{Me} treatment was still significant for all groups except for the intracellular uptake in the post-^{68}Ga study where no effect was noted (P = 0.33).

Since isotopes of the same element are expected to possess identical chemical properties, we hypothesised that the different distribution pattern was imputable to the different molarity of gallium in the samples for the ^{67}Ga and the ^{68}Ga experiments. In fact, in both experiments cells were treated with the same amount of activity (50 kBq). However, this corresponds to a different number of mole (and therefore concentration) of the radioisotopes in the sample, according to the equation reported below for a radioisotope "*i*":

$$Activity_i = \frac{ln2 N_A n_i}{t_{1/2_i}}$$

where activity is expressed in Bq, N_a is the Avogadro's number, n_i the number of moles of the isotope and $t_{1/2\,i}$ its half-life expressed in seconds [34]. Since ^{67}Ga has a 70-fold longer half-life than ^{68}Ga, this results in a 70-fold higher concentration of Ga^{3+} for the same activity in the same total volume in the case of ^{67}Ga. This higher concentration could saturate the intracellular pool of gallium so that any further cellular uptake would take place at the membrane level only. This hypothesis also explained the complete lack of effect of THP^{Me} on the intracellular uptake for the post-^{68}Ga

experiment, suggesting that for this group saturation of the intracellular pool was reached in the first 30 min, before addition of THP^{Me}.

To confirm this hypothesis the same experiments were repeated in which each sample was treated with a mixture of ^{67}Ga (25 kBq) and ^{68}Ga (25 kBq) and the uptake of each radioisotope measured by γ-counting using different energy windows. As is evident from **Figure 4.12**, both isotopes showed the same behaviour in these experiments, with the higher concentration of gallium driving uptake on the membrane.
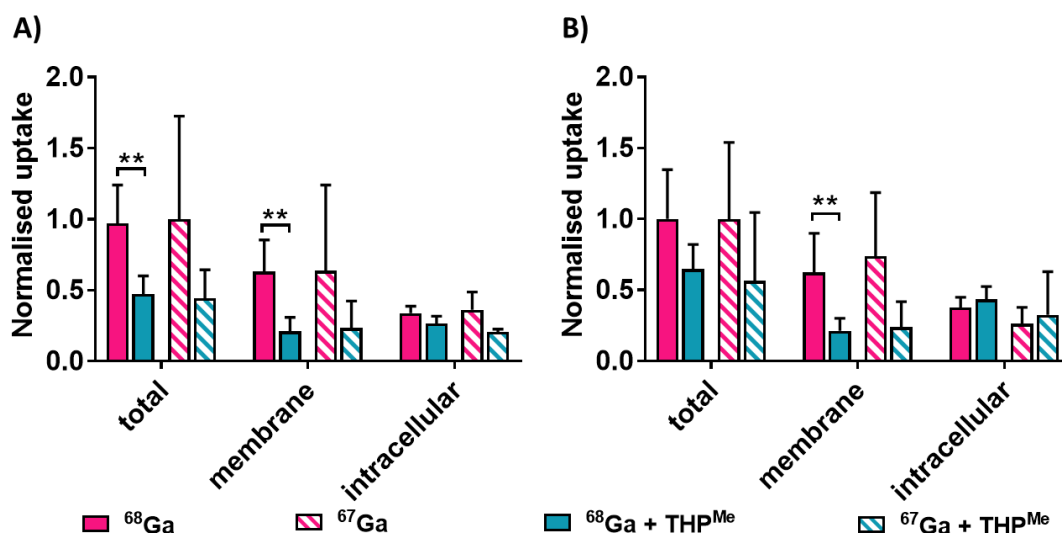
Figure 4.12. *Uptake of $^{67/68}$Ga in A375 cells with and without THP^{Me} treatment expressed as normalised uptake (mean ± SD, n = 3) for both pre-$^{67/68}$Ga (A) and post-$^{67/68}$Ga (B) experiments. A t-test was performed to evaluate the difference between ^{68}Ga and ^{67}Ga samples and between THP^{Me} treated samples and control for each isotope (* = P ≤ 0.05, ** = P ≤ 0.01).*

4.3.2 THP^{Me}-mediated ^{68}Ga blood clearance in healthy animals

Preclinical experiments in healthy BALB/c mice were initially carried out to evaluate to what extent intravenous injection of THP^{Me} could influence the *in vivo* biodistribution of ^{68}Ga. Three different studies were conducted and their results are reported in the sections below.

Dose finding study

In the first instance, a small pilot study was conducted to investigate whether THP^{Me} could effectively bind ^{68}Ga in blood, and the amount of the chelator that was needed to observe an influence on the *in vivo* biodistribution of the radiometal. Five different doses, ranging from 1 μg (1.2 nmol) to 500 μg (590 nmol) were tested and compared with a 0 μg control (saline injected). A 90 min dynamic PET/CT scan was performed for each mouse, ^{68}Ga-acetate was injected intravenously at time 0 using a cannula,

followed by THP^{Me} 45 min later. This amount of time was deemed sufficient to deliver enough of the injected ^{68}Ga from the circulation to the tissues, but not so long as to result in poor image quality, given the short half-life of ^{68}Ga.

Ex vivo biodistribution was performed at 90 min post ^{68}Ga injection. Percentage injected dose per gram (% ID/g) calculated for relevant organs are reported in **Figure 4.13**.
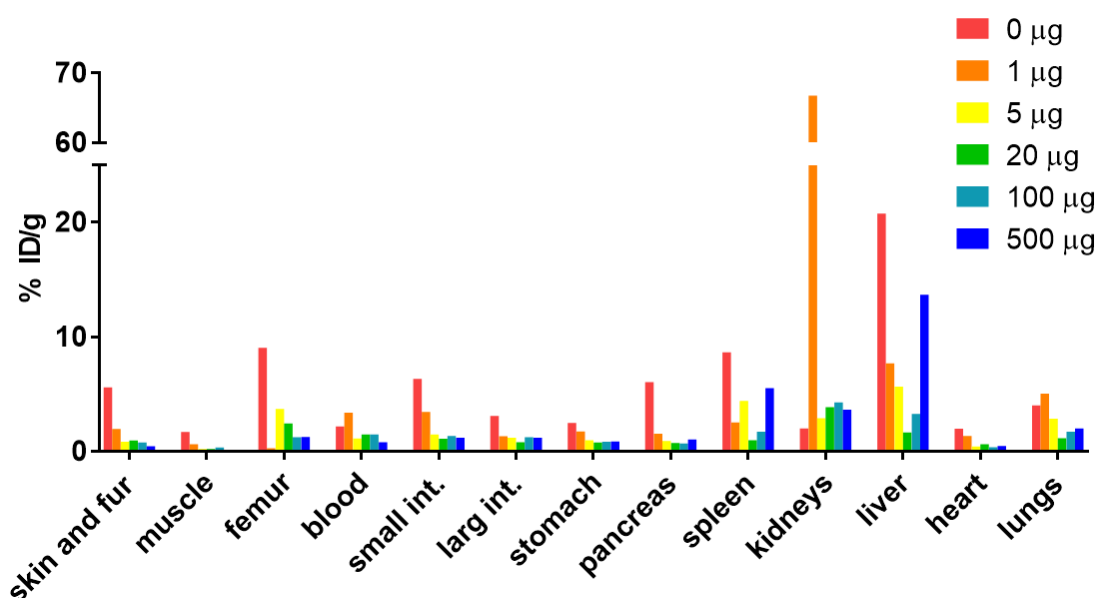
Figure 4.13. *Biodistribution of ^{68}Ga in selected organs expressed as % ID/g at different amounts of injected THP^{Me}. (N = 1, pilot study).*

Although this was a pilot experiment, with N =1 for each group, some qualitative considerations can be made. Notably, a difference was found for the activity in the blood pool when comparing treated animals (average of 1.7 ± 1.0 % ID/g, or 1.2 ± 0.3 % ID/g when excluding the 1 μg dose) and the mouse injected with saline (2.2 % ID/g). However, a larger difference was visible for most of the other organs, where the uptake was lowered for animals treated with THP^{Me}. Importantly, the graph also highlights high variability for the % ID/g values, with particularly high activity in the kidneys for the 1 μg dose (67 % ID/g vs an average of 3.4 % ID/g for the other animals) and in the liver for the 0 and 500 μg doses (20.8 and 13.7 % ID/g, respectively vs an average of 4.6 % ID/g for the other animals). PET/CT images confirmed this variability and showed how in the case of the liver, high uptake was visible from the beginning of the scan. Maximum intensity projections (MIP) for the 20 μg dose and the control are reported in **Figure 4.14**.
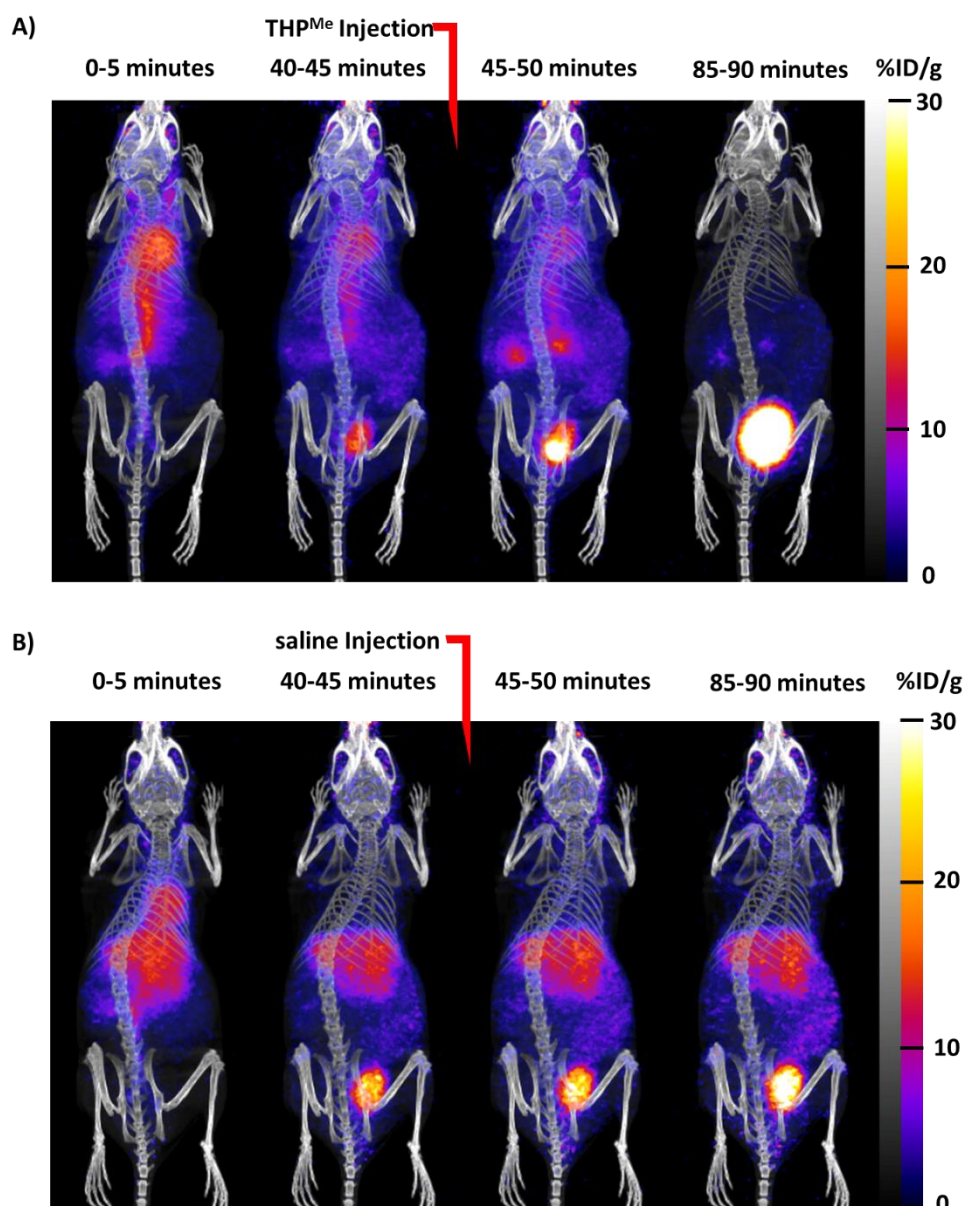
Figure 4.14. *Maximum intensity projections (MIP) for the 20 μg (upper panel) and 0 μg (lower panel) doses scaled with respect to the injected activity.*

Notably, despite the observed variability, in all the mice treated with THP^{Me} a sudden change in biodistribution was visible after THP^{Me} injection as shown in **Figure 4.14 A** for the 20 μg dose. ^{68}Ga accumulation in the kidneys and then in the bladder was observed as the activity was cleared from the blood into urine. No such effect was visible for the saline treated mouse (**Figure 4.14 B**).

Repetition of the experiment for both the 20 and 0 μg doses, confirmed both the reproducibility of the clearance effect and the high variability of ^{68}Ga-acetate biodistribution, as shown in **Figure 4.15**. In this case, the mouse injected with saline only (**Figure 4.15 B**) showed extremely low liver uptake compared to the previous control experiment (**Figure 4.14 B**). On the contrary the mouse injected with 20 μg of

THP^{Me} (**Figure 4.15 A**) presented higher liver and spleen uptake compared to the first mouse treated with the same dose (**Figure 4.14 A**). Importantly, notwithstanding this variability, the clearance effect was still visible in the 20 µg scan, while no clearance was observed for the control experiment. The reasons for the observed inconsistency in ^{68}Ga-acetate biodistribution are not completely understood, but likely related to differences in generator elutions (see **Discussion**).
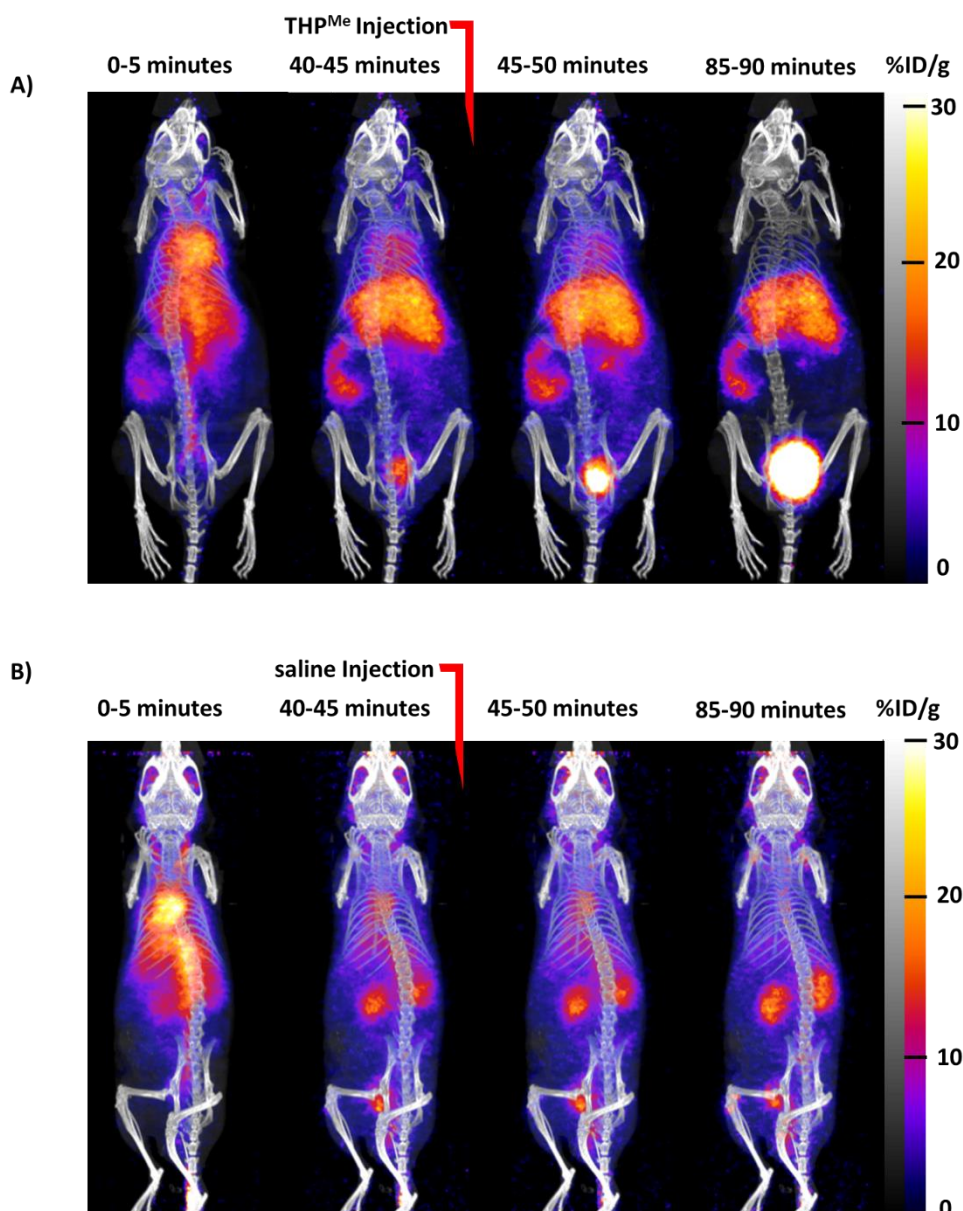
Figure 4.15. *Maximum intensity projections (MIP) for normal mice injected with 20 µg (upper panel) or 0 µg (lower panel) of THP^{Me}. Images are scaled with respect to the injected activity. Compared to **Figure 4.14**, a different initial ^{68}Ga biodistribution for the two animals is visible.*

To verify that blood clearance effect seen for THP^{Me} treated animals was actually due to *in vivo* chelation of ^{68}Ga, the urine of the mouse injected with 20 µg of the chelator (MIP shown in **Figure 4.14 A**) was analysed by reverse-phase HPLC, obtaining a single

peak in the radiochromatogram at 15 min 43 s (**Figure 4.16**). Comparison with the radiochromatogram obtained for [^{68}Ga(THP)] using the same method and displaying a unique peak at 15 min 28 s (**Figure 4.16**) confirmed *in vivo* chelation of ^{68}Ga by THP^{Me}.
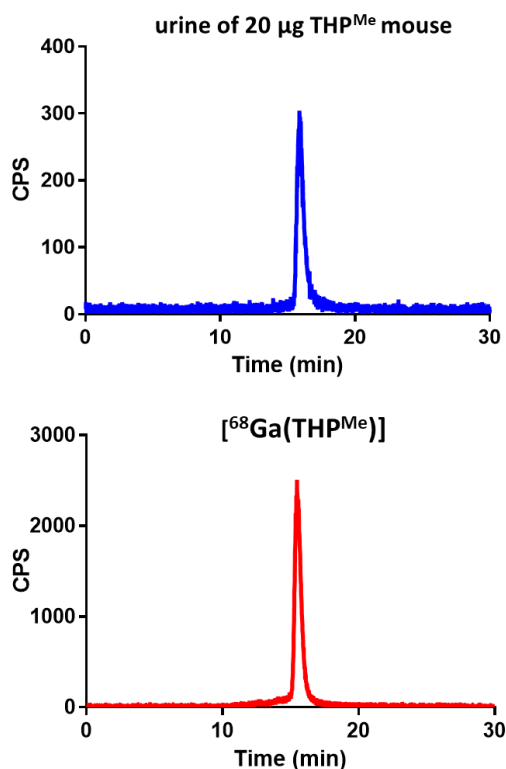
Figure 4.16. Comparison between the reverse-phase HPLC radiocromatograms for the urine of the mouse treated with 20 µg of THP^{ME} (top panel, retention time: 15 min 43 s) and for [^{68}Ga(THP^{Me})] (bottom panel, retention time: 15 min 28 s).

When the same procedure was applied to the urine of the saline treated mouse, no peak corresponding to [^{68}Ga(THP^{Me})] was observed in the radiochromatogram, and the activity remained trapped in the HPLC column. This behaviour is commonly observed for unchelated ^{68}Ga at neutral pH.

An alternative way to visualise the clearance effect is provided by time/activity curves, showing the amount (or concentration) of activity in different organs as a function of time, as quantified from dynamic PET scans. Representative examples of time/activity curves showing the amount of activity associated with heart (as a measure of blood), kidneys and bladder (as a measure of urine) are reported in **Figure 4.17 A** and **B** for mice with low liver uptake injected with 0 µg and 20 µg of THP^{Me}, respectively.
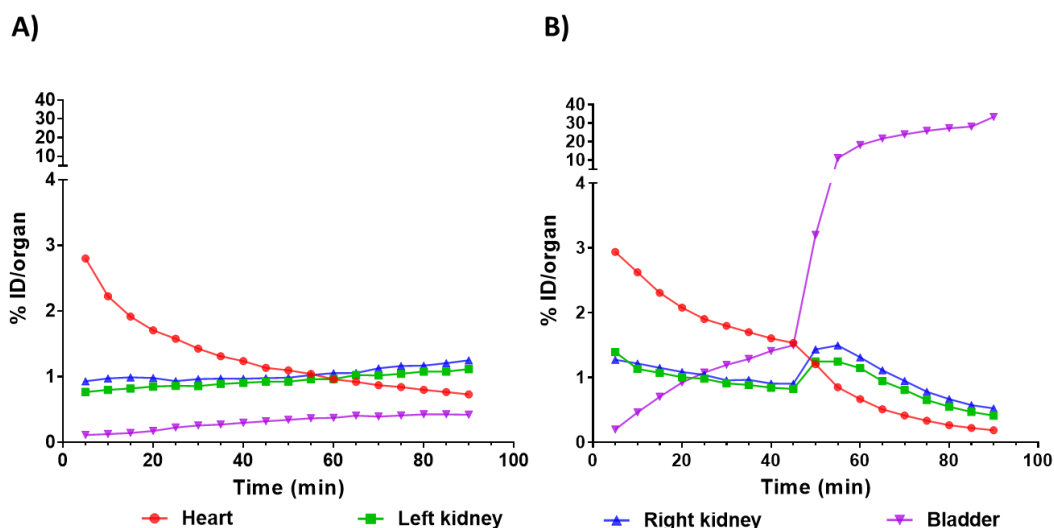
Figure 4.17. *time/activity curves showing the % ID in selected organs as a function of time, for a mouse injected with saline (0 µg THP^{Me}, A) or with 20 µg of THP^{ME} (B) at 45 min after ^{68}Ga injection. Each data point represents a 5 min interval (the end point of the time interval was set as "x" value for each data point).*

As it is clearly noticeable from the graphs, a sudden change of trend is visible for the animal injected with 20 µg of chelator between 45 and 50 min, with a sudden increase of activity in the bladder. A decrease in the activity in the heart is also visible, although less dramatic. % ID in the kidneys initially rose after THP^{Me} injection. followed by a decrease as the activity is moving towards the bladder. Owing to the already mentioned variability in ^{68}Ga-acetate biodistribution, time/activity curves for different mice displayed different absolute % ID/organ values (data not shown). However, they all showed a similar trend with a sudden change in the profile at 45-50 min for treated animals while no appreciable changes were visible for the control mice.

Overall this first experiment showed how THP^{Me} is able to bind ^{68}Ga *in vivo* when administered at 45 min post injection of the activity. This resulted in a sudden acceleration in the blood clearance of the activity and, accordingly, in lower ^{68}Ga uptake in most of the organs. The 20 µg dose showed the most promising results and no further improvement was found for the 100 µg and 500 µg doses, which were therefore not included in further investigation.

Delay finding study

The preliminary *in vivo* experiment highlighted ^{68}Ga clearance ability of THP^{Me} at 45 min post injection for THP^{Me} doses as low as 1 µg. The investigation was then repeated in a larger number of animals using two different time delays between injection of ^{68}Ga-acetate and THP^{Me}, with the aim of assessing the influence of this time interval on the clearance effect. Two extreme time intervals were chosen, namely 5 and 90

min, between injection of ^{68}Ga and of THP^{Me}. For each time delay, THP^{Me} doses of 1, 5 and 20 µg were investigated and compared to an injection of saline (0 µg dose). Four animals were randomly assigned to each group. Notably, biodistribution studies of mice belonging to the same group were spread over several days of experiments to avoid systematic error due to difference associated with external factors such as ^{68}Ga elution or time of the day and to unambiguously assign any significant differences to THP^{Me}-mediated clearance. This is all the more important given the high variability in ^{68}Ga biodistribution observed in the pilot experiment.

One animal per group also underwent dynamic PET/CT imaging. However, due to technical problems with the PET scanner, no CT was performed for the control (0 µg) mice, and therefore the scans are reported as PET only images (**Figure S1 and S2, Supplementary Information**). In both experiments mice were culled 15 min after THP^{Me} injection, organs harvested and % ID/g determined.

Ex vivo biodistribution for the 5 min delay groups (20 min post ^{68}Ga injection) is reported in **Figure 4.18**. A general trend is clearly visible in the graph: the activity in urine and in the organs involved in renal clearance increased with increasing amount of chelator injected. The opposite was true for blood and, most notably, for those organs where gallium tends to concentrate over time such as bone and liver [35].
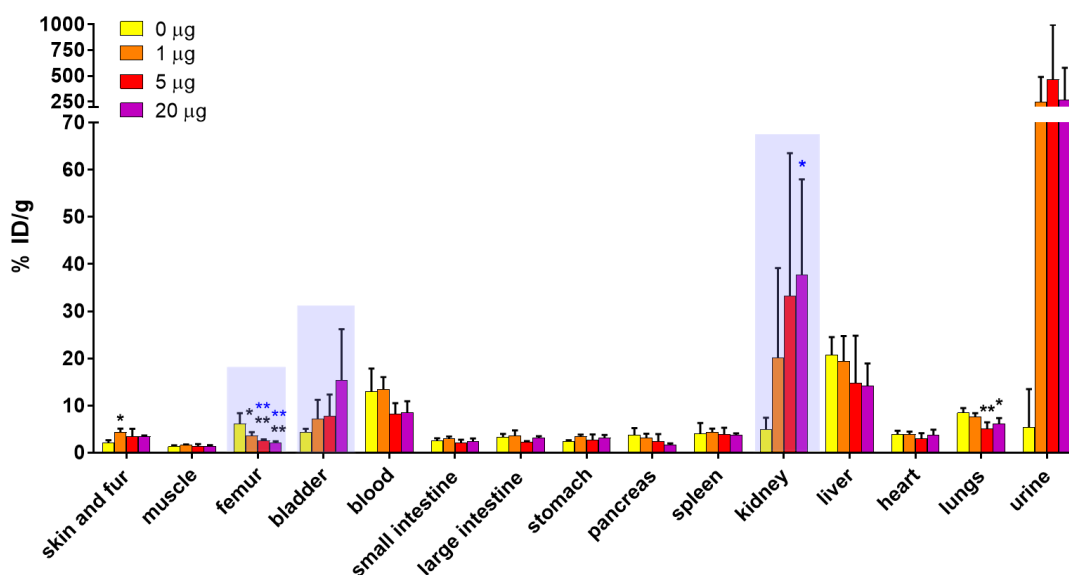
Figure 4.18. *Ex vivo biodistribution of ^{68}Ga in mice treated with different doses of THP^{Me}, with a delay of 5 min between the two injections. Values are expressed as mean ± SD (N = 4 except for urine where N = 3 for 0, 1 and 5 µg). Statistical analysis was performed for each organ using one-way ANOVA, followed by Dunnett post-hoc test to correct for multiple comparisons (black *). For the groups shaded in blue, unequal variances were obtained (Brown-Forsythe and Bartlett test) and Welch-adjusted t-test was also carried out (blue *). P values for a given concentration are evaluated in comparison with the relevant 0 µg value (* = P ≤ 0.05, ** = P ≤ 0.01).*

Importantly, these data are characterised by high variability, especially in those organs involved in excretory and metabolic pathways of gallium. Accordingly, the statistical significance of differences between groups is limited. Data were initially analysed by one-way ANOVA, which highlighted a significant difference in the femur % ID/g for each treated group compared to the control. Similarly, a difference from the control was found for the 5 and 20 µg groups in the lungs and, unexpectedly, for the 1 µg group in the skin and fur. Importantly for some organs (shaded in blue in **Figure 4.18**), unequal variances among the groups were calculated both by the Brown-Forsythe and Bartlett test, thus questioning the validity of one-way ANOVA for those groups. Re-analysis of those data was performed using a Welch-adjusted t-test between each of the treated groups and the control. According to this analysis, the kidneys % ID/g for 20 µg was also statistically different from the control, while the differences in the femur % ID/g remained statistically significant only for the 5 and 20 µg groups.

In the case of the 90 min delay experiment, the *ex vivo* biodistribution (**Figure 4.19**) showed significantly fewer differences between treated and untreated groups, although a trend was still visible in the kidneys. However, due to the large variability for this organ, no significant difference was found for the kidney uptake of the treated groups compared to the control.
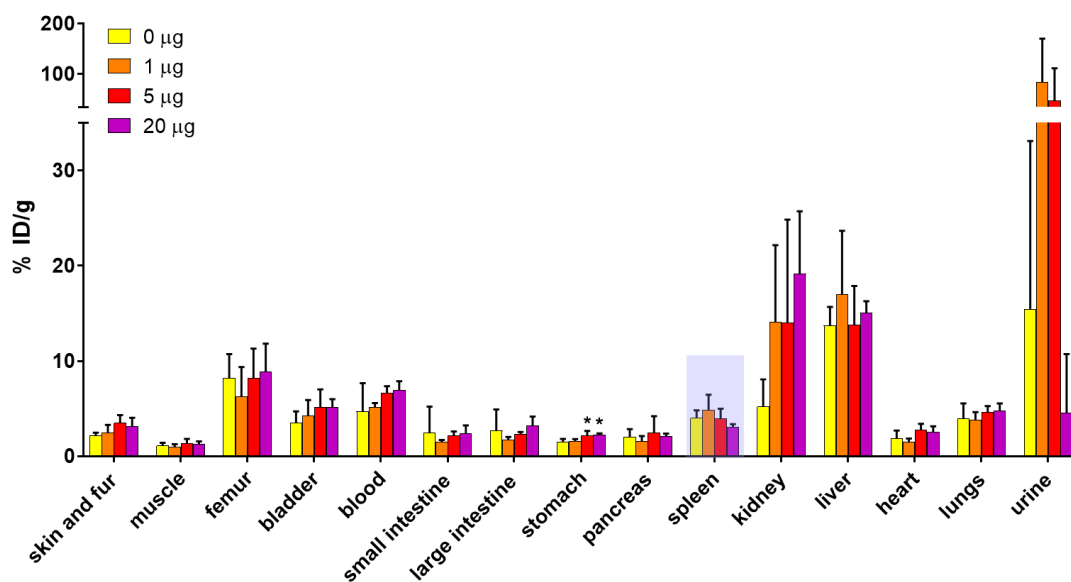
Figure 4.19. *Ex vivo biodistribution of ^{68}Ga in mice treated with different doses of THP^{Me}, with a delay of 90 min between the two injections. Values are expressed as mean ± SD (N = 4 except for the 20 µg group where N = 3 and for urine where N = 2 for 1 and 20 µg groups). Statistical analysis was performed for each organ using one-way ANOVA, followed by Dunnett post-hoc test to correct for multiple comparisons (black *). For the groups shaded in blue, unequal variances were obtained (Brown-Forsythe and Bartlett test) and Welch-adjusted t-test was also carried out (blue *). P values for a given concentration are evaluated in comparison with the relevant 0 µg value (* = P ≤ 0.05).*

Scarcity of statistical significance in both cases can be partially attributable to high variability in key organs, reducing the statistical power of the experiment compared to the predicted value for a sample size of n = 4 (see **Materials and Methods**). In an attempt to increase the statistical power of the experiment, the data of each experiment were regrouped as non-treated and treated group, with the latter group now having N = 12. *Ex vivo* biodistribution values for the regrouped data are reported in **Figure 4.20 A** and **B**. Statistical analysis of the data, in this new regrouped form, revealed statistically significant differences between treated and untreated group.
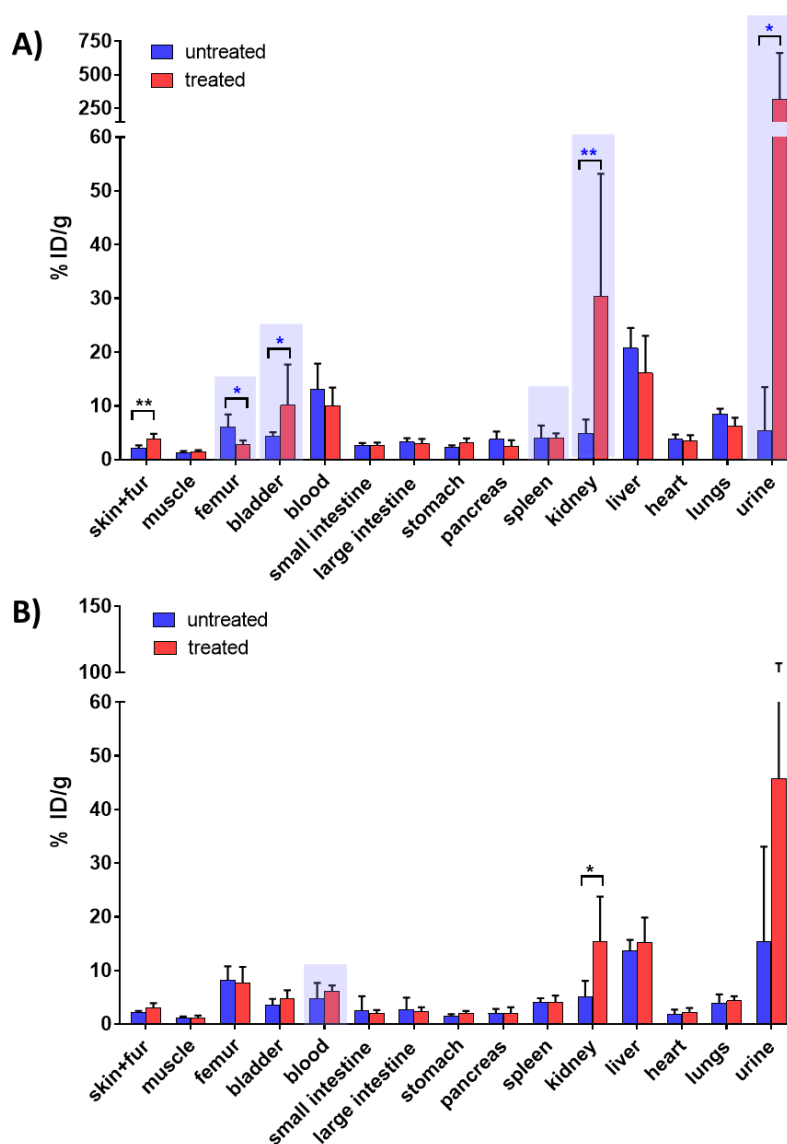
Figure 4.20. *Ex vivo biodistribution of ^{68}Ga in mice treated with THP^{Me} or saline at 5 min (A) or 90 min (B) after ^{68}Ga injection, regrouped as treated and untreated groups. Values are expressed as mean ± SD, N = 4 for the untreated groups, N = 12 for the 5 min treated group, N = 11 for the 90 min treated group except for urine (N = 8). Statistical analysis was performed for each organ using a t-test (black *). For the groups shaded in blue, unequal variances were obtained (F test) and therefore Welch-adjusted t-test was also carried out (blue *). P values for a given concentration are evaluated in comparison with the relevant 0 µg value (* = P ≤ 0.05, ** = P ≤ 0.01).*

For the 5 min time-delay group, a significantly reduced femur uptake was found for the treated group, together with significantly enhanced uptake in organs related to excretory pathways (kidney and urine/bladder). Unsurprisingly, the statistically significant increment observed for the skin and fur in the original data, is present also in this regrouped version. For the 90 min time-delay, only a trend in kidney uptake was observed and, accordingly, the only statistically significant difference arising for the regrouped version of the data is an increased kidney uptake for the treated group.

Overall, these results show that the clearance effect of THP^{Me}, originally observed at 45 min after ^{68}Ga injection, is also visible as soon as the ^{68}Ga enters the circulation (5 min delay), but is largely lost when using a delay of 90 min between activity and chelator injection.

4.3.3 THP^{Me}-mediated ^{68}Ga blood clearance in A375 xenografts

^{68}Ga-acetate uptake in A375 xenografts

The biodistribution of ^{68}Ga-acetate in NSG mice bearing A375 xenografts was evaluated, to assess tumour uptake of ^{68}Ga, and to verify whether timing of tumour accumulation is compatible with the time frame in which ^{68}Ga blood clearance is feasible. Alongside ^{68}Ga-acetate, ^{68}Ga-oxine, which displayed significantly higher uptake in A375 cells *in vitro* was also evaluated. 5 mice were randomly assigned to each group and treated with either ^{68}Ga-acetate or ^{68}Ga-oxine. A 4-hours dynamic PET/CT scan was then performed for 3 animals per group. *Ex vivo* biodistribution was determined for all animals by organ counting at 4 hours post ^{68}Ga injection.

Representative PET/CT images at different time points are shown for ^{68}Ga-acetate (**Figure 4.21 A**) and ^{68}Ga-oxine (**Figure 4.21 B**). From PET/CT images of mice injected with ^{68}Ga-acetate, a time/activity curve for the accumulation of the activity in the tumour was calculated (**Figure 4.22**).
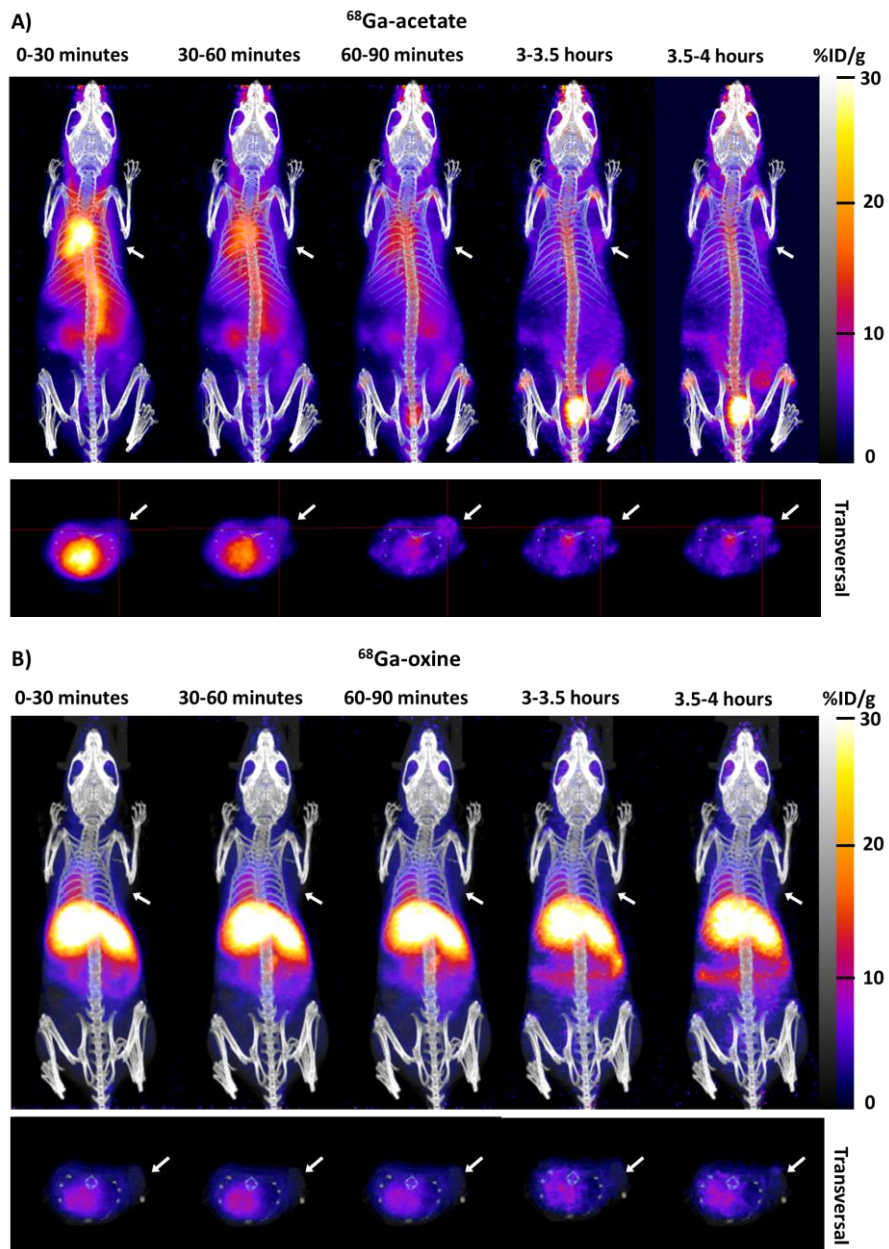
Figure 4.21. PET/CT images at different time points for a mouse injected with ^{68}Ga-acetate (A) or ^{68}Ga-oxine (B). For each image, MIP are shown in the upper panel (scaled with respect to the injected activity), a transverse section showing the tumour is displayed in the lower panel for the same time points. A white arrow is used to indicate the position of the tumour.
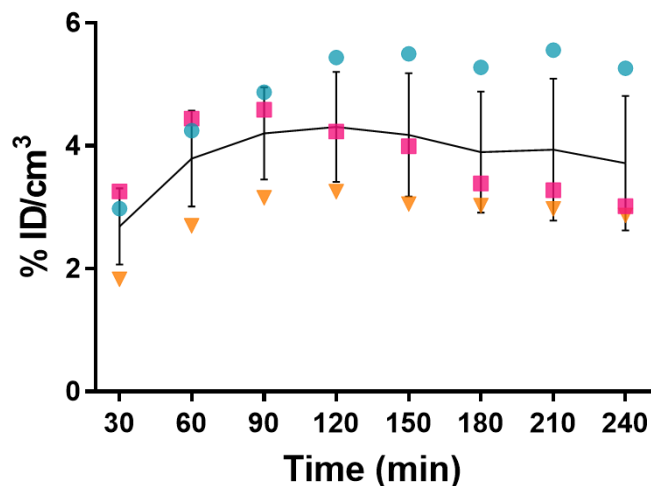
Figure 4.22. Time-activity curve describing accumulation of [68]*Ga-acetate into A375 xenografts, reported as concentration of activity (% ID/cm^3). Values are reported as single data points for each of the three mice for which a PET/CT scan was performed (coloured points). The end of the considered time interval was set as "x" value for each data point. Average and standard deviation at different time points are also reported (black line and error bars).*

Figure 4.21 A showed how tumour uptake of the radiometal was low but clearly visible from the PET/CT scan for mice injected with ^{68}Ga-acetate. Image contrast increased over time as a combined result of increased ^{68}Ga tumour uptake and blood clearance. Accordingly, no contrast was achieved at 30 min post injection, while tumour uptake became evident (and distinct from the blood pool) from 60 min post injection. Time activity curves for the 3 mice of the ^{68}Ga-acetate group that underwent PET/CT scan also showed tumour accumulation of ^{68}Ga increasing over time with maximum uptake visible between 1 and 2 hours, followed by a plateau or slight tumour wash out at the latest time points.

As expected, even at the latest time point, the achievable contrast was low (tumour-to-blood ratio = 0.87). High bone uptake was observed in all the mice injected with ^{68}Ga, uptake in the gut was also observed, while no significant liver uptake was observed. On the contrary, mice injected with ^{68}Ga-oxine showed extremely high liver uptake since the earliest time point, with uptake also visible in the myocardium and the gut. Unexpectedly, no uptake in the tumour was visible for those mice at any time point after ^{68}Ga-oxine injection.

Ex vivo biodistribution data, comparing mice injected with ^{68}Ga-acetate and ^{68}Ga-oxine, are reported in **Figure 4.23** and largely confirm the results shown in the PET/CT images.
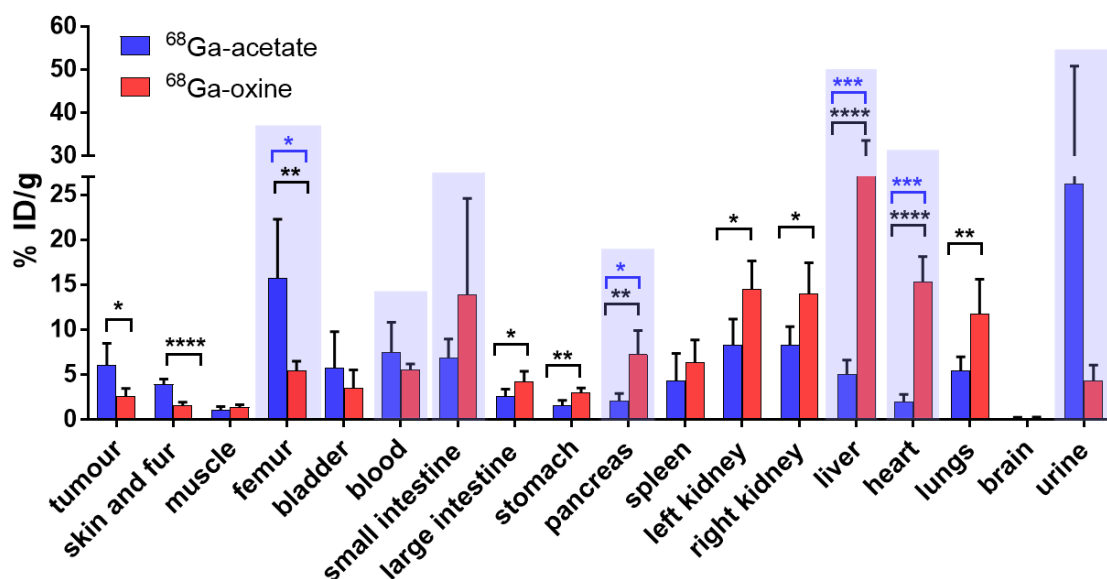
Figure 4.23. *Biodistribution of ⁶⁸Ga in mice treated with ⁶⁸Ga-acetate or ⁶⁸Ga-oxine, as determined by ex vivo organ counting at 4 hours post injection. Values are expressed as mean ± SD, N = 5. Statistical analysis was performed for each organ using a t-test (black *). For the groups shaded in blue, unequal variances were obtained (F test) and therefore Welch-adjusted t-test was also carried out (blue *). P values are defined as follows: * = P ≤ 0.05, ** = P ≤ 0.01, *** = P ≤ 0.001, **** = P ≤ 0.0001.*

Neither of the ^{68}Ga tracers accumulate in the brain (despite the lipophilic, uncharged character of ^{68}Ga-oxine), and uptake in muscles was minimal. A difference in uptake is visible for the rest of the organs, and becomes statistically significant whenever variability is small. Notably, ^{68}Ga-acetate presents significantly higher tumour uptake (6.1 ± 2.4 % ID/g) than ^{68}Ga-oxine (2.6 ± 0.9 % ID/g), highlighting different mechanisms of ^{68}Ga accumulation in tumours compared to uptake *in vitro* (see **Discussion**). ^{68}Ga-acetate uptake was remarkably higher than ^{68}Ga-oxine uptake also for skin and fur (3.9 ± 0.6 % ID/g vs 1.6 ± 0.3 % ID/g) and femur (15.7 ± 6.5 % ID/g vs 5.4 ± 1.2 % ID/g). On the contrary, ^{68}Ga-oxine uptake was higher in liver (27.7 ± 5.9 % ID/g vs 5.1 ± 1.5 % ID/g for ^{68}Ga-acetate) and heart (15.3 ± 2.8 % ID/g vs 2.0 ± 0.8 % ID/g for ^{68}Ga-acetate).

Comparison with DFO

Based on the results of the previous experiments in healthy mice, a time delay of 90 min between ^{68}Ga injection and THP^{Me} injection was deemed too long to observe an appreciable change of the biodistribution (except for the kidneys). On the other hand, in order for the blood clearance to provide appreciable contrast enhancement, the time delay should be long enough to allow accumulation of ^{68}Ga in the tumour prior to the clearance step. From the preliminary experiment in NSG mice bearing A375

xenografts, ^{68}Ga uptake in tumours reached its maximum between 1 and 2 hours post injection. Therefore, 60 min represented a good compromise between tumour accumulation and clearance effect and was chosen as the delay between the radiometal and blood clearance agent injections.

Before performing the experiment in xenograft models, a pilot experiment was carried out in normal animals using the new determined 60 min time delay. Alongside THP[Me], DFO was also evaluated as a clearing agent in this experiment. DFO is a clinically approved agent for the treatment of iron overload [17] and its clinical translation as a ^{68}Ga-blood clearance agent would therefore be facilitated compared to that of an unapproved molecule such as THP[Me]. Accordingly, a close comparison between the two molecules as ^{68}Ga blood-clearance agents was warranted.

Notably, DFO had been tested as a blood clearance agent in several studies, and found able to increase tumour-to-blood ratio when administered, either IV or IM, following ^{67}Ga-citrate injection [10,11,16]. However, only very high doses of the chelator, far above those in clinical use, were considered in these studies. Instead, when patients were treated IM with a clinically relevant dose of DFO (10 mg/kg) only a small contrast enhancement effect was visible [12].

In our experiment intravenous administration of DFO at the same low 24 nmol dose used for THP[Me] (corresponding to 15 µg of DFO), was investigated. 3 healthy mice were allocated per group, injected intravenously at time 0 with ^{68}Ga-acetate and then at 1 hour with either THP[Me], DFO or saline as a control. Mice were then culled at 2 hours post ^{68}Ga-acetate injection and *ex vivo* biodistribution carried out. One animal per group was also imaged for 25 min before and after the second injection. PET/CT images are shown in **Figure 4.24**, and *ex vivo* biodistribution is reported in **Figure 4.25**.
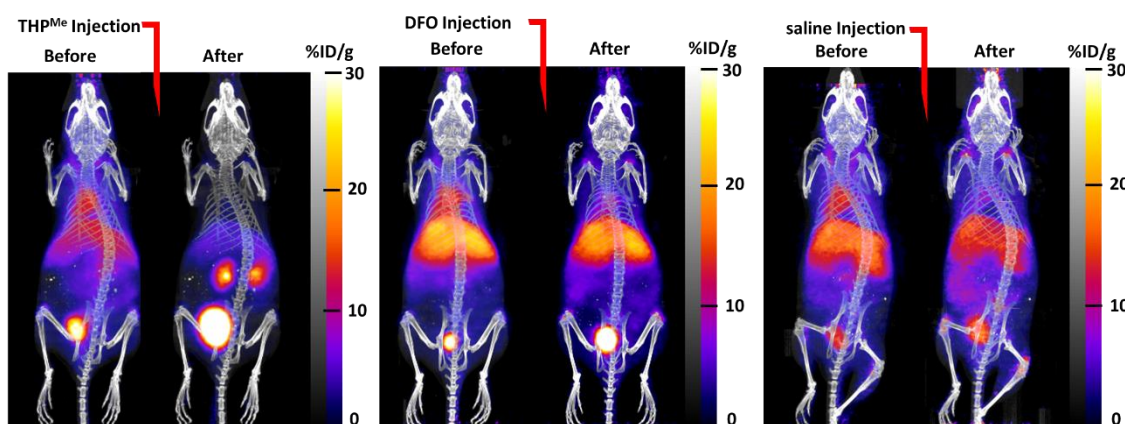
Figure 4.24. PET/CT images of normal mice injected with ^{68}Ga-acetate, followed at 1 hour post injection by treatment with 24 nmol of THP, DFO or saline as negative control.
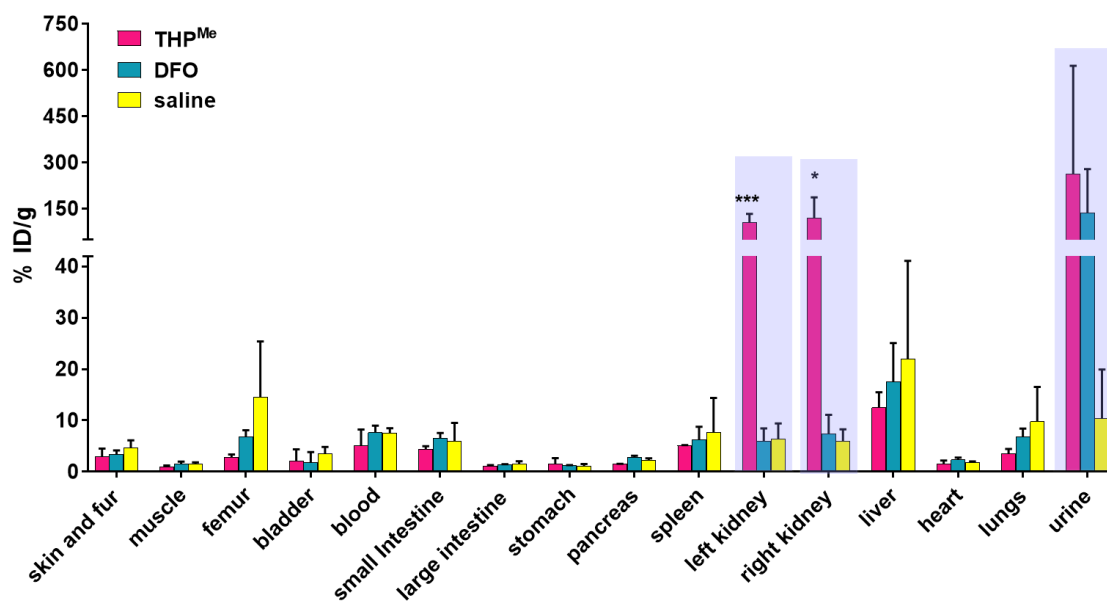
Figure 4.25. *Biodistribution as determined by ex vivo organ counting of ^{68}Ga in mice treated with ^{68}Ga-acetate followed at 1 hour post injection by administration of a blood clearance agent (THP^{Me} or DFO) or saline. Values are expressed as mean ± SD, N = 3. Statistical analysis was performed for each organ using ANOVA followed by Dunnett post-hoc comparison between each experimental group and the saline control (black *). For the groups shaded in blue, unequal variances were obtained (Brown-Forsythe and Bartlett test) and therefore Welch-adjusted t-test was also carried out (blue *). P values for each blood clearance agent are evaluated in comparison with the negative control group (* = P ≤ 0.05, *** = P ≤ 0.0001).*

From *ex vivo* biodistribution data, the only statistically significant difference between THP^{Me} and the control group was found in kidney uptake when using an ANOVA/Dunnett test. On the other hand, the clearance effect was clearly seen in the PET/CT images and the scarce statistical significance of biodistribution data is imputable to the low N number, as already observed in previous experiments. Data for THP^{Me} suggest that this chelator is efficient in accelerating renal clearance of ^{68}Ga when injected 60 min after the radiometal, resulting in increased kidney uptake and decreased accumulation in bones, liver and, to a lesser extent, in the blood. On the contrary, DFO does not seem to have an effect on ^{68}Ga blood clearance as shown in both the PET/CT scans and *ex vivo* biodistribution, which is similar to that of the control. However, a slightly lower uptake in the bones and increased activity in the urine was found, potentially indicating some effect on the clearance, whose significance may be hidden due to the low N number. Therefore, despite the lower efficiency observed in this experiment, it was decided to test DFO alongside THP^{Me} as a ^{68}Ga blood clearance agent in mice bearing A375 xenografts.

THP^{Me} and DFO as blood clearance agents for ^{68}Ga in A375 xenografts

In the final experiment, the clearance effect of THP and DFO, with saline as a control, was assessed in the same A375 xenograft model found to take up ^{68}Ga in the previous study. Similar to the experiment in normal mice, NSG mice bearing A375 xenografts were injected with ^{68}Ga-acetate, followed, at one-hour post injection by treatment with 24 nmol of one of the clearance agents or saline (5 animals per group). Mice were culled 2 hours after ^{68}Ga injection and *ex vivo* biodistribution performed. 3 mice per group were also scanned for 25 min before and after the second injection.

Representative PET/CT images for each group and *ex vivo* biodistribution for all the mice are displayed in **Figure 4.26** and **4.27**, respectively. For each group tumour-to-blood ratio was calculated from *ex vivo* biodistribution data (error was determined using the propagation of error formula for ratios of correlated values).
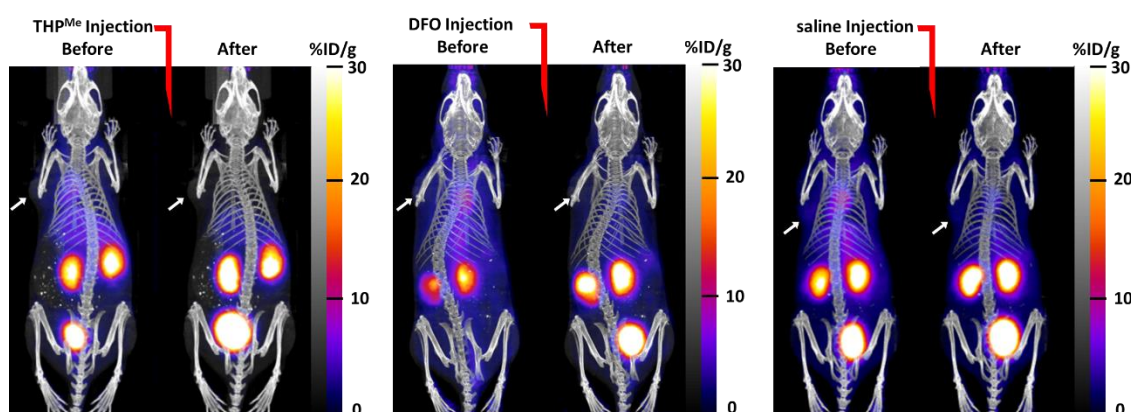
Figure 4.26. *PET/CT images of NSG mice bearing A375 xenografts, injected with ^{68}Ga-acetate, followed at 1 hour post injection by treatment with 24 nmol of THP, DFO or saline as negative control.Position of the tumour is indicated in each animal with a white arrow.*
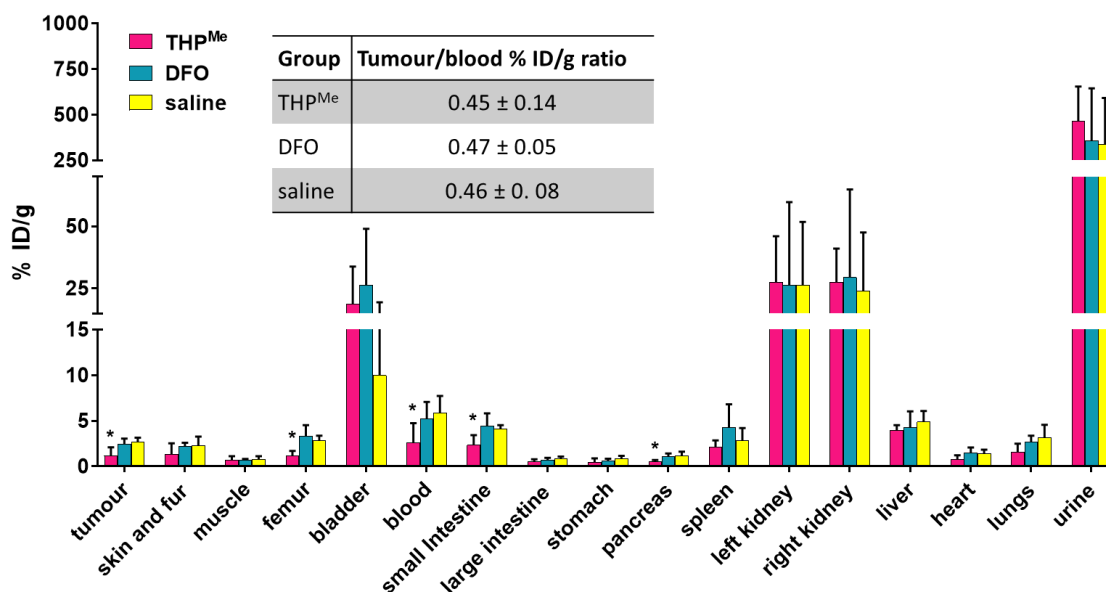
Figure 4.27. ^{68}Ga Biodistribution, as determined by ex vivo organ counting, in NSG mice bearing A375 xenograft, treated with a blood clearance agent (THP^{Me} or DFO) or saline at 1 hour post ^{68}Ga injection. Values are expressed as mean ± SD (N = 5). For each group tumour-to-blood ratio was calculated Statistical analysis was performed for each organ using ANOVA followed by Dunnett post-hoc comparison between each experimental group and the saline control. P values for each blood clearance agent are evaluated in comparison with the negative control group (* = P ≤ 0.05).

As is evident from both the PET/CT images and the biodistribution data, the experiment did not show any enhancement in the tumour to blood ratio, when using THP^{Me} or DFO at one hour after ^{68}Ga administration. However, the two distinct sets of data shed light on different aspects of the experiment outcome.

Ex vivo biodistribution showed a clear effect of THP^{Me} in reducing blood levels of ^{68}Ga and accumulation in bones and other organs. However, accumulation in tumours was also reduced, thus making the tumour to blood ratio unvaried compared to the saline control. Treatment with DFO did not have an effect on the biodistribution of ^{68}Ga. Unexpectedly, no increased uptake in kidneys or urine was visible for the THP^{Me} group compared to the control, but instead high % ID/g for both kidney and urine was found for all the three groups. Furthermore, tumour uptake in the control group was also found considerably lower than in the previous experiment (2.7 ± 0.5 % ID/g versus 6.1 ± 2.4 % ID/g). Although, in principle, this could be imputable to the different time points considered, the time activity curve for ^{68}Ga accumulation in tumours calculated for the first experiment (**Figure 4.22**) reveals only 15 % difference between tumour uptake at 2 and 4 hours.

When considering the PET/CT images new aspects of the experiment appear. In fact, for all the images, most of the activity seems located in the kidneys and /or bladder

even before the treatment with the clearance agent. Consequently, accumulation in all other organs is largely decreased, as it is evident when considering the tumours. Notably, in the particular case shown in the PET/CT of the THP^{Me} treated animal, the tumour does not seem to accumulate any ^{68}Ga even before injection with the chelator.

A better understanding of this unusual ^{68}Ga biodistribution can be obtained by comparing the *ex vivo* biodistribution for the control groups in the two experiments performed in the A375 xenograft model (**Figure 4.28**).
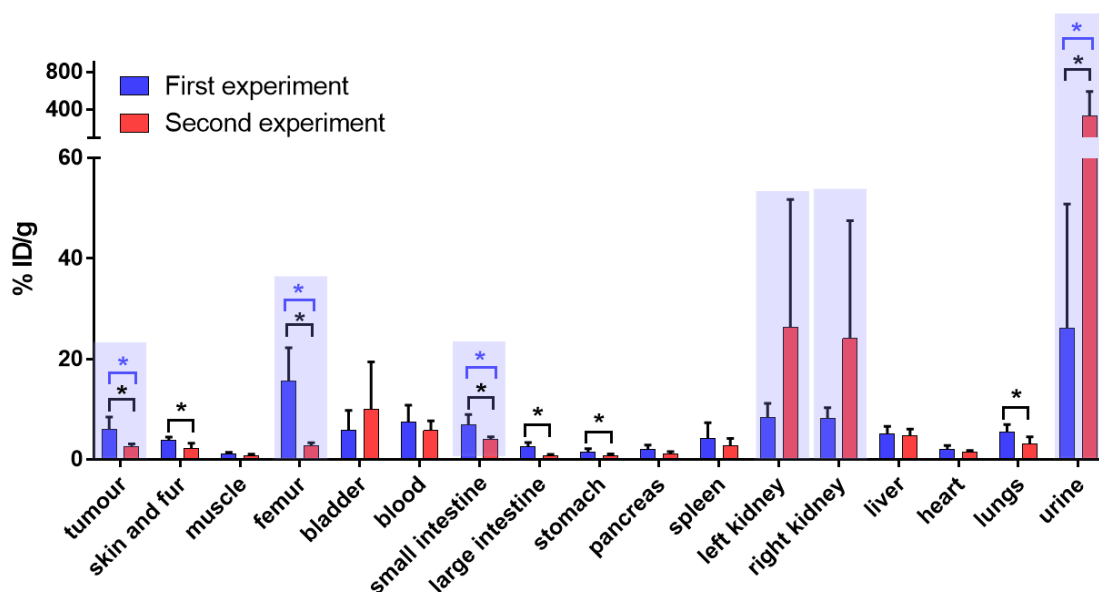
Figure 4.28. *Comparison of ^{68}Ga Biodistribution for NSG mice bearing A375 xenograft at 4 hours post injection (first experiment) and 2 hours post injection (second experiment). Mice belonging to the second experiment were also injected with saline at 1 hour after ^{68}Ga injection. Values are expressed as mean ± SD (N = 5). Statistical analysis was performed for each organ using a t-test. For the groups shaded in blue, unequal variances were obtained (F test) and therefore Welch-adjusted t-test was also carried out (blue *). * = P ≤ 0.05.*

Although the different time points for the biodistribution and saline injection for the second experiment do not allow a fair comparison between the two groups, some considerations can be made. Unsurprisingly, uptake in organs known to accumulate gallium is higher at later time points (*i.e.* in the first experiment). However, contrary to the expectations, uptake in organs associated to renal clearance is higher at earlier time points (*i.e.* in the second experiment). This suggests an abnormal clearance behaviour of ^{68}Ga in the second experiment, which may have influenced the biodistribution of ^{68}Ga in all the other organs.

4.4 Discussion

In this work, we assessed the THP^{Me} chelator as a blood clearance agent to be used in combination with ^{68}Ga salts for cancer imaging, with the aim of improving image contrast by enhancing the tumour-to-blood activity ratio.

It is important, for this type of study, to administer gallium in a form that provides ionic ^{68}Ga^{3+}, able to accumulate in cancer cells via transferrin-dependent and/or independent mechanisms. Although radioactive gallium is mainly administered in clinic as gallium citrate this was avoided in our study, since citrate itself could potentially hamper THP^{Me} *in vivo* complexation by acting as a competing ligand. Instead, ammonium acetate was used to buffer the ^{68}Ga eluate. Acetate represents a weaker chelator for Ga^{3+} than citrate, and, although able to prevent precipitation of poorly soluble gallium hydroxide, cannot compete efficiently with THP^{Me} for gallium binding [36].

As a cancer model for this study, we chose the human melanoma cell line A375, whose xenografts were previously found to take up unchelated ^{68}Ga by our group. Notably, this cell line is known to overexpress transferrin receptors [37] and is therefore able to take up gallium via transferrin-dependent mechanisms.

4.4.1 Uptake of ^{68}Ga-acetate in the A375 melanoma model

Uptake of ^{68}Ga-acetate in A375 cells was first evaluated *in vitro* using cells in suspension, and then *in vivo* in mice bearing A375 xenografts. This set of studies aimed to characterise the model in terms of ^{68}Ga uptake to obtain a better understanding of the effect of THP^{Me} in the selected biological system.

In vitro assays were carried out in HBSS buffer, rather than full cell culture medium, to avoid presence of bovine transferrin from foetal calf serum that could compromise cellular uptake of gallium. In fact, bovine transferrin is able to complex gallium with an affinity similar to human transferrin, but unlike human transferrin, this protein does not efficiently interact with the Tfr receptors expressed on human cancer cells to deliver its gallium payload [38,39]. Cell culture medium supplemented with human serum or apotransferrin could have been used for the assay to exploit transferrin-mediated uptake of gallium as well as transferrin-independent mechanisms. However, comparison of ^{68}Ga uptake in A375 in DMEM medium with and without human serum, performed by our group, showed no significant difference between the two groups for incubation periods shorter than 4 hours (**Figure 4.29**).
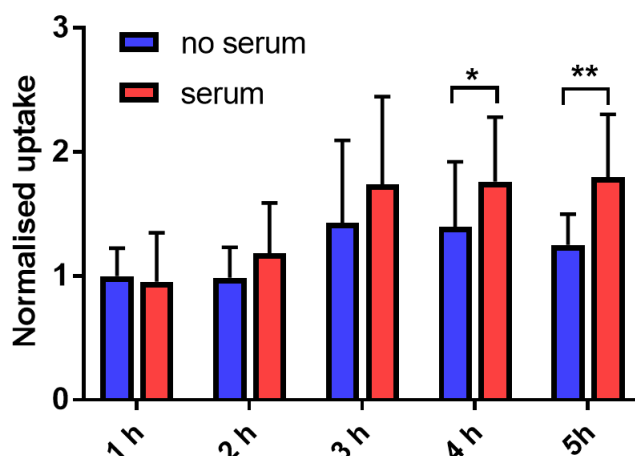
Figure 4.29. *Comparison between cellular uptake of* ^{68}Ga*-acetate in A375 cells in medium with or without human serum at different time points, expressed as a normalised uptake w/r to A375 uptake of* ^{68}Ga*-acetate at 1-hour incubation (mean ± SD, n = 8). A t-test was performed to evaluate the difference between the two groups at each time point. P values are defined as follows: * = 0.033, **= 0.0056. Reproduced with permission of Fahad Al-Salemee (KCL).*

Since incubation periods longer than 2-3 hours are not relevant for a short-lived isotope such as ^{68}Ga, a transferrin-free buffer was preferred in our experiments to avoid any additional ligand (serum proteins, glutamine and other amino acids) that could interfere with ^{68}Ga uptake. For the same reason, use of BSA as a supplement to reduce non-specific uptake was avoided after verifying that its absence did not increase non-specific binding to the plastic. HBSS, whose concentration of phosphate salts is lower than PBS, was chosen as a buffer, to reduce the risk of gallium precipitation as poorly soluble gallium phosphate.

In these conditions, A375 cells demonstrated a ^{68}Ga uptake significantly different from non-specific ^{68}Ga binding to plastic, with most of the gallium located in the intracellular fraction (70-80 %). However, the absolute extent of the uptake was found variable among different experiments, (ranging from 2 to 10 % of the total added activity). Mechanisms for transferrin-independent cellular uptake of gallium are currently unknown, raising concerns that the observed variability may be dependent on experimental factors that could vary between different experiments, such as amount of activity used, passage number of the cells, confluency of the cell culture flask. Some uptake studies were therefore conducted to investigate the influence of these factors on cellular uptake of ^{68}Ga and showed that the percentage uptake was not influenced by the amount of activity added to each tube (in the 18-70 kBq range utilised for the experiments), nor the passage number or the confluency of the cell culture flask.

Variability in cellular uptake of gallium was also visible between different cells in the same sample, as observed in ^{67}Ga microautoradiography experiments. Interestingly, higher membrane uptake was observed for these cells both in MAR images and in ^{67}Ga uptake studies performed on the same batch of cells. This apparent discrepancy between ^{68}Ga and ^{67}Ga uptake was found attributable to the different concentrations of the two metal ions at a given amount of activity, owing to their different half-life. In fact, when cells were incubated with both isotopes, ^{68}Ga presented the same distribution of activity as ^{67}Ga, owing to the increased total concentration of the metal ion.

[68]Ga uptake was also investigated in NSG mice bearing A375 xenografts. Although tumour uptake was found to be moderate but significant (6.5 ± 2.4 % ID/g), tumour to blood ratio was still poor at 4 hours post injection (0.87 ± 0.06). Notably, femur displayed the highest % ID/g among all organs in the *ex vivo* biodistribution and PET images confirmed accumulation in bones, mainly joints and spine, although variability was observed. This suggests that transferrin-independent mechanisms for uptake are taking place and could potentially contribute to tumour accumulation of [68]Ga. Notably, variability in liver uptake (commonly found for BALB/c mice in previous studies) was not observed in this case, with consistently low liver uptake shown by all mice. Although this suggests inter-strain variability in ^{68}Ga biodistribution, it could also be hypothesised that presence of the tumour in the NSG mouse somehow altered biodistribution of the radiometal.

4.4.2   Uptake of ^{68}Ga-oxine in the A375 melanoma model

The lipophilic ^{68}Ga-oxine complex could in principle be used as an alternative way to deliver ^{68}Ga to cancerous tissues, exploiting the increased membrane permeability of oxine complexes. Ga-oxine (*Tris*(8-quinolonato)gallium(III)) has recently been investigated clinically as an orally-available gallium anticancer drug (also known as KP46 and FFC11, see **Chapter 2**)[40,41]. Although its mechanisms of accumulation in cancerous tissues are not completely understood, several studies suggest that gallium-oxine, even when administered orally, reaches the tumour intact and only then releases gallium [21], contrary to other orally-available gallium drugs, which already leak gallium in the gastrointestinal tract.

Here ^{68}Ga-oxine uptake was investigated both *in vitro* and *in vivo,* in the same A375 melanoma model considered for ^{68}Ga-acetate. As expected, owing to its lipophilicity (Log P = 0.88 [32]), ^{68}Ga-oxine was found to accumulate into cancer cells *in vitro* to a

higher extent compared to ^{68}Ga-acetate. However, higher non-specific ^{68}Ga-oxine binding to plastic was also found in buffer-only samples.

A different result was obtained for *in vivo* tumour uptake. When ^{68}Ga-oxine was injected intravenously in NSG mice bearing A375 melanoma xenografts, no tumour uptake was visible in the PET images and very little accumulation was measured from *ex vivo* biodistribution at 4 hours after ^{68}Ga-oxine injection. Instead, ^{68}Ga-oxine accumulated in the liver and, intriguingly, in the myocardium (15.3 ± 2.8 % ID/g). High uptake of ^{68}Ga-oxine in the heart may be of interest as a basis for designing tracers for myocardial imaging applications.

Several reasons can be hypothesised to explain the discrepancy between the expected tumour accumulation of this tracer and the experimentally determined biodistribution, where cancerous tissue showed very little % ID/g. Surprisingly, despite interest in the use of *tris*(8-quinolonato)gallium(III) as an anti-cancer agent, its biodistribution in tumour models has never been investigated, although studies in healthy animals (using inductively-coupled plasma atomic emission) exist [42]. It is therefore impossible to predict in which frame time and to what extent, if at all, gallium-oxine accumulates into tumours. If we assume, mainly based on the preclinical/clinical evidence that the complex possesses anticancer activity, that gallium-oxine does indeed accumulate in tumours, the different behaviour displayed in our investigation is likely due to either the different administration route or the timing in which the biodistribution was assessed. If the intravenous administration of ^{68}Ga-oxine was responsible for its lack of tumour accumulation, it must be concluded that, when administered orally, gallium-oxine actually releases gallium in the gastrointestinal tract and that gallium then reaches the tumour either as gallate or GaTf complex. On the contrary, when administered intravenously, gallium-oxine does not release gallium and the gallium does not bind to Tf but rather, owing to its hydrophobicity, accumulates in the liver. If the short time points considered for ^{68}Ga-oxine are instead responsible for the lack of tumour uptake, it must be concluded that both routes of administration initially lead to liver uptake of the radiotracer. There, the complex is metabolised and can then re-enter the circulation and accumulate into tumours. Notably, both the hypotheses presented disagree with the common opinion that gallium-oxine reaches the tumour intact when administered orally. Experimental investigation of the proposed hypotheses would require a preclinical experiment where ^{68}Ga-oxine is administered orally in the same A375 xenograft model and its biodistribution followed over the same amount of time. Overall, it appears that several questions and anomalies

need to be resolved about the pharmacodynamics and pharmacokinetics of this gallium anti-cancer drug.

4.4.3 THP^{Me} influence on ^{68}Ga-acetate uptake

The influence of THP^{Me} on the biological behaviour of gallium-68 acetate was investigated in several ways, including the assessment of its effect on ^{68}Ga accumulation in A375 cells and evaluation of its ability to clear gallium from circulation *in vivo* in healthy and tumoured animals. To be useful as a contrast-enhancing tool in the context of cancer imaging with ^{68}Ga salts, THP^{Me} should be able to remove ^{68}Ga efficiently from circulation while leaving ^{68}Ga tumour uptake unaltered or only marginally affected.

The main goal of the *in vitro* investigation was to verify that ^{68}[Ga(THP^{Me})] itself could not accumulate into A375 cells and that THP^{Me} could not deplete the intracellular pool of gallium. Two different experiments were performed, in which cells were treated with THP^{Me} before or after addition of ^{68}Ga. Importantly, total incubation time with ^{68}Ga was different for the two experiments, resulting in different absolute values for ^{68}Ga uptake. However, this was not considered an issue since data were normalised (uptake of non-treated sample set equal to 1 for each experiment) and only differences in uptake between treated and untreated samples was considered.

Incubation with THP^{Me} before addition of gallium was found to reduce gallium uptake in A375 cells, suggesting that THP^{Me} can bind gallium in the medium and that this process competes with cellular accumulation of the radiometal. The extent of the reduced uptake was larger at higher chelator concentration, reflecting an increased efficacy/rapidity of ^{68}Ga binding at increasing concentration of the chelator. When the order of the two incubation steps was reversed, the decrease in uptake was found less significant and did not depend on concentration of the chelator. Analysis of the cellular distribution of ^{68}Ga showed that, in this experiment, the chelator was mainly decreasing membrane binding of gallium while intracellular uptake was only marginally affected. This result suggests that THP^{Me} is not able to remove gallium already internalised in cells. The uptake reduction observed in this experiment is likely due to complexation of extracellular ^{68}Ga competing with further cellular uptake of the radiometal. Notably, when the same experiment was performed with gallium-67, for which intracellular uptake may be saturated due to higher concentration of gallium at equal amount of radioactivity, no effect whatsoever was observed for the cells treated with THP^{Me} after addition of ^{68}Ga (post-gallium samples). This supports the hypothesis that THP^{Me} cannot remove internalised gallium, but also suggests that, in these

194

conditions, the intracellular pool of gallium is saturated in as little as 30 min and further uptake only happens at the membrane level.

In vivo studies with THP[Me] were initially conducted in healthy mice to test the chelator's ability to bind gallium *in vivo*, sequestering it from transferrin and clearing it from the circulation. In a first dose-finding study, THP[Me] was found able to chelate ^{68}Ga *in vivo*, when injected 45 min after the radiometal, at doses as low as 1 μg (1.2 nmol). The blood clearance effect was very evident in the PET/CT images, but less dramatic in *ex vivo* biodistribution data, where the main decrease in uptake was found for organs where gallium tends to accumulate (such as femur and liver). This suggests that THP[Me] treatment significantly increases the renal clearance of the activity from the blood, which in turn reduces delivery of the radiometal to the different organs. However, complete removal of residual blood pool activity could not be achieved. This was also observed in image-derived time/activity curves, where only a relatively mild decrease in % ID for the heart (considered as a measure of blood uptake), was visible after THP[Me] injection, despite the dramatic % ID increase in bladder.

Importantly, even in this pilot study, high variability in biodistribution of ^{68}Ga was observed when administered as ^{68}Ga-acetate, particularly concerning uptake in the liver. In one particular case high spleen uptake was also observed (**Figure 4.15 A**), likely resulting from the presence of colloidal gallium for that particular ^{68}Ga-acetate batch [43]. Although the reasons behind formation of colloidal gallium species are not fully understood, it is worth noting that an elution from an "old" ^{68}Ga generator, potentially richer in metal contaminants, was used for that mouse. Presence of other metal ions is known to favour formation of Ga(III) colloids [44]. To avoid the same situation, only relatively new and regularly eluted generators were used for further experiments and high spleen uptake was not re-encountered.

The high variability observed in ^{68}Ga biodistribution could be imputable to several factors, such as time of the day, mice diet and metabolism, different elution in terms of metal impurity or pH, depth of anaesthesia. Therefore, in further experiments, precautions were taken so that we could unambiguously assign any observed effect to THP[Me]-mediated clearance instead of other, difficult-to-control, variables. Confounding effects that could be avoided were eliminated (*e.g.* mice were maintained under anaesthesia all the time). To minimise the effect of other factors, the different experimental groups were spread over different cages, time of the day, generator elutions, day of experiment. On the other hand, the higher variability resulting from this choice, not only decreased the possibility of type 1 error (false

positive) as desired, but also increased the possibility of type 2 error (false negative), reducing the overall statistical power of the experiments.

Before moving to A375 xenografts, more studies in healthy animals were performed, aimed at understanding the influence of the time delay between ^{68}Ga and chelator injection on the blood clearance effect of THP^{Me}, and at comparing the effect of this chelator with the effect of DFO. In the first experiment, the effect of two extremely different time delays, namely 5 and 90 min, between ^{68}Ga and THP^{Me} injection was evaluated. A clear effect of the THP^{Me} was visible when the chelator was injected 5 min after ^{68}Ga, while a delay of 90 min resulted in a very small difference between control and THP^{Me}-treated mice. This observed difference is at least partially attributable to the fact that, for the 90 min experiment, the % ID/g in the blood had already decreased before the THP^{Me} injection, thus limiting the possible clearance effect of the chelator. Notably, a P value of 0.026 was obtained by t-test comparison of % ID/g in blood for the control groups of the two experiments, suggesting a significant decrease in blood activity even in the 90 min study. On the other hand, *ex vivo* biodistribution was performed 15 min after injection of the chelator and the resulting % ID/g in the blood may differ from that at the time of THP^{Me} injection (especially for the 5 min group). Remarkably, data from both experiments confirmed the inability of THP^{Me} to remove ^{68}Ga from the circulation completely. Whether this is due to continuous re-equilibration between blood and perfused organs, or to a fraction of non-labile gallium present in the blood pool, is still uncertain.

Interestingly, the % ID/g associated with kidneys in the 90 min delay experiment was significantly higher for animal treated with THP^{Me}, while no significant decrease in the % ID/g for other organs was observed. This discrepancy is only apparent because the biodistribution graphs compare concentrations (% ID/g), rather than total amount of uptake (% ID). A large increase in concentration, for small organs such as the kidneys, can actually reflect a relatively small difference in the total uptake of the organ. On the other hand, for a large, high-capacity system such as the skeleton, a very small change in the % ID/g can account for a large difference in % ID. Therefore, in principle, the small % ID/g decrease observed for bone could underlie the increased kidney activity. Unfortunately, since no measure of the total % ID in the skeleton was available (only femur activity was measured in *ex vivo* biodistribution, and no quantification of the images was possible due to lack of CT), this hypothesis cannot be demonstrated. Finally, an increased skin and fur uptake was observed for treated animals in the 5 min group. Since, for all these mice, skin and fur was removed from the abdomen, we can hypothesise that contamination from urine happened. Contamination is much more

likely for treated animals, which in general had more activity in the urine than control animals. To avoid this issue, in further experiments skin and fur were collected from the ears of the mice (less likely to be contaminated with urine), and the issue did not recur.

Overall, for both experiments, standard deviations were very high for THP^{Me} treated mice, especially in those organs involved in renal excretion of the activity, suggesting that clearance worked to a different extent in different experiments. Although this can be explained by several reasons related to the different mice, generator elutions *et cetera*, the simplest explanation is difference in the success of THP^{Me} injection (i.e. how much of the injected volume was actually injected IV and not subcutaneously). In fact, this second injection was performed on mice that have been under anaesthesia for up to 90 minutes and was therefore difficult due to lower body temperature and consequent shrinkage of blood vessels. Furthermore, contrary to the injection of the radiometal, when the chelator is injected there is no way to quantify the amount of chelator remaining in the tail and to correct the administered dose accordingly. Although a cannula was used to ensure the needle was kept in the same position used for the radiometal injection, on a few occasions the vein occluded due to blood clotting and injection of THP^{Me} was then performed with an insulin syringe. Notably, the rate at which ^{68}Ga is cleared from the kidneys, which was found very variable between experiments, could also be attributable to a variable success of the THP^{Me} injection. While a successful IV injection can quickly clear ^{68}Ga from the blood, through the kidneys and into the bladder, a less successful injection (subcutaneous) can still have a blood clearance effect, but mediated by the slow diffusion of the chelator into the circulation. As a result, ^{68}Ga clearance is in this case slower and the activity is present in the kidney for longer.

Based on the results from these clearance experiments, and on the observation that ^{68}Ga starts to selectively accumulate in tumours from 30-60 min post injection, 60 min was chosen as a suitable time delay between injections in animals bearing A375 xenografts. The 24 nmol dose (20 µg of chelator) was chosen as a suitable chelator dose. These conditions were first tested in healthy mice and, on this occasion, the effect of THP^{Me} was compared to that of the hydroxamate based chelator DFO, which had previously been investigated for similar purposes. The two chelators were administered *via* the same route (IV) and, notably, at the same dose (24 nmol) to investigate which chelator possessed higher blood clearance capability. This was important since DFO is already approved for clinical use in the treatment of iron overload and could therefore represent a privileged candidate for clinical translation.

The study showed that the clearance effect was still visible when THP^{Me} was injected 60 min after ^{68}Ga, not only in kidneys but also in femur and liver, although the difference was not significant due to low N number and high variance. The clearance effect observed by injection of DFO was significantly smaller than that seen for THP^{Me} (especially in kidney), but some reduced uptake in femur and liver and increased excretion of ^{68}Ga in urine was still visible. It was therefore decided to investigate both THP^{Me} and DFO as clearance agents in a cancer model.

Finally, the blood clearance ability of THP^{Me} and DFO was finally evaluated in NSG mice bearing A375 xenografts using both PET/CT and *ex vivo* biodistribution. Unexpectedly, in this experiment neither THP^{Me} nor DFO were able to selectively clear ^{68}Ga from the blood pool and thus they did not enhance tumour-to-blood ratio. In particular, while DFO appeared not to have an effect on ^{68}Ga biodistribution and clearance, data for THP^{Me} suggest that this chelator clears gallium equally from both blood and tumour tissue, leaving the tumour-to-blood ratio unaffected. However, although extremely valuable, *ex vivo* biodistribution only represents a snapshot of the activity distribution at a given time and does not give us any information on what happened between ^{68}Ga injection and culling of the animal. This information can be instead provided by dynamic PET imaging, which in this case was extremely important to correctly interpret the data. In fact, PET/CT images unexpectedly showed how gallium was mostly cleared from the blood of all animals very quickly after administration, so that activity was already largely in the kidneys/bladder before the second injection. In this situation, the clearance effect observed for THP^{Me} is attributable to *in vivo* chelation of residual circulating radiometal, preventing further accumulation in the tumour or in other organs. Notably, this increased renal clearance also explains why the % ID/g measured for the kidneys (**Figure 4.28**) is extremely high not only for the THP^{Me}-treated group but also for the DFO-treated group and the control.

The reasons behind this unexpectedly fast clearance of ^{68}Ga are uncertain and cannot easily be explained by considering any of the classical species that Ga^{3+} is known to form in serum. For example, quick renal clearance was previously observed in mice overloaded with iron, depleted in the transferrin pool or not expressing the transferrin receptor, and was attributed to gallium presence as [Ga(OH)$_4$]$^-$. However, in all those cases uptake in the bones was also increased [45,46], while, in our case % ID/g in the femur is largely decreased compared to the first experiment. On the other hand, full binding to transferrin should produce low bone uptake but also increase the uptake in highly perfused organs and, notably, the overall clearance time [47]. Finally, colloidal gallium should accumulate mainly in liver/spleen [43].

Overall, with this experiment we cannot definitively conclude whether THP^{Me} can be used as a blood clearance agent in this model. The same conclusions hold, in principle, also for DFO, since rapid renal clearance also affected biodistribution in the DFO-treated animals. However, inability of this chelator to influence biodistribution of gallium, both in healthy animals and xenograft models makes it safe to rule out any blood clearance efficacy of DFO when injected IV at a 24 nmol dose (15 µg, $\approx$ 0.75 mg/kg). Importantly, while this dose already exceeds the clinically used dosage for IV administration (0.25 mg/kg/min), the therapeutic dose for IM administration is 1000 mg/kg, therefore IM administration of DFO at this higher dose could potentially be investigated as an alternative to THP^{Me}.

Repetition of this final experiment is warranted, but requires prior understanding of the reasons behind the observed fast clearance, in order to avoid its recurrence. The causes of the variable uptake seen in liver and bones should also be investigated in order to reduce variability and increase reproducibility and significance of our data.

Preliminary data from our laboratories suggest that part of the variability in ^{68}Ga biodistribution could be related to different generator elutions. In particular, the first elution of the day (up to 24 hours elapsed from previous elution) was generally found to give higher liver and spleen uptake and lower bone uptake compared to successive elutions. More experiments are needed to verify this hypothesis.

4.5 Conclusion

In this work, the use of radioactive gallium salts for cancer imaging was reassessed using ^{68}Ga-acetate combined with THP^{Me} as a blood clearance agent, with the aim of increasing tumour-to-blood ratio and, accordingly, image contrast at short time points.

A375 human melanoma cells were found to moderately accumulate gallium through transferrin independent mechanisms *in vitro*. Significant uptake was also found in A375 xenografts *in vivo* with maximum uptake occurring between 1 and 2 hours after ^{68}Ga injection. Although transferrin dependent mechanisms were likely involved in the *in vivo* studies, the intense bone uptake observed suggests that transferrin independent mechanism were still prevalent. ^{68}Ga-oxine was also able to transport gallium into A375 cells *in vitro*, but unable to deliver the radiometal to the tumour *in vivo* when injected intravenously. Further studies with ^{68}Ga-oxine were therefore abandoned. Interestingly, high uptake in the myocardium was found for ^{68}Ga-oxine and warrants further exploration.

THP^{Me} was found able to influence the biodistribution of ^{68}Ga-acetate in healthy mice when injected 5 to 60 min after the radiometal. The chelator was effective at a 1 mg/kg dosage (20 µg per mouse), at least 40-fold lower than what previously tested in the literature for other blood clearance agents [11]. *In vitro* experiments demonstrated that [^{68}Ga(THP^{Me})] does not accumulate in A375 cells and that THP^{Me} cannot deplete the intracellular pool of gallium. Therefore, THP^{Me} was deemed an interesting chelator to investigate as a blood clearance agent in A375 xenografts at 24 nmol (20 µg) and with a delay of 1 hour between injection of activity and chelator. DFO, whose ^{67}Ga blood clearance activity had been previously examined in the literature, was also tested in the same conditions, although superiority of THP^{Me} at this concentration was already established in a previous experiment in healthy animals. Unfortunately results of the final experiment were confounded by an extremely quick clearance of the activity for all animals, whose reasons are currently unknown. Repetition of the experiment will require further understanding of the reason for the unusual *in vivo* behaviour observed for ^{68}Ga in the last experiment.

In general, ^{68}Ga-acetate biodistribution was found to be extremely variable and unpredictable in different mice for all our experiments and this resulted in high standard deviations and reduced statistical power of the studies. Although similar issues were previously reported for ^{67}Ga-citrate studies, both at a preclinical and clinical level, the choice of using a weak Ga ligand may have exacerbated the problem. Providing gallium in a more stable chelate form (but not as stable as gallium-oxine)

could help in reducing variability. Potentially, gallium citrate could be used, even at the cost of increasing the required THP^{Me} dosage in case citrate can compete for *in vivo* binding of ^{68}Ga. Alternatively, transferrin itself could be used, upon verification that ^{68}Ga-transferrin can actually accumulate in A375 tumours in the same time range observed for ^{68}Ga-acetate (or at least in a time frame compatible with the use of ^{68}Ga). Notably, in this last case it would be interesting to compare human and mouse transferrin in their ability to deliver ^{68}Ga to the xenograft tumour.

Finally, investigation should be repeated in different tumour models, possibly characterised by higher ^{68}Ga uptake. Lymphoma is the cancer that more widely benefited from ^{67}Ga-citrate historically and would represent the ideal model for this investigation. However, establishment of a transgenic lymphoma mouse model is relatively complex compared to that of xenograft tumours [48]. Alternatively, screening different human cancer cell lines for uptake of ^{68}Ga could identify the most promising cell lines to use for establishing tumour xenografts in future investigation. In this regard, a preliminary experiment in a SW1222 colorectal cancer xenograft model was attempted and will be discussed in **Chapter 5**.

4.6 References

1. Larson, S. M., Milder, M. S., and Johnston, G. S. (1973) Interpretation of Ga-67 photoscan. *J. Nucl. Med.* **14**, 208-214.
2. Yamamoto, F., Tsukamoto, E., Nakada, K., Takei, T., Zhao, S. J., Asaka, M., and Tamaki, N. (2004) F-18-FDG PET is superior to Ga-67 SPECT in the staging of non-Hodgkin's lymphoma. *Ann. Nucl. Med.* **18**, 519-526.
3. Kostakoglu, L., and Goldsmith, S. J. (2000) Fluorine-18 fluorodeoxyglucose positron emission tomography in the staging and follow-up of lymphoma: is it time to shift gears? *Eur. J. Nucl. Med.* **27**, 1564-1578.
4. Sanchez-Crespo, A., Andreo, P., and Larsson, S. A. (2004) Positron flight in human tissues and its influence on PET image spatial resolution. *Eur. J. Nucl. Med. Mol. Imaging* **31**, 44-51.
5. Vorster, M., Maes, A., Jacobs, A., Malefahlo, S., Pottel, H., Van de Wiele, C., and Sathekge, M. M. (2014) Evaluating the possible role of Ga-68-citrate PET/CT in the characterization of indeterminate lung lesions. *Ann. Nucl. Med.* **28**, 523-530.
6. Behr, S. C., Aggarwal, R., Seo, Y., Aparici, C. M., Chang, E., Gao, K. T., Tao, D. H., Small, E. J., and Evans, M. J. (2016) A feasibility study showing Ga-68 citrate PET detects prostate cancer. *Mol. Imaging Biol.* **18**, 946-951
7. Sephton, R. (1981) Relationships between the metabolism of Ga-67 and iron. *Int. J. Nucl. Med. Biol.* **8**, 323-331.
8. Santos, M. A., Gil, M., Gano, L., and Chaves, S. (2005) Bifunctional 3-hydroxy-4-pyridinone derivatives as potential pharmaceuticals: synthesis, complexation with Fe(III), Al(III) and Ga(III) and in vivo evaluation with Ga-67. *J. Biol. Inorg. Chem.* **10**, 564-580.
9. Hurwitz, S. R., Hagan, P. L., and Alazraki, N. P. (1975) Distribution of Ga-67 following intravenous administration - effects of disodium Edetate therapy. *J. Nucl. Med.* **16**, 280-283.
10. Hoffer, P. B., Samuel, A., Bushberg, J. T., and Thakur, M. (1979) Effect of desferoxamine on tissue and tumor retention of Ga-67 - concise communication. *J. Nucl. Med.* **20**, 248-251.
11. Larson, S. M., Rasey, J. S., Grunbaum, Z., and Allen, D. R. (1979) Pharmacologic enhancement of ga-67 tumor-to-blood ratios for EMT-6 sarcoma (BALB/c mice). *Radiology* **130**, 241-244.
12. Koizumi, K., Tonami, N., and Hisada, K. (1982) Deferoxamine mesylate enhancement of Ga-67 tumor-to-blood ratios and tumor imaging. *Eur. J. Nucl. Med.* **7**, 229-233.
13. Moerlein, S. M., Welch, M. J., and Raymond, K. N. (1982) Use of tricatecholamide ligands to alter the biodistribution of Ga-67 - concise communication. *J. Nucl. Med.* **23**, 501-506.
14. Hammersley, P. A. G. (1984) Relative tumor enhancement of Ga-67 uptake by desferrioxamine. *Eur. J. Nucl. Med.* **9**, 467-471.
15. Oster, Z. H., Som, P., Sacker, D. F., and Atkins, H. L. (1980) The effects of deferoxamine mesylate on Ga-67 distribution in normal and abscess-bearing animals - concise communication. *J. Nucl. Med.* **21**, 421-425.
16. Hoffer, P. B., Samuel, A., Bushberg, J. T., and Thakur, M. (1979) Desferoxamine mesylate (desferal) - contrast-enhancing agent for Ga-67 imaging. *Radiology* **131**, 775-779.
17. Moeschlin, S., and Schnider, U. (1963) Treatment of primary and secondary hemochromatosis and acute iron poisoning with a new, potent iron-eliminating agent (Desferrioxamine-B). *N. Engl. J. Med.* **269**, 57-66.
18. Novartis. (2011) Desferal: Prescribing information.
19. Hofman, M. S., Eu, P., Jackson, P., Hong, E., Binns, D., Iravani, A., Murphy, D., Mitchell, C., Siva, S., Hicks, R. J., Young, J. D., Blower, P., and Mullen, G. E.

(2017) Cold Kit PSMA PET Imaging: Phase I study of ^{68}Ga-THP-PSMA PET/CT in patients with prostate cancer. *J. Nucl. Med.* (ahead of print, doi:10.2967/jnumed.117.199554).

20. Chitambar, C. R. (2012) Gallium-containing anticancer compounds. *Future Med. Chem.* **4**, 1257-1272.

21. Timerbaev, A. R. (2009) Advances in developing tris(8-quinolinolato)gallium(III) as an anticancer drug: critical appraisal and prospects. *Metallomics* **1**, 193-198.

22. Zhou, T., Neubert, H., Liu, D. Y., Liu, Z. D., Ma, Y. M., Kong, X. L., Luo, W., Mark, S., and Hider, R. C. (2006) Iron binding dendrimers: A novel approach for the treatment of haemochromatosis. *J. Med. Chem.* **49**, 4171-4182.

23. Yano, Y., Budinger, T. F., Ebbe, S. N., Mathis, C. A., Singh, M., Brennan, K. M., and Moyer, B. R. (1985) Ga-68 lipophilic complexes for labeling platelets. *J. Nucl. Med.* **26**, 1429-1437.

24. Kozlowski, J. M., Hart, I. R., Fidler, I. J., and Hanna, N. (1984) A human-melanoma line heterogeneous with respect to metastatic capacity in athymic nude-mice. *J. Natl. Cancer Inst.* **72**, 913-917.

25. Cornelissen, B., Darbar, S., Hernandez, R., Kersemans, V., Tullis, I., Barber, P. R., Smart, S., Vojnovic, B., Reilly, R., and Vallis, K. A. (2011) ErbB-2 blockade and prenyltransferase inhibition alter epidermal growth factor and epidermal growth factor receptor trafficking and enhance In-111-DTPA-hEGF auger electron radiation therapy. *J. Nucl. Med.* **52**, 776-783.

26. Puncher, M. R. B., and Blower, P. J. (1994) Radionuclide targeting and dosimetry at the microscopic level - the role of microautoradiography. *Eur. J. Nucl. Med.* **21**, 1347-1365.

27. Bin Othman, M. F. (2017) *Potential of Gallium-67 as a Therapeutic Radionuclide*, PhD Thesis, King's College London.

28. Szanda, I., Mackewn, J., Patay, G., Major, P., Sunassee, K., Mullen, G. E., Nemeth, G., Haemisch, Y., Blower, P. J., and Marsden, P. K. (2011) National electrical manufacturers association NU-4 performance evaluation of the PET component of the NanoPET/CT preclinical PET/CT scanner. *J. Nucl. Med.* **52**, 1741-1747.

29. Magdics, M., Szirmay-Kalos, L., Toth, B., Legrady, D., Cserkaszky, A., Balkay, L., Domonkos, B., Voelgyes, D., Patay, G., Major, P., Lantos, J., Buekki, T. (2011) Performance evaluation of scatter modeling of the GPU-based "Tera-Tomo" 3D PET reconstruction. *2011 IEEE (Nss/Mic)*, 4086-4088.

30. Millipore, E. (2012) Scepter™ 2.0 Cell Counter: product description. EMD Millipore, Merck.

31. Ghosh, S., Das, T., Sarma, H. D., and Banerjee, S. (2017) Preparation and preliminary bioevaluation of Ga-68-oxine in lipiodol as a potential liver imaging agent. *J. Radioanal. and Nucl. Chem.* **311**, 263-268.

32. Rudnev, A. V., Foteeva, L. S., Kowol, C., Berger, R., Jakupec, M. A., Arion, V. B., Timerbaev, A. R., and Keppler, B. K. (2006) Preclinical characterization of anticancer gallium(III) complexes: Solubility, stability, lipophilicity and binding to serum proteins. *J. Inorg. Biochem.* **100**, 1819-1826.

33. Jonkhoff, A. R., Huijgens, P. C., Versteegh, R. T., Vandieren, E. B., Ossenkoppele, G. J., Martens, H. J. M., and Teule, G. J. J. (1993) Ga-67 radiotoxicity in human U937 lymphoma-cells. *Br. J. Cancer* **67**, 693-700.

34. Saha, G. B. (2010) *Fundamentals of nuclear pharmacy*, Springer Science & Business Media.

35. Sephton, R. G., Hodgson, G. S., Deabrew, S., and Harris, A. W. (1978) Ga-67 and Fe-59 distributions in mice. *J. Nucl. Med.* **19**, 930-935.

36. Morfin, J.-F., and Toth, E. (2011) Kinetics of Ga(NOTA) formation from weak Ga-Citrate complexes. *Inorg. Chem.* **50**, 10371-10378.

37. Shen, X., Hu, G.-b., Jiang, S.-j., He, F.-r., Xing, W., Li, L., Yang, J., Zhu, H.-f., Lei, P., and Shen, G.-x. (2009) Engineering and characterization of a

baculovirus-expressed mouse/human chimeric antibody against transferrin receptor. *Protein Engineering Design & Selection* **22**, 723-731.

38. Sephton, R. G., and Harris, A. W. (1975) Gallium-67 citrate uptake by cultured tumor-cells, stimulated by serum transferrin. *J. Natl. Cancer Inst.* **54**, 1263-1266.

39. Young, S. P., and Garner, C. (1990) Delivery of iron to human-cells by bovine transferrin - implications for the growth of human-cells in vitro. *Biochemical Journal* **265**, 587-591.

40. Collery, P., Jakupec, M. A., Kynast, B., and Keppler, B. K. (2006) Preclinical and early clinical development of the antitumor gallium complex KP46 (FFC11). in *Metal Ions in Biology and Medicine, Vol 9* (Editors: Alpoim, M. C., and Morais, P. V.). pp 521-524.

41. Hofheinz, R. D., Dittrich, C., Jakupec, M. A., Drescher, A., Jaehde, U., Gneist, M., Graf von Keyserlingk, N., Keppler, B. K., and Hochhaus, A. (2005) Early results from a phase I study on orally administered tris(8-quinolinolato)gallium(III) (FFC11, KP46) in patients with solid tumors--a CESAR study (Central European Society for Anticancer Drug Research--EWIV). *Int. J. Clin. Pharmacol. Ther.* **43**, 590-591.

42. Collery, P., Domingo, J. L., and Keppler, B. K. (1996) Preclinical toxicology and tissue gallium distribution of a novel antitumour gallium compound: Tris(8-quinolinolato)gallium(III). *Anticancer Res.* **16**, 687-691.

43. Petrik, M., Vlckova, A., Novy, Z., Urbanek, L., Haas, H., and Decristoforo, C. (2015) Selected Ga-68-siderophores versus Ga-68-colloid and Ga-68-citrate: biodistribution and small animal imaging in mice. *Biomedical Papers-Olomouc* **159**, 60-66.

44. Ehrhardt, G. J., and Welch, M. J. (1978) New germanium-68-gallium-68 generator. *J. Nucl. Med.* **19**, 925-929.

45. Hayes, R. L., Carlton, J. E., and Byrd, B. L. (1965) Bone scanning with gallium-68 - A carrier effect. *J. Nucl. Med.* **6**, 605-609.

46. Tsan, M. F., and Scheffel, U. (1986) Mechanism of Ga-67 accumulation in tumors. *J. Nucl. Med.* **27**, 1215-1219.

47. Weiner, R. E. (1996) The mechanism of Ga-67 localization in malignant disease. *Nucl. Med. Biol.* **23**, 745-751.

48. Kohnken, R., Porcu, P., and Mishra, A. (2017) Overview of the Use of Murine Models in Leukemia and Lymphoma Research. *Frontiers in Oncology* **7**

5 Pretargeting *via* metal chelation exploiting the Ga(III) *tris*(hydroxypyridinone) couple

5.1 Introduction

The development and clinical translation of monoclonal antibodies (mAb), following the advent of hybridoma technology in 1975 [1], represented a paradigm shift in cancer therapy. In a field dominated by small-molecule chemotherapeutics, whose selectivity was often solely based on the accelerated metabolism of tumour cells, antibody-based therapy introduced the ability to selectively target cancer lesions expressing a particular antigen [2]. The therapeutic activities of mAbs may result from direct action (agonistic/antagonistic) on the target receptor, or indirect mechanisms such as recruitment of the immune system or through effects on tumour vasculature and stroma. Many antibodies may function by a combination of direct and indirect mechanisms [2].

Monoclonal antibodies can also be employed as highly selective vectors for the delivery of drugs or, notably, radionuclides. Depending on the decay properties of the radioisotope, radiolabelled mAbs can be useful for cancer diagnosis (immunoSPECT/immunoPET) or radioimmunotherapy [3]. Non-metallic radioisotopes such as iodine-131 can be incorporated directly into antibodies by chemical modification of an amino acid side-chain [4]. Direct radiolabelling with radiometals has been explored for ^{99m}Tc and ^{188}Re, using disulfide bond reduction to create free sulfhydryl groups able to coordinate the M(V) metal ion [5]. Nevertheless, radiometals incorporation into proteins generally involve a chelating moiety, which can be a polyhistidine-tag inserted into the amino acid sequence of the antibody, like in the case of ^{99m}Tc [6], or more commonly a bifunctional chelator (BFC) covalently bound to an antibody through an amino acid side-chain. This useful approach has found wide applicability and allows for a variety of radioisotope/amino acid residue matchings by simply changing the chelating or functional group of the BFC. Conjugation of the bifunctional chelator to the antibody can be site-specific, exploiting single cysteines engineered into the amino acid sequence or, more commonly, free thiols generated by reduction of disulfide bonds [7]. Alternatively, non-specific conjugation to amino groups (lysine side chains and amino terminus) can be performed [8]. A schematic representation of a radioimmunoconjugate is presented in **Figure 5.1**. Several chelating systems useful for gallium were described in **Chapter 1**, and chelators for different radiometals have been extensively described in the literature [9].
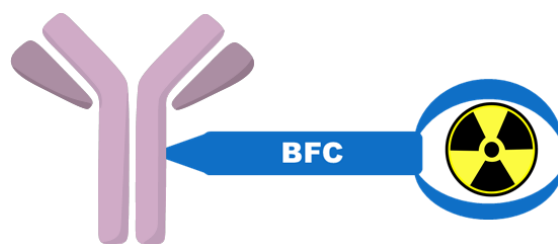
Figure 5.1. *Schematic representation of a radioimmunoconjugate showing an antibody covalently attached to a bifunctional chelator (BFC), which is in turn coordinating a radiometal via its chelating moiety.*

Antibody fragments were also developed, such as the antigen binding fragments (Fab, $F(ab)_2$ and Fab') obtained by enzymatic digestion of the full antibody, which could be radiolabelled following the same principles, but offered modulation of the pharmacokinetics due to the lower size (**Figure 5.2**) [10].

5.1.1 Clinical application and limitations

Despite the numerous potential advantages of radiolabelled antibodies over conventional imaging and radiotherapeutic agents, only four radiolabelled full-length mAbs and two radiolabelled Fab' have been approved by the FDA for cancer imaging/treatment since the approval of ^{111}In-satumomab pendetide in 1992 as reported in **Table 5.1**. Even more surprisingly, four of them have been subsequently withdrawn from the market [11]. In addition, despite the growing popularity of PET and the increasing number of clinical trials involving mAb radiolabelled with positron-emitting isotopes [12], no immunoPET derivatives have been approved for clinical use so far.

Table 5.1. *FDA-approved radioantibodies for cancer imaging (orange) and treatment (light blue).*

Name	Trade Name	Agent	Indication	Approval
Satumomab pendetide	OncoScint	^{111}In-murine anti-TAG-72 IgG	Colorectal and ovarian cancer	1992 (withdrawn)
Nofetumomab merpentan	Verluma	^{99m}Tc-murine anti-EGP-1 Fab'	Small cell lung cancer	1996 (withdrawn)
Arcitumomab	CEA-scan	^{99m}Tc-murine anti-CEA Fab'	Colorectal cancer	1996 (withdrawn)
Capromab pendetide	ProstaScint	^{111}In-murine anti-PSMA	Prostate cancer	1996
Ibritumomab tiuxetan	Zevalin	^{90}Y-murine anti-CD20 IgG +rituximab	B-cell lymphoma	2002
Tositumomab "anti b1"	Bexxar	^{131}I-murine anti-CD20 IgG + unlabeled tositumomab	B-cell lymphoma	2003 (withdrawn)

While the reasons behind the limited clinical success of radiolabelled antibodies are multiple and certainly include both the cost and technical difficulties associated with their preparation and administration [13], the slow pharmacokinetic properties of full-length and Fab derivative antibodies also represent an important limitation for their routine clinical utilisation. In fact, partly owing to the high molecular weight of antibodies, tumour accumulation and blood clearance of radioactivity is slow, requiring extended periods of time (6-48 hours or more) to reach an adequate tumour-to-blood ratio. Accordingly, only radioisotopes with half-life > 6 hours can be used to label the antibody, to deliver sufficient radioactivity to the target tissue to allow effective imaging or therapy. In addition, the slow blood clearance of these radioimmunoconjugates results in an increased exposure of non-target organs to radiation, and limits the maximum radiation dose that can be administered to a patient for therapeutic purposes [14].

Today, different types of antibody-like molecules are also available alongside full-length mAbs and Fabs, such as minibodies, diabodies and single domain antibody fragments (dAb), as well as the fusion proteins scFv (single chain variable fragments) and affibodies. A schematic representation of their structure is provided in **Figure 5.2,** alongside an approximate molecular weight. Because of the lower molecular weight of these molecules, they display faster tumour uptake and blood-clearance than full-length antibodies, thus allowing higher doses of radiation to be injected. On the other hand, often these derivatives show lower tumour accumulation and higher kidney uptake compared to full-length antibodies [15,16].
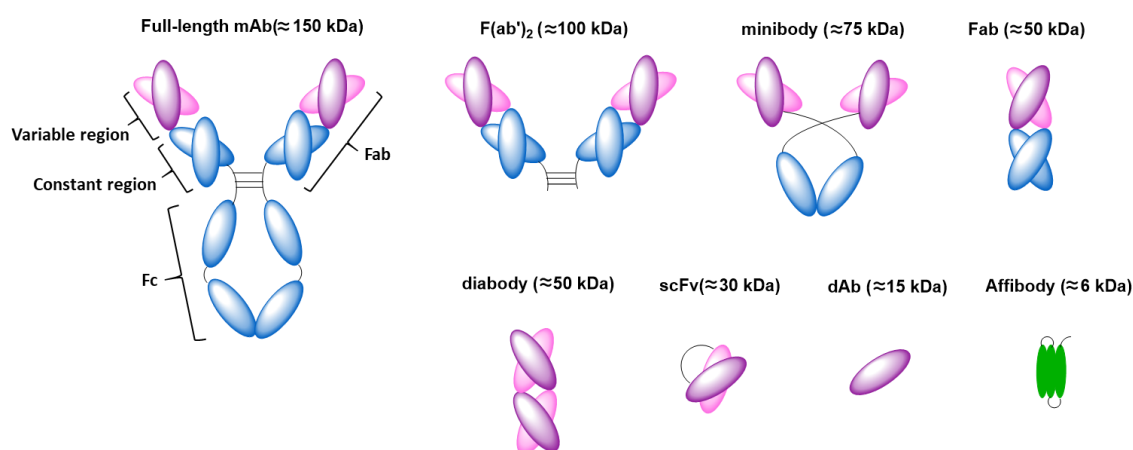

Figure 5.2. *Schematic representation and approximate molecular weight of different antibody fragments and antibody-like molecules, in comparison with a full-length antibody.*

5.1.2 Pretargeting approaches to imaging and therapy with antibodies

Pretargeting represents a promising alternative to traditional radioimmunotherapy /radioimmunodiagnostic techniques. As mentioned in **Chapter 2**, pretargeting combines the exquisite selectivity of antibodies with the favourable pharmacokinetics of small molecules and is based on decoupling the slow antigen-targeting performed by the antibody from the delivery of the radioisotope [17]. In a pretargeting approach, the unlabelled antibody is administered first and allowed to reach its tumour target; then a radioactive probe is delivered to radiolabel the antibody at its receptor site. Here the antibody-BFC-radioisotope triad is reconstructed *in vivo* exploiting a high-affinity chemical pair (schematic representation of pretargeting strategies and high-affinity chemical pairs is reported in **Figure 5.3**). Since this radiolabelled probe is far smaller than the antibody, the probe quickly reaches its target antibody and clears from the blood pool, thus reducing exposure of non-target organs to radiation and enabling the use of short-lived radioisotopes. Importantly, the pretargeting approach also presents some limitations, such as the need for a target receptor (i) highly expressed on cancer cells surface and (ii) internalising slowly upon antibody binding, so that the pretargeted antibody is accessible to the radiolabelled probe. Furthermore, to achieve sufficient tumour uptake of the radiotracer, relatively large amounts of antibody are needed which may results in toxicity. Four major approaches to pretargeting, exploiting different high-affinity chemical pairs, have emerged in the last decades and are extensively discussed in a number of recent reviews [15,17,18]. A summary of these strategies is presented in the paragraphs below.

An early pretargeting method employed bispecific mAbs. These are artificial antibodies consisting of two different arms: one to target the tumour receptor in an early pretargeting stage, the second to specifically bind the hapten moiety of a radiolabelled probe injected after the bispecific mAb is cleared from the blood [19]. This is the pretargeting strategy most widely investigated in clinics, and underwent an extensive optimisation of the type of haptens and antibody constructs. The most recent and promising examples exploit a trivalent construct in which two Fab moieties are targeting the desired tumour antigen and the third is binding to a histamine-succinyl-glycine hapten moiety of the radiolabelled probe [20] (see **Chapter 2** for clinical application using ^{68}Ga).

In a different strategy, the outstanding affinity of streptavidin for biotin [21,22] is exploited in two different ways. The two-step method, developed by Hnatowich, utilises a streptavidin-conjugated antibody that pretargets the tumour antigen. After

excess immunoconjugate has cleared from the blood (*e.g.* using a blood clearing agent such as glycosylated avidin), radiolabelled biotin is administered and binds to the pretargeted streptavidin-conjugated antibody [22]. The reverse combination: biotinylated mAb followed by radiolabelled streptavidin probe, was also tested but found less effective due to slow blood clearance of streptavidin. In a second approach, referred to as three-step pretargeting, a biotinylated antibody is administered and allowed to reach its target, followed by glycosylated avidin to clear excess immunoconjugate from the blood to the liver. Streptavidin is then injected and binds to prelocalised biotinylated mAbs, creating the functional pretargeted complex that can finally interact with radiolabelled biotin molecules, administered in the final step [23]. Although this pretargeting strategy is very promising, the immunogenicity of streptavidin is a major obstacle for its clinical translation [24].

A third pretargeting approach investigates the use of two complementary DNA-analogue fragments, one conjugated to the antibody and the other to the radiolabelled chelator, acting as bridging agents between the two molecules [25]. While native phosphodiester DNA suffers from *in vivo* hydrolysis by nucleases, the use of synthetic, non-immunogenic DNA analogues based on a different backbone, such as phosphorodiamidate morpholino oligomers [26,27] and peptide nucleic acids [28], has proved to be more successful.

A more recent approach to pretargeting exploits "click" reactions between a suitable diene and dienophile couple. Compared to the previous approaches, this strategy exploits a covalent bond between antibody and probe rather than relying on high affinity non-covalent interactions [17]. To be useful for pretargeting purposes, a chemical reaction needs to proceed quickly at low concentration and in the absence of catalyst, but also to be completely bioorthogonal, so that it would not interact with endogenous molecules [29]. While Staudinger ligation and strain-promoted alkyne–azide cycloaddition were initially considered for pretargeting purposes, an inverse electron demand Diels-Alder (IEDDA) cycloaddition has recently gained attention due to its faster kinetics [18]. In particular, promising preclinical results have been obtained, exploiting an IEDDA cycloaddition between a radiolabelled tetrazine-chelator and a *trans*-cyclooctene conjugated antibody [30,31].

The concept of pretargeting *via* metal chelation proposed by our group [32] is based on the hypothesis that a suitable metal/chelator couple could be used as the high-affinity chemical pair, able to bind *in vivo*. In a first step, an integer antibody-BFC immunoconjugate would be administered and allowed to reach its target, then radiolabelling of the immunoconjugate would be performed *in vivo*, following the

injection of an ionic or weakly complexed formulation of the radiometal. A schematic comparison of metal chelation pretargeting against more traditional pretargeted strategies is presented in **Figure 5.3**. Notably, pretargeting *via* metal chelation does not involve any radiosynthetic work, thus minimising handling of the radioisotope and, consequently, operator exposure to radiation. Compared to traditional pretargeting strategies, this new approach could allow for a quick and easy protocol, well-suited for clinical translation.

High-affinity couple
Antibody arm/hapten
Streptavidin/biotin
Complementary oligonucleotides
Diene/dienophile

Radiometal/BFC
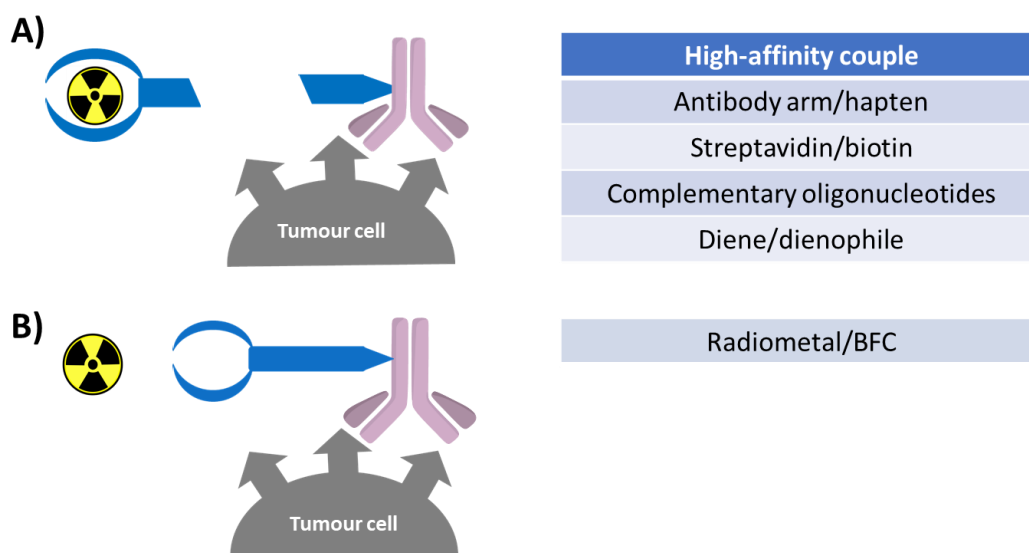
Figure 5.3. Schematic representation of pretargeting strategies employing different high-affinity chemical pairs. Traditional pretargeting strategies (A) employ radiolabelled probes to bind the pretargeted antibodies. On the contrary, in the pretargeting via metal chelation strategy (B), the radiometal could be administered as a salt, avoiding any radiosynthetic procedure.

Owing to the great selectivity of THP^{Me} chelators for Ga(III) (as discussed in **Chapters 1** and **3**) and to their ability to radiolabel rapidly with ^{68}Ga *in vivo,* in extremely mild conditions (as described in **Chapter 4**), the *tris*(hidroxypyridinone)/^{68}Ga(III) couple seemed ideal to test the pretargeting *via* metal chelation hypothesis. In this chapter, two different attempts to assess the feasibility of this approach have been investigated. In the first approach, a new THP^{Me}-dithiophenolmaleimide derivative (THP^{Me}-mal-DTP) has been conjugated site-specifically to an anti-CEA antibody and its pretargeting capability tested *in vitro* in LS174T colon cancer cells expressing the carcinoembryonic antigen (CEA). In the second approach, undertaken as part of a research visit at the Memorial Sloan Kettering cancer centre (MSKCC, New York) and Hunter College (New York), a non-site-specific conjugation of THP^{Me}-Ph-NCS to an huA33 antibody was adopted. In this case, the pretargeting *via* metal chelation hypothesis was evaluated *in vivo* exploiting a xenograft SW1222 colon carcinoma model expressing the A33 antigen.

5.2 Materials and methods

5.2.1 Equipment and consumables

THP^{Me}-NH$_2$ was obtained from Chematech (France). Unless otherwise stated, all reagents and buffers were purchased from Sigma-Aldrich and used without further purification. The full-length human IgG1 anti-CEA antibody ME1 was kindly provided by Dr Miranda Rota (Prof. Chester laboratories, UCL). The fully humanized IgG1 huA33 was obtained from the Ludwig Institute and the Olivia Newton-John Cancer Research Institute [33]. The DFO-huA33 conjugate used for ^{89}Zr radiolabelling was previously produced in Zeglis' laboratory according to published procedures [31]. All the buffers used for the huA33 experiments were prepared using Chelex-treated deionised water. Preparative HPLC was carried out using an Agilent Zorbax XDB-C18 column (21.2 x 150 mm, 5 μm) with a 5 mL/min flow rate and UV detection at 214 nm on an Agilent 1200 LC system. Mobile phase A was water with 0.1 % TFA, and mobile phase B was acetonitrile with 0.1 % TFA. A gradient from 0 % to 100 % B (1 %/min) was employed. Analytical size-exclusion HPLC was performed on the same system using an BioSep SEC-s2000 column (145 Å, 300 x 7.8mm, 5 μm) with a 1 mL/min flow rate and UV detection at 280 or 254 nM coupled to a LabLogic Flow-Count detector with a sodium iodide probe (B-FC-3200). Mobile phase was PBS (2 mM EDTA was added for radiolabelling experiments).

^{68}Ga was obtained from E&Z generator, by elution with 5 mL of 0.1 M ultrapure HCl (Fluka). The eluate was collected in ≈1 mL fractions and the activity of all fractions was measured with a dose calibrator (Capintec). The highest activity fraction was used for radiolabelling. ^{89}Zr was produced at Memorial Sloan Kettering Cancer Center through proton-beam bombardment of yttrium foil [34], and isolated as ^{89}Zr-oxalate.

Uptake of radioactivity in cells and organs was measured using a LKB Wallac 1282 Compugamma Gamma-counter at KCL, an Automatic Wizard gamma–counter (Perkin-Elmer) at MSKCC.

5.2.2 Synthesis of THP^{Me}-Ph-NCS

Bn-THP^{Me}-Ph-NCS was synthesised according to published procedures [35]. Briefly, *p*-phenylene-NCS (135 mg, 0.77 mmol) and DIPEA (75 μL, 0.44 mmol) were added to a solution of THP^{Me}-NH$_2$ (75 mg, 0.077 mmol) in DMF (2 mL) under stirring. After 15 min the DMF was removed under high-vacuum and the crude residue purified by preparative HPLC, yielding 43.7 mg of Bn-THP^{Me}-Ph-NCS (0.035 mmol, 45 % yield). Benzyl deprotection was then performed by addition of 5 mL of BCl$_3$ solution (1 M in

dichloromethane) and stirring under nitrogen followed by quenching with methanol on ice, solvent removal by rotary evaporation and purification *via* preparative HPLC to give 27.2 mg of THP^Me-Ph-NCS (0.028 mmol, 80 % yield). Product purity was verified by ^{1}H NMR and high-resolution mass spectrometry.

5.2.3   Synthesis of THP^Me-mal-DTP

The dithiophenolmaleimide derivative of THP^Me was obtained as part of a collaboration with Dr Ma (KCL). Briefly, benzyl deprotection of THP^Me-NH$_2$ (115 mg, 0.11 mmol) was performed as described above to give 86 mg of product (0.08 mmol, 85 % yield). dithiphenolmaleimide-NHS ester (10 mg, 0.02 mmol) was dissolved in DMSO (500 µL) and mixed with debenzylated THP^Me-NH$_2$ (20 mg, 0.023 mmol in 200 µL of DMSO). DIPEA (14 µL, 0.09 mmol) was added to the reaction mixture and the solution stirred at room temperature for 15 min before purification using preparative HPLC to yield 10 mg of pure product (0.009 mmol, 41 % yield).

^{1}H NMR (DMSO-d6, 400 MHz) δ: 1.70 (t, 2H, mal-CH$_2$-**CH$_2$**-CH$_2$ CONH),1.79 (t broad, 6H, CH$_2$-**CH$_2$**-CO-NH-CH$_2$-pyridinone), 2.04 (t broad, 6H, **CH$_2$**-CH$_2$-CO-NH-CH$_2$-pyridinone), 2.17 (t, 2H, CONH-CH$_2$-**CH$_2$**-CO-NH), 2.46 (s, 9H, C^6-**CH$_3$**), 3.17 (t, 2H, CONH-**CH$_2$**-CH$_2$-CO-NH), 3.40 (t, 2H, mal-**CH$_2$**-CH$_2$-CH$_2$-CONH), 3.75 (s, 9H, N^1-**CH$_3$**), 4.51 (d, 6H, CO-NH-**CH$_2$**-pyridinone), 6.83 (s, 3 H, **C^5-H** in pyridinone), 7.22 (m, 10 H, S-**Ph**), 7.78 (broad, 1 H, mal-CH$_2$-CH$_2$-CO-**NH**), 8.46 (t, 3 H, CO-**NH**-CH$_2$-pyridinone).

5.2.4   Anti-CEA conjugation to THP^Me-mal-DTP

Prior to conjugation, the anti-CEA antibody (0.5 mL of 0.855 mg/mL PBS solution) was loaded onto a PD10 column previously equilibrated with borate buffer (pH 8.2, 50 mM sodium tetraborate, 50 mM NaCl, 5 mM EDTA) and eluted to give 215 µL of a 1.940 mg/mL anti-CEA solution (98 % yield) as measured by spectrophotometric measurement on a Nanodrop 2000 spectrophotometer (Thermo scientific). Purity of the sample was verified by size-exclusion HPLC (mobile phase: PBS)

1.03 µl of a 10 mM solution of *tris*(2-carboxyethyl)phosphine (TCEP, 10.3 nmol, 8 eq. or 2eq./disulfide bridge) was added to 100 µL of the antibody solution (1.3 nmol), the mixture was vortexed and incubated for 2 hour at 37°C , after which THP^Me-mal-DTP (15.5 nmol, 12 equivalents) was added and the mixture vortexed and incubated at 37°C for one hour. All conjugation steps were monitored by SDS-PAGE (Sodium dodecyl sulfate polyacrylamide gel electrophoresis, see below). The conjugation solution was then left at room temperature for 24 hours to promote maleimide hydrolysis to the more stable open form, favoured by the slightly basic pH of the borate buffer. The

immunoconjugate was then purified by ultracentrifugation with 50000 molecular weight cut off (MWCO) filters (vivaspin 500, MWCO 50000, GE healthcare) using ammonium acetate 0.2 M as a buffer. 200 µL of an THP^{Me}-mal-Anti-CEA solution in 0.2 M ammonium acetate were obtained and concentration was determined by NanoDrop measurements to be 89 ± 0.13 mg/mL for a 92 % recovery yield. Purity of the immunoconjugate was verified by size-exclusion HPLC (mobile phase: PBS).

5.2.5 SDS-PAGE

Gel preparation

Stacking and resolving acrylamide gels were prepared by mixing acrylamide with water, *tris*(hydroxymethyl)aminomethane (TRIS) buffer at pH 8.8 and sodium dodecyl sulfate (SDS) in the quantities reported in **Table 5.2**. Tetramethylethylenediamine (TEMED) and ammonium persulfate (APS) were then added to initiate the polymerisation.

Table 5.2. *Ingredients for the preparation of resolving and stacking acrylamide gel.*

	Resolving gel (12 % acrylamide)	Stacking gel (4 % acrylamide)
ACRYLAMIDE	6.4 mL	2 mL
2.5 M TRIS (PH 8.8)	4 mL	2.5 mL
DEIONISED H$_2$O	5.3 mL	5.3 mL
SDS (10 % W/V)	160 µL	100 µL
TEMED	16 µL	10 µL
APS (90 %)	160 µL	100 µL

Two glass plates were assembled onto a setting rig, the resolving gel was prepared as described above, added between the plates and covered by 1 mL of ethanol. The resolving gel was left setting while the stacking gel was prepared according to **Table 5.2**, then the ethanol was removed and the stacking gel added. A comb was positioned at the top of the rig to create the wells for sample loading.

Loading buffer (5x stock) was prepared by mixing glycerol (8 mL), water (4 mL), SDS (1.6 mL, 10 % w/v in water), 0.5 M tris-HCl buffer (1 mL, pH 6.8) and bromophenol pH 6.8 (0.2 mL). 1 L of running buffer pH 8.3 (10x stock) was also prepared by dissolving TRIS (*tris*(hydroxymethyl)aminomethane, 30 g), glycine (14 g) and SDS (10 g) in water. Both buffers were diluted to 1x with water prior to use.

Sample preparation and analysis

The following samples were analysed in duplicate:

- Native antibody
- Antibody + TCEP (after a 2-hours incubation)
- Antibody + TCEP + THP^{Me}-mal-DTP (after 1-hour incubation)

Samples for SDS-PAGE were prepared by mixing 4 μL of protein (10 μg), 2 μL of loading buffer and 4 μL of milliQ water, then denatured by shaking for 5 min at 75 °C. 5 μL of sample were loaded into each well, and one lane was dedicated to a broad-range MW marker (10-250 kDa, BioLabs). A 35 mA current was applied to the plates for 45 min. The gel was then washed with water and stained with Coomassie blue (0.05 % Coomassie brilliant blue R250 in 40 % methanol, 10 % glacial acetic acid and 50 % water), by covering it with the dye and heating for 1 min with a microwave heater. Finally, the gel was washed with water three times, then covered in a de-staining solution (10 % acetic acid, 10 % methanol in water) and left shaking for 1 hour at 37 °C until the gel was clear.

5.2.6 HuA33 conjugation to THP^{Me}-Ph-NCS

A solution of huA33 in PBS (7 μM, 0.8 mL, pH 7.4) was adjusted to pH 8.8-9.0 with a 0.1 M solution of Na$_2$CO$_3$, and 5, 10, 30 or 50 equivalents of THP^{Me}-Ph-NCS (10 mM in DMSO) were added in small aliquots to prevent precipitation. The reaction mixture was shaken for one hour at room temperature, then purified by size-exclusion chromatography on a PD-10 column (Sephadex G-25M PD-10 column, GE Healthcare) in ammonium acetate 0.2 M (for preliminary radiolabelling) or PBS (for preclinical experiments) and concentrated using centrifugal filtration units with a 50000 molecular weight cut off (Amicon^{TM} ultra 2mL, Millipore Corp). The final concentration of the immunoconjugate was measured spectrophotometrically using a Shimadzu Biospec nano (considering ε_{280} = 2.1 10^5 L/mol cm) and used to determine the conjugation yield (**Table 5.3**).

5.2.7 MALDI-ToF mass spectrometry

THP^{Me}-Ph-NCS-huA33 Immunoconjugates were analysed by MALDI-ToF MS/MS using a Bruker ultraflex MALDI-ToF/ToF (Bruker Daltonic GmbH) according to the following procedure. 1 μL of each sample (1 mg/mL) was mixed with 1 μL of sinapic acid (10 mg/ml in 50 % acetonitrile: water and 0.1 % TFA). 1 μL of the sample/matrix solution was spotted onto a stainless-steel target plate and allowed to dry. Ions were analysed in positive mode and external calibration was performed by use of a standard protein mixture (BSA). The measure was repeated three times for both the native antibody and each conjugation batch. The difference between the average mass of the

immunoconjugate, as determined by a profile measurement of the sample and that of the native antibody was divided by the exact mass of the chelator to determine the average number of chelators per antibody.

5.2.8 ^{68}Ga radiolabelling of immunoconjugates

THP^{Me}-mal-Anti-CEA radiolabelling:

80 µL of a THP^{Me}-mal-Anti-CEA solution (0.15 mg/mL, ≈ 1µM in 0.2 M ammonium acetate) was mixed with 80 µL of ^{68}Ga eluate (≈ 8 MBq) at room temperature and pH ≈ 5.5. Radiolabelling was verified *via* size-exclusion radioHPLC using (mobile phase: PBS + 2 mM EDTA).

THP^{Me}-Ph-NCS-HuA33 radiolabelling

Radiolabelling of the immunoconjugate at a final concentration of 1 µM was performed in two different sets of conditions.

- pH 5.5 (verification of conjugation):
  400 µL of the highest activity fraction (≈ 88 MBq) were mixed with 100 µL of ammonium acetate 4 M, and 42 µL of the neutralised solution (≈ 4 MBq) added to an immunconjugate solution (3 µL, 15 µM in ammonium acetate 0.2 M).
- pH 7 (evaluation of the radiolabelling in the conditions required for *in vivo* experiment):
  410 µL of the highest activity fraction were adjusted to pH 7 using ammonium acetate (0.2 M, 400 µL) and sodium carbonate (0.1 M, 400 µL). 40 µL of this solution (≈5 MBq) were added to 40 µL of immunoconjugate (2 µM in ammonium acetate 0.2 M or PBS). In a variation of the experiment the effect of a 45 min delay between gallium eluate neutralisation and radiolabelling was also investigated.
  A similar radiolabelling procedure was also applied to the native antibody (≈ 1 MBq, final antibody concentration = 7.5 µM) to verify that presence of chelator was necessary for successful radiolabelling.

The radiolabelling mixture was incubated for 5 min at 37 °C. Success of the radiolabelling was verified by iTLC using 50 mM EDTA in water as a mobile phase. The radiolabelling mixture was also applied to a PD10 column preconditioned with ammonium acetate 0.2 M (or PBS, depending on the radiolabelling mixure) to trap residual THP^{Me}-Ph-NCS. The eluted fractions were analysed by iTLC and the residual activity trapped on the PD10 was also measured.

5.2.9 DFO-huA33 radiolabelling with^{89}Zr

^{89}Zr-oxalate (50 μL, 57 MBq), was diluted with 1 M oxalic acid to 100 μL, buffered to pH 7.5 using Na_2CO_3 1M (106 μL) and added to 400 μL of DFO-huA33 solution in PBS (1.53 mg/mL, ≈ 10 μM). The radiolabelling mixture was agitated for one hour at 37 °C. EDTA (50 mM solution in water) was added to a final concentration of 1 mM. ITLC analysis of the crude radiolabelling mixture (50 mM EDTA in water as a mobile phase) confirmed quantitative radiolabelling. The radiolabelling mixture was then applied to a PD10 column preconditioned with PBS, the resulting fractions analysed by iTLC and the activity trapped on the column measured. The highest activity fractions were used to prepare doses for injections.

5.2.10 Cell culture

Human colorectal cancer cell line SW1222 expressing the A33 antigen was obtained from Sigma-Aldrich and maintained in Minimum Essential Medium (Gibco^{TM}, ThermoFisher). LS174T colon adenocarcinoma cell line expressing the CEA antigen was donated by Prof. Barbara Pedley's group (UCL) and cultured in DMEM low glucose. The A375 melanoma cell line used as a negative control was provided by Sophia Karagiannis's group (KCL) and cultured in DMEM high glucose (4500 mg/L glucose, Gibco^{TM}, ThermoFisher). Cell culture media were supplemented with 10 % foetal calf serum, L-glutamine (2 mM), penicillin (100 units/mL), and streptomycin (0.1 mg/mL). Cell cultures were maintained at 37 °C in a humidified atmosphere of 5 % CO_2. A trypsin EDTA solution was used to passage the cells according to the formulation below:

- 0.25 % trypsin/0.53 mM EDTA in Hank's Buffered Salt Solution without calcium and magnesium for experiments performed at MSKCC.
- 0.05 % trypsin, 0.02 % EDTA in PBS for experiments performed at KCL.

LS174T cells were also passed through a 40 μm strainer (Falcon) before transferring them into a new flask/plate to avoid the formation of clumps.

5.2.11 Uptake assay with pre-labelled ^{68}Ga-THP^{Me}-mal-Anti-CEA

A preliminary uptake assay was performed to evaluate the specificity of the immunoconjugate for the CEA receptor and to optimise the conditions for pretargeting experiments. LS174T and A375 cells were plated 48 hours prior to the experiment in a 24-well plate (50000 cells/well). Prior to the experiment, cell culture medium was replaced with fresh medium or HBSS (200 μL).

Cells were treated with ^{68}Ga-THP^{Me}-mal-Anti-CEA at two different THP^{Me}-mal-Anti-CEA concentrations (1 µg/mL and 0.1 µg/mL), by addition of 6 µL of 33.5 µg/mL and 3.35 µg/mL radiolabelled solutions, respectively. Two extra groups were added for the experiment in complete medium, namely the 10 µg/mL and ^{68}Ga group. In the 10 µg/mL group, cells were treated with the radiolabelling mixture (1 µg/mL) in presence of a 10-fold excess (10 µg/mL) of unlabelled immunoconjugate. In the ^{68}Ga group, cells were treated with acetate buffered ^{68}Ga, obtained by mixing equal volumes of ^{68}Ga eluate and 0.2 M ammonium acetate, as a negative control. One well per cell line was not treated and utilised to count the cells at the end of the experiment.

Cells were incubated at 37 °C for 1 hour, after which the supernatant was removed and the cells washed twice with HBSS (200 µL), lysed with 0.1 M NaOH (200 µL) and γ-counted. Supernatant solution and washings were also collected and γ-counted. The percentage of the added activity that was taken up by the cells (% uptake) was determined for each sample, dividing the counts in the lysate by the sum of counts in the supernatant, washings and lysate and multiplying by 100.

5.2.12 *In vitro* Pretargeting experiment

LS174T and A375 cells were plated 48 hours prior to the experiment (50000 cells/well) in a 24-well plate. Six different groups were considered as described below, concentration refers to final immunoconjugate concentration in the well.

- Direct radiolabelling (Pre-radiolabelled immunoconjugate,1 µg/mL, N = 3)
- Pretargeting (1 µg/mL, N = 6)
- Pretargeting 3x (3 µg/mL, N = 3)
- Pretargeting w/o wash (1 µg/mL, N = 3)
- Pretargeting with excess natural gallium (1 µg/mL, 9 µg/mL Ga(NO$_3$)$_3$, N = 3)
- ^{68}Ga only (N = 3)

Prior to the experiment, cell culture medium was refreshed (200 µL), then 6 µL of a 33.5 µg/mL solution of THP^{Me}-mal-Anti-CEA was added to each well designated for 1 µg/mL pretargeting (6 µL of a 100 µg/mL THP^{Me}-mal-Anti-CEA solution was added to the wells designated for 3 µg/mL pretargeting). Cells were incubated at 37 °C for 1 hour, the medium was then changed for all the wells except the "pretargeting w/o wash" group.

^{68}Ga-THP^{Me}-mal-Anti-CEA (immunoconjugate concentration = 33.5 µg/mL, pH= 5.5) for the direct radiolabelling group was prepared as described in the previous paragraph and analysed by HPLC. Activity for pretargeting experiments and the ^{68}Ga-only control

was prepared by mixing ^{68}Ga eluate with an equal volume of ammonium acetate 0.2 M (pH = 5.5). 6 μL of ^{68}Ga-THP^{Me}-mal-Anti-CEA was added to the direct radiolabelling wells, 6 μL of acetate buffered ^{68}Ga solution was added to the remaining wells (≈150 kBq/well). For the excess natural gallium group, 5 μL of a 0.35 mg/mL solution of gallium nitrate in water were also added to the sample (final Ga^{3+} concentration 9 μg/mL, 9:1 ratio of gallium to immunoconjugate). Cells were incubated at 37 ˚C for one hour after which the supernatant was removed and the cells washed twice with HBSS (200 μL), lysed with 0.1 M NaOH (200 μL) and γ-counted. Supernatant solution and washings were also collected and γ-counted and % uptake determined as described above.

5.2.13 Immunoreactive fraction

A saturation-binding immunoreactivity assay was performed for ^{68}Ga-THP^{Me}-Ph-NCS-huA33 (5 and 10 equivalents batches) following a modified literature procedure [36]. 10 μL of a radioimmunoconjugate solution in (0.4 ng/μL in PBS supplemented with 1 % bovine serum albumin, ≈ 70 kBq) were added to a suspension of 2.0×10^7 SW1222 colorectal cancer cells in 100 μL of medium. The resulting mixture was agitated by pipetting and incubated for one hour on ice. Cells were then centrifuged (600 RCF for 5 min) and the supernatant carefully removed. The cells were then washed three times by resuspension of the pellet in 1 mL of ice-cold PBS followed by centrifugation and removal of the supernatant. Radioactivity in the cell pellet, supernatant and washings was measured by γ-counting. After background correction of the data, the immunoreactive fraction was calculated by dividing the counts in the cell pellet by the sum of the counts in the cell pellet, media, and three washings and multiplying by 100. The experiment was performed in triplicate.

5.2.14 Xenograft model

The SW122 xenografts were established by Kimberly Edwards (Research Technician at MSKCC). All *in vivo* experiments in this chapters were performed in collaboration with Dr Pierre Adumeau (Dr Zeglis laboratory, Hunter College).

Athymic nude female mice (Athymic Nude-nu, 8-10 weeks old) were obtained from Charles River Laboratories (Wilmington, MA). Animals were housed in ventilated cages, given food and water *ad libitum,* and were allowed to acclimatise for approximately 1 week prior to tumour cells inoculation. SW1222 tumours were induced on the left shoulder by a subcutaneous injection of 5×10^6 cells in suspension in 150 μL of a 1:1 mixture of fresh media and BD Matrigel (BD Biosciences). The xenografts were

monitored daily until an ideal size for imaging and biodistribution was reached ($\approx$100-150 mm^3) in 2-3 weeks.

5.2.15 PET imaging experiments

Mice were randomly assigned to the different experimental groups (for each group N = 5). For all the experiments in this chapter administration of antibody/radiotracers was performed *via* tail vein injection on conscious mice after gentle warming with a heat lamp. Approximately five min prior to imaging, mice were anaesthetised by inhalation of 2 % isoflurane/oxygen gas mixture and positioned on the bed of a MicroPET Focus scanner (Concorde MicroSystem Inc.). 1 % isoflurane anaesthesia was maintained throughout the scan. Static scans of 10 min each were recorded at different time points after injections. An energy window of 350-700 keV and a coincidence timing window of 6 ns were used. Data were sorted into 2-dimensional histograms by Fourier re-binning, and transverse images were reconstructed by filtered back-projection (FBP) into a 128 × 128 × 63 (0.72 × 0.72 ×1.3 mm) matrix. The imaging data were normalised to correct for non-uniformity of PET response, dead-time count losses, positron branching ratio, and physical decay to the time of injection. No attenuation, scatter, or partial-volume averaging correction was applied. Activity concentrations (% ID/g) were calculated from the counting rates in the reconstructed images by use of a system calibration factor derived from the imaging of a mouse-sized water-equivalent phantom containing ^{68}Ga or ^{89}Zr. Images were analysed using ASIPro VMTM software (Concorde Microsystems). Mice were sacrificed by CO_2 asphyxiation. Details of the different experiments performed are described below.

Imaging with ^{89}Zr-DFO-huA33 (positive control)

Mice were injected with ^{89}Zr-DFO-huA33 in saline (200 µL, $\approx$ 7 MBq, 88 µg) and imaged at 25 hours after injection. At 26 hours post injection, mice were sacrificed.

Pretargeting experiments

Mice were injected with 100 µg of THP^{Me}-Ph-NCS-huA33 in saline using either the 10 eq. or the 30 eq. batch (5 mice per group). After 24 hours, mice were injected with 8-10 MBq of ^{68}Ga-acetate (pH 7). PET imaging of the 5 mice was performed from 50 min to 90 min after injection (10 min per mouse) and then repeated one hour after. Mice were sacrificed 3 hours after ^{68}Ga-acetate injection and their *ex vivo* biodistribution performed.

^{68}Ga-only control

Mice were injected with 8-10 MBq of ^{68}Ga-acetate (pH 7) and imaging performed as described for the pretargeting experiments, from 1 to 2 hours following administration of the radioactivity. Mice were culled at 3 h post injection and *ex vivo* biodistribution performed.

^{68}Ga followed by THP^{Me} blood clearance

Mice were injected with 10-11 MBq of ^{68}Ga-acetate (pH 7). Imaging of two of the mice at 40 and 50 min after injection was performed. A solution of THP^{Me} in saline (3 mg/mL) was prepared and pH adjusted to 7 with Na_2CO_3. A 400 µg/mL solution was prepared by dilution of the stock solution in saline. At 1 hour after gallium injection, 20 µg of THP^{Me} (24 nmol, in 50 µL of saline) were also administered intravenously and all mice imaged from 20 to 60 min after THP^{Me} injection. Mice were sacrificed 3 hours after the ^{68}Ga injection and the *ex vivo* biodistribution of the activity assessed.

5.2.16 *Ex vivo* Biodistribution

For all ^{68}Ga experiments, tissues were harvested and weighed and *ex vivo* biodistribution assessed by γ-counting. The whole organ was collected in the case of tumour, heart, lungs, liver, spleen, stomach (unemptied) and kidneys. The femur was used as representative of bone, skin and fur was collected from the ears, muscle from the hindlimb and blood by a cardiac puncture. Only part of the small and large intestine (unemptied) were collected. All organs were washed in water to eliminate residual blood. Calibration of the γ-counter with known amounts of activity allowed determination of the decay-corrected CPM/MBq conversion coefficient, which was used to calculate % injected dose (% ID) in each organ. In the reported data, the residual activity in the tail (as a result of an imperfect IV injection) was subtracted from the total activity injected. Tail-corrected % ID were calculated and % ID/g obtained by dividing the tail-corrected % ID of each organ by its weight.

5.2.17 Statistical analysis of the data

Data obtained for *in vitro* and *in vivo* studies were analysed using GraphPad Prism, version 7.04 for Windows (GraphPad software). For all the statistical analysis comparing two groups, Student's t-test was used. ANOVA was used to analyse results where more than two groups were compared. In this case, Brown-Forsythe test was used to verify the hypothesis of equal variances between groups and Tukey post-hoc test was employed to correct for multiple comparisons.

5.3 Results

In this work, the pretargeting *via* metal chelation hypothesis has been investigated in two different antigen/antibody models, targeting the carcinoembryonic antigen (CEA) and the transmembrane glycoprotein A33, respectively. Two different bifunctional derivatives of THP^{Me} were used to allow site-specific modification (THP^{Me}-mal-DTP, for the anti-CEA antibody) and non-specific conjugation (THP^{Me}-Ph-NCS, for huA33 antibody) to the antibody. An *in vitro* approach was used for the anti-CEA study, while the huA33 pretargeting experiments were performed *in vivo*. Owing to all these differences between the approaches, the results of the two pretargeting attempts will be described separately in the following sections.

5.3.1 First attempt: THP^{Me}-mal-Anti-CEA conjugate

In this first set of experiments, an anti-CEA-THP^{Me} immunoconjugate was produced by site-specific conjugation. A full-length anti-CEA antibody possessing 4 disulfide bonds was kindly provided by the laboratory of Prof. Kerry Chester (UCL) The newly synthesised bifunctional THP^{Me} derivative THP^{Me}-mal-DTP (**Figure 5.4**), developed as a collaboration between Blower/Ma (KCL) and James Baker laboratories (UCL) was chosen as a suitable chelator. The dibromo-/dithiophenol-maleimide platform allows binding of the chelator to two free cysteine residues upon disulfide bonds reduction, generating new cysteine bridges that can help to maintain the integrity and quaternary structure of the antibody [37-39].

Figure 5.4. *Structure of the dithiophenolmaleimide THP^{Me} derivative (THP^{Me}-mal-DTP) used in this work.*

Immunoconjugate production and purification

The anti-CEA antibody was transferred to borate buffer containing 5 mM EDTA to chelate any free metal present. HPLC analysis of the antibody (**Figure 5.5**) shows a single peak in the chromatogram with a retention time of 7 min 6 s.

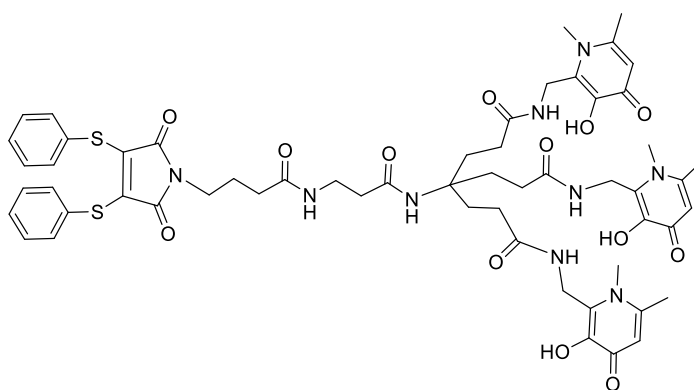

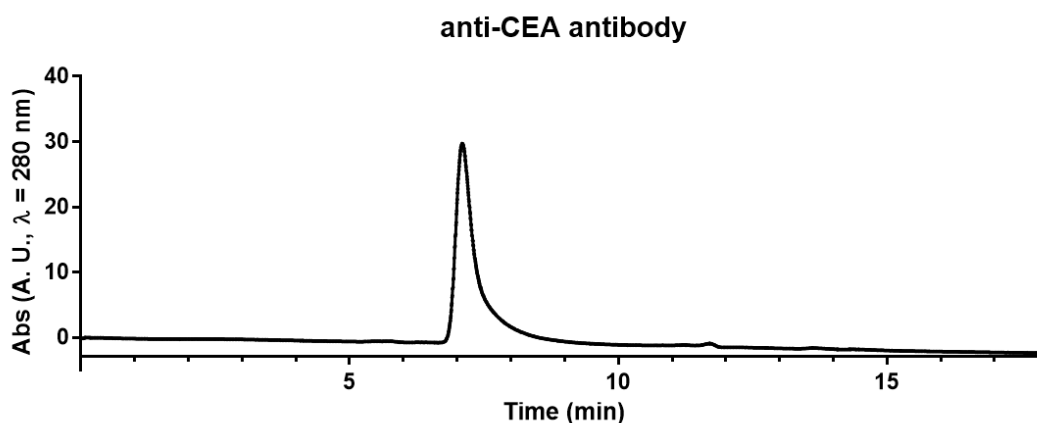
anti-CEA antibody

Figure 5.5. *Size-exclusion HPLC chromatogram of anti-CEA antibody. Only one peak is visible at 7 min 6 s, assigned to the antibody molecule.*

Conjugation to THP^{Me}-mal-DTP was carried out upon reduction of disulfide bonds using *tris*(2-carboxyethyl)phosphine)(TCEP). The reaction was performed in duplicate and sampling at every step (intact antibody, antibody after TCEP treatment, antibody after conjugation) allowed monitoring of the reaction using SDS-PAGE as represented in **Figure 5.6**.
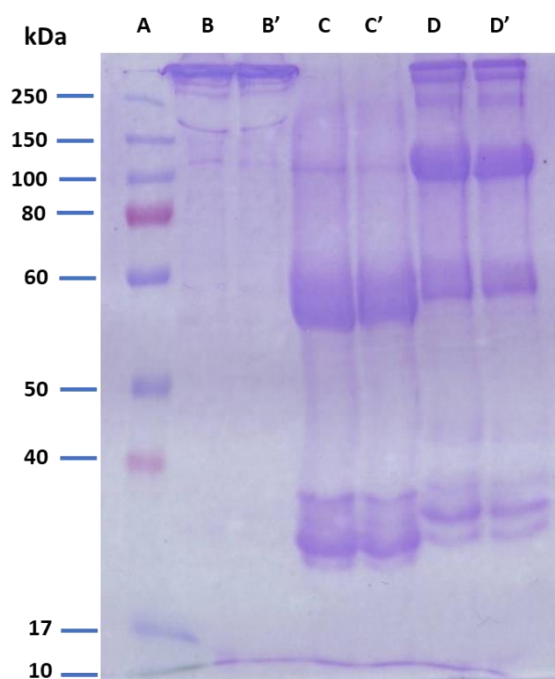

Figure 5.6. *SDS-page monitoring of the reaction between the anti-CEA antibody and the dithiophenolmaleimide-THP^{Me}. Description of the lanes is as follows: A) molecular marker (250-10 kDa), B) intact antibody, C) antibody after exposure to TCEP (two hours), D) antibody after 1-hour reaction with 12 equivalents of THP^{Me}-mal-DTP.*

As expected, even after denaturation of the sample (5 min at 75 °C, prior to gel loading), the intact antibody (lane B and B') showed only one band representing the full-length antibody with all the chains covalently connected by disulfide bonds.

222

Conversely, after a 2-hour treatment with the reducing agent TCEP (line C and C') the first band disappeared, replaced by two bands at lower molecular weight, representing the heavy and light side chains of the antibody, respectively. Finally, after 1 h incubation with 12 equivalents of the THP^Me-mal-DTP at 37 °C (lane D, D'), a full-length antibody band is visible again, indicating successful attachment of THP^Me-mal-DTP and correct rebridging of the side chains. The new band at an intermediate molecular weight suggests incorrect/partial rebridging of the side chains to obtain only half of the antibody (one heavy chain + one light chain). Finally, lower molecular weight bands are also visible indicating an incomplete conjugation/partial rebridging.

The newly produced conjugate was left in the conjugation buffer overnight, at room temperature, to favour maleimide hydrolysis, to an open, unreactive form (**Figure 5.7**), which increases the stability of the conjugate towards reaction with free thiols [38].
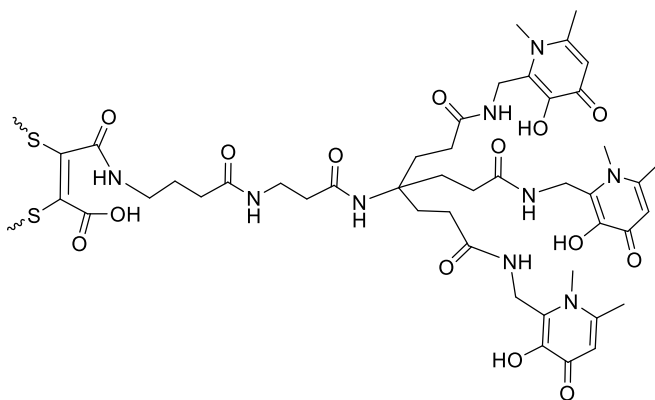

Figure 5.7. *Schematic representation of the mal-THP^Me chelator after hydrolysis of the maleimide moiety to the more stable open form. Wavy bonds are connecting the chelator to the antibody.*

Purification from excess chelator/EDTA and transfer into ammonium acetate buffer (more suitable for radiolabelling) was then performed by ultracentrifugation. Size-exclusion HPLC was carried out on the immunoconjugate (**Figure 5.8**), showing only one peak at 7 min 5 s, at λ = 254 nm, confirming the purity of the immunoconjugate and the absence of free chelator or EDTA (see **Figure 5.10** for EDTA retention time).
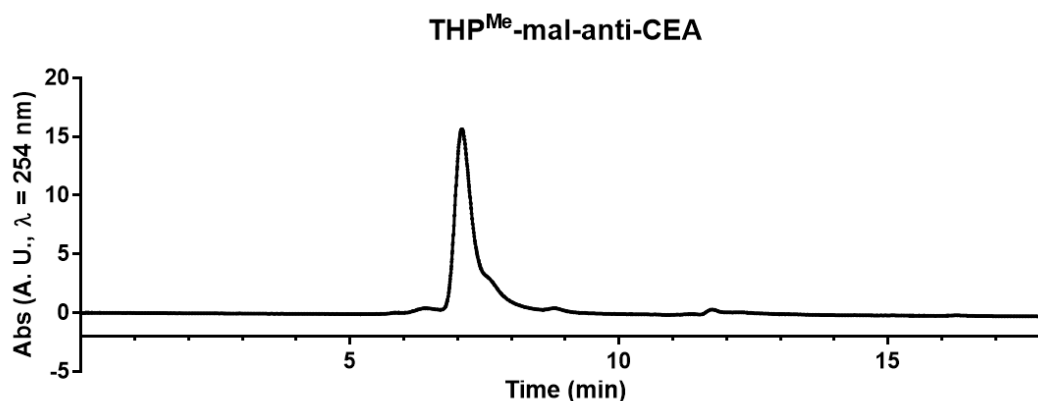
Figure 5.8. *HPLC analysis of THP^Me-mal- Anti-CEA immunoconjugate (λ = 254 nm) showing a single peak at 7 min 5 s, ascribed to anti-CEA-THP^Me-mal.*

Radiolabelling of the new immunoconjugate (0.5 µM in 0.1 M ammonium acetate) was performed at room temperature and pH 5.5 and verified using size-exclusion chromatography. EDTA was added to the PBS mobile phase (to a final concentration of 2 mM), to complex any unbound gallium for quantification of radiochemical yield (**Figure 5.9**).
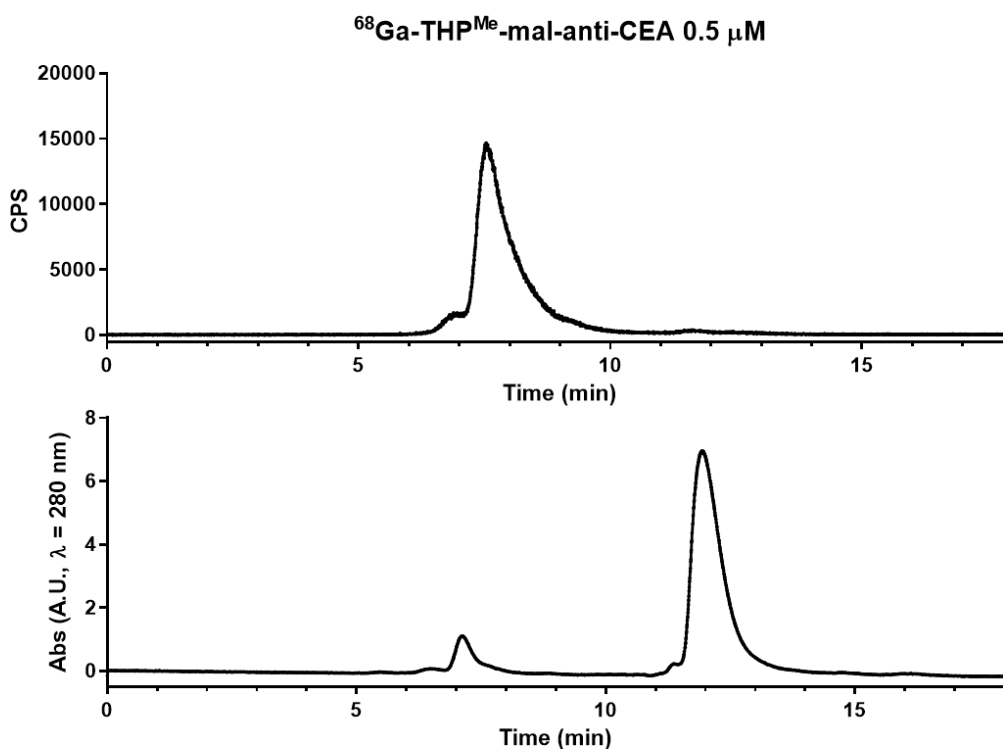

Figure 5.9. *HPLC analysis of the THP^Me-mal-Anti-CEA radiolabelling mixture (0.5 µM). Top panel displays the radiochromatogram showing one main peak at 7 min 28 s assigned to the radiolabelled immunoconjugate. Bottom panel shows the UV chromatogram (λ = 280 nm) with a small peak at 7 min 6 s (immunoconjugate) and the main peak at 11 min 54 s min (EDTA).*

The radiochromatogram showed a quantitative radiolabelling of the immunoconjugate in these conditions, with one main peak in the chromatogram (retention time: 7 min 28 s) attributed to ^{68}Ga-THP^{Me}-mal-anti-CEA. The small side peak visible at lower retention time can be assigned to radioimmunoconjugate aggregates. In the UV chromatogram for the same radiolabelling reaction, only a small peak for the immunoconjugate is visible at 7 min 6 s, due to low concentration, while the main peak at 11 min 54 s is imputable to EDTA. On the contrary, when unchelated ^{68}Ga was analysed in the same conditions (**Figure 5.10**) all the activity eluted at 11 min 58 s as [^{68}Ga(EDTA)]. In the UV chromatogram only the EDTA peak was present.
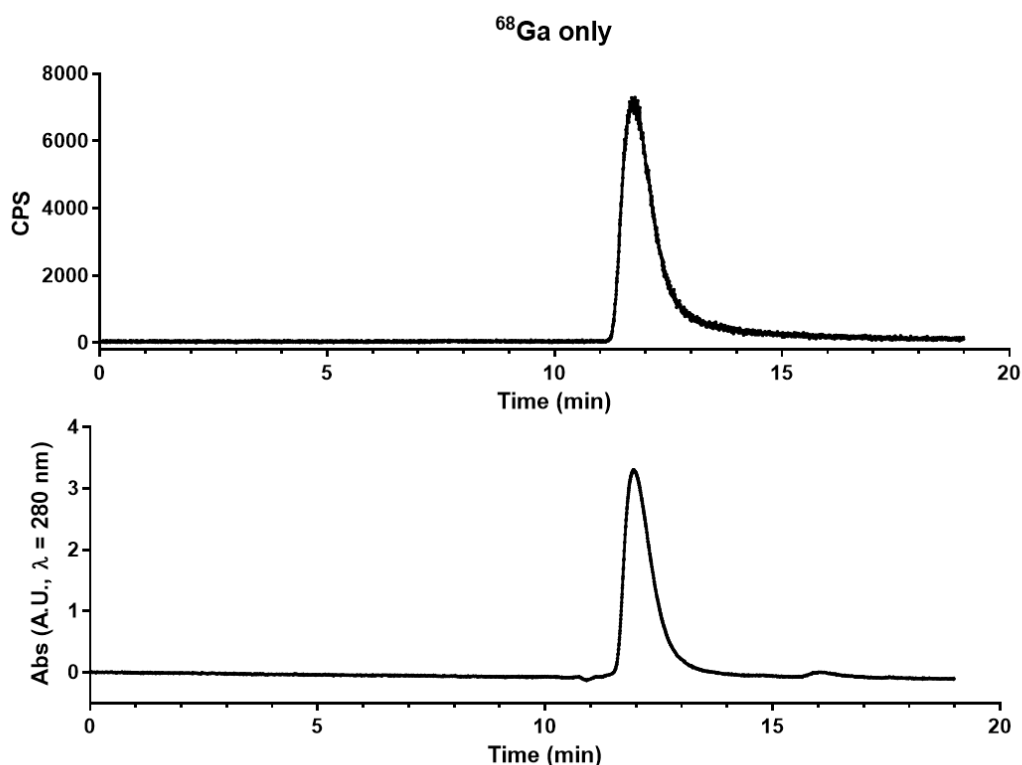

Figure 5.10. *HPLC analysis of the unchelated ^{68}Ga. Top panel shows the radiochromatogram with one peak at 11 min 48 s assigned to [^{68}Ga(EDTA)]. Bottom panel presents the UV chromatogram (λ = 280 nm), showing one peak at 11 min 54 s (EDTA).*

Uptake assays with pre-radiolabelled ^{68}Ga-THP^{Me}-mal-Anti-CEA

The human colon adenocarcinoma cell line LS174T, known to express the CEA antigen [40] and extensively used in pretargeting studies employing anti-CEA immunoconjugates [41], was utilised for *in vitro* experiments. The human melanoma A375 cancer cell line, which does not express the target antigen, was used as a negative control [42]. In preliminary uptake assays, the specific uptake of directly radiolabelled THP^{Me}-mal-anti-CEA was evaluated to find suitable conditions for

pretargeting studies (antibody concentration, assay buffer), and to verify that the immunoconjugate retained affinity for its target receptor. Radiolabelling of the immunoconjugate was carried out at 0.22 µM (33.5 µg/mL) concentration in 0.1 M ammonium acetate, achieving quantitative radiochemical yield as demonstrated by HPLC analysis (**Figure 5.11**).
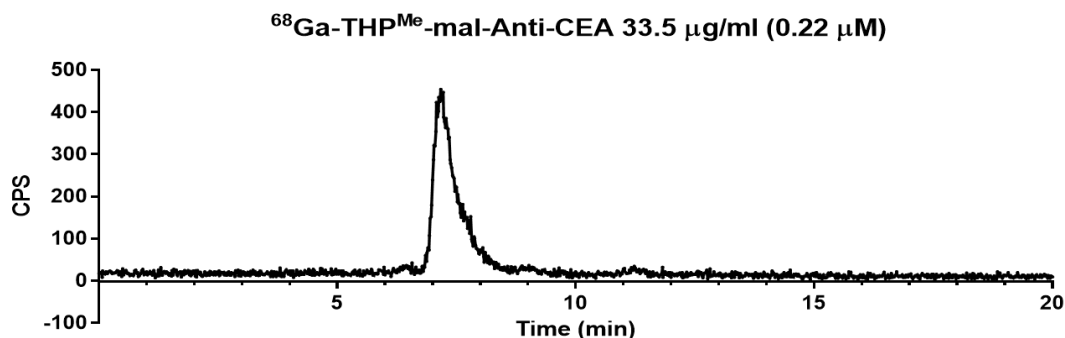

Figure 5.11. *HPLC radiochromatogram for the* ^{68}*Ga-labelled THP^{Me}-mal-Anti-CEA (0.22 µM) used for uptake assays with the direct radiolabelled antibody.*

LS174T and A375 cells in HBSS were treated with the radiolabelled mixture (at 0.1 and 1 µg/mL immunoconjugate concentration) and the percentage of the added activity that was taken up by the cells (% uptake) determined for each well. The same experiment was repeated in complete medium. In this case, cells were also treated with unchelated ^{68}Ga as a negative control (^{68}Ga group), and with the 1 µg/mL radiolabelled mixture in presence of an excess of unlabelled immunoconjugate (10 µg/mL group), to test whether this immunoconjugate concentration was sufficient to saturate the target receptor. Results are reported in **Figure 5.12**, statistically significant differences between the groups are highlighted.
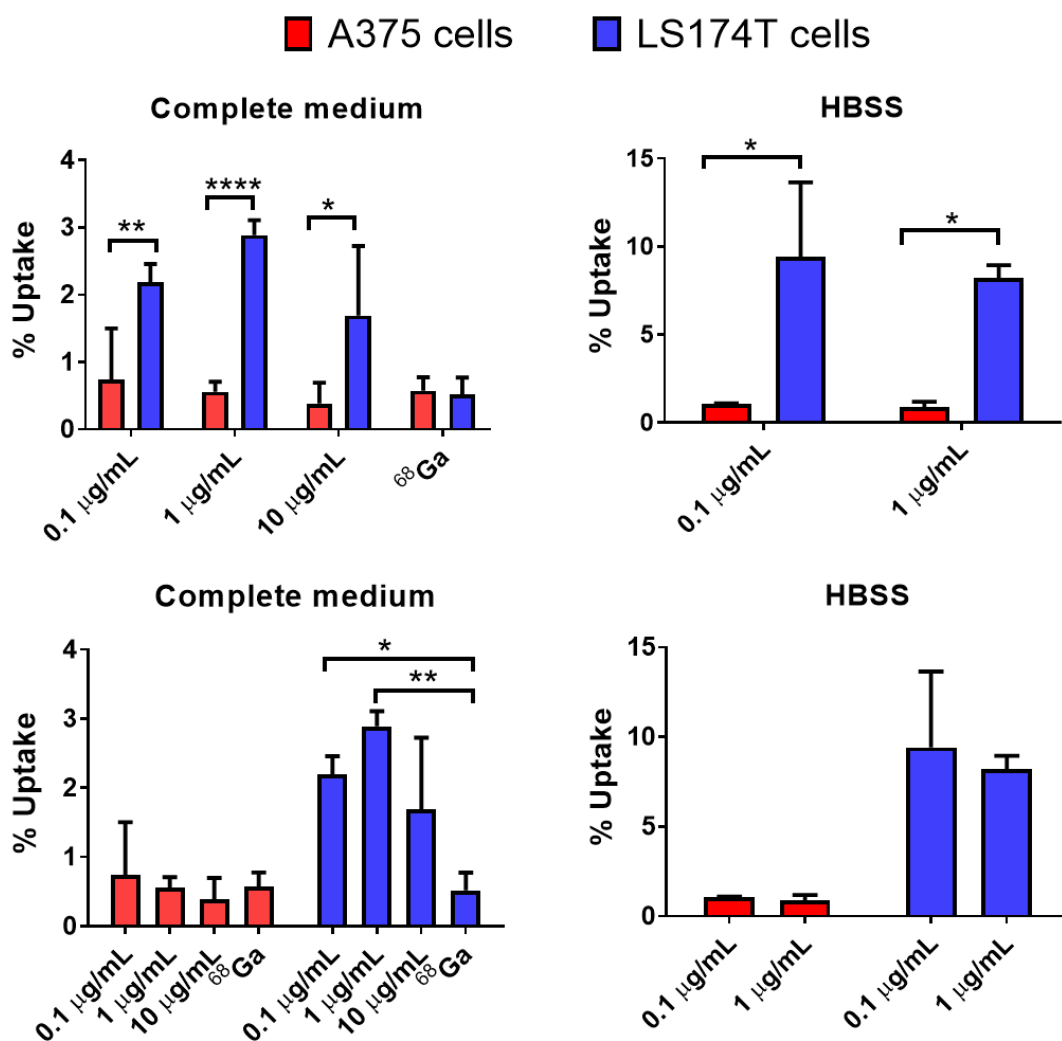
Figure 5.12. *Uptake of ^{68}Ga-THP^{Me}-mal-Anti-CEA in LS174T and A375 cell line in full medium (left panel) or HBSS (right panel). Values are expressed as mean ± SD (N = 3). In the top panel the two cell lines are compared (t-test for each immunoconjugate concentration), in the bottom panel the same results are displayed comparing different immunoconjugate concentration for the same cell line (one-way ANOVA followed by Tukey's post hoc test). P values are defined as follows: * = P ≤ 0.05, **= P ≤ 0.01, *** = P ≤ 0.001 and **** = P ≤ 0.0001.*

Uptake of the ^{68}Ga-THP^{Me}-mal-Anti-CEA radioimmunoconjugate (at 0.1 and 1 μg/mL) was seen for LS174T cells both when using HBSS as a buffer and in complete medium. Non-specific uptake of ^{68}Ga-THP^{Me}-mal-Anti-CEA in A375 cells was low demonstrating specific targeting of the CEA antigen. Addition of excess unlabelled THP^{Me}-mal-Anti-CEA, to reach a final immunoconjugate concentration of 10 μg/mL, resulted in a reduction of the uptake in LS174T cells, due to partial blocking of the receptor by the unlabelled conjugate. However, persistence of some uptake in these conditions suggest that an immunoconjugate concentration of 10 μg/mL is not sufficient to completely saturate the receptor. Uptake of unchelated ^{68}Ga in LS174T cells was significantly

lower than ^{68}Ga-THP^{Me}-mal-Anti-CEA uptake and, notably, did not differ from ^{68}Ga uptake in A375 cells.

The 1 µg/mL concentration in complete medium was selected for pretargeting experiments. Complete medium was preferred to HBSS, despite the lower cellular uptake percentage, since it was deemed more representative of the *in vivo* conditions. The 1 µg/mL concentration group was selected since it displayed larger difference between CEA positive and negative cell line compared to the 0.1 µg/mL group.

Pretargeting experiment

In this experiment, the % uptake for cells treated with the directly radiolabelled antibody (1 µg/mL) was compared with the uptake obtained in cells pretargeted with the unlabelled immunoconjugate (1 µg/mL antibody concentration), followed by replacement of medium and treatment with acetate buffered gallium-68. In order to obtain a robust set of data, the following groups were also considered:

- Pretargeting w/o wash: where the medium was not refreshed between incubation with immunoconjugate and treatment with ^{68}Ga.
- Pretargeting 3x: in which the concentration of antibody in the well was increased to 3 µg/mL.
- Pretargeting natural gallium: where excess natural gallium was mixed with ^{68}Ga prior to addition to have a nominal 9:1 µg ratio between gallium and immunoconjugate.
- ^{68}Ga only: where no immunoconjugate was used.

The experiment was planned so that all the samples experienced the same conditions with the only variable being the treatment. At first, all pretargeted cells were treated with the relevant concentration of antibody, while the direct radiolabelling and ^{68}Ga only sample were treated with the same volume/concentration of buffer. After 60 min incubation medium was changed for all samples except the pretargeting w/o group. All the cells were then incubated with activity (radiolabelled antibody for the direct radiolabelling group, acetate buffered ^{68}Ga for the other groups) for further 60 min, then washed, lysed and the activity present in the lysate versus supernatant/washings quantified by γ-counting. The results (cell-bound activity expressed as percentage of the total activity) are reported in **Figure 5.13**.
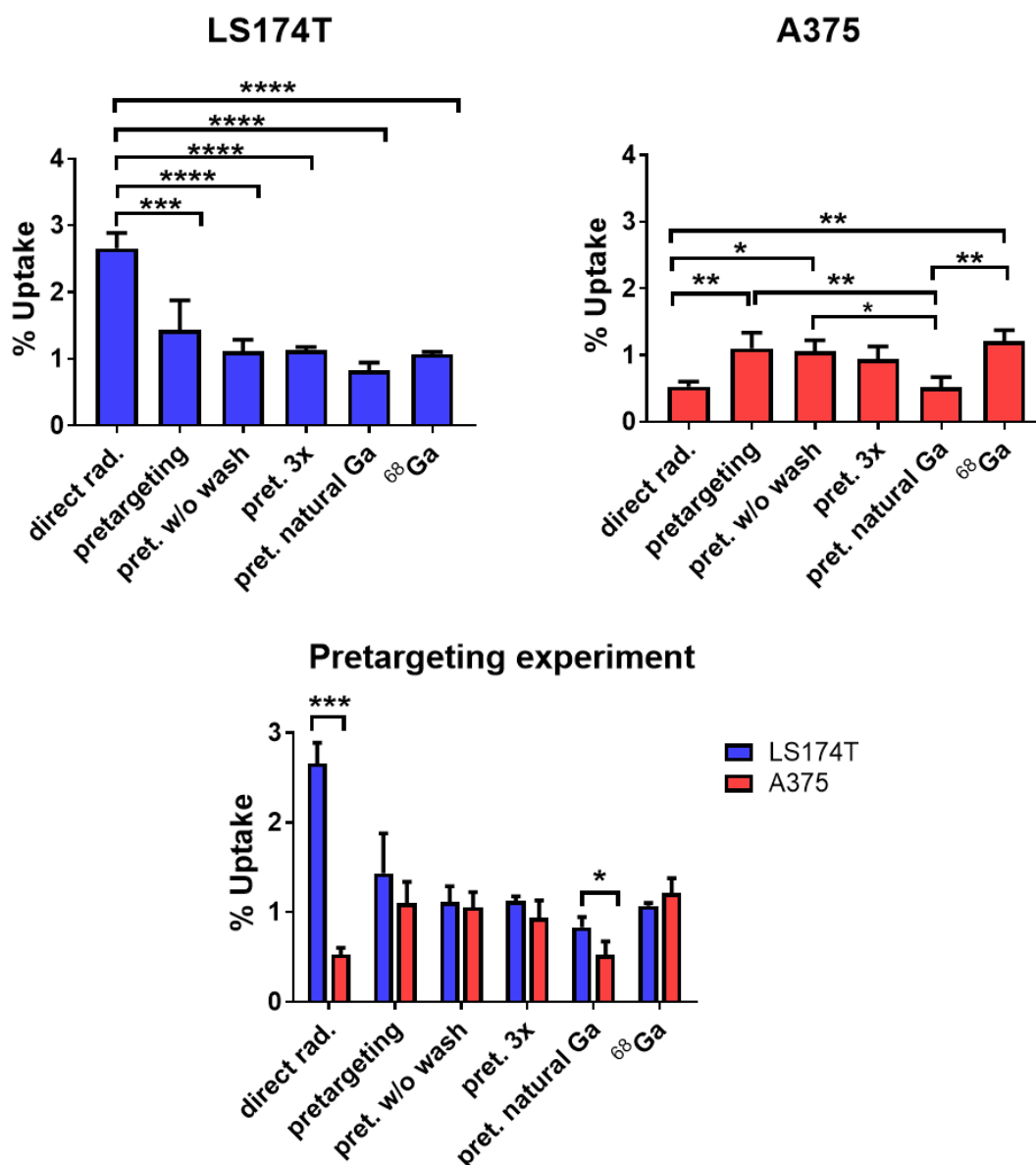
Figure 5.13. ^{68}Ga uptake comparing direct radiolabelling, unchelated ^{68}Ga and different pretargeting groups. Uptake for LS174T (left) and A375 cells (right) are reported in the top panel while the bottom panel displays all the data together. Values are expressed as mean ± SD (n = 3, n = 6 for pretargeting groups). Different groups within each cell line, were compared using one-way ANOVA followed by Tukey's multiple comparison test. For each of the groups the two cell lines were also compared using a t-test. P values are defined as follows: * = P ≤ 0.05, ** = P ≤ 0.01, *** = P ≤ 0.001 and **** = P ≤ 0.0001.

These results were analysed both by comparing different groups within a single cell line (using one-way ANOVA) and by comparing the two cell lines for each of the groups (using a t-test). A significant pretargeting effect could not be seen in either case. LS174T and A375 cells differed significantly when comparing the two direct radiolabelling groups, where LS174T cells showed, as expected, higher uptake of the radiolabelled antibody (2.7 ± 0.1 % for LS174T cells vs 0.5 ± 0.04 % for A375 cells). Higher ^{68}Ga uptake for LS174T cells was also visible in the pretargeting with natural gallium

group, where the blocking effect of natural gallium was more evident for A375 cells. When comparing the various groups for LS174T cells, the only significant difference was found between the direct radiolabelling group and the rest. To a lesser extent this was also seen in A375 cells, with direct radiolabelling in this case hampering ^{68}Ga uptake compared to the ^{68}Ga-only control. Interestingly, for A375 cells a significant suppression of the uptake was also seen for the pretargeting in the presence of natural gallium group. Notably, no other significant difference was found between any of the pretargeting groups and the ^{68}Ga-only control for either cell line, suggesting that no radiolabelling took place in the medium (see **Discussion**). This is likely due to the low concentration of chelator available for binding in each well. In fact, since antibody concentration in the medium was 7 nM (21 nM for the pretargeting 3x group), concentration of the available chelator was certainly lower than 28 nM (84 nM for the pretargeting 3x), which is the maximum value corresponding to 1 chelator per disulfide bond (4 chelators per antibody) with all the immunoconjugate molecules being cell-bound and available for binding. ^{68}Ga radiolabelling in this concentration range is extremely challenging even for an outstanding Ga^{3+} chelator such as THP^{Me}.

5.3.2 Second attempt: THP^{Me}-Ph-NCS conjugate

In the second set of experiments, non-specific conjugation was employed with the aim of achieving higher chelator concentration at the target site by increasing the number of chelators/antibody with non-specific conjugation. The isothiocyanate derivative THP^{Me}-Ph-NCS (**Figure 5.14**) was synthesised following literature procedures [35] and conjugated to the huA33 antibody available in the MSKCC and Hunter College laboratories (New York), where this work was performed during a research visit.
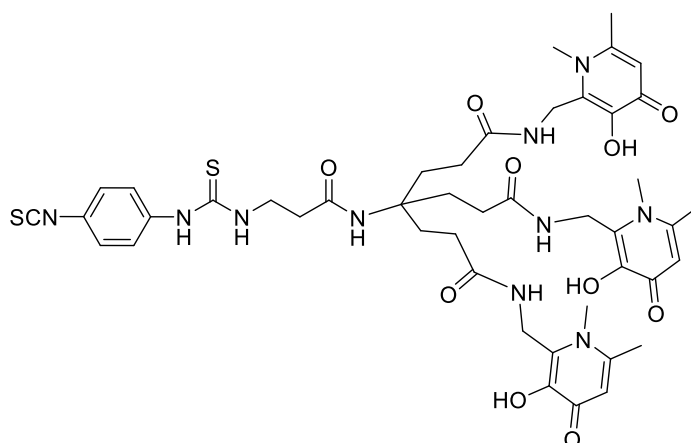

Figure 5.14. Structure of the THP^{Me}-Ph-NCS chelator used in this work [35].

Immunoconjugate production and purification

Conjugation of the THP[Me]-Ph-NCS to the huA33 was performed according to a modified literature procedure [8,30], by slowly adding a DMSO solution of the chelator to a solution of the antibody in PBS at pH 8.8-9.0. Two initial batches of immunoconjugate were produced using 5 and 10 equivalents of chelator per antibody. Different ratios (20, 30, 40 and 50 equivalents) were further explored in the following weeks. Immunoconjugate purification was performed by size-exclusion chromatography, followed by ultracentrifugation. Yields for each batch, as calculated by spectrophotometric measurements, as well as other characterisation data for the immunoconjugates, are reported in **Table 5.3**. Although attention was paid to avoid precipitation during the addition of the chelator to the reaction mixture, precipitation was observed for the 50 equivalents batch during overnight storage in the fridge. Samples from the 5, 10 and 30 equivalents batches underwent MALDI measurements to determine the average number of chelators per antibody.

Radiolabelling

To verify the success of the conjugation, radiolabelling of the THP[Me]-Ph-NCS-huA33 conjugate was initially performed at the usual slightly acidic pH obtained by neutralisation with ammonium acetate buffer. Quantitative radiolabelling was obtained for both 5 equivalent and 10 equivalents batches at antibody concentration as low as 1 μM, confirming successful conjugation. **Figure 5.15** shows an iTLC obtained for the radiolabelled immunoconjugate compared with that obtained for a mixture of ^{68}Ga and a native antibody.

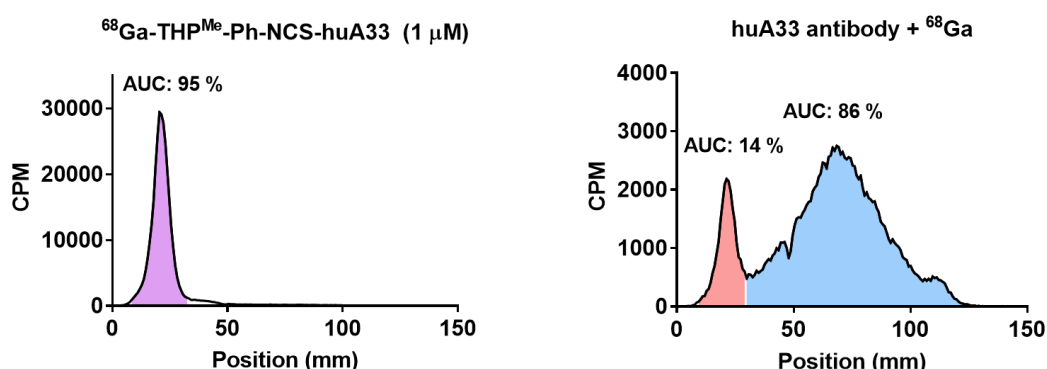***Figure 5.15.*** *iTLC profiles of the crude radiolabelling mixture for the THP[Me]-Ph-NCS-huA33conjugate (left) and the native huA33 antibody (right). For every peak, the area under the curve (AUC) has been calculated and reported as a percentage.*

In this mobile phase, the radiolabelled antibody stays at the baseline of the iTLC while any unchelated metal smears throughout the iTLC strip [43]. It is clear from **Figure**

5.15 that conjugation to THP^{Me}-Ph-NCS is necessary for successful radiolabelling: while quantitative radiolabelling is observed for the immunoconjugate, the native antibody has only 14 % of the radioactivity associated. Purification of both mixtures on a size-exclusion column allowed removal of excess chelator and unbound ^{68}Ga. For the native antibody only 3 % of the activity eluted from the column in the void volume suggesting that most of the ^{68}Ga was either non-chelated or only loosely bound to the antibody. On the contrary, 97.5 % of the activity was eluted in the column void volume for the THP^{Me}-Ph-NCS-huA33 immunoconjugate, confirming quantitative radiolabelling.

Radiolabelling of the immunoconjugate was also investigated in conditions that more closely resemble those of preclinical experiments. Neutral pH is desirable for intravenous (IV) injection in conscious mice, therefore the effect of eluate neutralisation to pH 7-7.2 on radiolabelling was evaluated. Notably, also in these conditions the immunoconjugate was able to bind gallium quantitatively at 1 μM for all tested batches (**Table 5.3**). In addition, to take into account the time interval between eluate neutralisation and injection of the mice, the effect of a 45 min delay between eluate neutralisation and radiolabelling of the 10 equivalent batch was investigated (**Figure 5.16**). Remarkably, also in this case radiolabelling was quantitative and recovery from size-exclusion column purification was > 95 %.

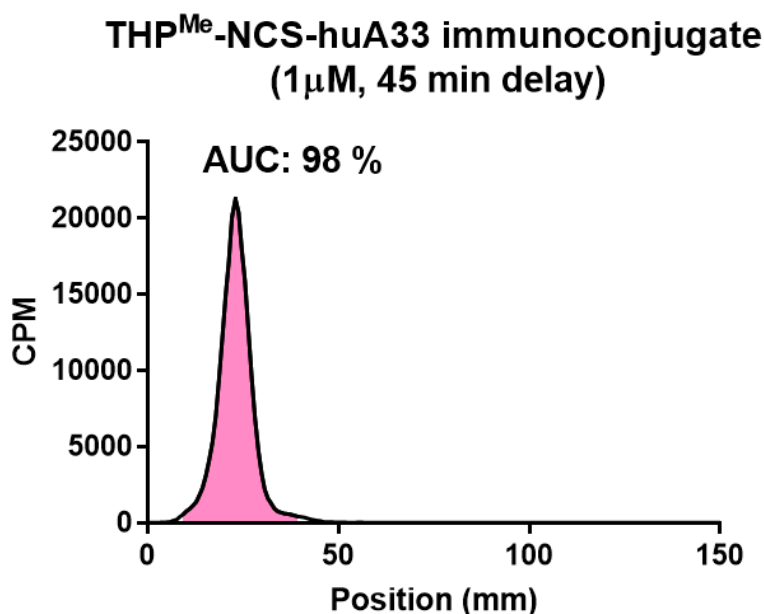**Figure 5.16**. *iTLC profile and AUC for THP^{Me}-Ph-NCS-huA33 radiolabelling (1 μM) at pH 7, with 45 min delay between neutralisation of the ^{68}Ga eluate and radiolabelling of the immunoconjugate.*

Radiolabelling of the DFO-huA33 immunoconjugate with ^{89}Zr was carried out for use as a positive control for *in vivo* experiments. ^{89}Zr radiolabelling was achieved in nearly

quantitative yield (97 % of the activity eluted from the PD10 column in the void volume) and purity was confirmed by iTLC analysis of the eluted fractions (**Figure 5.17**).
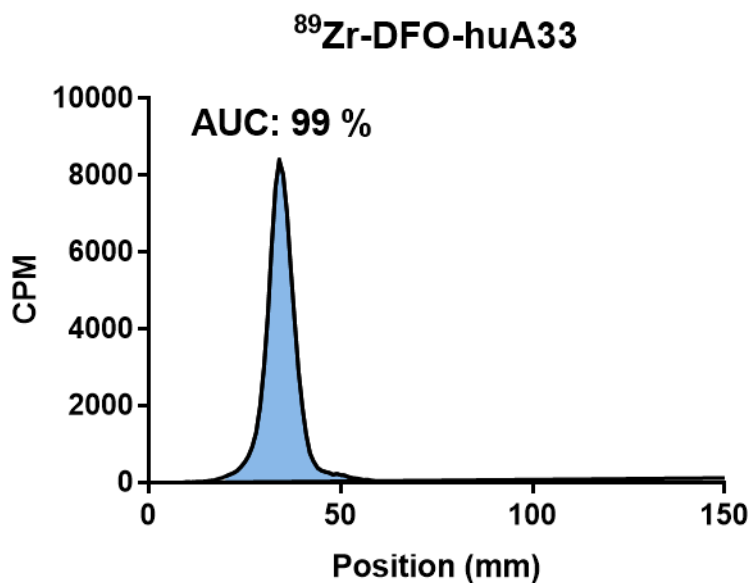

Figure 5.17. *iTLC profile and AUC for huA33-DFO (6.7 µM) radiolabelling with ^{89}Zr at pH 7.5 (fraction 2).*

Immunoreactive fraction measurements

To verify that conjugation to the chelator did not impair the antibody ability to bind its target receptor, the immunoreactive fraction was determined for both the 5 and 10 equivalent batches *via* a saturation-binding immunoreactivity assay [36]. The results are presented in **Table 5.3**. In this experiment, a large excess of antigen was employed, able to bind the totality of the added radioimmunoconjugate (100 % uptake). Accordingly, the observed uptake percentage reflects the immunoreactive fraction of the radioimmunoconjugate batch. For both the considered batches, only marginal detriment of the immunoreactivity was measured, with immunoreactivity fractions equal or superior to 90 %. Based on these results, the 10 equivalents batch was selected to perform preclinical experiments. Due to time constraints no immunoreactive fraction measurements were performed for the 30 equivalents batch.

Quantification of chelators/antibody ratio

Quantification of the number of chelators per antibody was performed by MALDI. Examples of m/z spectra of the 5, 10 and 30 equivalent batches as well as of the native antibody are reported below (**Figure 5.18**).
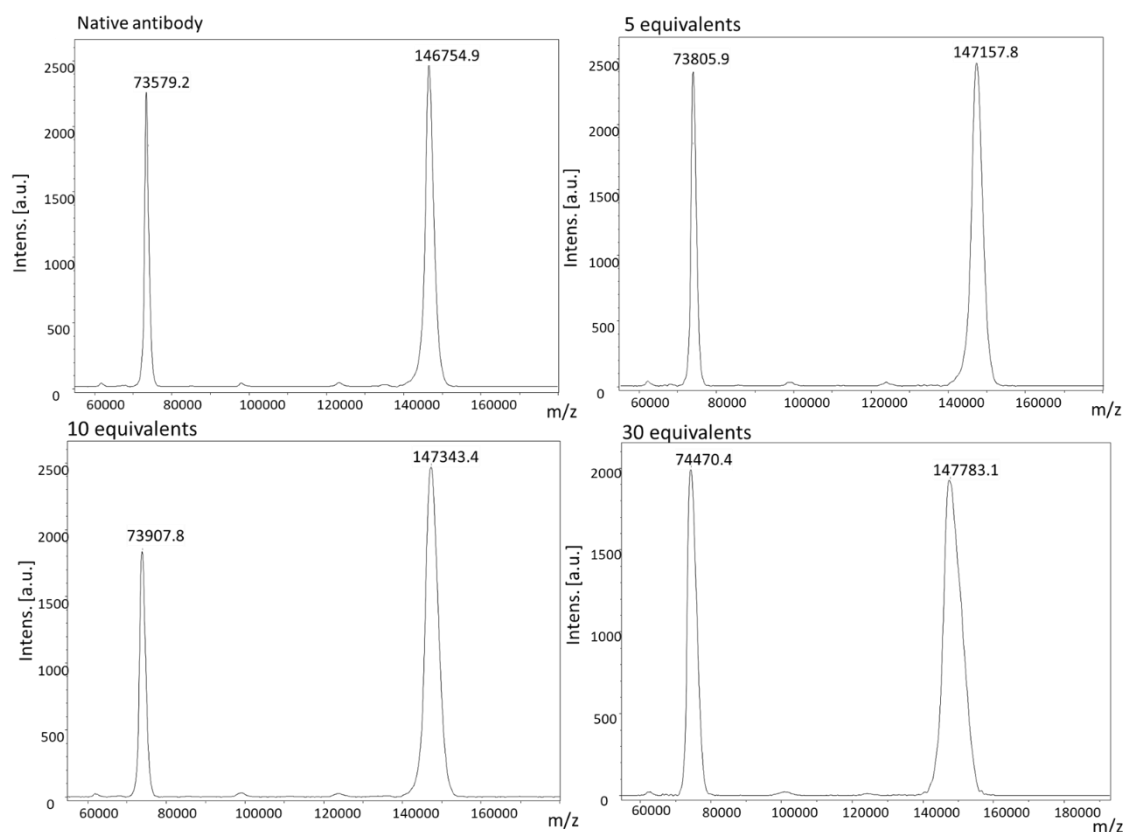
Figure 5.18. *Examples of MALDI mass spectra for the native antibody and different batches of immunoconjugate. The data are presented as profile m/z spectra, showing both [M]$^+$ and [M]$^{2+}$ species. The reported m/z values represent the average mass of the immunoconjugate in the sample.*

The average number of chelators/antibody (**Table 5.3**) was calculated from the average [M]$^+$ species measured according to the equation below, using as M$_{chelator}$ = 960.36 g/mol.

$$\frac{N^o Chelators}{antibody} = \frac{\frac{\sum_i^n [M_{immunoconjugate}]_i}{n} - \frac{\sum_i^n [M_{antibody}]_i}{n}}{M_{chelator}}$$

Table 5.3. *Summary of characterisation data for the different THP^{Me}-Ph-NCS-huA33 conjugates. Batches used for in vivo experiment are highlighted in pink. Immunoreactive fractions data are reported as average ± SD. *radiolabelling of the 50 equivalents batch was not performed since precipitation occurred during overnight storage in the fridge.*

Immunoconjugate batch	Conjugation Yield	Radiolabelling at 1 µM	Immunoreactive fraction	Number of chelators/antibody
5 eq	85.7 %	quantitative	92.7 ± 0.7	0.4
10 eq	85.9 %	quantitative	89.2 ± 3.1	0.6
20 eq	88.9 %	quantitative	N/A	N/A
30 eq	85.3 %	quantitative	N/A	1
40 eq	87.3 %	quantitative	N/A	N/A
50 eq	92.4 %	*	N/A	N/A

In vivo imaging and biodistribution

Preclinical experiments were performed in nude mice bearing human SW1222 colon cancer xenografts. Different groups, of 5 mice each, were considered, as discussed below. Initially, as a positive control, 5 mice were injected with ^{89}Zr-labelled huA33-DFO immunoconjugate. Imaging was performed at 25 hours following radioimmunoconjugate administration. Examples of the PET images are shown in **Figure 5.19**.
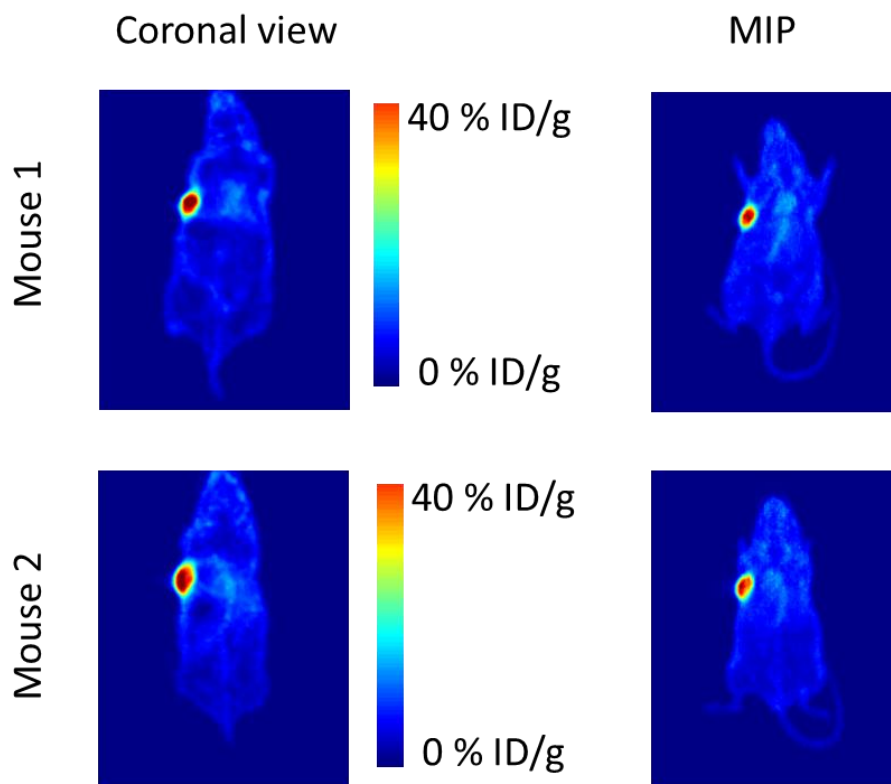

Figure 5.19. *Representative PET images illustrating the biodistribution of ^{89}Zr-DFO-huA33 in nude mice bearing SW1222 xenografts at 25 h post injection. Coronal views are shown on the left, maximum intensity projections (MIP) on the right.*

As it is evident from the images, the huA33 antibody was able to selectively target the tumour tissue, while accumulation in other organs was minimal. As a result, high contrast PET images were obtained.

The second group of mice to be imaged was the pretargeting group. Mice were pretreated with 100 μg of the THP^{Me}-Ph-NCS-huA33 conjugate (10 equivalents batch) followed, after 24 hours, by acetate buffered ^{68}Ga (pH ≈ 7). Injections of the activity were performed all at the same time (10 min range) to ensure uniformity in the Ga^{3+} speciation at the time of injection. Therefore, imaging of the mice had to be staggered with respect to the injection times with the first mouse scanned at 50 min after the injection of ^{68}Ga and the last scanned at 90 min after injection. The scanning was then

repeated in the same order to investigate the effect of a longer delay between ^{68}Ga injection and PET imaging on image quality and contrast. Two examples of PET scans at 50 min and 1 h 10 min (followed by 1 h 50 min and 2 h 10 min scans) are reported in **Figure 5.20**. *Ex vivo* biodistribution was performed at 3 h after gallium injection and is reported in **Figure 5.22**. Both the PET scans and the biodistribution data showed some accumulation of ^{68}Ga in the tumour. However, most of the activity was still in the blood even at 3 h after the ^{68}Ga injection and uptake in non-target organs, such as liver and bones, was also visible.
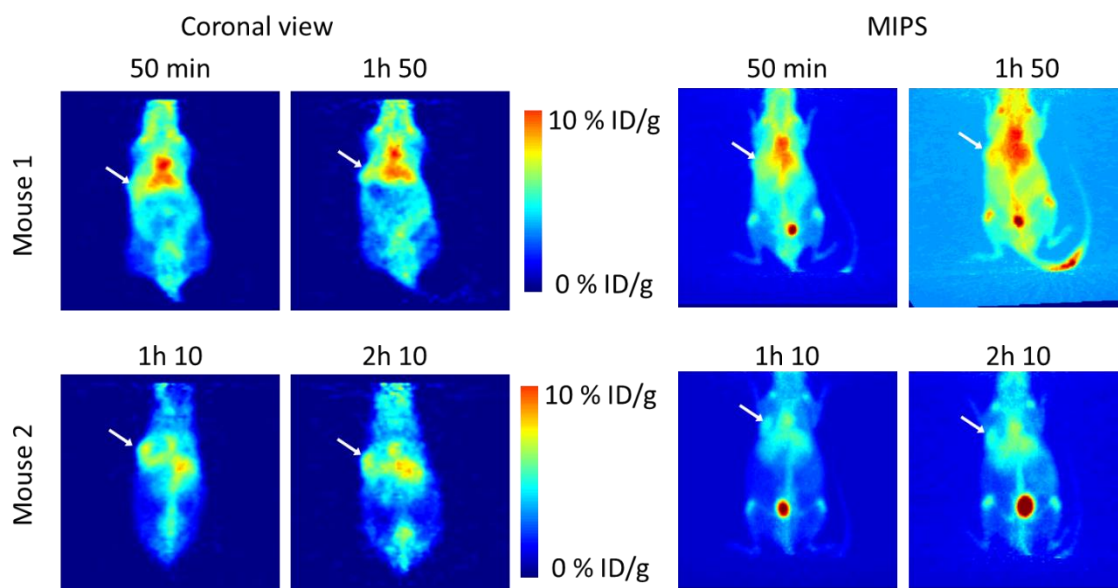
Figure 5.20. *PET images showing the biodistribution of ^{68}Ga in nude mice bearing SW1222 xenografts, pretreated with THP^{Me}-Ph-NCS-huA33 (10 equivalents batch) 24 hours before ^{68}Ga injection. For each mouse two scans of 10 min each were performed at ≈ 1 and 2 hours post ^{68}Ga injection. Images are reported as coronal view (left panel) and MIPS (right panel). White arrows indicate location of the tumour.*

To investigate whether the uptake visible in tumours was attributable to pretargeting or to simple accumulation of gallium in cancer a third group of mice was injected with acetate buffered ^{68}Ga, without prior injection of antibody-chelator conjugate. Imaging and *ex vivo* biodistribution were performed as in the previous group and the results are shown in **Figures 5.21** and **5.22**, respectively.
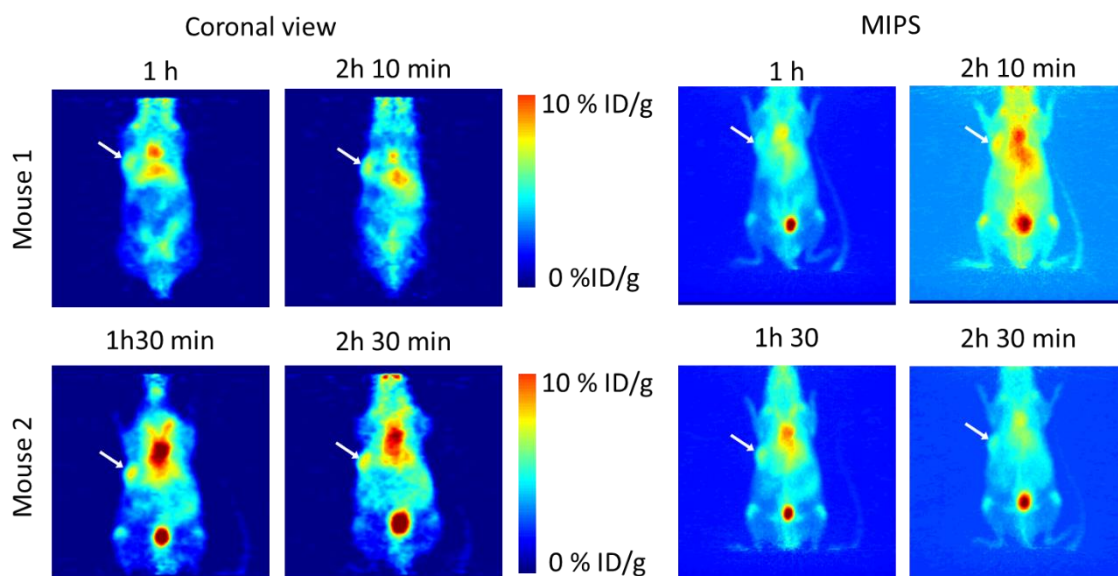
Figure 5.21. *PET images illustrating the biodistribution of ^{68}Ga in nude mice bearing SW1222 xenograft at ≈ 1 and 2 h after ^{68}Ga injection. For each mouse coronal view (left panel) and MIPS (right panel) are reported. White arrows indicate location of the tumour.*

Figure 5.22 *Ex vivo ^{68}Ga biodistribution in nude mice bearing SW1222 xenografts at 3 hours after ^{68}Ga injections, comparing mice pretreated with THP^{Me}-Ph-NCS-huA33 (10 equivalents batch) 24 hours before ^{68}Ga injection (red), with mice that were not pretreated with any immunoconjugate (control group, blue). For each group N = 5, data are presented as mean ± SD. For each organ, comparison between the two groups was performed by t-test.*

As was already evident from a visual comparison of the PET images, no difference was found between the pretargeting and the ^{68}Ga-only control group. A comparison between the two biodistributions (**Figure 5.22**, t-test performed for each organ) also revealed no significant difference in tumour ^{68}Ga uptake for the two groups (10.8 ± 1.5 % ID/g in the pretargeting group vs 12.9 ± 2.5 % ID/g in the ^{68}Ga group). The only significant difference among the considered organs was found for blood, whose

uptake was higher for the ^{68}Ga-only group (19.1 ± 1.4 % ID/g) compared to the pretargeting group (14.4 ± 2.6 % ID/g).

MALDI analysis of the immunoconjugate used (only available after the experiment) revealed an average of only 0.6 chelators/antibody, suggesting that a low concentration of the chelator at the tumour site could be the cause of the negative results of this first pretargeting experiment. In a second attempt at pretargeting we aimed at increasing the number of chelators per antibody and, accordingly, the concentration of chelator available for *in vivo* radiolabelling. MALDI analysis of the 30 equivalents chelators/antibody batch revealed an average of 1 chelator per antibody, which represented only a modest increase from the 10 equivalents batch. However, since this was the highest ratio achievable without precipitation in the conjugation mixture we decided to use this new batch to carry out a second preclinical pretargeting experiment. Images of the PET scans and a graph showing the *ex vivo* biodistribution for the three groups considered are reported in **Figure 5.23** and **5.24**.
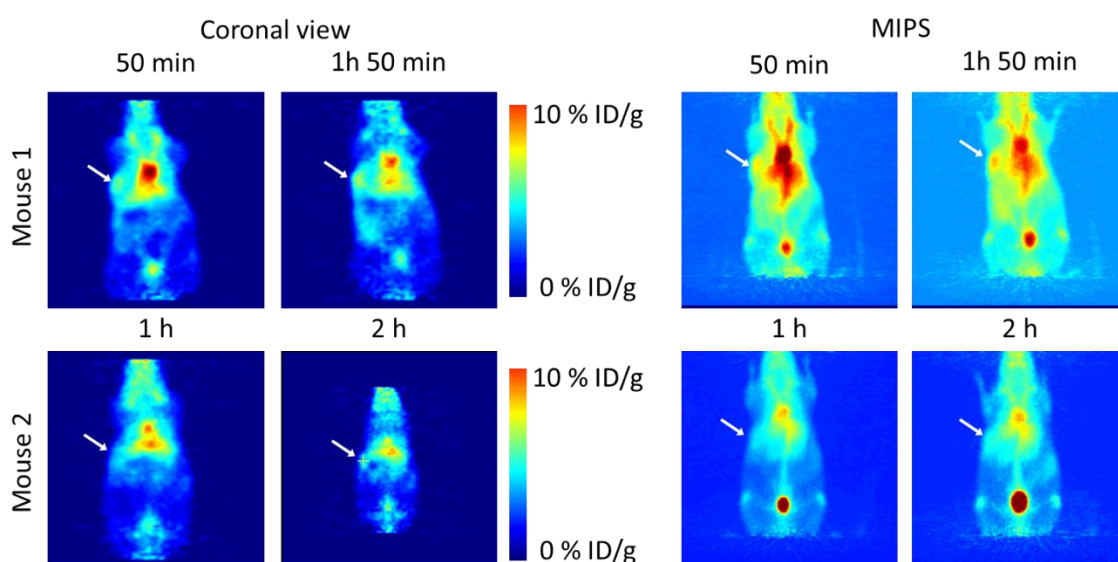
Figure 5.23. *PET images displaying the biodistribution of ^{68}Ga in nude mice bearing SW1222 xenografts, pretreated with THP^{Me}-Ph-NCS-huA33 (30 equivalents batch) 24 hours before ^{68}Ga administration. Scans performed at ≈ 1 and 2 hours after ^{68}Ga injections are reported as coronal view (left panel) and MIPS (right panel). White arrows indicate location of the tumour.*

Once again, no significant difference was found in the tumour uptake of the 30 equivalent pretargeting group and the gallium only control as visible from the PET images and from biodistribution data. ANOVA analysis of the data revealed lower uptake in the bones for the pretargeting 30 eq. group (6.0 ± 1.1 % ID/g) compared to both the gallium only group (11.4 ± 2.4 % ID/g) and the pretargeting experiment 10 eq. group (10.1 ± 2.4 % ID/g).
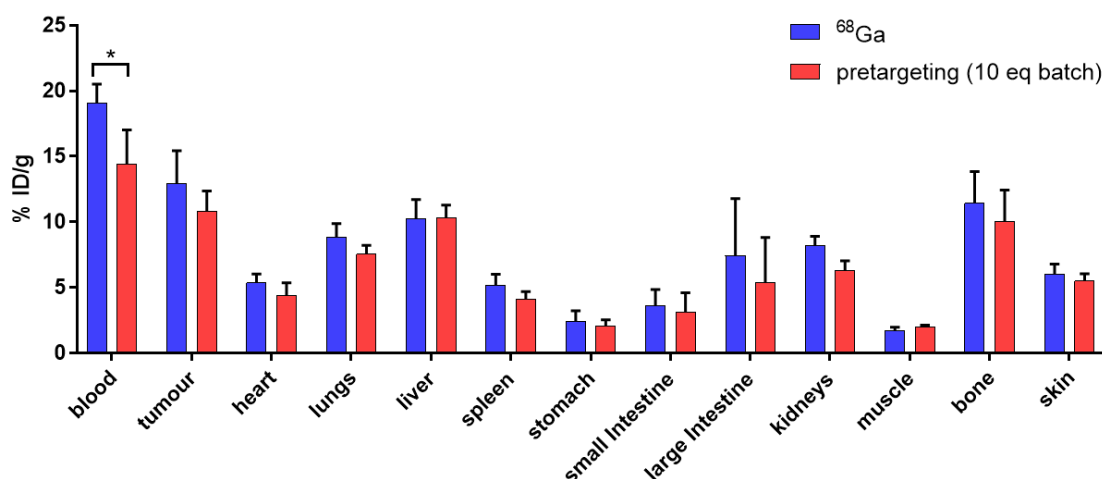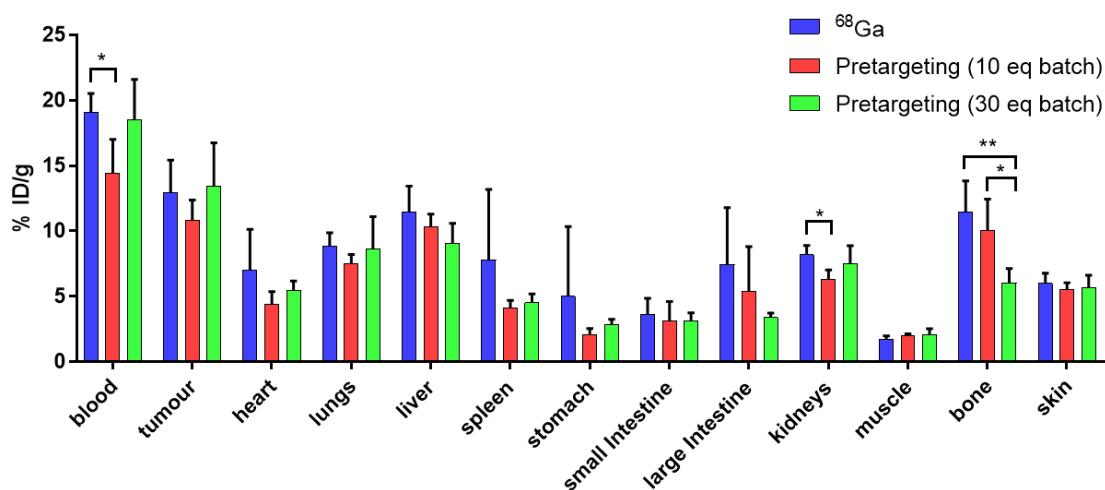
Figure 5.24. *Ex vivo ^{68}Ga biodistribution in nude mice bearing SW1222 xenografts at 3 hours after ^{68}Ga injections, comparing mice pretreated with THP^{Me}-Ph-NCS-huA33 10 equivalents batch (red), or 30 equivalents batch (green) 24 hours before ^{68}Ga administration, and mice that were not pretreated with any immunoconjugate (control group, blue). For each group N = 5, data are presented as mean ± SD. Comparison among the groups was performed using one-way ANOVA for each organ.*

Owing to the failure of the pretargeting experiments, the planned isotype control experiments were not performed resulting in a spare group of 5 mice bearing SW1222 xenografts. Given the relatively high accumulation of free gallium in this tumour (exceeding the % uptake found for the melanoma model in **Chapter 4**) a clearance experiment was performed, using THP^{Me} as a blood clearance agent with the aim to increase the tumour-to-blood activity ratio.

In this final experiment mice were injected with ^{68}Ga followed, at one hour post injection of the activity, by THP^{Me} (20 µg, 24 nmol). Mice were then imaged (from 20 min after THP^{Me} injection). Two of the mice were also imaged before between the first and second injection, in order to compare the PET images before and after THP^{Me}-mediated blood clearance. An example of PET images is presented below (**Figure 5.25**). *Ex vivo* biodistribution was also performed at 3h from the ^{68}Ga injection and compared to that of the ^{68}Ga control group (**Figure 5.26**).
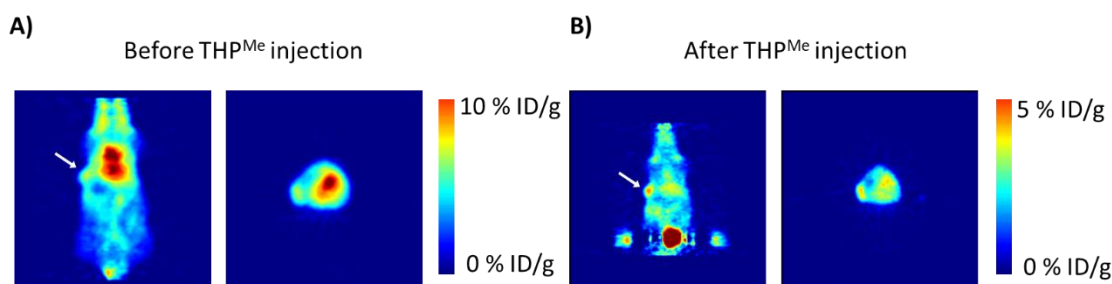
Figure 5.25. *Example PET images illustrating the biodistribution of ^{68}Ga in a nude mouse bearing SW1222 xenografts before (A) and after (B) the injection of THP^{Me} as a blood clearance agent. For both scans coronal view (left panel) and transverse view (right panel) are reported. Hot spots visible outside the mouse body in the coronal projection B are image artefacts due to the extremely high proportion of the activity in the bladder. White arrows indicate location of the tumour*
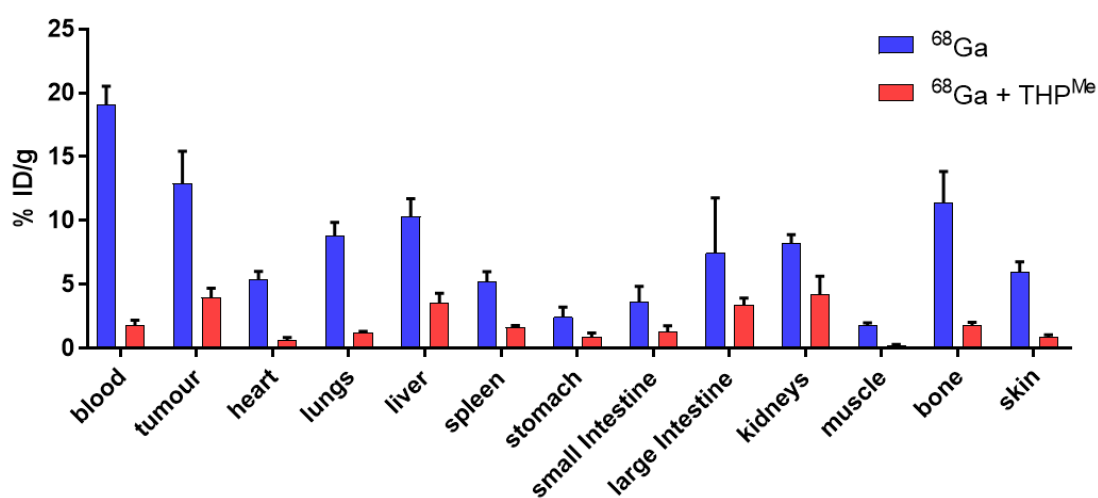
Figure 5.26. *Ex vivo ^{68}Ga biodistribution at 3 hours after ^{68}Ga injections in nude mice bearing SW1222 xenografts, comparing mice treated with THP^{Me} at one hour post ^{68}Ga injections and the control group. For each group N = 5. Data are presented as mean ± SD. Comparison between the two groups was performed with a t-test for each of the organs.*

Both PET images and biodistribution revealed the dramatic effect of THP^{Me} clearance, which notably decreased the uptake of ^{68}Ga in every organ. A t-test performed for every organ revealed significantly reduced uptake in all organs aside from the large intestine, probably as a result of the larger variability in the % ID/g for this organ. P values are reported in **Table 5.4** alongside means and tumour/organ ratios

Table 5.4. *Comparison between mean %ID/g and tumour/organ ratio for* ^{68}*Ga and* ^{68}*Ga + THP^{Me} groups. P values resulting from a t-test comparing the two groups for each organ are also reported.*

	P value	^{68}Ga		^{68}Ga + THP	
		Mean	tumour/organ	Mean	tumour/organ
Blood	5.71E-09	19.08	0.68	1.75	2.27
Tumour	6.29E-05	12.91	1.00	3.97	1.00
Heart	3.87E-07	5.36	2.41	0.66	5.98
Lungs	2.01E-07	8.83	1.46	1.20	3.32
Liver	1.43E-05	10.30	1.25	3.52	1.13
Spleen	9.45E-06	5.21	2.48	1.63	2.44
Stomach	0.004019	2.42	5.33	0.89	4.47
Small intestine	0.003237	3.66	3.53	1.31	3.03
Large intestine	0.07185	7.45	1.73	3.40	1.17
Kidneys	0.000557	8.19	1.58	4.21	0.94
Muscle	6.37E-07	1.76	7.36	0.25	16.09
Bone	2.07E-05	11.43	1.13	1.81	2.19
Skin	6.5E-07	5.99	2.15	0.86	4.62

Interestingly, the clearance effect is far more noticeable for the blood than for the tumour. Accordingly, the tumour to blood ratio increased from 0.68 in the ^{68}Ga-only control to 2.27 in the blood clearance experiment (> threefold increase).

5.4 Discussion

5.4.1 Choice of models for pretargeting experiments

The choice of appropriate models is of fundamental importance when designing any pretargeting experiment to avoid misinterpretation of the results. In this work, the high-affinity chemical pair was fixed and consisted of a THP^{Me}-based chelator and ^{68}Ga^{3+}, with the latter administered in an acetate buffered solution that proved to be effective for *in vivo* radiolabelling (see **Chapter 4**). On the other hand, other parameters such as the reactive chemical function of the THP^{Me} chelator and an appropriate antigen/antibody pair needed to be identified. Depending on the THP^{Me} chelator employed, site specific or non-specific conjugation to the antibody can be performed. While more control of the conjugation and on the immunoreactivity of the resulting immunoconjugate is gained using site specific attachment, non-specific conjugation allows, in principle, attachment of a higher number of chelators to the antibody. Both high affinity for the target receptor (undiminished immunoreactivity) and high availability of pretargeting sites (number of chelators/antibody) are important to obtain good image quality in a pretargeted experiment so any choice of bifunctional chelator should be a good compromise between the two. When considering the antigen/antibody couple, the main concerns are the high affinity of the antibody for the selected antigen and a slow internalisation rate of the antibody-antigen complex. High affinity is needed to ensure efficient binding to the antigen expressing tumour *in vivo*. Slow internalisation is important to maintain high immunoconjugate availability on the tumour surface, thus allowing the radiolabelled probe to bind *in vivo*. Finally, depending on the selected antigen/antibody couple, a cancer cell line overexpressing the desired antigen has to be chosen.

5.4.2 First attempt: THP^{Me}-mal-Anti-CEA conjugate

In the first set of experiments, a site-specific conjugation was used, exploiting the dithiophenolmaleimide technology developed by Baker and co-workers. The dithiphenolmaleimide derivative of THP^{Me} was site-specifically attached upon disulfide-bonds reduction to a fully human anti-CEA antibody targeting the slowly-internalising carcinoembryonic antigen [44]. The success of the conjugation was verified by SDS-PAGE, which showed both full and partial rebridging of the disulfide bonds upon reaction with the BFC. Subsequent hydrolysis of the maleimide moiety (overnight incubation at room temperature and pH > 8) ensured stability against protein displacement by free thiols. Successful radiolabelling was obtained in the mild

conditions usually employed for THP^{Me} ligands at an immunoconjugate concentration as low as 0.22 μM.

The human colorectal cancer cell line LS174T, known to express the carcinoembryonic antigen [40], was chosen for the *in vitro* uptake studies using the new synthesised immunoconjugate. The human melanoma cell line A375, not expressing the targeted antigen [42], was used as a negative control. Binding of the anti-CEA antibody to its target antigen may be impaired following treatment with trypsin, which is likely to affect peripheral membrane glycoproteins such as the CEA [45]. Therefore, uptake assays were performed on cells plated 48 h prior to the experiment to allow them to fully recover from trypsin treatment. In each experiment, one well per group was used to count the cells, to verify that the number of cells did not differ significantly between control and experimental group (*e.g.* as a result of a different duration of the cell cycle for the two cell lines). The THP^{Me}-mal-Anti-CEA conjugate retained affinity for the target receptor, as confirmed by uptake assays using the directly radiolabelled immunoconjugate. In A375 cells the uptake of ^{68}Ga-THP^{Me}-mal-Anti-CEA was minimal and similar to the % uptake measured for unchelated ^{68}Ga, while LS174T cells showed significant radioimmunoconjugate accumulation at an immunoconjugate concentration as low as 0.1 μg/mL. Although the absolute uptake was higher when the experiment was performed in HBSS we decided to carry out the pretargeting experiments in complete medium, as these conditions were likely to be more representative of an *in vivo* situation in which other chelating agents (transferrin, amino acids, *etc*.) can compete with the immunoconjugate for ^{68}Ga binding. 1 μg/mL was established as an ideal concentration of THP^{Me}-mal-Anti-CEA conjugate to maximise uptake. Notably, a 10-fold excess of unlabelled THP^{Me}-mal-Anti-CEA could not completely saturate the target antigen (uptake still visible, although reduced, for the 10 μg/mL group).

A reasoned choice of positive and negative controls for the pretargeting experiment was important to generate solid data that could attribute the success or the failure of the experiment solely to pretargeting and not to any other factors. The directly radiolabelled antibody represented the positive control, unchelated ^{68}Ga (without prior addition of antibody-chelator conjugate) the negative control. A pretargeting group with 3 times higher immunoconjugate concentration was included (pretargeting 3x), to account for concentration effects. Another group, in which the medium was not refreshed before the addition of the activity, was also included (pretargeting w/o wash), to evaluate the effect of unbound immunoconjugate available for radiolabelling in the medium. A final group was introduced to evaluate the effect of excess gallium

(pretargeting natural Ga), which should impair ^{68}Ga radiolabelling of the pretargeted immunoconjugate. For all these, A375 cells were evaluated alongside LS174T.

For LS174T cells, ^{68}Ga uptake in the pretargeting group was significantly lower than for the directly radiolabelled control, and no different from the ^{68}Ga-only group, showing how the measured uptake is only attributable to unchelated gallium. Similarly, no significantly different uptake was measured for either the pretargeting w/o wash, the pretargeting 3x or pretargeting the natural gallium group. Had the pretargeting worked, a decrease in uptake should have been visible for both the w/o wash and the natural gallium groups, due to radiolabelling of unbound immunoconjugate or to natural gallium blocking of antigen-bound immunoconjugate, respectively. Finally, an increased uptake for the pretargeting 3x group would have suggested that some pretargeting was taking place, but was not measurable at the 1 µg/mL concentration. Overall, the results obtained for LS174T already gave a clear indication of pretargeting failure in the tested conditions.

Additional confirmation of the failure was given by comparison with ^{68}Ga uptake in the control cell line A375. As already seen in the preliminary experiments, no difference between the uptake of unchelated gallium in the two cell lines was visible. On the contrary, a significantly reduced uptake was seen for the directly radiolabelled immunoconjugate in A375 cells compared to LS174T, unsurprisingly, since in this case ^{68}Ga is bound to the anti-CEA antibody for which A375 cells lack the target antigen. No difference between % uptake in the two cell lines was visible for the pretargeting, pretargeting 3x and pretargeting w/o group confirming the hypothesis that in all these groups all the uptake is due to unchelated ^{68}Ga. Interestingly, a significant difference was found between the pretargeting natural gallium groups where, unexpectedly, uptake in A375 cells but not in LS174T, was significantly decreased (P = 0.0062) by an excess of natural gallium, suggesting a saturation of ^{68}Ga uptake in this cell line at high gallium concentration (similar to what was seen in **Chapter 4** for ^{67}Ga uptake studies).

Notably, the obtained results not only proved that pretargeting did not take place in the experimental conditions, but also suggest that the reason of this failure is unsuccessful radiolabelling in the medium at the tested concentration (immunoconjugate concentration of 1 µg/mL, 7 nM). In fact, if the antibody could successfully bind ^{68}Ga, the percentage uptake measured for the pretargeting w/o wash group in the A375 cell should be lower than the unchelated gallium uptake (since free gallium would be sequestered by the immunoconjugate present in the solution). Notably, even increasing the immunoconjugate concentrations three times did not improve the results, suggesting that a 3 µg/mL immunoconjugate concentration (21

nM) was still too low to achieve radiolabelling of the pretargeted THP^{Me}-mal-Anti-CEA. Notably, saturation of the CEA antigen was probably not achieved at this concentration, since the preliminary uptake assay showed incomplete saturation even at 10 µg/mL of THP^{Me}-mal-Anti-CEA. Although further increase of the immunoconjugate concentration could have led to a measurable pretargeting effect, this was not tested due to low availability of THP^{Me}-mal-Anti-CEA. More importantly, the use of very high immunoconjugate concentration is undesirable and would eliminate any advantages of pretargeting over direct radiolabelling antibody, whose binding was already visible at the 30-fold lower concentration of 0.1 µg/mL. On the other hand, increasing the number of chelators/antibody *via* non-specific conjugation methods seemed a feasible way to increase the availability of the chelator for ^{68}Ga binding without increasing the amount of immunoconjugate used.

5.4.3 Second attempt: THP^{Me}-Ph-NCS conjugate

A second attempt at testing the metal chelation pretargeting hypothesis was carried out in collaboration with MSKCC and Hunter College during a five-week research visit. In this set of experiments, a fully human huA33 antibody was exploited, targeting the transmembrane glycoprotein A33 expressed in 95 % of colorectal carcinomas [46], including the colorectal cancer cell line SW1222 used in this experiment. The A33 protein does not become internalised or shed upon binding to the antibody, and is therefore an ideal model for pretargeting experiments. In addition, this antigen/antibody/cell line triad has been extensively exploited by Lewis and Zeglis in preclinical pretargeting studies to validate the bioorthogonal click chemistry approach [30,31,43], thus representing an excellent model to test a new pretargeting strategy. Previous studies in the same model suggest that site-specific conjugation does not improve image contrast and quality [30]. Therefore, in the attempt to increase the number of chelators available per antibody, a non-specific conjugation was exploited using the THP^{Me} isothiocyanate derivative THP^{Me}-Ph-NCS.

Conjugation of the selected antibody was initially performed using 5 and 10 equivalents of THP^{Me}-Ph-NCS and its success was demonstrated by efficient radiolabelling of the purified immunoconjugates in the mild conditions typical for THP^{Me}. In the same conditions, the native antibody could not specifically bind gallium, thus demonstrating how the THP^{Me} chelator is responsible for ^{68}Ga labelling. Further radiolabelling tests were performed in conditions more similar to those planned for the *in vivo* studies. In these experiments, the generator eluate was adjusted to a physiological pH (compatible with IV injection in non-anaesthetised mice). Furthermore, the introduction of a 45 min delay between eluate neutralisation and radiolabelling was

evaluated to account for the time to prepare syringes and mice prior to ^{68}Ga injection. Testing these conditions was important to rule out any effect of different gallium speciation over pH range or time when considering the results of preclinical experiments. In fact, in our experience, unchelated gallium often displays a variable behaviour after the pH is raised above 3, presumably owing to the multitude of species present in these conditions (see **Chapter 1**). An immunoreactivity assay, performed in conditions of large antigen excess to ensure quantitative huA33 binding to A33 receptor, [36], showed only a marginal impairment of the immunoreactivity, for both the radiolabelled immunoconjugate batches, towards SW1222 cells. Based on these results the 10 equivalents batch was employed for the initial *in vivo* experiments.

Imaging using a ^{89}Zr-labelled DFO-huA33 immunoconjugate confirmed the ability of the antibody to image SW1222 tumours with great selectivity. Imaging using a directly radiolabelled THP^{Me}-hua33 derivative would have been an even stronger positive control for our experiment but this could not be performed for several reasons. In the first instance, THP chelators are very selective for gallium, as highlighted in the previous chapters, and a ^{89}Zr radiolabelled derivative would have seen demetallation in serum over time [47]. Imaging with ^{67}Ga, was possible in principle, but the isotope was not available at MSKCC at the time of the experiment. Finally, ^{68}Ga imaging of a directly labelled conjugate was simply unfeasible due to the short half-life of the isotope. The first preclinical studies using ^{68}Ga were therefore the pretargeting experiment (using the 10 equivalents batch) and the negative control that only employed acetate buffered gallium-68. Unfortunately, *in vivo* imaging and biodistribution did not highlight any difference between the pretargeted and ^{68}Ga-only group, suggesting that the tumour uptake visible in the pretargeting group was solely attributable to uptake of unchelated ^{68}Ga in the tumour. Different hypotheses were formulated to account for the failure of this pretargeting experiment. Similar to what was hypothesised for the anti-CEA antibody, the concentration of chelator may have been not sufficient for effective radiolabelling. Alternatively, THP^{Me} chelator could have interacted with endogenous metals during the 24 hours between the immunoconjugate administration and the ^{68}Ga injection, thus becoming not available for ^{68}Ga radiolabelling.

MALDI analysis of the immunoconjugate, only available after the first set of *in vivo* experiments, seemed to support the first hypothesis. In fact, only an average of 0.6 chelators per antibody were found in the case of the 10 equivalents batch. Although this is an average number, and likely includes immunoconjugate molecules with few chelators attached, the value itself is particularly low considered the general

assumption that non-specific conjugation can lead to a higher number of chelator/antibody molecules.

A final pretargeting attempt was conducted using an antibody reacted with 30 equivalents of chelator (maximum amount that allowed conjugation without any aggregation/precipitation of the immunoconjugate). Unfortunately, also in this case no significant difference in the tumour uptake of ^{68}Ga was visible. Although MALDI analysis of this new batch showed a modest increase in the chelator/antibody ratio (up to 1 chelator/antibody molecules on average), this may have been not enough to allow pretargeted imaging using this approach. On the other hand, some differences in biodistribution observed for this last group suggest that there may be other reasons contributing to the failure of this second attempt. In fact, a decreased uptake in bones was evident for this third group of animals and uptake in liver and large intestines was also reduced although to a lesser extent. Since all these organs are involved in clearance routes of free gallium (especially bone), the decreased uptake suggests that part of the gallium may actually bind the antibody *in vivo*, but this does not result in increased tumour uptake. No measurements of the immunoreactive fraction of the 30 equivalents immunoconjugate batch were performed due to time constraints so it is not possible to know whether the immunoreactive fraction decreased compared with the 89 % measured for the 10 equivalents batch. In any case, it is reasonable to imagine that antibodies with more chelators attached will bind to their target antigen with lower affinity compared to those with a higher number of chelators (in fact, the MALDI measurements only yielded an average value, but the distribution of chelators/antibody is likely to be not uniform). In the presence of an excess of antibody with no/few chelators, those immunoconjugate molecules with several chelators are less likely to bind to their target antigen, but more likely to bind ^{68}Ga, and their residual circulating fraction could therefore bind part of the ^{68}Ga injected 24 h after antibody administration, diminishing unchelated gallium uptake in bones/liver/intestine without significantly altering the ^{68}Ga tumour uptake.

Overall, no pretargeting-related tumour uptake was observed in these *in vivo* experiments and notably, no improvement was visible when using the 30 equivalents compared to the 10 equivalents batch. If this were a consequence of impaired affinity of the immunoconjugate, that would automatically rule out the THP^{Me}-Ph-NCS chelator for pretargeting purposes. If instead, this were due to an insufficient number of chelator molecules per antibody, this would still be an irresolvable problem, as conjugation of more than 1 THP^{Me}-Ph-NCS moiety per antibody was not possible and resulted in precipitation of the immunoconjugate, likely due to aggregation.

The use of larger amount of immunoconjugate may help to increase the number of antibodies molecules bound to the tumour antigen. However, considering the non-uniformity of the immunoconjugate population this may results in antibody molecules possessing 0-1 chelator saturating the antigen pool and leaving those immunoconjugate with more chelators attached (and more likely to radiolabel) in the blood stream. In fact, this strategy had already been exploited by Zeglis for the same antibody/antigen pair (using 300 μg of immunoconjugate [31]), but no improvement on the tumour uptake was measured. On the contrary, an increased blood-pool activity was found due to increase in circulating immunoconjugate molecules.

Notably, although unsuccessful from a pretargeting point of view, these studies highlighted a good uptake of unchelated gallium in SW1222 tumours. This led us to use those mice originally allocated for isotype control to evaluate the use of THP^{Me} as a blood clearance agent to increase their tumour-to-blood activity ratio as described in **Chapter 4**. The experiment was performed in the same conditions employed for the A375 melanoma models, in terms of delay between injections and amount of THP^{Me} administered, with the only difference being that mice were injected when awake and, accordingly the pH of the ^{68}Ga and THP solutions injected was 7-7.2 (instead of pH 5-6 employed in the A375 model). Notably, in this experiment THP^{Me} was able to clear ^{68}Ga from the blood much more efficiently than from the tumours, resulting in a threefold enhancement of the tumour-to-blood activity ratio (shifting its value from <1 to >2) as calculated from the *ex vivo* biodistribution data at 3 hours. PET images of the mice before and after THP^{Me} treatment also showed increased image contrast and better tumour visualisation, despite poor quality owing to the massive accumulation of activity in the bladder. These results together suggest that the SW1222 colon carcinoma could be a good model to further investigate the use of unchelated ^{68}Ga to image tumours with use of THP^{Me} as a blood clearing agent.

Notably, a reduced variability in ^{68}Ga-acetate biodistribution was also observed in these experiments, compared to those performed for the A375 xenografts. Several factors were changed between the two set of experiments (generators, pH of injection, strain of mice, time under anaesthesia) and therefore it is difficult to ascribe this different behaviour to a particular cause. However, the higher pH of the ^{68}Ga-acetate solution used in SW1222 experiments is likely to have played a role in this, by increasing the reproducibility of ^{68}Ga speciation. Further experiments are needed to investigate this hypothesis.

5.5 Conclusions

In conclusion, the pretargeting by metal chelation strategy failed for both the different models investigated. These findings suggest that a step back should be taken and the feasibility of the approach re-examined. Although immunoPET is certainly the field that would benefit more from pretargeting, antibodies are complex molecules and their complexity increases upon conjugation to a chelator. Conversely, while peptide-based imaging would not benefit from pretargeting in a clinical setting, it could represent an ideal system for a proof-of-concept study evaluating new pretargeting strategies. Peptides are more prone to chemical modification and easier to characterise than antibodies. Conjugation of a peptide with a chelator and subsequent purification will result in a single 1:1 species ruling out the presence of unconjugated peptide that could block the target antigen in pretargeting experiments. The somatostatin antagonists JR11 and LM3, developed by Fani and colleagues for the imaging of neuroendocrine tumours [48], possess exquisite targeting properties and do not internalise upon antigen binding. Conjugation of these peptide to THP^{Me} could easily be performed exploiting the routes already established for the somatostatin agonist THP^{Me}-TATE and other peptide derivatives. Furthermore, conjugation to three THP^{Me} molecules per peptide is also possible exploiting the dendritic systems that we previously developed [49], thus increasing the concentration of chelator available at the tumour site. Somatostatin antagonists therefore represent an ideal model to test the feasibility of the pretargeting *via* metal chelation approach using THP^{Me} and gallium-68, before evaluation in a clinically-relevant model.

5.6 References

1. Weiner, L. M., Surana, R., and Wang, S. (2010) Monoclonal antibodies: versatile platforms for cancer immunotherapy. *Nat. Rev. Immunol.* **10**, 317-327.
2. Scott, A. M., Wolchok, J. D., and Old, L. J. (2012) Antibody therapy of cancer. *Nat. Rev. Cancer* **12**, 278-287.
3. Moek, K. L., Giesen, D., Kok, I. C., de Groot, D. J. A., Jalving, M., Fehrmann, R. S. N., Hooge, M. N. L.-d., Brouwers, A. H., and de Vries, E. G. E. (2017) Theranostics Using Antibodies and Antibody-Related Therapeutics. *J. Nucl. Med.* **58**, 83S-90S.
4. Gupta, S., Batra, S., and Jain, M. (2014) Antibody Labeling with Radioiodine and Radiometals. *Methods Mol. Biol.* **1141**, 147-157.
5. Mather, S. J., and Ellison, D. (1990) Reduction-mediated Tc-99m labeling of monoclonal-antibodies. *J. Nucl. Med.* **31**, 692-697.
6. Badar, A., Williams, J., de Rosales, R. T., Tavare, R., Kampmeier, F., Blower, P. J., and Mullen, G. E. (2014) Optimising the radiolabelling properties of technetium tricarbonyl and His-tagged proteins. *EJNMMI Res.* **4**, 14-14.
7. Adumeau, P., Sharma, S. K., Brent, C., and Zeglis, B. M. (2016) Site-specifically labeled immunoconjugates for molecular imaging-part 1: cysteine residues and glycans. *Mol. Imaging Biol.* **18**, 1-17.
8. Cooper, M. S., Sabbah, E., and Mather, S. J. (2006) Conjugation of chelating agents to proteins and radiolabeling with trivalent metallic isotopes. *Nat. Protoc.* **1**, 314-317
9. Price, E. W., and Orvig, C. (2014) Matching chelators to radiometals for radiopharmaceuticals. *Chem. Soc. Rev.* **43**, 260-290.
10. van Dongen, G., Visser, G. W. M., Hooge, M., De Vries, E. G., and Perk, L. R. (2007) Immuno-PET: A navigator in monoclonal antibody development and applications. *Oncologist* **12**, 1379-1389.
11. Walsh, G. (2014) Biopharmaceutical benchmarks 2014. *Nat. Biotechnol.* **32**, 992-1000.
12. Lamberts, L. E., Williams, S. P., van Scheltinga, A. G. T. T., Lub-de Hooge, M. N., Schroeder, C. P., Gietema, J. A., Brouwers, A. H., and de Vries, E. G. E. (2015) Antibody Positron Emission Tomography Imaging in Anticancer Drug Development. *J. Clin. Oncol.* **33**, 1491-1503
13. Green, D. J., and Press, O. W. (2017) Whither radioimmunotherapy: to be or not to be? *Cancer Res.* 77, 2191-2196.
14. Barbet, J., Bardies, M., Bourgeois, M., Chatal, J.-F., Cherel, M., Davodeau, F., Faivre-Chauvet, A., Gestin, J.-F., and Kraeber-Bodere, F. (2012) Radiolabeled antibodies for cancer imaging and therapy. *Methods Mol. Biol.* **907**, 681-697.
15. Sharkey, R. M., Chang, C. H., Rossi, E. A., McBride, W. J., and Goldenberg, D. M. (2012) Pretargeting: taking an alternate route for localizing radionuclides. *Tumor Biol.* **33**, 591-600.
16. Forster, G. J., Santos, E. B., Smith-Jones, P. M., Zanzonico, P., and Larson, S. M. (2006) Pretargeted radioimmunotherapy with a single-chain antibody/streptavidin construct and radiolabeled DOTA-biotin: Strategies for reduction of the renal dose. *J. Nucl. Med.* **47**, 140-149.
17. Patra, M., Zarschler, K., Pietzsch, H. J., Stephan, H., and Gasser, G. (2016) New insights into the pretargeting approach to image and treat tumours. *Chem. Soc. Rev.* **45**, 6415-6431.
18. Altai, M., Membreno, R., Cook, B., Tolmachev, V., and Zeglis, B. M. (2017) Pretargeted Imaging and Therapy. *J. Nucl. Med.* **58**, 1553-1559.
19. Goldenberg, D. M., Chang, C.-H., Rossi, E. A., McBride, W. J., and Sharkey, R. M. (2012) Pretargeted Molecular Imaging and Radioimmunotherapy. *Theranostics* **2**, 523-540.

20. Bourgeois, M., Bailly, C., Frindel, M., Guerard, F., Cherel, M., Faivre-Chauvet, A., Kraeber-Bodere, F., and Bodet-Milin, C. (2017) Radioimmunoconjugates for treating cancer: recent advances and current opportunities. *Expert Opin. Biol. Ther.* **17**, 813-819.

21. Chaiet, L., and Wolf, F. J. (1964) Properties of streptavidin biotin-binding protein produced by streptomycetes. *Arch. Biochem. Biophys.* **106**, 1-5.

22. Hnatowich, D. J., Virzi, F., and Rusckowski, M. (1987) Investigations of avidin and biotin for imaging applications. *J. Nucl. Med.* **28**, 1294-1302.

23. Sharkey, R. M., and Goldenberg, D. M. (2005) Perspectives on cancer therapy with radiolabeled monoclonal antibodies. *J. Nucl. Med.* **46**, 115S-127S

24. Goldenberg, D. M., Chang, C.-H., Sharkey, R. M., Rossi, E. A., Karacay, H., McBride, W., Hansen, H. J., Chatal, J.-F., and Barbet, J. (2003) Radioimmunotherapy: is avidin-biotin pretargeting the preferred choice among pretargeting methods? *Eur. J. Nucl. Med. Mol. Imaging* **30**, 777-780.

25. Kuijpers, W. H. A., Bos, E. S., Kaspersen, F. M., Veeneman, G. H., and Van Boeckel, C. A. (1993) Specific recognition of antibody oligonucleotide conjugates by radiolabeled antisense nucleotides - a novel-approach for 2-step radioimmunotherapy of cancer. *Bioconjugate Chem.* **4**, 94-102.

26. Liu, G., Dou, S., Liu, Y., Wang, Y., Rusckowski, M., and Hnatowich, D. J. (2011) Y-90 labeled phosphorodiamidate morpholino oligomer for pretargeting radiotherapy. *Bioconjugate Chem.* **22**, 2539-2545.

27. Liu, G. Z., Mang'era, K., Liu, N., Gupta, S., Rusckowski, M., and Hnatowich, D. J. (2002) Tumor pretargeting in mice using Tc-99m-labeled morpholino, a DNA analog. *J. Nucl. Med.* **43**, 384-391.

28. Leonidova, A., Foerster, C., Zarschler, K., Schubert, M., Pietzsch, H. J., Steinbach, J., Bergmann, R., Metzler-Nolte, N., Stephan, H., and Gasser, G. (2015) In vivo demonstration of an active tumor pretargeting approach with peptide nucleic acid bioconjugates as complementary system. *Chem. Sci.* **6**, 5601-5616

29. Meyer, J. P., Adumeau, P., Lewis, J. S., and Zeglis, B. M. (2016) Click chemistry and radiochemistry: the first 10 years. *Bioconjugate Chem.* **27**, 2791-2807.

30. Cook, B. E., Adumeau, P., Membreno, R., Carnazza, K. E., Brand, C., Reiner, T., Agnew, B. J., Lewis, J. S., and Zeglis, B. M. (2016) Pretargeted PET imaging using a site-specifically labeled immunoconjugate. *Bioconjugate Chem.* **27**, 1789-1795.

31. Zeglis, B. M., Sevak, K. K., Reiner, T., Mohindra, P., Carlin, S. D., Zanzonico, P., Weissleder, R., and Lewis, J. S. (2013) A Pretargeted PET imaging strategy based on bioorthogonal Diels-Alder click chemistry. *J. Nucl. Med.* **54**, 1389-1396.

32. Blower, P. J., Cooper, M. S., Nawaz, S., O'Neill, A., Koers, A., Sunassee, K., Berry, D. J., Mullen, G. E. D., and Ballinger, J. R. (2012) Metal ion chelation as a basis for pretargeting. *Eur. J. Nucl. Med. Mol. Imaging* **39**, S262.

33. King, D. J., Antoniw, P., Owens, R. J., Adair, J. R., Haines, A. M. R., Farnsworth, A. P. H., Finney, H., Lawson, A. D. G., Lyons, A., Baker, T. S., Baldock, D., Mackintosh, J., Gofton, C., Yarranton, G. T., McWilliams, W., Shochat, D., Leichner, P. K., Welt, S., Old, L. J., and Mountain, A. (1995) Preparation and preclinical evaluation of humanized A33 immunoconjugates for radioimmunotherapy. *Br. J. Cancer* **72**, 1364-1372.

34. Holland, J. P., Sheh, Y., and Lewis, J. S. (2009) Standardized methods for the production of high specific-activity zirconium-89. *Nucl. Med. Biol.* **36**, 729-739.

35. Ma, M. T., Cullinane, C., Imberti, C., Baguna Torres, J., Terry, S. Y. A., Roselt, P., Hicks, R. J., and Blower, P. J. (2015) New tris(hydroxypyridinone) bifunctional chelators containing isothiocyanate groups provide a versatile platform for rapid one-step labeling and PET imaging with $^{68}Ga^{3+}$. *Bioconjugate Chem.* **27**, 309-318.

36. McDevitt, M. R., Finn, R. D., Ma, D., Larson, S. M., and Scheinberg, D. A. (1999) Preparation of alpha-emitting Bi-213-labeled antibody constructs for clinical use. *J. Nucl. Med.* **40**, 1722-1727.

37. Smith, M. E. B., Schumacher, F. F., Ryan, C. P., Tedaldi, L. M., Papaioannou, D., Waksman, G., Caddick, S., and Baker, J. R. (2010) Protein modification, bioconjugation, and disulfide bridging using bromomaleimides. *J. Am. Chem. Soc.* **132**, 1960-1965.

38. Ryan, C. P., Smith, M. E. B., Schumacher, F. F., Grohmann, D., Papaioannou, D., Waksman, G., Werner, F., Baker, J. R., and Caddick, S. (2011) Tunable reagents for multi-functional bioconjugation: reversible or permanent chemical modification of proteins and peptides by control of maleimide hydrolysis. *Chem. Commun.* **47**, 5452-5454.

39. Schumacher, F. F., Nobles, M., Ryan, C. P., Smith, M. E. B., Tinker, A., Caddick, S., and Baker, J. R. (2011) In situ maleimide bridging of disulfides and a new approach to protein PEGylation. *Bioconjugate Chem.* **22**, 132-136.

40. Shi, Z. R., Tsao, D., and Kim, Y. S. (1983) Subcellular-distribution, synthesis, and release of carcinoembryonic antigen in cultured human-colon adenocarcinoma cell-lines. *Cancer Res.* **43**, 4045-4049.

41. Schoffelen, R., Sharkey, R. M., Goldenberg, D. M., Franssen, G., McBride, W. J., Rossi, E. A., Chang, C. H., Laverman, P., Disselhorst, J. A., Eek, A., van der Graaf, W. T. A., Oyen, W. J. G., and Boerman, O. C. (2010) Pretargeted immuno-positron emission tomography imaging of carcinoembryonic antigen-expressing tumors with a bispecific antibody and a Ga-68- and F-18-labeled hapten peptide in mice with human tumor xenografts. *Mol. Cancer Ther.* **9**, 1019-1027.

42. Chowdhury, S., Chester, K. A., Bridgewater, J., Collins, M. K., and Martin, F. (2004) Efficient retroviral vector targeting of carcinoembryonic antigen-positive tumors. *Mol. Ther.* **9**, 85-92.

43. Adumeau, P., Carnazza, K. E., Brand, C., Carlin, S. D., Reiner, T., Agnew, B. J., Lewis, J. S., and Zeglis, B. M. (2016) A pretargeted approach for the multimodal PET/NIRF imaging of colorectal cancer. *Theranostics* **6**, 2267-2277.

44. Schmidt, M. M., Thurber, G. M., and Wittrup, K. D. (2008) Kinetics of anti-carcinoembryonic antigen antibody internalization: effects of affinity, bivalency, and stability. *Cancer Immunol. Immunother.* **57**, 1879-1890.

45. Rutzky L. (1985) *Advances in Cell Culture,* Vol **4**, (Editors: Maramorosch, K., and Sato, G.), Academic Press.

46. Garinchesa, P., Sakamoto, J., Welt, S., Real, F. X., Rettig, W. J., and Old, L. J. (1996) Organ-specific expression of the colon cancer antigen A33, a cell surface target for antibody-based therapy. *International Journal of Oncology* **9**, 465-471.

47. Ma, M. T., Meszaros, L. K., Paterson, B. M., Berry, D. J., Cooper, M. S., Ma, Y., Hiderd, R. C., and Blower, P. J. (2015) Tripodal tris(hydroxypyridinone) ligands for immunoconjugate PET imaging with $^{89}Zr^{4+}$: comparison with desferrioxamine-B. *Dalton Trans.* **44**, 4884-4900.

48. Fani, M., Nicolas, G. P., and Wild, D. (2017) Somatostatin receptor antagonists for imaging and therapy. *J. Nucl. Med.* **58**, 61S-66S.

49. Imberti, C., Terry, S. Y. A., Cullinane, C., Clarke, F., Cornish, G. H., Ramakrishnan, N. K., Roselt, P., Cope, A. P., Hicks, R. J., Blower, P. J., and Ma, M. T. (2017) Enhancing PET signal at target tissue in vivo: dendritic and multimeric Tris(hydroxypyridinone) conjugates for molecular imaging of $\alpha_V\beta_3$ integrin expression with gallium-68. *Bioconjugate Chem.* **28**, 481-495.

6 Final remarks and future work

In the past two decades, the use of the positron emitting radiometal ^{68}Ga in radionuclide molecular imaging has seen an unprecedented blossoming, well documented by the continuous and rapid growth of research publications concerning this PET radioisotope (**Figure 6.1**)[1, 2].
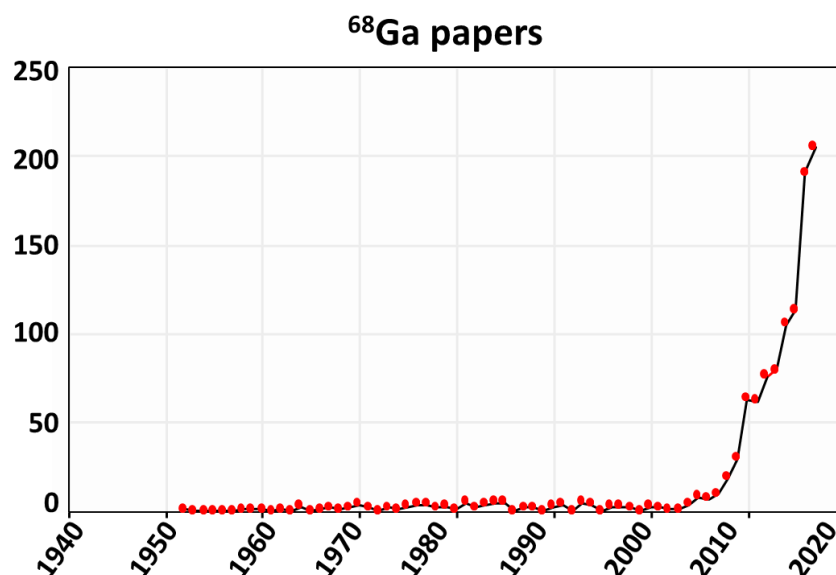

Figure 6.1. *Number of papers containing gallium-68, ^{68}Ga or Ga-68 in the title published each year in the 1940-2017 period (as retrieved from Web of Science, Dec 2017).*

The popularity of this radioisotope is likely to raise even more rapidly in the next decade, stimulated by the recent introduction of the first pharmaceutical grade generator and the approval of [^{68}Ga]Ga-DOTA-TATE (NETSPOT®, approved by FDA [3]) and [^{68}Ga]Ga-DOTA-TOC (SOMAKIT TOC ®, approved by EMA [4]), as imaging agents for the diagnosis and staging of neuroendocrine tumours.

The main advantage of ^{68}Ga is its ready availability from a long-lived, bench-top generator, reducing production costs and technical complexity compared to cyclotron-produced isotopes. In addition, generator-based production of gallium-68 opens the possibility, unique among PET radiometals, of one-step, kit-based radiolabelling procedures. This opportunity could boost even more the clinical utility of ^{68}Ga making it the workhorse of PET imaging, in the same way in which ^{99m}Tc is the workhorse of SPECT. On the other hand, ^{68}Ga radiolabelling still present some unresolved issues, such as the presence of metal contaminants in the generator eluate (at concentrations higher than that ^{68}Ga^{3+} itself) and the, likely related, inability ^{68}Ga radiotracers to achieve high specific activity in the radiolabelling.

Clinical use of ^{68}Ga is mainly based on receptor imaging with radiolabelled peptides, whose pharmacokinetics is compatible with its short half-life. Unsurprisingly, research in this field has been mainly focusing on the development of new peptide-based ^{68}Ga tracers for the imaging of cancer, although other applications, such as imaging of infection and inflammation, are also being investigated [5]. Other important areas of research include the development of (i) better quality generators and purification systems, to decrease presence of metal contaminants in the ^{68}Ga eluate, (ii) improved chelators for Ga(III), moving away from the old "one (chelator) fits all (metals)" paradigm.

Our group has developed a *tris*(hydroxypyridinone) chelator THP^{Me}, able to complex [68]Ga^{3+} rapidly in extremely mild conditions. Notably, neither eluate pre-processing nor radiotracer purification are required for THP^{Me} radiolabelling to achieve quantitative radiochemical purity, thus making this chelator ideal for kit-type ^{68}Ga radiolabelling. The bioconjugate derivative THP^{Me}-PSMA has successfully completed a first in human investigation and is now undergoing a multi-centre clinical trial for the imaging of prostate cancer [6].

The extreme facility of ^{68}Ga labelling displayed by THP^{Me} stimulated further investigation on this chelator to understand the reasons behind its outstanding affinity for gallium and to explore potential new approaches to ^{68}Ga imaging arising from THP^{Me} properties. Development of novel THP-based chelators with different chemical properties, but with preserved or even improved affinity for ^{68}Ga is also important, to create a library of THP chelators that could be used for different applications. In this work, we aimed at answering, at least partially, these questions through a multidisciplinary project that spanned from synthetic chemistry, through radiochemistry, to *in vitro* and *in vivo* experiments.

In the first part of this work, a new *tris*(hydroxypyridinone) chelator THP^{H} was developed, by replacing the classical N^1-Me pyridinone units with new N^1-H precursors. Notably, this small chemical change resulted in the need for different synthetic strategies compared to THP^{Me} synthesis. THP^{H} was found able to bind ^{68}Ga quantitatively in the same extremely mild conditions employed for THP^{Me}, forming a 1:1 = Ga:THP^{H} species. A thorough side-by-side characterisation of the two chelators (and resulting metal complexes) allowed us to highlight chemical differences between the two ligands, and also to shed some light on their effectiveness in binding [68]Ga. For both chelators, ligand affinity for Ga(III) was found superior to the affinity for Fe(III), as shown in spectrophotometric titrations. Although the measured preference for Ga(III) may be only be descriptive of a short-term situation, owing to a slow attainment

of thermodynamic equilibrium for these complexes, this still holds true in ^{68}Ga radiolabelling experiments, where short reaction time is essential. Indeed, competition experiments in a radiolabelling setting showed how the presence of excess iron only marginally affects ^{68}Ga radiolabelling for both ligands. Reasons for this preference are likely to be found in the tripodal structure of these chelators, which may impose geometric constraints for metal coordination that fits Ga(III) better than Fe(III). In fact, no preference whatsoever was observed for the bidentate hydroxypyridinone chelator deferiprone. Notably, THP^H was found to be even more selective than THP^{Me} for Ga(III), and showed significantly lower affinity for Fe(III).

Future continuation of this project should aim at extending the library of THP compounds and their bifunctional derivatives. In this regard, the benzylated *tris*(hydroxypyranone) BnTHPO, developed as a synthetic intermediate *en route* to THP^H, holds great promise as a versatile platform for the synthesis of a library of *tris*(hydroxypyridinone) chelators with tunable properties and metal preferences. Notably, synthesis of more water-soluble derivatives is also to be sought, to enable structural characterisation of the resulting gallium complex, expanding our knowledge on the Ga(III) coordination environment for THP ligands. Development of bifunctional derivatives for THP^H and other THP chelators will enable conjugation to peptides and other relevant biomolecules. Importantly, given the remarkably mild condition for ^{68}Ga radiolabelling of THP chelators, they could also be attached to small proteins (such as the scFv fusion proteins), whose pharmacokinetics is compatible with the short half-life of the radiometal.

In a second part of this work, we tried to explore new possibilities for ^{68}Ga imaging, relying on the ability of THP^{Me} to bind Ga(III) in extremely mild conditions. In the first instance, we investigated the use of THP^{Me} as a blood clearance agent, in the context of cancer imaging with gallium salts. The strategy of exploiting the tumour localising properties of gallium was widely used in the past with ^{67}Ga-citrate, but failed to be translated to ^{68}Ga imaging, owing to the mismatch between the short half-life of this isotope and the slow blood clearance of unchelated gallium. Therefore, we investigated the use of THP^{Me} as a ^{68}Ga blood clearance agent, to be administered after the injection of the radiometal, with the aim of enhancing tumour-to-blood ratio and, accordingly, image contrast at short time points. The conditions for ^{68}Ga *in vivo* chelation were studied first in normal animals, showing that 24 nmol of THP^{Me} are able to effectively bind previously administered ^{68}Ga, when injected up to one hour after the radiometal. The [^{68}Ga(THP^{Me})] complex was quickly excreted renally, resulting in an accelerated blood clearance of the radiometal and in lower accumulation in bones

and other organs. However, the high variability observed in ^{68}Ga biodistribution (probably due to subtle variation in generator eluate, pH, elution time *etc.)*, often confounded the clearance effect, whose significance was only evident when large sample sizes were considered. The clearance properties of THP^{Me} were also investigated in xenografts bearing mice, in cancer models that were found able to accumulate ^{68}Ga in tumour when injected with ^{68}Ga-acetate. The experiment was originally performed in an A375 melanoma model, but lead to inconclusive results, owing to an unexpectedly fast clearance of the radiometal and poor accumulation into tumours and other organs. Notably, when a similar experiment was performed in a colon cancer model (SW1222 xenografts) a three-fold increase in the tumour-to-blood ratio was observed for mice treated with THP^{Me} one hour after ^{68}Ga injection, highlight the potential of THP^{Me} as a blood clearance agent in this model. Importantly, high variability in ^{68}Ga biodistribution was observed throughout the whole project and seems intrinsically linked to the use of unchelated/loosely chelated forms of gallium, highlighting the complexity of gallium speciation in living organisms. Variability could possibly be reduced in future experiments, by administering gallium in a form that is more stable (*e.g.* citrate complex, transferrin complex, or $[Ga(OH)_4]^-$), but still able to both deliver the radiometal to the tumour and to cede it to THP^{Me} in the blood clearance step. Different species of transferrins (human, mouse *etc.*) could also be investigated with this purpose.

A final section of this work was also inspired by the ability of THP^{Me} to coordinate ^{68}Ga *in vivo*. In this case, a new pretargeting strategy was explored, referred to as pretargeting *via* metal chelation, based on THP and Ga(III) as a high affinity chemical pair able to bind *in vivo*. Compared to other pretargeting strategies, this approach would have the advantage of almost eliminating any preparative radiochemistry, thus greatly simplifying its clinical translation. In this work, two different derivatives of THP^{Me}, namely THP^{Me}-Mal-DTP and THP^{Me}-Ph-NCS, were attached to the non-internalising antibodies anti-CEA and huA33, respectively. The ability of these immunoconjugates to undergo pretargeted ^{68}Ga uptake was investigated *in vitro* (using the THP^{Me}-mal-anti-CEA derivative), or *in vivo* (using the THP^{Me}-Ph-NCS-huA33 immunconjugate) in cancer models expressing the relevant target antigens. Unfortunately, neither of these attempts succeeded, possibly due to a low availability of the THP^{Me} chelating moiety at the antigen site (owing to the low number of chelators/antibody and/or to the presence of non-conjugated antibody). Increasing the number of chelators per antibody represents a possible solution to this technical limitation. However, this was found not feasible for THP-Ph-NCS with precipitation of the immunoconjugate visible when 50 equivalents of chelator were used for the

conjugation procedure. Other bifunctional THP^{Me} derivatives could in principle be tested to achieve higher chelator/antibody ratio, but we suggest that first a step back is taken and the pretargeting hypothesis explored in a simpler peptide-based model. In addition, a more fundamental problem can be recognised for our pretargeting approach: the interaction between the two components of the high affinity chemical pair (in our case ^{68}Ga^{3+} and THP^{Me}) should be bio-orthogonal to avoid interference with biological processes. Despite the high affinity of THP^{Me} for ^{68}Ga^{3+}, its complexation is certainly not bio-orthogonal. In fact, ^{68}Ga^{3+} can interact with transferrin and, in this or other forms, it can accumulate in several organs, including tumours. THP^{Me} itself, despite its preference for Ga(III) over Fe(III), can still interact with iron or other metals in the time between immunoconjugate and ^{68}Ga injection. Overall, these considerations do not exclude the possibility of pretargeting by metal chelation, but suggest that the use of a different, truly bio-orthogonal radiometal/chelator couple should be preferred.

In conclusion, this work shows how the potential for ^{68}Ga imaging of cancer is vast and expanding. In this context, outstanding Ga(III) chelators such as the *tris*(hydroxypyridinone) ligands here investigated, not only provide useful tools for the development of novel receptor-targeting ^{68}Ga tracers, but also open new opportunities in ^{68}Ga imaging, exploiting their ability to bind gallium in extremely mild conditions. Although the first attempts in this direction were only partially successful, they contribute to our knowledge of the THP/Ga(III) system and pave the way to further investigation with improved THP chelators. The development of the THP^{H} ligand described in this work represents the first step in the creation of a library of THP chelators with enhanced chemical properties and Ga(III) selectivity.

6.1 References

1. Velikyan, I. (2015) Continued rapid growth in Ga-68 applications: update 2013 to June 2014. *J. Label. Compd. Radiopharm.* **58**, 99-121.
2. Velikyan, I. (2015) Ga-68-based radiopharmaceuticals: production and application relationship. *Molecules* **20**, 12913-12943.
3. Mullard, A. (2016) FDA approvals for the first 6 months of 2016. *Nat. Rev. Drug Discov.* **15**, 523-523.
4. Advanced Accelerator Applications (2016) Advanced Accelerator Applications Announces European Commission Approval of SomaKit TOC™. (Press Release).
5. Velikyan, I. (2018) Prospective of Ga-68 radionuclide contribution to the development of imaging agents for infection and inflammation. *Contrast Media Mol. Imaging.* (ahead of print, https://doi.org/10.1155/2018/9713691).
6. Hofman, M. S., Eu, P., Jackson, P., Hong, E., Binns, D., Iravani, A., Murphy, D., Mitchell, C., Siva, S., Hicks, R. J., Young, J. D., Blower, P., and Mullen, G. E. (2017) Cold Kit PSMA PET Imaging: Phase I study of ^{68}Ga-THP-PSMA PET/CT in patients with prostate cancer. *J. Nucl. Med.* (ahead of print, doi:10.2967/jnumed.117.199554).

Supplementary information

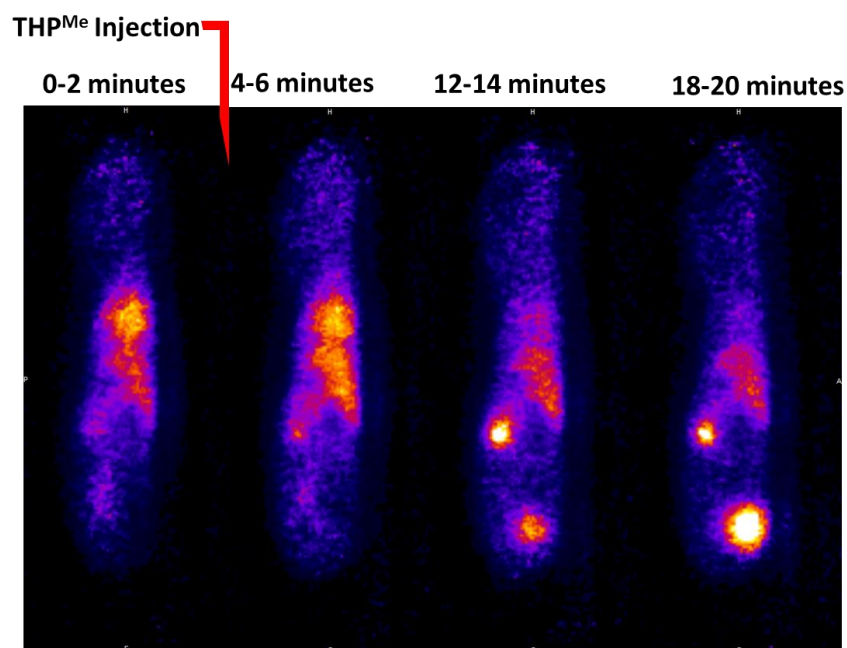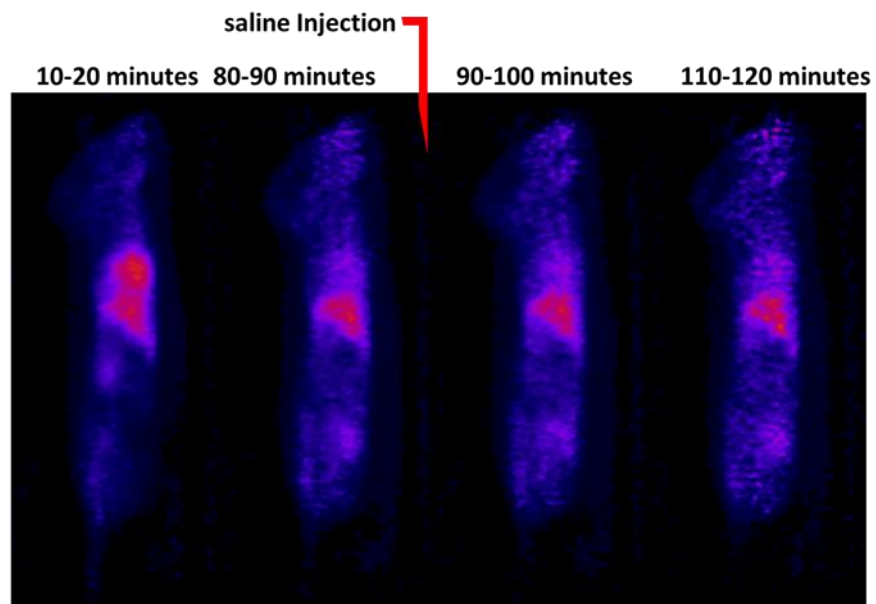**PET images of mice injected with THP^{Me} at 5 minutes after ^{68}Ga injection**

A)
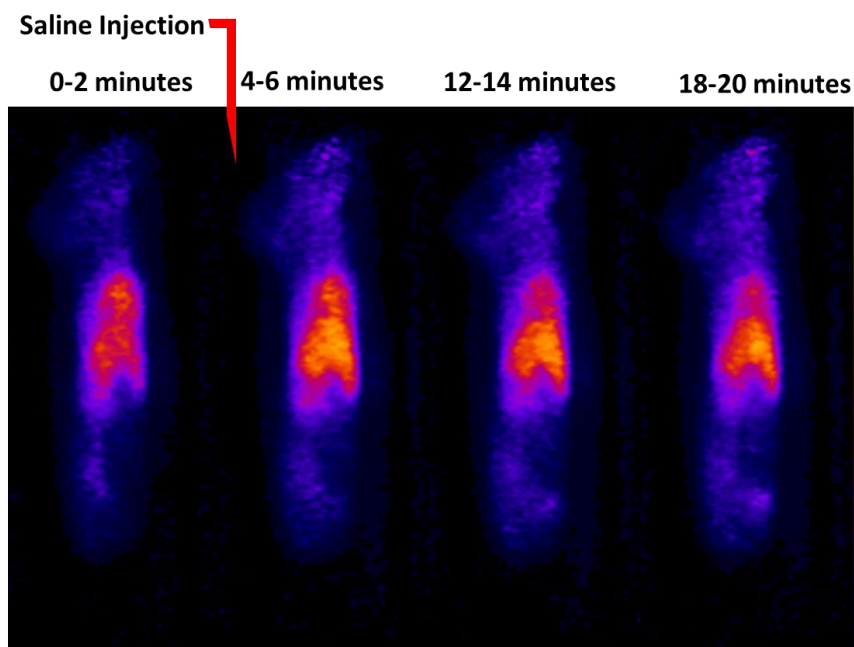
B)

Figure S 1. *PET images (sagittal view) for healthy mice injected with 0 µg (A) or 20 µg (B) of THP^{Me} 5 minutes after injection of ^{68}Ga.*

PET images of mice injected with THP^{Me} at 90 minutes after ⁶⁸Ga injection
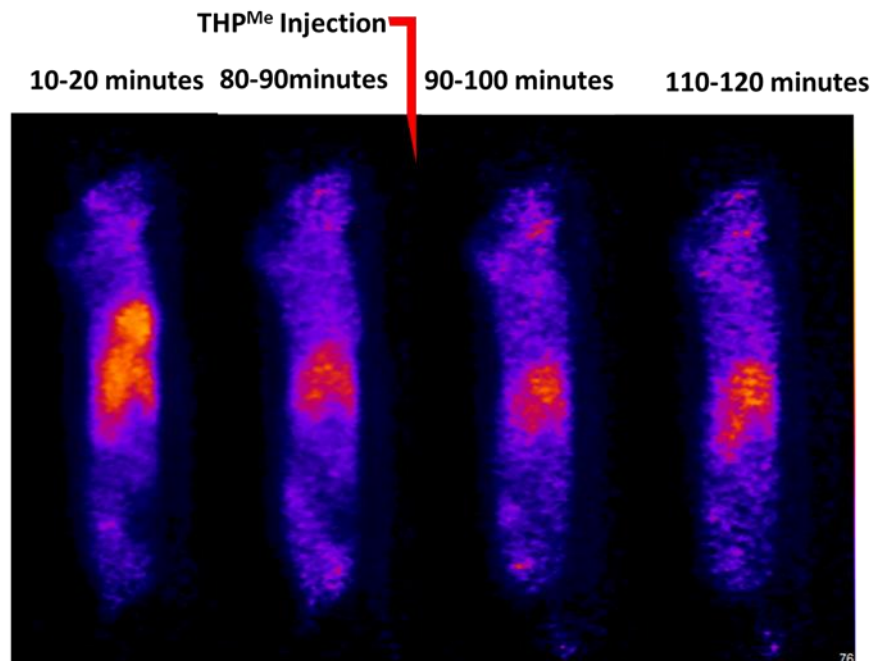
A)

B)

Figure S 2. PET images (sagittal view) for healthy mice injected with 0 µg (A) or 20 µg (B) of THP^{Me} 90 minutes after injection of ⁶⁸Ga.